NASA/TM–20210011034

Computational Analysis of the X-57 Maxwell Airplane at Unpowered Conditions (Preliminary Fuselage)

Karen A. Deere, Jeffrey K. Viken, Sally A. Viken and Melissa B. Carter
NASA Langley Research Center, Hampton, Virginia

Michael R. Wiese and Norma L. Farr
Craig Technologies, Hampton, Virginia

April 2022

NASA STI Program Report Series

Since its founding, NASA has been dedicated to the advancement of aeronautics and space science. The NASA scientific and technical information (STI) program plays a key part in helping NASA maintain this important role.

The NASA STI program operates under the auspices of the Agency Chief Information Officer. It collects, organizes, provides for archiving, and disseminates NASA's STI. The NASA STI program provides access to the NTRS Registered and its public interface, the NASA Technical Reports Server, thus providing one of the largest collections of aeronautical and space science STI in the world. Results are published in both non-NASA channels and by NASA in the NASA STI Report Series, which includes the following report types:

- TECHNICAL PUBLICATION. Reports of completed research or a major significant phase of research that present the results of NASA Programs and include extensive data or theoretical analysis. Includes compilations of significant scientific and technical data and information deemed to be of continuing reference value. NASA counterpart of peer-reviewed formal professional papers but has less stringent limitations on manuscript length and extent of graphic presentations.
- TECHNICAL MEMORANDUM. Scientific and technical findings that are preliminary or of specialized interest, e.g., quick release reports, working papers, and bibliographies that contain minimal annotation. Does not contain extensive analysis.
- CONTRACTOR REPORT. Scientific and technical findings by NASA-sponsored contractors and grantees.
- CONFERENCE PUBLICATION. Collected papers from scientific and technical conferences, symposia, seminars, or other meetings sponsored or co-sponsored by NASA.
- SPECIAL PUBLICATION. Scientific, technical, or historical information from NASA programs, projects, and missions, often concerned with subjects having substantial public interest.
- TECHNICAL TRANSLATION. English-language translations of foreign scientific and technical material pertinent to NASA's mission.

Specialized services also include organizing and publishing research results, distributing specialized research announcements and feeds, providing information desk and personal search support, and enabling data exchange services.

For more information about the NASA STI program, see the following:

- Access the NASA STI program home page at http://www.sti.nasa.gov
- Help desk contact information:

https://www.sti.nasa.gov/sti-contact-form/
and select the "General" help request type.

NASA/TM–20210011034

Computational Analysis of the X-57 Maxwell Airplane at Unpowered Conditions (Preliminary Fuselage)

Karen A. Deere, Jeffrey K. Viken, Sally A. Viken and Melissa B. Carter
NASA Langley Research Center, Hampton, Virginia

Michael R. Wiese and Norma L. Farr
Craig Technologies, Hampton, Virginia

National Aeronautics and
Space Administration

Langley Research Center
Hampton, Virginia 23681-2199

April 2022

Acknowledgments

Resources supporting this work were provided by the NASA High-End Computing (HEC) Program through the NASA Advanced Supercomputing (NAS) Division at Ames Research Center. The authors appreciate the HEC program and NAS because this work would not have been possible without these critical resources and support staff. Additionally, the authors thank Paul Yoo of NASA Ames for sharing results and a surface mesh, which was critical in determining the geometry differences in the fuselage of the configurations used in STAR-CCM+ and USM3D solutions.

Available from:

NASA STI Program / Mail Stop 148
NASA Langley Research Center
Hampton, VA 23681-2199
Fax: 757-864-6500

Abstract

The X-57 Maxwell is an all-electric airplane that implements a distributed electric propulsion system to demonstrate that high-efficiency electric propulsion can be integrated with aerodynamics to increase the performance of an airplane. To this end, distributed electric fans were installed on the wing to provide increased flow over the wing at the low takeoff and landing speeds of the X-57. The low-speed lift augmentation allows for a reduction in wing area for cruise optimization. The X-57 wing area was reduced to 42 percent of the wing area of the baseline aircraft, a Tecnam P2006T. With this reduced wing area and the electric propulsion system, it is estimated that the X-57 will cruise on less than one-third the total energy compared to the baseline aircraft. To meet the cruise performance goal at a Mach number of 0.233 at an altitude of 8000 feet, the X-57 has a cruise lift coefficient of 0.7516 and needs to have a cruise drag coefficient of 0.05423 or less. The USM3D computational solver was used to investigate the X-57 performance, without the distributed electric propulsion high-lift system operating. The unpowered X-57 performance is of interest to quantify if the X-57 can meet the cruise drag performance goal, and to document the lift performance of the very small wing at takeoff and landing conditions. The primary configurations investigated in this paper include the cruise configuration with no flap deflection, a takeoff configuration with a 10° flap deflection, and a landing configuration with a 30° flap deflection. The conditions for the cruise configuration were a flight unit Reynolds number of 1.32E+06 per foot, an altitude of 8000 feet, a Mach number of 0.233, and angles of attack from $-2°$ to 24°. At the cruise lift coefficient of 0.7516, the computed drag coefficient is 0.05275. This computed drag is less than the drag coefficient of 0.05423 that is required to meet the X-57 airplane performance goal. However, the computational airplane is a completely smooth geometry and does not account for protuberance drag, nor the drag from steps and gaps in the actual X-57 airplane. Therefore, based upon the CFD drag calculation there is a 10-percent margin to account for some of the differences between the as-built metal fuselage and empennage construction, and the smooth computational geometry. The computed cruise drag also does not account for an induced drag reduction due to the wing-tip propellers and a drag reduction due to laminar flow achieved on the wing. The computed lift to drag ratio is 14.14 at the cruise lift coefficient of 0.7516, and the maximum computed lift to drag ratio is 15.8. The maximum lift coefficient for the cruise configuration was 2.13 at an angle of attack of 15°. The conditions for the takeoff configuration with a 10° flap deflection were a flight unit Reynolds number of 0.986E+06 per foot, an altitude of 2500 feet, a Mach number of 0.149, and angles of attack from $-2°$ to 22°. The maximum lift coefficient for the takeoff configuration was 2.21 at an angle of attack of 16°. The conditions for the landing configuration with a 30° flap deflection were a flight unit Reynolds number of 0.922E+06 per foot, an altitude of 2500 feet, a Mach number of 0.139, and angles of attack from $-2°$ to 24°. The maximum lift coefficient for the landing configuration was 2.58 and occurred at two angles of attack, 10° and 14°. Based on the unpowered maximum lift coefficient of 2.58 for the 30° flap deflection, along with computations of the distributed electric propulsion lift augmentation (not shown in this paper), the X-57 Maxwell is estimated to meet its powered landing goal of a maximum lift coefficient of 4.0.

Contents

List of Figures

List of Tables

Nomenclature

α = angle of attack, degrees, Figure 8
a_∞ = freestream speed of sound, feet/second
b_{ref} = reference span, inches
β = angle of sideslip, degrees, Figure 8
$cfl1$ = numerical field in USM3D input file representing the minimum CFL number
$cfl2$ = numerical field in USM3D input file representing the maximum CFL number
c_{ref} = reference chord, mean aerodynamic chord, 25.56 inches
C_L = lift coefficient = lift force / (q_∞ S_{ref})
$C_{L,max}$ = maximum lift coefficient = maximum lift force / (q_∞ S_{ref})
C_D = drag coefficient = drag force / (q_∞ S_{ref})
C_Y = side force coefficient = side force / (q_∞ S_{ref})
C_l = rolling moment coefficient = rolling moment / (q_∞ S_{ref} c_{ref})
C_m = pitching moment coefficient = pitching moment / (q_∞ S_{ref} c_{ref})
C_n = yawing moment coefficient = yawing moment / (q_∞ S_{ref} b_{ref})
C_p = pressure coefficient = ($p - P_\infty$) / (q_∞)
δ_1 = height of the first node off the surface, inches
$delta_t$ = time step used for nondimensionalization in USM3D, Equation 3, inch/step
$D_{t,char}$ = distance a signal travels in one time step, Equation 2, inch/step
γ = gamma, specific heat ratio
$log(r/r0)$ = log scale L2-norm of the mean flow residue, normalized by the initial value
$log(tnu/tnu0)$ = log scale L2-norm of the turbulent residue, normalized by the initial value
L/D = lift to drag ratio
L_{char} = characteristic length, inches
M = freestream Mach number
N = number of time steps
P = pressure, generic expression, psf
P_∞ = freestream static pressure, psf
q_∞ = freestream dynamic pressure = ρ V^2 / 2, psf
ρ_∞ = freestream density, slugs/feet^3
Re = unit Reynolds number, per foot
Re_c = Reynolds number based on reference chord
$ReUe$ = freestream Reynolds number per unit length, specified in millions
$R1$ = grid growth rate 1
$R2$ = grid growth rate 2
S_{ref} = reference area, 66.67 feet^2
s = primary length scale at the source center
S = stretched length scale at the source center
T = temperature, °F
T_∞ = freestream temperature, °F
u = dimensional velocity, feet/second
U = nondimensional velocity used in USM3D = u / a_∞
V_∞ = freestream velocity, feet/second or fps
x, y, z = Cartesian coordinates, inches
xmc = moment center in X-direction (streamwise direction), inches
ymc = moment center in Y-direction (spanwise direction), inches
y^+_{cell} = nondimensional height of the first cell in the boundary layer

y^+_{node} = nondimensional height of the first node in the boundary layer
zmc = moment center in Z-direction (normal direction), inches

Acronyms and Abbreviations

CAD	Computer Aided Design
CFL	Courant–Friedrichs–Lewy [number]
DEP	Distributed Electric Propulsion
GB	Gigabyte
GEOLAB	GEOmetry LABoratory
KCAS	Knots Calibrated Airspeed
KEAS	Knots Equivalent Airspeed
KTAS	Knots True Airspeed
LE	Leading Edge
LES	Large Eddy Simulation
LGC	Landing Gear Cover
NASA	National Aeronautics and Space Administration
NPS	Nacelles, Pylons, Strakes
POR	percent over range convergence equation
RANS	Reynolds-averaged Navier-Stokes (equations)
SA	Spalart-Allmaras [turbulence model]
TB	Terabyte
TN	Wing-Tip Nacelle
QCR	Quadratic Constitutive Relation
TetrUSS	NASA Tetrahedral Unstructured Software System
VG	Vortex Generator

1 Introduction

The X-57 Maxwell is an all-electric airplane that will use a distributed electric propulsion (DEP) system to increase lift at takeoff and landing conditions, and will cruise efficiently at a Mach number of 0.233 (150 knots true airspeed (KTAS)) at an altitude of 8,000 feet (Refs. [1–3]). A concept image of the X-57 Maxwell aircraft is shown in Figure 1. The DEP system includes twelve high-lift, electrically-powered propellers that are positioned along the wing leading edge, used to increase the dynamic pressure over the wing for a boost of lift at takeoff and landing conditions. The high-lift propellers fold conformally onto the high-lift nacelles at cruise conditions to minimize drag when the DEP system is not needed. The electrically-powered cruise propellers are located on the wing-tip nacelles. Some previous computational results on earlier variations of the airplane are discussed in Refs. [4–10].

The NASA and industry X-57 Maxwell team are researching the airplane to determine if the emission-free airplane is also a more efficient design than the predecessor airplane, the Tecnam P2006T. The primary goal of the X-57 project is to demonstrate an approximately 5x lower energy use compared to the Tecnam P2006T, with a minimum goal of a 3x energy reduction (Ref. [1]). The lower energy use comes from a combination of improved aerodynamic efficiency from reducing the wing area, an improvement in motor efficiency, and an improvement in propulsion efficiency from the wing-tip propeller operating opposite the wing-tip vortex to reduce drag. To meet the cruise performance goal at a Mach number of 0.233 and at an altitude of 8000 feet, the X-57 has a cruise lift coefficient of 0.7516 and needs to have a cruise drag coefficient of 0.05423 or less. A derivative objective is a 30 percent reduction in total operating cost with zero in-flight carbon emissions. One of the secondary objectives includes a 15 dB reduction in noise compared to the P2006T airplane when measured by ground assets. The X-57 Maxwell airplane will follow the noise certification procedure for propeller-powered general aviation aircraft. The certification point is a flyover that is 8,202 feet down the takeoff flight path from the start of ground roll. The certification procedure requires takeoff at maximum weight, takeoff power maintained until a 50-foot obstacle is cleared, using best climb speed, with flap and gear retracted in the second segment of climb, and a maximum power maintained throughout the second segment of climb.

In the X-57 Maxwell project, the development and analysis of the airplane was divided into four phase modifications or Mods, with each phase (Mod) focusing on a different aircraft configuration. The Mod 1 aircraft configuration is the original Tecnam P2006T aircraft, shown in Figure 2. The P2006T aircraft has a wing loading of 17 psf, a wing span of 37.4 feet, a root chord of 4.57 feet (54.84 inches), and a tip chord of 2.9 feet (34.8 inches). The Mod 2 aircraft configuration is an electric version of the P2006T, with electric motors and X-57 cruise propellers replacing the original combustion engines and propellers on the P2006T aircraft. A front view of the Mod 2 configuration with the electric motors running is shown in Figure 3. The Mod 2 aircraft configuration will be tested at the NASA Armstrong Flight Research Center for engine safety and service during taxi tests, and then will be flight tested to certify the electric motors, the batteries and the instrumentation. For the Mod 3 aircraft configuration, the wing from the P2006T aircraft will be replaced with the X-57 wing and the Mod 2 electric cruise motors and propellers will be moved out to the wing-tip nacelles, see Figure 4. Finally, the Mod 4 aircraft configuration has the 12 high-lift motors and propellers integrated into the smaller wing of the X-57 aircraft for the final, all-electric X-57 Maxwell aircraft, see Figure 5. Again, the high-lift propellers will only be operational at takeoff and landing conditions to produce the extra lift needed on the smaller wing at low airspeeds. The X-57 Maxwell airplane has a higher wing loading of 45 psf, a smaller wing span of 31.6 feet (379.47 inches) and a shorter mean aerodynamic chord of 2.13 feet (25.56 inches) than the original Tecnam P2006T airplane.

The X-57 Maxwell airplane has only 42 percent of the wing area of the original Tecnam P2006T wing, but with an increased gross weight. The increased gross weight was determined by accounting for the increased weight of the batteries compared to the original Tecnam engines and gas tanks. The primary driver of reducing the wing area was to reduce drag and increase the efficiency of the X-57. The smaller wing area reduces the total wetted area and the skin friction drag. The wing aspect ratio was increased from 8.8 to 15.0 for the X-57 to minimize the induced drag penalty of the increased gross weight. The minimum wing area was determined based upon the limits of the powered high-lift augmentation, wing structural stiffness, and wing internal volume. The X-57 wing loading is 2.5 times the original Tecnam P2006T airplane. The X-57 will experience smaller g-loadings in gusts with such a large increase in wing loading compared to the original Tecnam P2006T airplane. For airplanes with the propeller plane behind the center of gravity (CG), the tip mounted propellers can be stabilizing (Ref. [11]). The X-57 tip-mounted propellers are ahead of the CG, and should reduce the directional stability in gusts. The directional stability of the X-57 airplane with the tip mounted propellers will be evaluated in the flight tests.

The purpose of this paper was to document the performance of the X-57 Maxwell aircraft, Mod 3 configuration at unpowered and unblown conditions using the computational fluid dynamics (CFD) software, USM3D. The primary configurations investigated in this paper include a cruise configuration with no flap deflection, a takeoff configuration with a 10° flap deflection, and a landing configuration with a 30° flap deflection. The cruise configuration with an undeflected flap was computed at a flight unit Reynolds number (*Re*) of Re = 1.32E+06/ft for an altitude of 8000 feet, a Mach number (M) of $M = 0.233$ or 133 knots calibrated airspeed (KCAS) or 150 knots true airspeed (KTAS), and angles of attack (α) from $\alpha = -2°$ to $\alpha = 24°$. The takeoff configuration with a 10° flap was computed at $Re = 0.986\text{E}{+}06/\text{ft}$ for an altitude of 2500 feet, $M = 0.149$ (94 KCAS, 97.5 KTAS), and angles of attack from $\alpha = -2°$ to $\alpha = 22°$. The landing configuration with a 30° flap deflection was computed at $Re = 0.922\text{E}{+}06/\text{ft}$ for an altitude of 2500 feet, $M = 0.139$ (88 KCAS, 91.3 KTAS), and angles of attack from $\alpha = -2°$ to $\alpha = 24°$.

Results from the CFD flow solvers LAVA and STAR-CCM+ at the same conditions are published in Ref. [12], however, the fuselage geometry at the wing root for the configuration discussed in this paper is slightly different than the fuselage used with LAVA and STAR-CCM+. The configurations herein used the OpenVSP analytic fuselage geometry (preliminary fuselage), while a wind-tunnel model fuselage geometry was scaled up to full size for the LAVA and STAR-CCM+ solutions. The geometries compare well except for the fuselage-wing-root junction where the smaller X-57 wing replaced the larger P2006T wing. The results from LAVA and STAR-CCM+ were computed with a local time stepping or steady-state Reynolds-averaged Navier-Stokes (RANS) approach, while the current solutions were computed with global time stepping or time-accurate RANS approach. A time-accurate RANS approach was believed to be more appropriate for high-lift configurations near stall and for configurations with flow separation, as was expected for the X-57 Maxwell airplane. However, it may take a hybrid model of RANS combined with a Large Eddy Simulation (LES) approach to more accurately predict $C_{L,max}$ and stall.

Since there are no reliable experimental performance data for the X-57 airplane, the CFD results from three NASA centers (Langley, Armstrong and Ames) were compared to establish some uncertainty bounds for the force and moment coefficients. The NASA Langley Research Center used the Langley developed USM3D code. The NASA Armstrong Flight Research Center used the commercially developed STAR-CCM+ code. The NASA Ames Research Center used the Ames developed LAVA code. The CFD data were provided to the controls group for the piloted simulator software and were also used in the critical design review.

This is the first paper in a series of NASA technical memorandum papers from NASA Langley on the X-57 Maxwell airplane. The first set of papers will discuss results using the preliminary fuselage that was available the first three years of the project. This paper documenting the unblown and unpowered performance will be followed by a paper showing the results for the X-57 with cruise power, and then with a paper showing results for the X-57 with high-lift blowing across the wing. Finally, the second set of papers will include the X-57 flight fuselage and fairing. This second set of papers with the flight fuselage will show the effects of the flight fuselage as compared to the preliminary fuselage, the effects of motor failures with and without aileron deflections, and the effects of the updated takeoff flap setting to 20°, on the aerodynamic coefficients.

Figure 1. Concept Image of the X-57 Maxwell Airplane.

Figure 2. Mod 1, the Tecnam P2006T Airplane.

Figure 3. Mod 2, the Tecnam P2006T Airplane with Electric Cruise Motors.

Figure 4. Concept Image of Mod 3, the X-57 Maxwell Airplane with Cruise Propellers Operating and High-Lift Propellers Stowed.

Figure 5. Concept Image of Mod 4, the X-57 Maxwell Airplane with Cruise Propellers and High-Lift Propellers Operating.

2 Methods Description

This section describes the details for generating the computational data in this report. The NASA Tetrahedral Unstructured Software System (TetrUSS) (Ref. [13]) developed at the NASA Langley Research Center (LaRC) was used for this computational study. TetrUSS includes a model preparation tool called GridTool (Ref. [14]), the grid generation software codes called VGRID and POSTGRID, and the computational flow solver called USM3D. The USM3D flow solver has internal software to calculate forces and moments. Additionally, the NASA Langley-developed codes USMC6 (Ref. [15]) and Tet2Tec were used for analyzing the solutions. Unfortunately, the VGRID and POSTGRID codes have not been maintained for years. Therefore, the authors added the HeldenMesh grid generation software (Ref. [16]), developed by Helden Aerospace Inc., to their set of tools. Recently, colleagues at NASA Langley confirmed that the HeldenMesh software developed similar and improved meshes to those created with VGRID and POSTGRID for the Space Launch System (SLS) configuration (Ref. [17]). Additionally, the SLS grids made with HeldenMesh were generated within weeks instead of months with VGRID and POSTGRID, while obtaining qualitatively similar results (Ref. [17]).

2.1 Freestream Conditions

The freestream flow conditions studied in the paper are listed in Table 1. The USM3D inputs for the freestream flow conditions include Mach number, Reynolds number per unit length specified in millions ($ReUe$), and temperature. The landing configuration with the 30° flap deflection was computed for angles of attack from $\alpha = -2°$ to $\alpha = 24°$ at the 88 KCAS conditions. The takeoff configuration with the 10° flap deflection was computed for angles of attack from $\alpha = -2°$ to $\alpha = 22°$ at the 94 KCAS conditions. The cruise configuration with no flap deflection was computed for angles of attack from $\alpha = -2°$ to $\alpha = 24°$ at the 133 KCAS condition.

Table 1. Freestream Conditions for Each Configuration.

Configuration	$KCAS$	$Mach$	$Altitude$ (feet)	ρ_∞ (slugs/feet^3)	T_∞ (°F)	Re (1/ft)	$ReUe$ (E+06)
Landing	88	0.139	2500	0.002208	50.08	0.922E+06	0.07688
Takeoff	94	0.149	2500	0.002208	50.08	0.986E+06	0.08213
Cruise	133	0.233	8000	0.001868	30.47	1.320E+06	0.11002

2.2 Initial and Boundary Conditions

A no-slip boundary condition was used on all solid surfaces. For these subsonic flow conditions, a characteristic inflow and outflow boundary condition was used at the inflow face of the computational domain and at the downstream outflow face of the computational domain. The inflow boundary condition was implemented by setting the Mach number, the Reynolds number per unit length (specified in millions), and the temperature. A characteristic inflow and outflow boundary condition was used along the farfield boundaries of the computational domain. The characteristic boundary condition uses the fixed and extrapolated Riemann invariants of the incoming and outgoing waves along characteristic directions defined normal to the boundary. Local velocity components and the speed of sound are computed from the invariants, density is computed from the entropy relationship, and pressure is computed from the ideal gas law using the square of the speed of sound.

2.3 Input File and Solution Procedure

A typical input file for USM3D is shown in Figure 6. The parameters from the input file will be typed in parentheses in this section of the paper. For each USM3D solution, the flow conditions are specified with the freestream Mach number (Mach), the angle of attack in degrees (alpha), the sideslip angle in degrees (beta), the freestream Reynolds number per unit length specified in millions (ReUe), and the freestream temperature in degrees Rankine (Tinf, dR). For each geometric configuration, the user must specify the reference area (sref), the reference chord (cref), the reference span (bref), the moment center in the X-direction (xmc), the moment center in the Y-direction (ymc), and the moment center in the Z-direction (zmc). For this work, the configurations were made in units of inches within the grid. Therefore, the reference lengths (cref, bref, xmc, ymc, zmc) were specified in inches and the reference area was specified in square inches.

At the start of a new solution there is no restart file (irest = 0). Each solution was started with a local time stepping or steady-state Reynolds-averaged Navier-Stokes (RANS) approach (itimeacc = 0) for up to 15,000 iterations. Then, the solution was continued with global time stepping or time-accurate RANS approach (itimeacc = -2) until convergence or solution periodicity.

A typical input file for the steady-state RANS approach (itimeacc = 0) is shown in Figure 6. The Courant–Friedrichs–Lewy (CFL) number was typically adjusted from –1.0 (dt/cfl1 = -1.0) to 50 (cfl2 = 50), over 1000 iterations (iramp = 1000). The code was run without relaxation (crelax = 1.0) for the steady-state RANS approach. First-order spatial accuracy was used until the residual dropped two orders of magnitude, and then the code automatically switched to second-order spatial accuracy (iorder = -2). The number of iterations is set with the parameter ncyc (ncyc = 15000). If the solution was continued from a restart file, then irest = 1 and the CFL number remained constant at 50 (dt/cfl1 = cfl2 = 50, iramp = 0).

A typical input file for the time-accurate RANS approach (itimeacc = -2) is shown in Figure 7. The Newton 3-point backward differencing scheme (without pseudotime) was used with a relaxation coefficient (crelax = 0.7) and with second-order spatial accuracy (iorder = 2). In time-accurate mode, the time step (deltat), the number of steps (ntstep), and the number of subiterations (ncyc) become important, while the CFL settings are ignored. The nondimensional time step for the cruise configuration (deltat = 4.29) was chosen for a signal to pass over the aircraft in 1-inch increments. The number of steps varied per job submittal, but this example used 3400 steps (ntstep = 3400). For each time step, 15 subiterations (ncyc = 15) were used to allow the solution residuals to drop at least two orders of magnitude.

Finally, the turbulence model was specified with the ivisc parameter. The fully turbulent calculations were computed using the Spalart-Allmaras (SA) turbulence model (ivisc = 2) and the Spalart nonlinear shear stress model (iqcrflg = 1).

2.4 Computer Platform

All of the solutions were computed at the NASA Advanced Supercomputing (NAS) center at the NASA Ames Research Center. The Pleiades Supercomputer at NAS has 241,324 total cores with a total memory of 927 TB. The cruise configuration cases were set up to use 24 nodes or 560 total Haswell cores. The Haswell nodes have 128 GB per node. The takeoff and landing configuration cases were set up to use 30 nodes or 600 total Ivy cores. The Ivy nodes have 64 GB per node.

2.5 Coordinate System

The USM3D reference coordinate system is shown in Figure 8. The positive y-axis is aligned with the pilot's right wing. The positive x-axis must be in the direction of the freestream flow and the y-axis and z-axis must be specified normal to the x-axis. The angle of attack α or (alpha) is defined in the x-z plane and the sideslip angle β or (beta) is defined in the y-z plane.

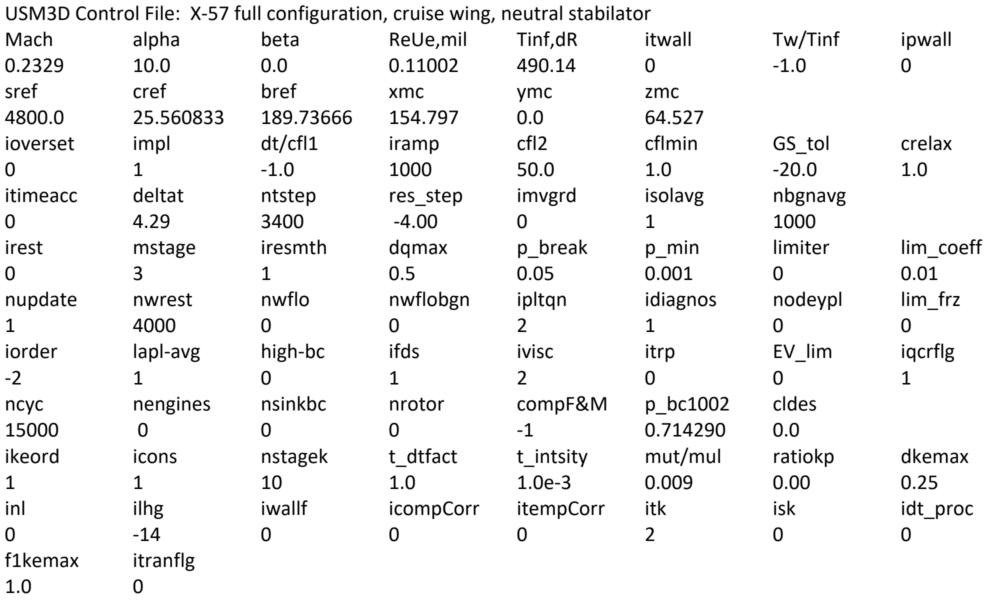

```
USM3D Control File:  X-57 full configuration, cruise wing, neutral stabilator
Mach         alpha        beta         ReUe,mil     Tinf,dR      itwall       Tw/Tinf      ipwall
0.2329       10.0         0.0          0.11002      490.14       0            -1.0         0
sref         cref         bref         xmc          ymc          zmc
4800.0       25.560833    189.73666    154.797      0.0          64.527
ioverset     impl         dt/cfl1      iramp        cfl2         cflmin       GS_tol       crelax
0            1            -1.0         1000         50.0         1.0          -20.0        1.0
itimeacc     deltat       ntstep       res_step     imvgrd       isolavg      nbgnavg
0            4.29         3400          -4.00       0            1            1000
irest        mstage       iresmth      dqmax        p_break      p_min        limiter      lim_coeff
0            3            1            0.5          0.05         0.001        0            0.01
nupdate      nwrest       nwflo        nwflobgn     ipltqn       idiagnos     nodeypl      lim_frz
1            4000         0            0            2            1            0            0
iorder       lapl-avg     high-bc      ifds         ivisc        itrp         EV_lim       iqcrflg
-2           1            0            1            2            0            0            1
ncyc         nengines     nsinkbc      nrotor       compF&M      p_bc1002     cldes
15000         0           0            0            -1           0.714290     0.0
ikeord       icons        nstagek      t_dtfact     t_intsity    mut/mul      ratiokp      dkemax
1            1            10           1.0          1.0e-3       0.009        0.00         0.25
inl          ilhg         iwallf       icompCorr    itempCorr    itk          isk          idt_proc
0            -14          0            0            0            2            0            0
f1kemax      itranflg
1.0          0
```

Figure 6. A Typical USM3D Input File for Running Steady-State RANS for the X-57 Maxwell Configuration.

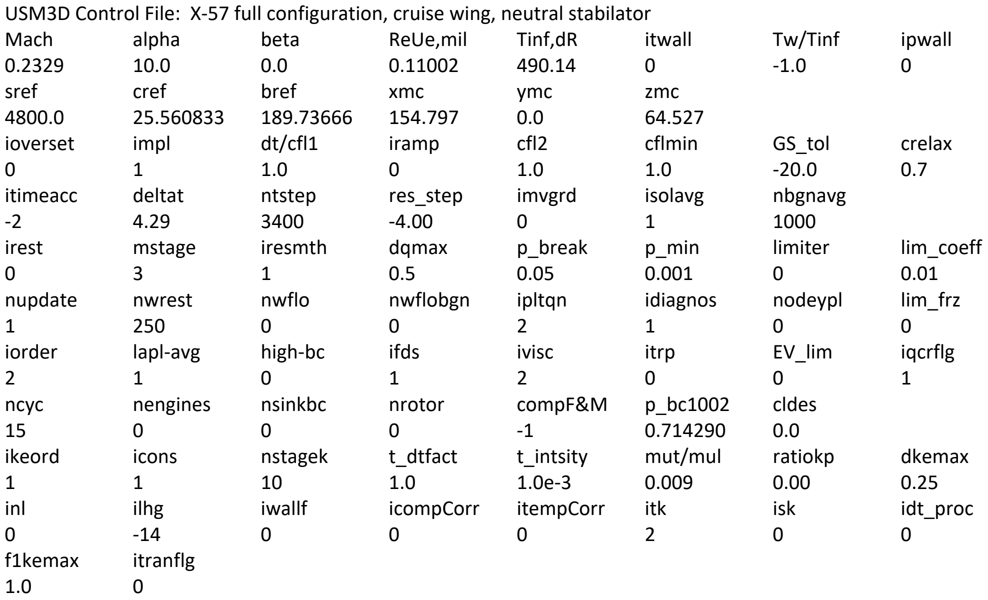

```
USM3D Control File:  X-57 full configuration, cruise wing, neutral stabilator
Mach         alpha        beta         ReUe,mil     Tinf,dR      itwall       Tw/Tinf      ipwall
0.2329       10.0         0.0          0.11002      490.14       0            -1.0         0
sref         cref         bref         xmc          ymc          zmc
4800.0       25.560833    189.73666    154.797      0.0          64.527
ioverset     impl         dt/cfl1      iramp        cfl2         cflmin       GS_tol       crelax
0            1            1.0          0            1.0          1.0          -20.0        0.7
itimeacc     deltat       ntstep       res_step     imvgrd       isolavg      nbgnavg
-2           4.29         3400         -4.00        0            1            1000
irest        mstage       iresmth      dqmax        p_break      p_min        limiter      lim_coeff
0            3            1            0.5          0.05         0.001        0            0.01
nupdate      nwrest       nwflo        nwflobgn     ipltqn       idiagnos     nodeypl      lim_frz
1            250          0            0            2            1            0            0
iorder       lapl-avg     high-bc      ifds         ivisc        itrp         EV_lim       iqcrflg
2            1            0            1            2            0            0            1
ncyc         nengines     nsinkbc      nrotor       compF&M      p_bc1002     cldes
15           0            0            0            -1           0.714290     0.0
ikeord       icons        nstagek      t_dtfact     t_intsity    mut/mul      ratiokp      dkemax
1            1            10           1.0          1.0e-3       0.009        0.00         0.25
inl          ilhg         iwallf       icompCorr    itempCorr    itk          isk          idt_proc
0            -14          0            0            0            2            0            0
f1kemax      itranflg
1.0          0
```

Figure 7. A Typical USM3D Input File for Running Time-Accurate RANS for the X-57 Maxwell Configuration.

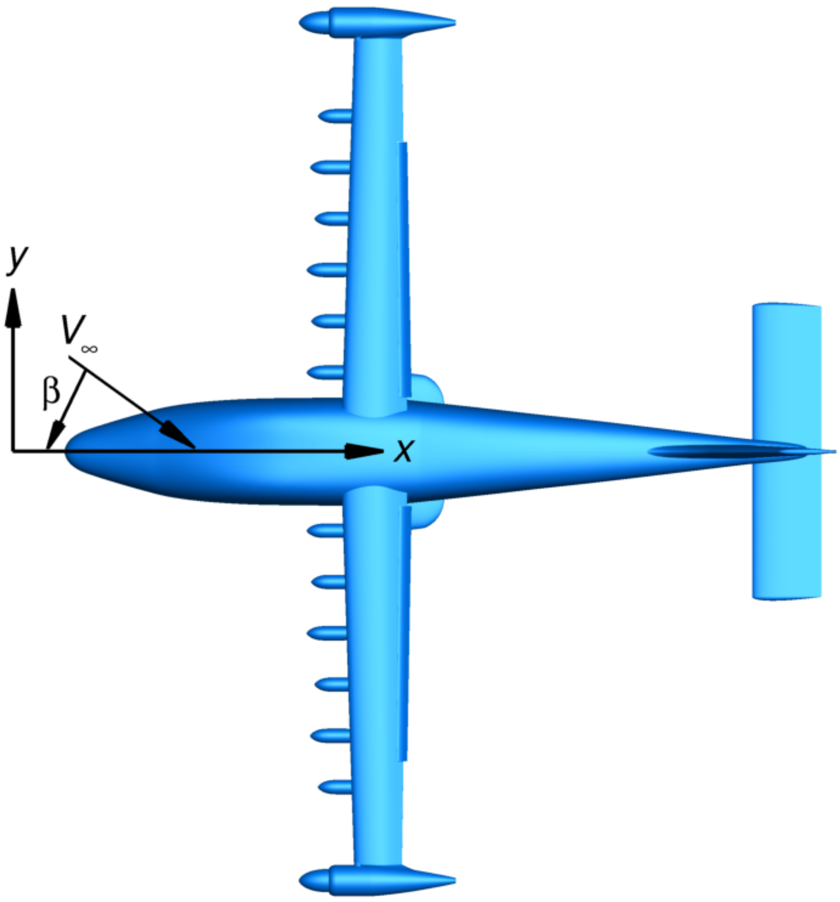

(a) Top View, XY Plane

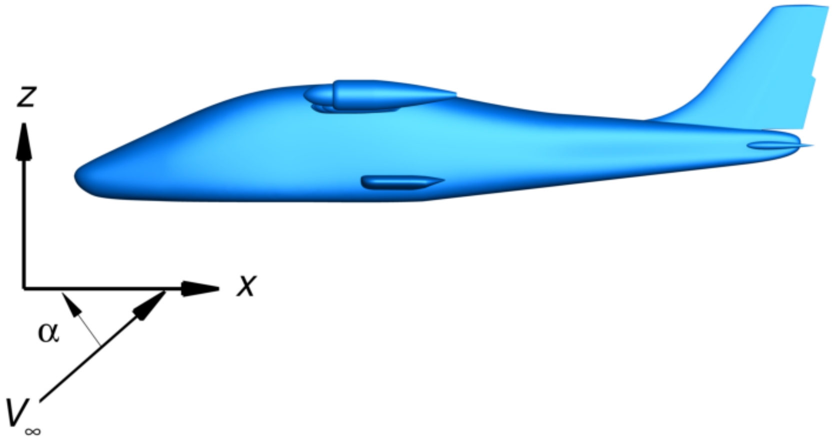

(b) Side View, XZ Plane

Figure 8. The USM3D Coordinate System.

2.6 Geometry

The Vehicle Sketch Pad (OpenVSP) software (Refs. [18, 19]) was used to generate the geometry of the unpowered X-57 Maxwell Mod 3 configuration, which had no high-lift blowing propellers nor cruise propellers. The X-57 Maxwell has a root chord that is nearly half the original Tecnam P2006T root chord (54.84 inches). Figure 9(a) shows a top down view of the airplane's wireframe with the Tecnam wing shaded blue and the X-57 wing shaded green (with a pink and blue arrow highlighting the boundary). Figure 9(b) shows an isometric view of the wing root region, with the larger Tecnam wing shaded blue and the smaller X-57 wing shaded green. Therefore, the intersection of the X-57 wing into the fuselage is completely different than the original Tecnam P2006T. The fit routine in the OpenVSP software was used to modify the original computer aided design (CAD) of the isolated fuselage, to define the new fuselage outer mold line (OML) using analytical curves in both the x-y and y-z planes. This fuselage will be referred to as the 'VSP fuselage'. The VSP fuselage was used for CFD computations at NASA Langley for the first three years before the actual X-57 flight fuselage geometry was available. During the structural design for the X-57 Maxwell, it was discovered that the VSP fuselage would not contain the hardware that was designed to attach the X-57 Mod 3 wing to the original Tecnam P2006T fuselage structure. A final 'X-57 fuselage' was designed to completely contain the structure required to support the wing. In follow-on papers, the final X-57 flight fuselage geometry will be modeled in NASA Langley computational results. However, this paper reports results for the X-57 Mod 3 geometry with the VSP fuselage.

The NASA LaRC GEOmetry LABoratory (GEOLAB) supported this effort by preparing the CAD geometry from OpenVSP for grid generation. The OpenVSP geometry was imported into the commercial CAD package, Siemens NX. All components were intersected; the flap bracket fairings were cleaned and trimmed for the flap setting to create a solid bracket volume. The final geometry was sewn together to create a single, water-tight configuration.

The shaded surface geometry for the X-57 Mod 3 configuration used in this computational work is shown in Figures 10 to 14. The cruise configuration with no flap deflection is shown in Figure 10, a takeoff configuration with a 10° flap deflection is shown in Figure 11, and a landing configuration with a 30° flap deflection is shown Figure 12. The landing gear cover is below the wing root, near the bottom of the fuselage. The horizontal stabilator is in the neutral position at 0°. All three configurations have the same wing-tip nacelle with vortex generator (VG) and a wing-tip fairing that is shown in Figure 13. A top-down view of the landing configuration with the 30° flap deflection is shown in Figure 14 to highlight the staggering of the high-lift nacelles, which is done to keep the propeller planes at different locations in case of propeller failure. The nacelle numbering scheme for the semispan configurations in this paper is also shown in Figure 14.

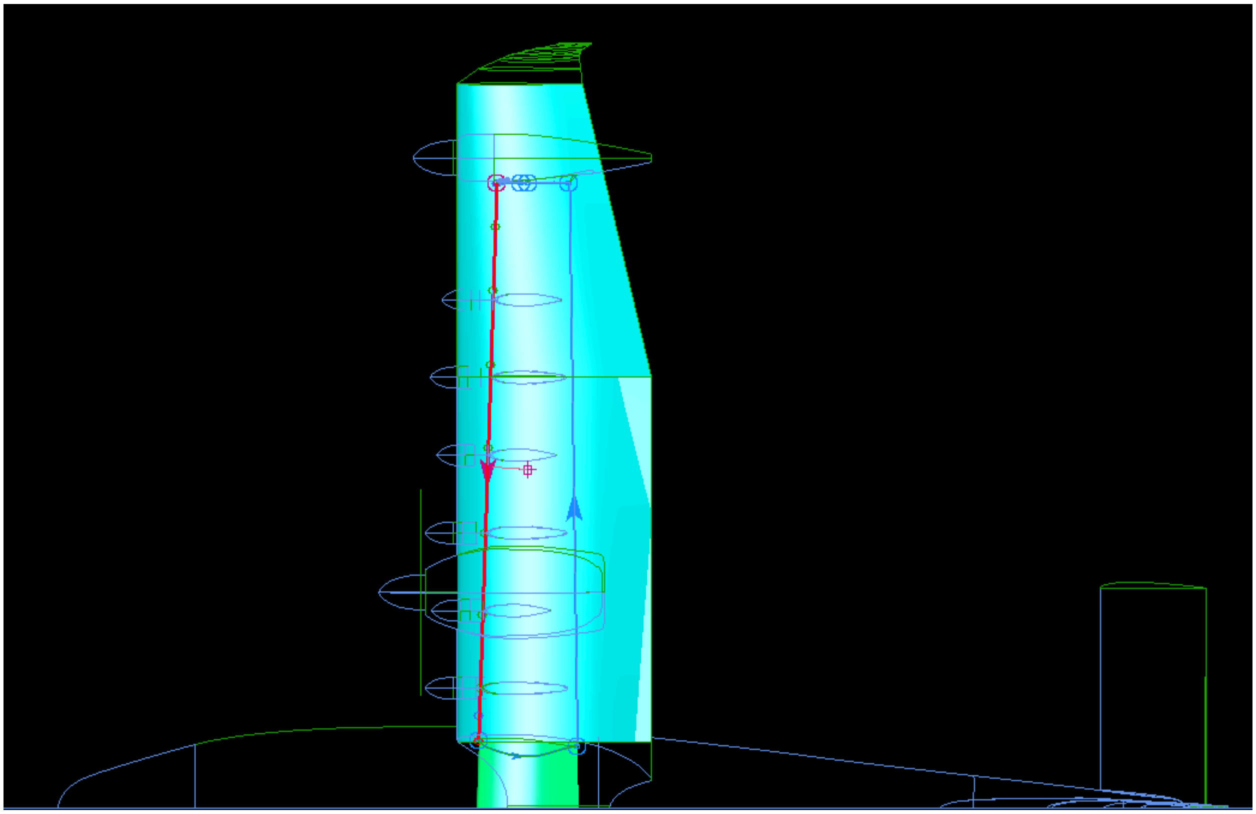

(a) Top Down View of the Smaller X-57 Wing Inside of the Tecnam Wing

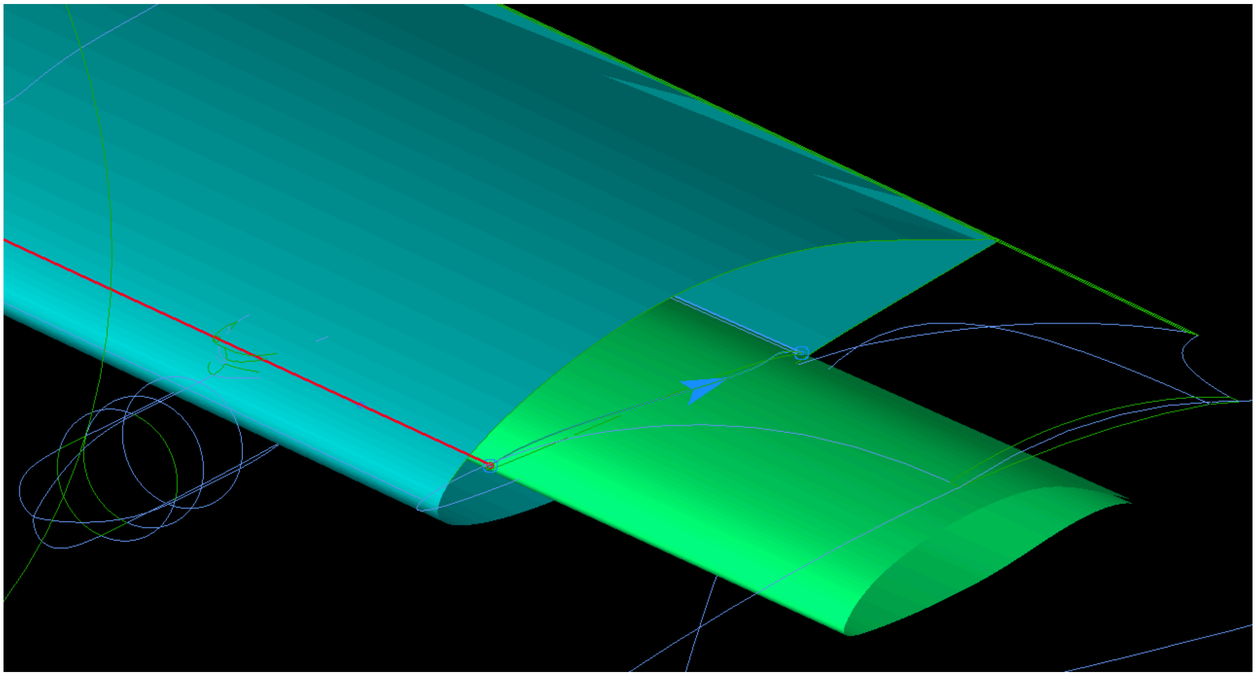

(b) Isometric View of Wing Root Region with the Smaller X-57 Wing Inside of the Tecnam Wing

Figure 9. Comparison of the Tecnam Wing (blue) and the X-57 Wing (green).

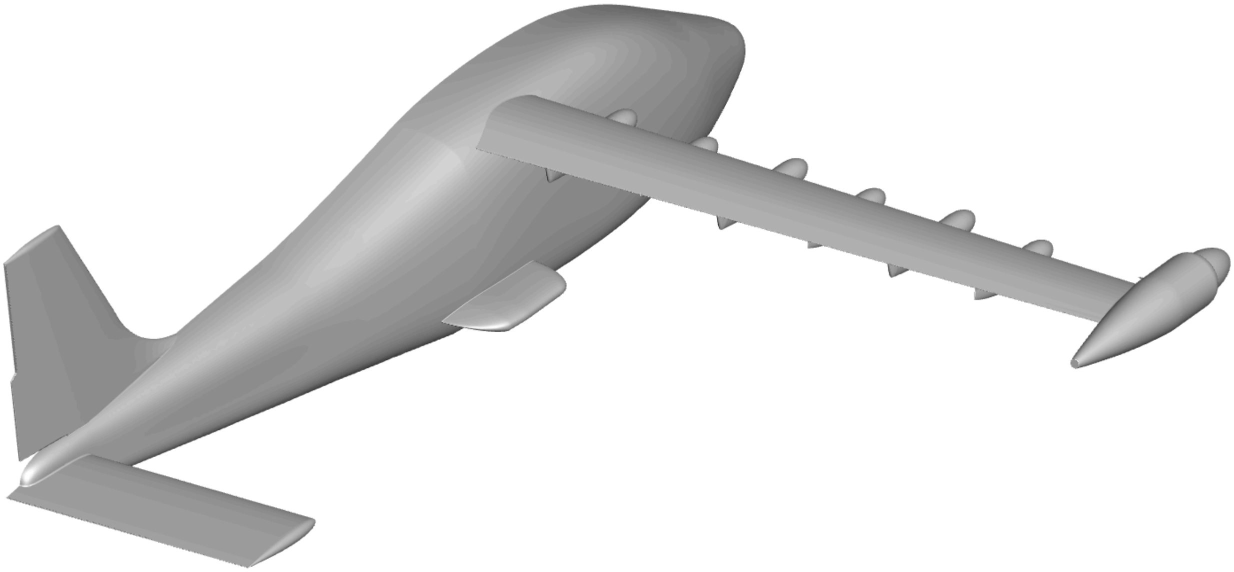

(a) Semispan Geometry

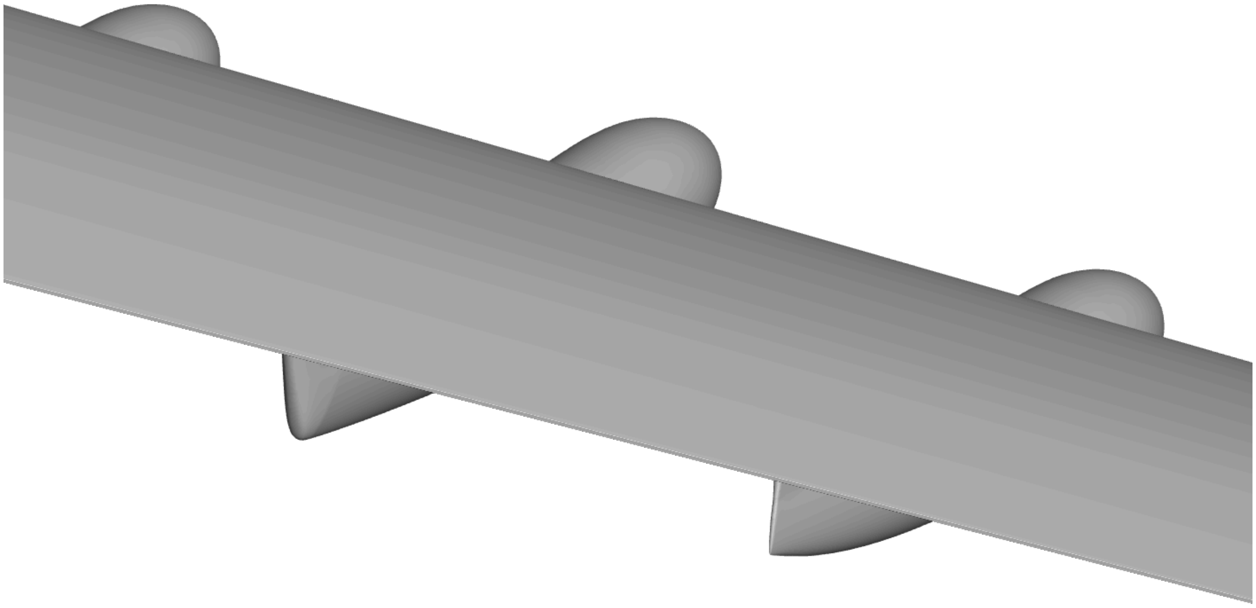

(b) No Flap Deflection

Figure 10. The Unpowered, X-57 Maxwell Mod 3 Cruise Configuration Geometry.

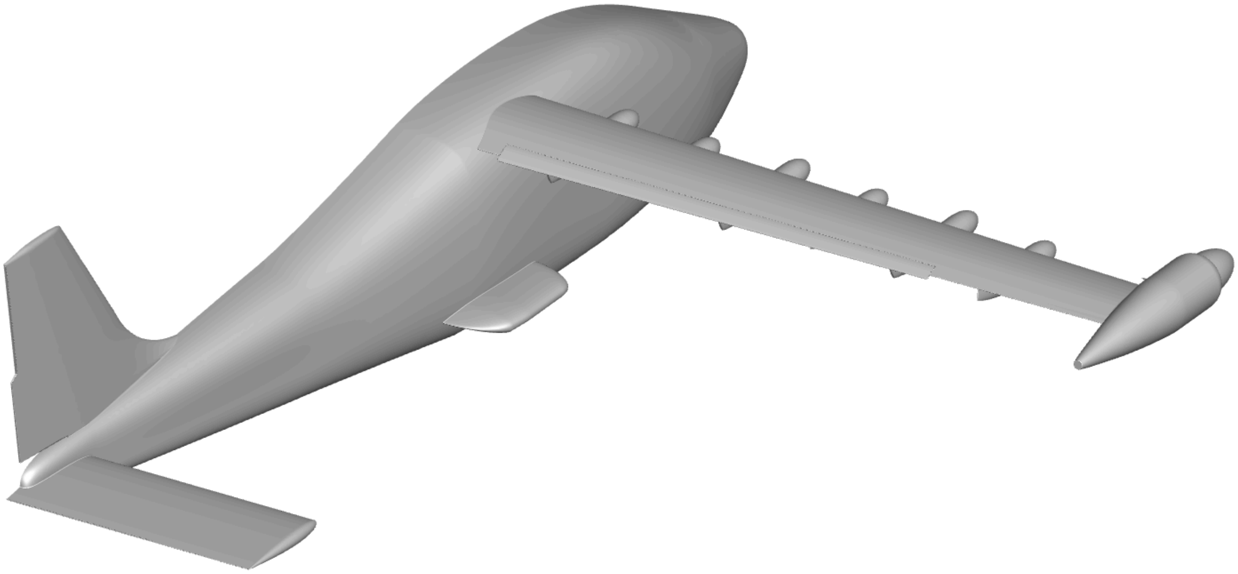

(a) Semispan Geometry

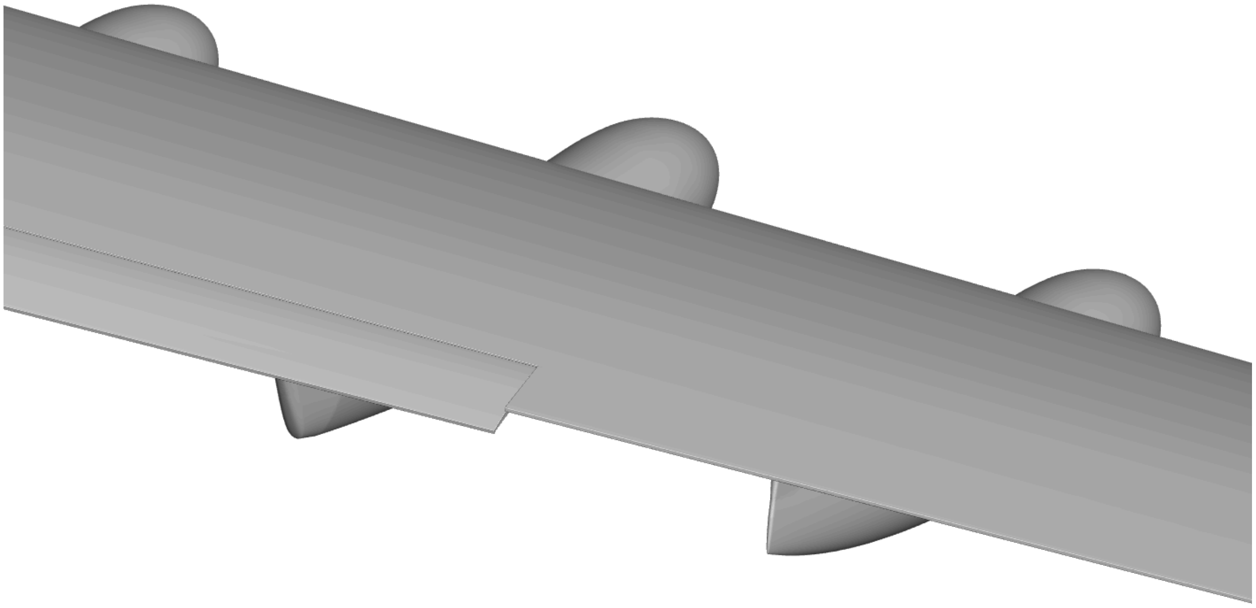

(b) 10° Flap Deflection

Figure 11. The Unpowered, X-57 Maxwell Mod 3 Takeoff Configuration Geometry.

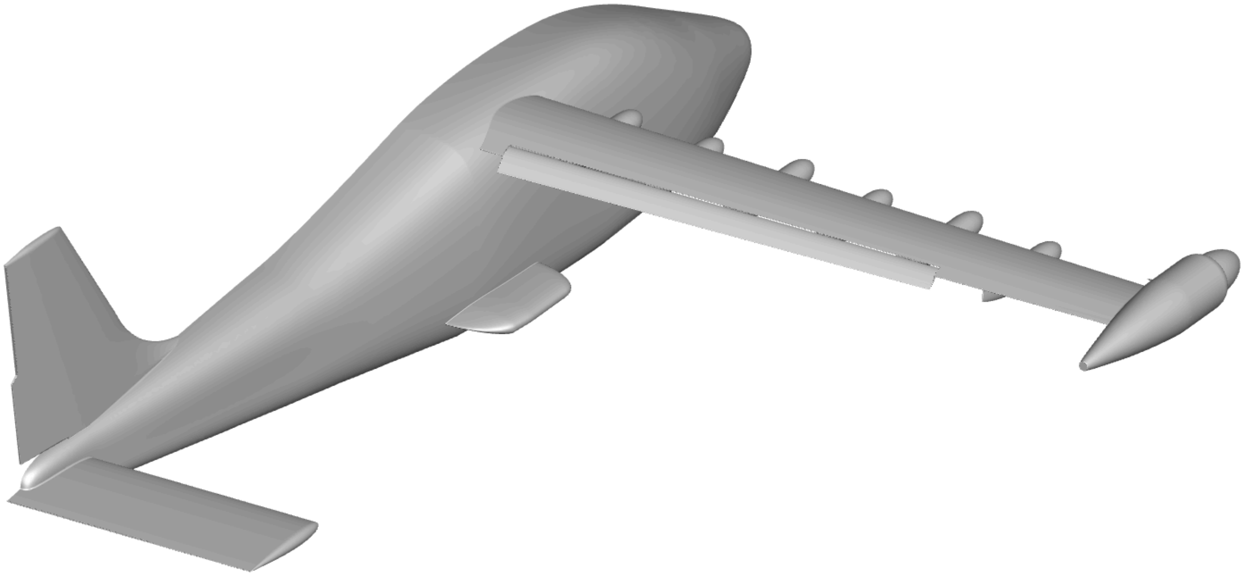

(a) Semispan Geometry

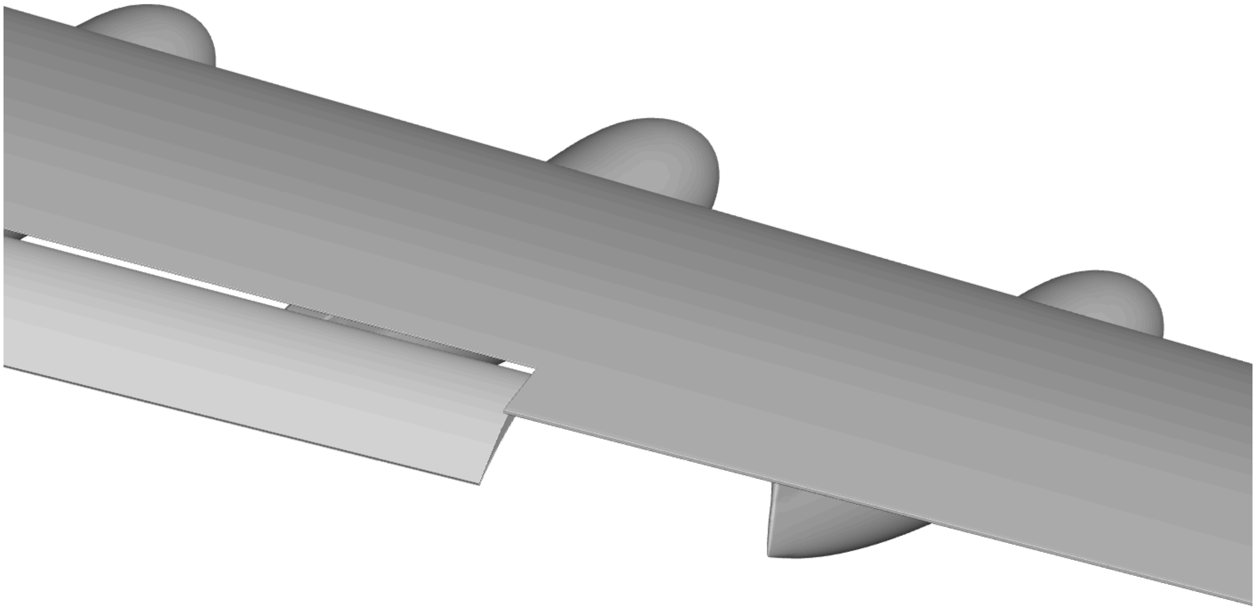

(b) 30° Flap Deflection

Figure 12. The Unpowered, X-57 Maxwell Mod 3 Landing Configuration Geometry.

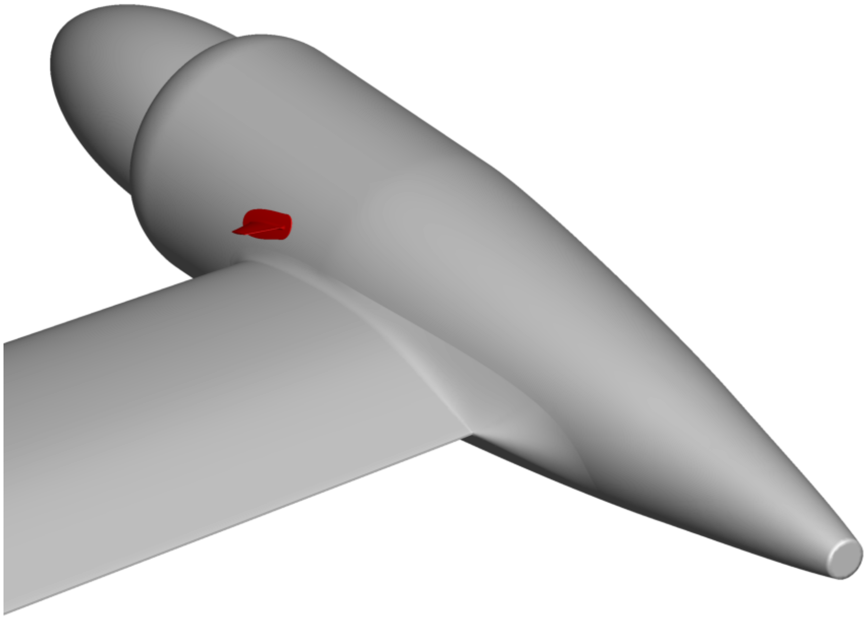

Figure 13. The Wing-Tip Nacelle, Wing-Tip Fairing, and Vortex Generator (Shown in Red).

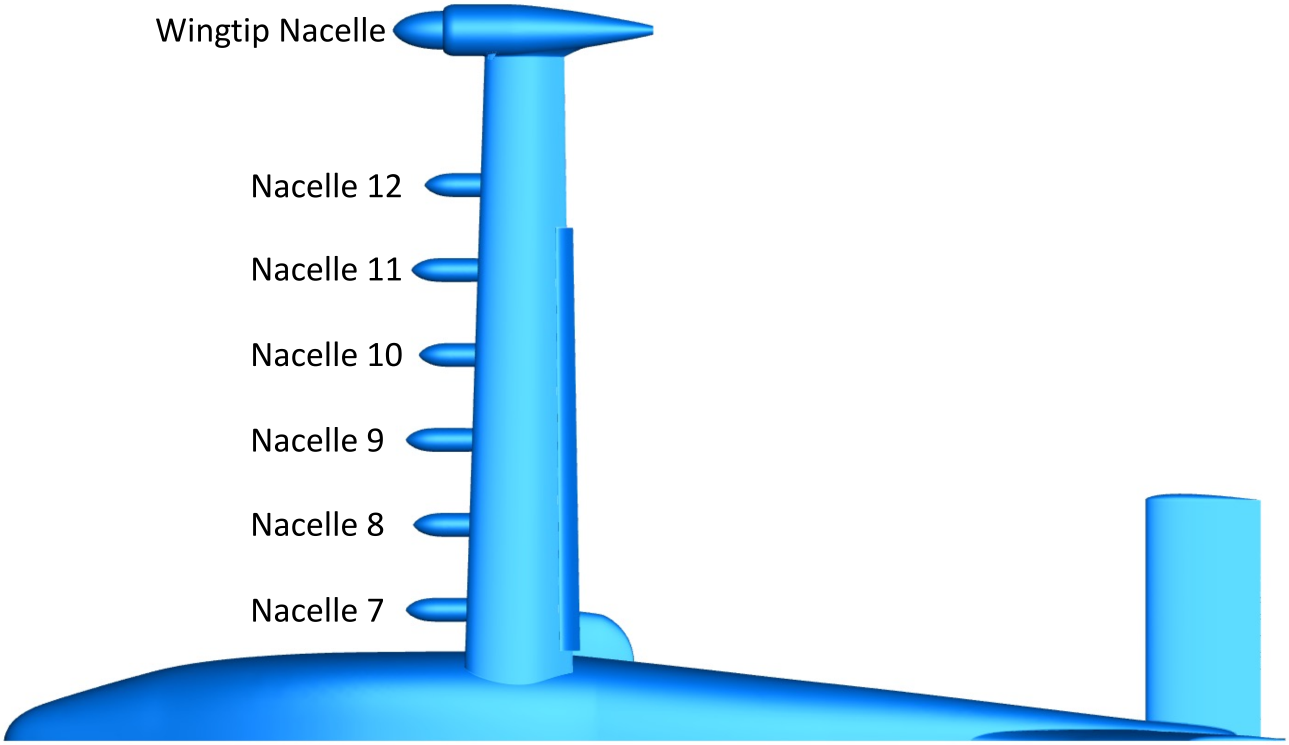

Figure 14. A Top Down View of the Landing Configuration to Display the Staggered High-Lift Nacelles.

2.7 Grid Generation

The NASA LaRC GEOLAB also supported the grid generation effort in providing many of the meshes used in this investigation. The geometry definition was prepared in GridTool (Ref. [14]) by creating surface patches on the configuration and by placing sources throughout the domain to capture configuration characteristics. The sources are shown in yellow in Figure 15. The source placement is very similar for all three configurations, except for the additional sources along the flap (Figure 15(b)) that are not present in the cruise configuration (Figure 15(a)). Therefore, the takeoff configuration is neglected from Figure 15 since it is nearly identical to the landing configuration, except for the flap deflection angle.

The GridTool software has an internal boundary-layer calculator that was used to generate the parameters needed to create the viscous portion of the mesh. The calculator is based on flat plate boundary layer theory that was introduced by Prandtl for steady, two-dimensional laminar flow over a flat plate. The inputs to the calculator include the Reynolds number based on reference chord (Re_c), the reference chord (c_{ref}), a growth rate ($R2$), the nondimensional first node height (y^+_{node}), and the number of layers in the boundary layer. The outputs from the calculator include another growth rate ($R1$) and the dimensional first node height (δ_1).

The computational mesh was generated with the HeldenMesh unstructured grid generation software (Ref. [16]). The HeldenMesh software uses an advancing layers method similar to Ref. [20] to create a boundary layer mesh of 3 cells per node as the mesh grows from the surface. Then an advancing front method, similar to Ref. [21], is used to generate the inviscid volume mesh from the boundary layer to the farfield. The volume growth rate is computed with Equation 1.

$$\delta_j = \delta_1[1 + R1(1 + R2)^{(j-1)}]^{(j-1)} \tag{1}$$

The HeldenMesh software produced an unstructured, tetrahedral mesh needed for USM3D and wrote three output files to run the code; projectname.cogsg, projectname.mapbc and projectname.bc. For these grids, the cell-size sourcing was all done with GridTool and the projectname.rst output file from GridTool was used with a HeldenMesh input file to generate the computational domain. The HeldenMesh input file included the name of GridTool file (projectname.rst), the type of output files (cogsg), a refinement factor, a smoothing iteration, a maximum cell size (global smax), a geometric growth rate of sources, and an exponential growth rate of sources in the volume. The refinement factor is a way to easily scale the size of the sources. The smoothing iteration parameter is the number of quality improvement cycles to perform, which includes node smoothing and edge or face swapping. The 'global smax' parameter can be a specific size of the largest cell, or it can be set to a very large number to maintain a constant growth rate to the boundaries. The geometric source growth rate dictates how large the mesh grows as a function of distance from the source and affects the growth on the surface and in the volume. The suggested geometric source growth rate for a fine mesh is 0.1, or it can be set up to 0.5 for a coarse mesh. The exponential source growth rate dictates the growth in the volume and a value of 0 is recommended in the user's manual.

The high-lift workshop gridding guidelines (Ref. [22]) were used as a guide to generate the meshes in this study. The gridding guidelines emphasize the number of cells along the wing and flap trailing edges should have at least 9 cells across the edge and a first cell height of $y^+_{cell} = 0.44$ for a fine mesh. As will be discussed in Section 2.7.4, the authors determined that it was important to use stretching along the wing leading edge to reduce the faceting that can occur from isotropic triangles on a curved surface, for a better representation of the leading-edge curvature. The computational domain was set at ($-10{,}000 \leq x \leq 10{,}000$), ($0 \leq y \leq 10{,}000$), and ($-10{,}000 \leq z \leq 10{,}000$), which is approximately 29 body lengths from the geometry.

Figure 16 shows the mesh on the fuselage and empennage for the takeoff configuration, which is representative of the overall surface mesh on the three configurations. Figures 17 to 19 show zoomed in views of the mesh details on the three configurations, since the surface mesh is very fine and it is difficult to show details on the full configuration in one picture. The parameters used to generate each mesh are detailed in the next three subsections.

2.7.1 Cruise Configuration, No Flap Deflection

For the cruise configuration, no flap deflection, the boundary layer was specified for a $y^+_{cell} = 0.2$. The first node height was computed as δ_1 = 1.26e-4 inches and a growth rate computed as $R1$ = 0.1139, using the GridTool boundary layer calculator with inputs of Re_c = 2,811,692, c = 25.56 inches, a growth rate of $R2$ = 0.02, and 32 nodes (96 cells) in the boundary layer. A refine factor of 1.5, a smoothing iteration of -5, a global smax of 450, a geometric source growth rate of 0.2, and an exponential growth rate of 0 were used in the HeldenMesh input file. These settings generated a mesh with 165 million tetrahedral cells and 1.2 million surface triangles. Several plots of the surface mesh on different regions of the cruise configuration are shown in Figure 17.

2.7.2 Takeoff Configuration, $10°$ Flap Deflection

For the takeoff configuration, 10 deg flap deflection, the boundary layer was specified for a y^+_{cell} = 0.2. The first node height was computed as δ_1 = 1.74e-4 inches and a growth rate computed as $R1$ = 0.1216, using the GridTool boundary layer calculator with inputs of Re_c = 2,099,183, c = 25.56 inches, a growth rate of $R2$ = 0.02, and 30 nodes (90 cells) in the boundary layer. A refine factor of 1.5, a smoothing iteration of -5, a global smax of 10000, a geometric source growth rate of 0.2, and an exponential growth rate of 0 were used in the HeldenMesh input file. These settings generated a mesh with 176 million tetrahedral cells and 1.4 million surface triangles. Several plots of the surface mesh on different regions of the landing configuration are shown in Figure 18.

2.7.3 Landing Configuration, $30°$ Flap Deflection

For the landing configuration, 30 deg flap deflection, the boundary layer was specified for a y^+_{cell} = 0.2. The first node height was computed as δ_1 = 1.743e-4 inches and a growth rate computed as $R1$ = 0.1216, using the GridTool boundary layer calculator with inputs of Re_c = 1,963,924, c = 25.56 inches, a growth rate of $R2$ = 0.02, and 30 nodes (90 cells) in the boundary layer. A refine factor of 1.5, a smoothing iteration of -5, a global smax of 10000, a geometric source growth rate of 0.2, and an exponential growth rate of 0 were used in the HeldenMesh input file. These settings generated a mesh with 174 million tetrahedral cells and 1.3 million surface triangles. Several plots of the surface mesh on different regions of the takeoff configuration are shown in Figure 19.

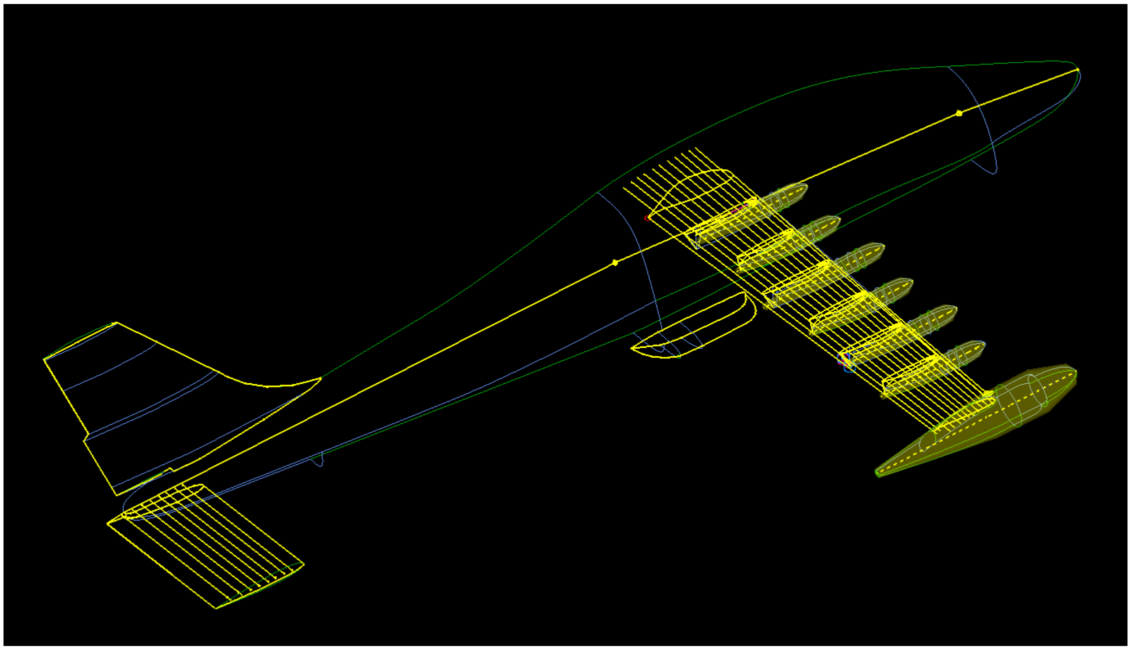

(a) Cruise Configuration, No Flap Deflection

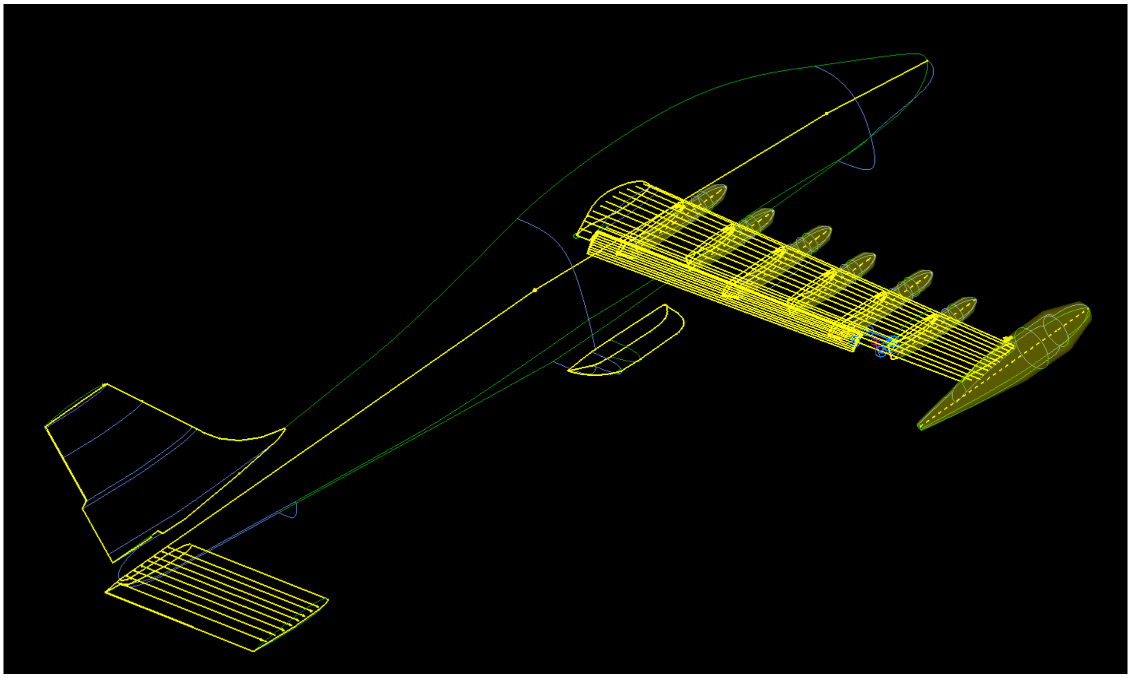

(b) Landing Configuration, 30° Flap Deflection

Figure 15. Sources Used to Create Surface Cell Resolution.

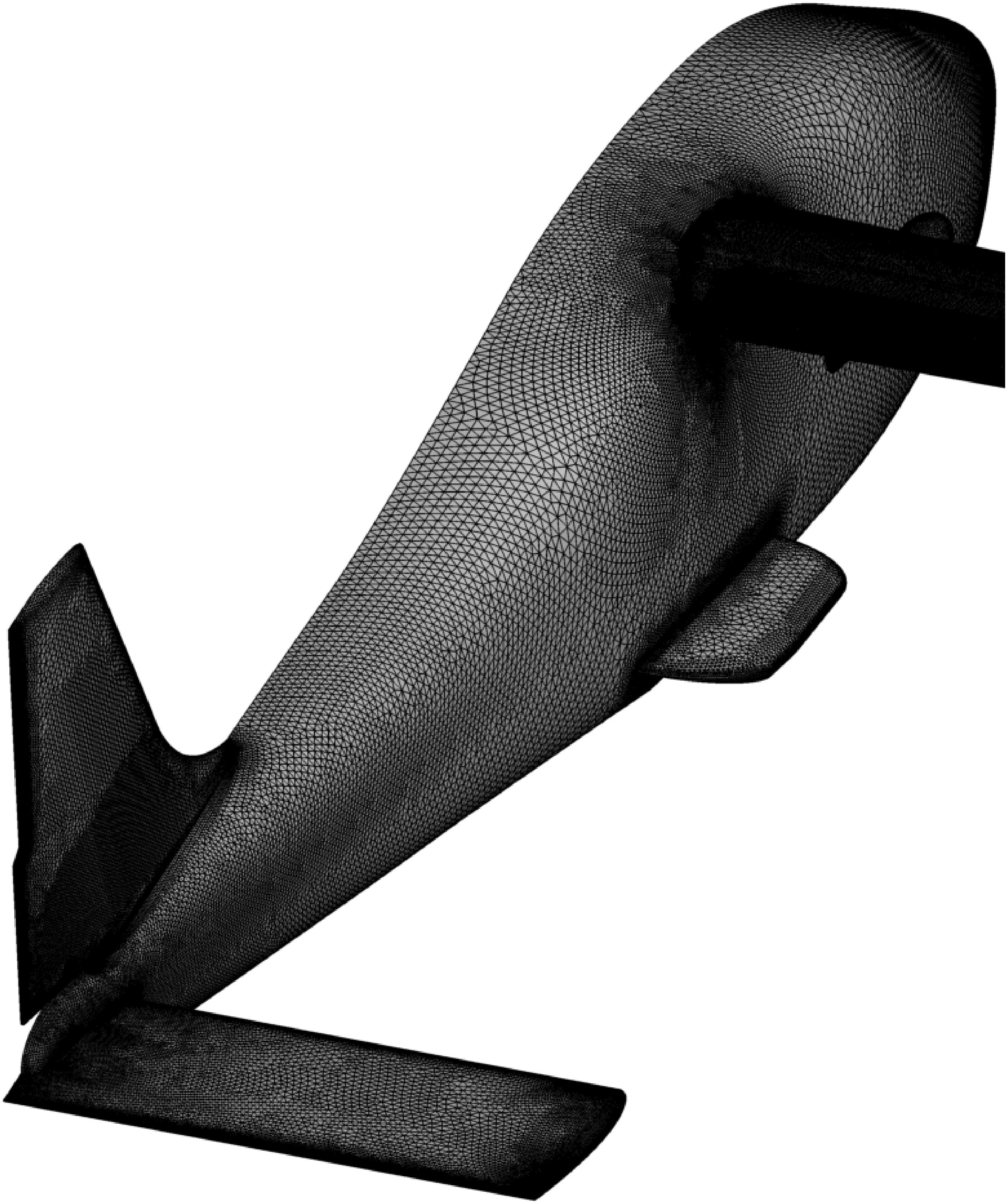

Figure 16. Surface Mesh on the Fuselage and Empennage.

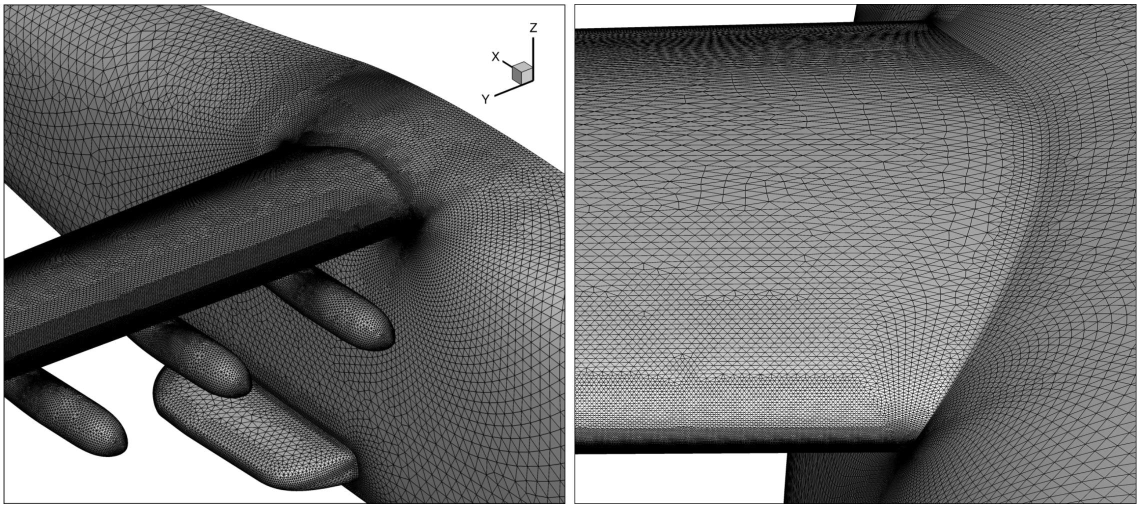

(a) Inboard Wing with Nacelles 7-9 and Landing Gear Cover (LGC)

(b) Wing Root, Wing Leading Edge

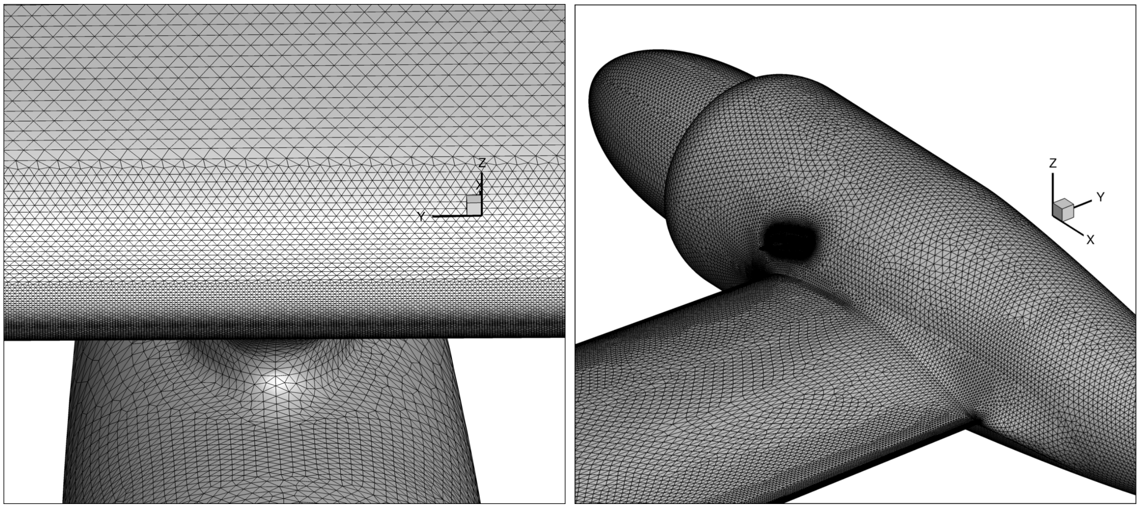

(c) Wing Leading Edge, Nacelle 7

(d) Tip Nacelle

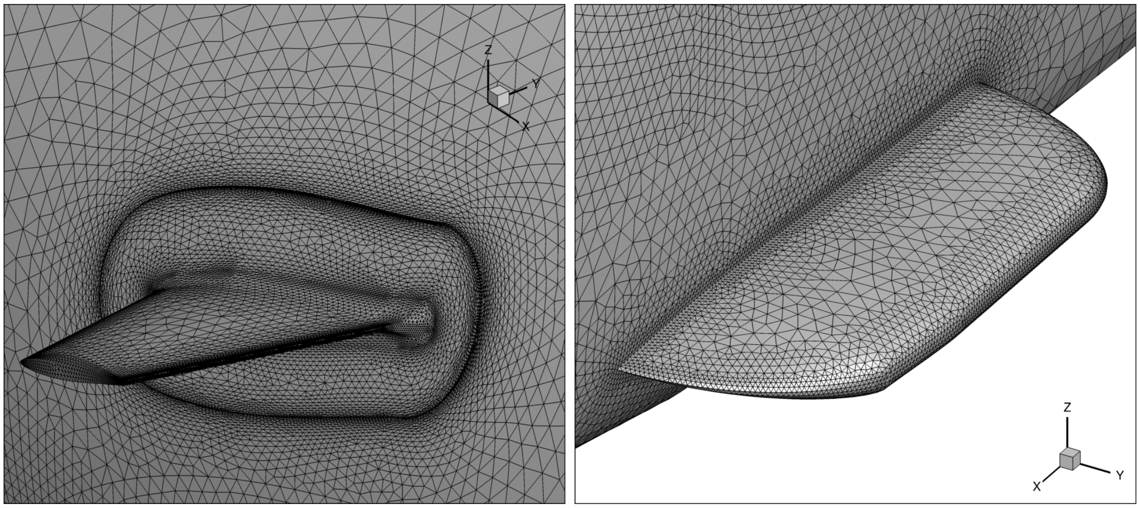

(e) Vortex Generator

(f) Landing Gear Cover (LGC)

Figure 17. Surface Mesh Details for the X-57 Cruise Configuration, No Flap Deflection.

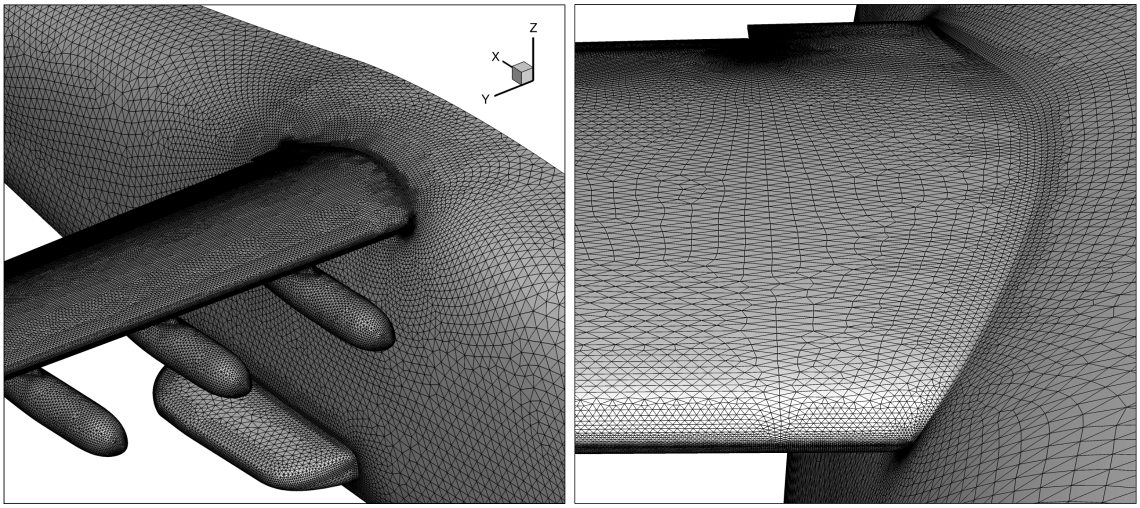

(a) Inboard Wing with Nacelles 7-9 and LGC (b) Wing Root, Leading Edge

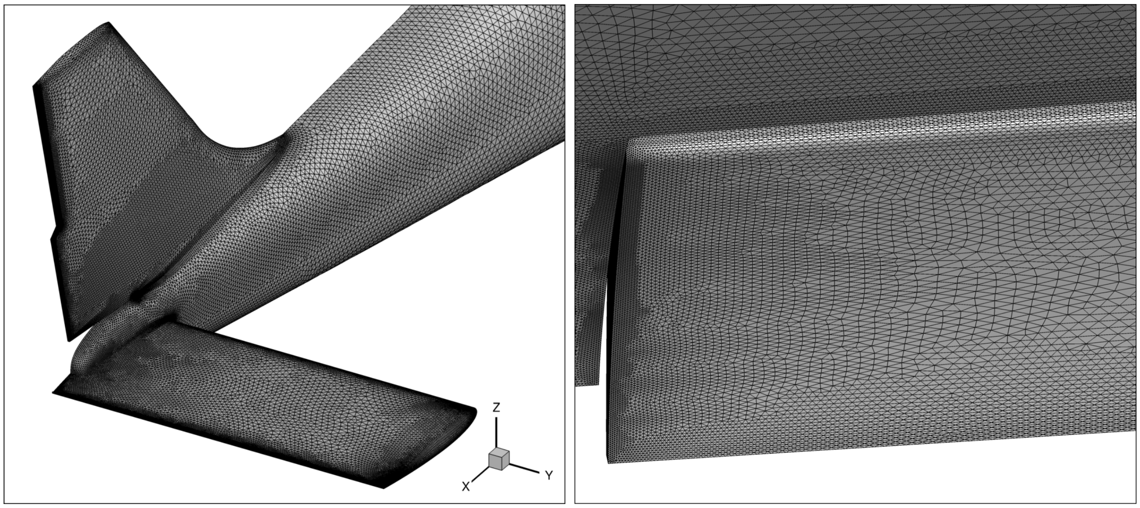

(c) Empennage (d) Outboard Flap, Lower Surface and Leading Edge

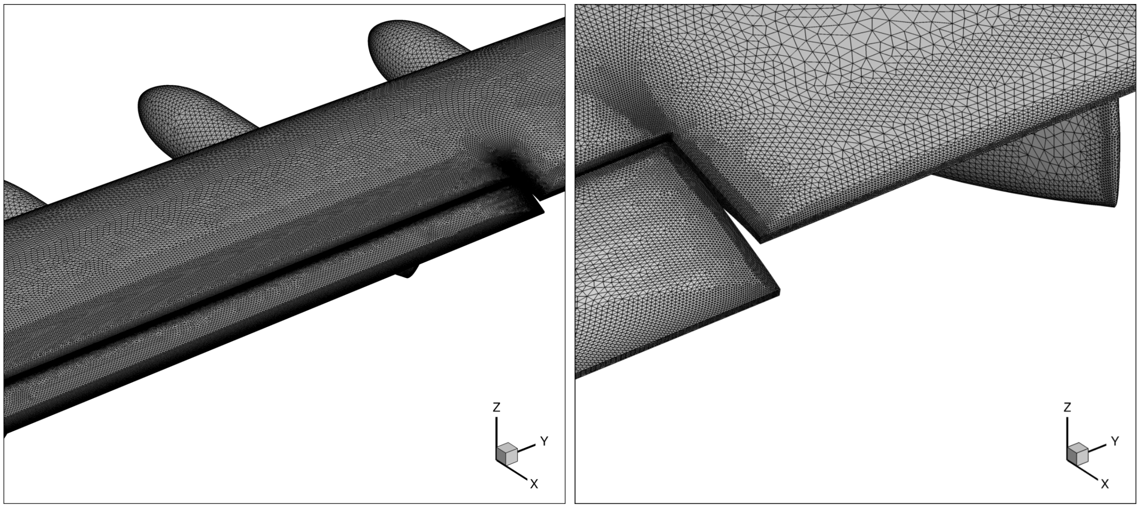

(e) Outboard Wing and Flap, Nacelles 11 and 12 (f) Outboard Flap, Upper Surface and Trailing Edges

Figure 18. Surface Mesh Details for the X-57 Takeoff Configuration, 10° Flap Deflection.

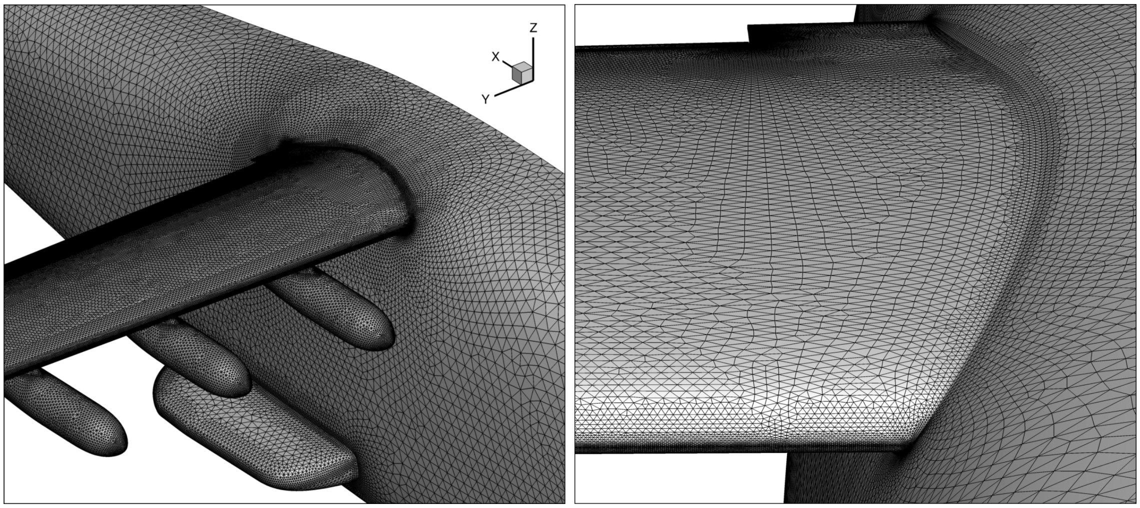

(a) Inboard Wing with Nacelles 7-9 and LGC

(b) Wing Root, Leading Edge at the Bottom

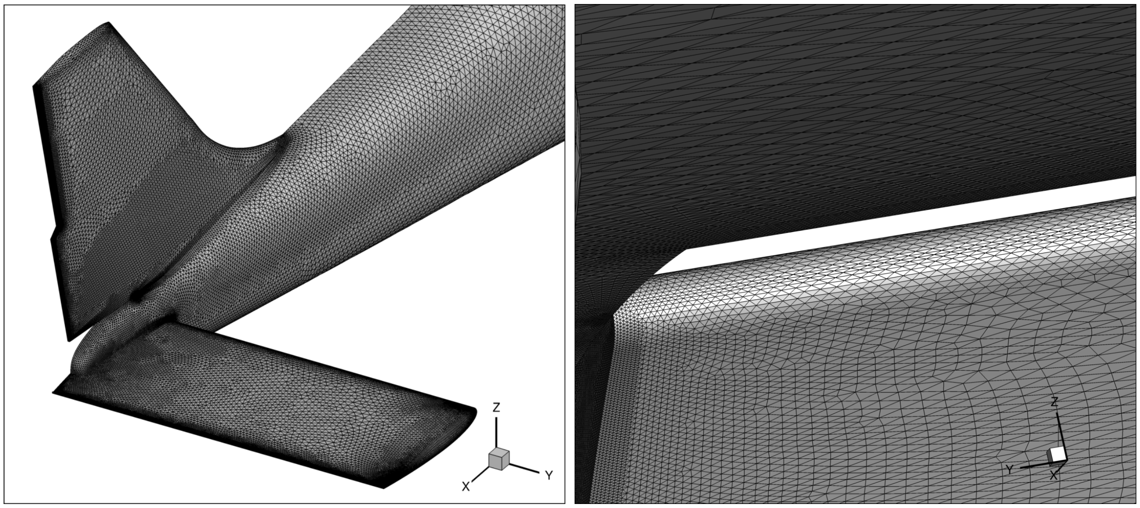

(c) Empennage

(d) Outboard Flap Leading Edge, with Whitespace for the Gap between the Flap and Wing

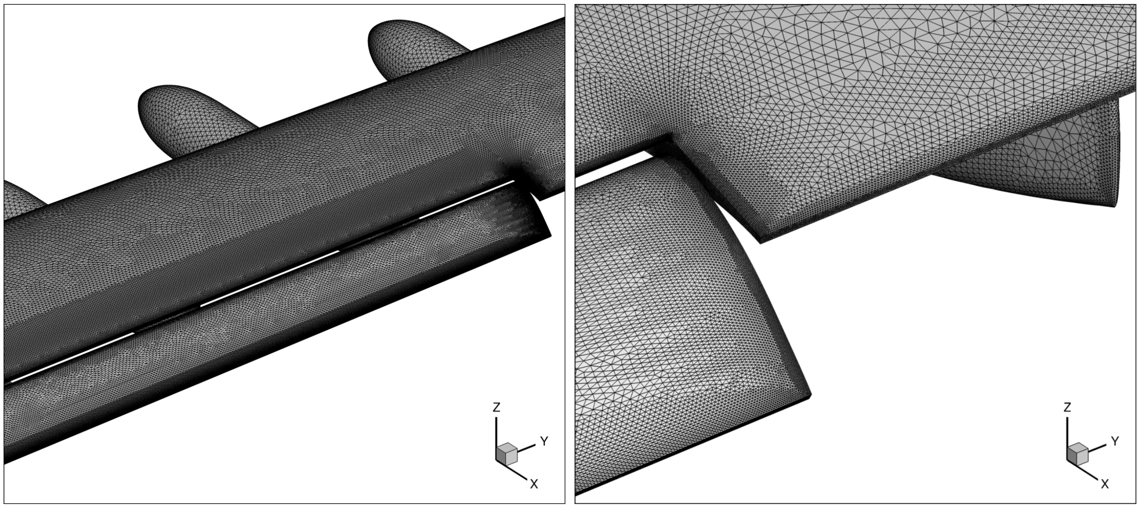

(e) Outboard Wing and Flap, Nacelles 11 and 12

(f) Outboard Flap, Upper Surface and Trailing Edges

Figure 19. Surface Mesh Details for the X-57 Landing Configuration, 30° Flap Deflection.

2.7.4 Grid Improvements; Cruise Configuration

A study was conducted on the grid resolution along the wing leading edge (LE) to determine if changes would impact lift coefficient. Cell stretching (from the wing root to the wing tip) and wing LE cell size were investigated. The original wing-LE mesh had unstretched cells along the wing LE and thus, the triangles on the surface around the wing leading-edge curvature were equilateral triangles. Figure 20(a) shows the equilateral triangles around the curved LE, zoomed into the region around y = 95 inches (solid black line). Figure 20(b) shows the stretched wing-LE mesh with the LE cells stretched by a factor of five (stretch wing 5x) in the y direction out the wingspan. These stretched cells along the wing LE allowed for smoother leading-edge curvature. In contrast, the unstretched wing LE cells resulted in very minor faceting that was only detected when highly zoomed into the leading edge, but which had a large impact on peak minimum pressure, and thus, lift. Figure 21 shows the comparison of the airfoil and leading-edge curvature at a span station of y = 95 inches. These airfoils look identical in Figure 21(a), but the faceting on the original wing-LE mesh is noticeable in Figure 21(b) with two red straight lines inset from the smooth blue line, representing the leading-edge curvature of the stretched wing 5x.

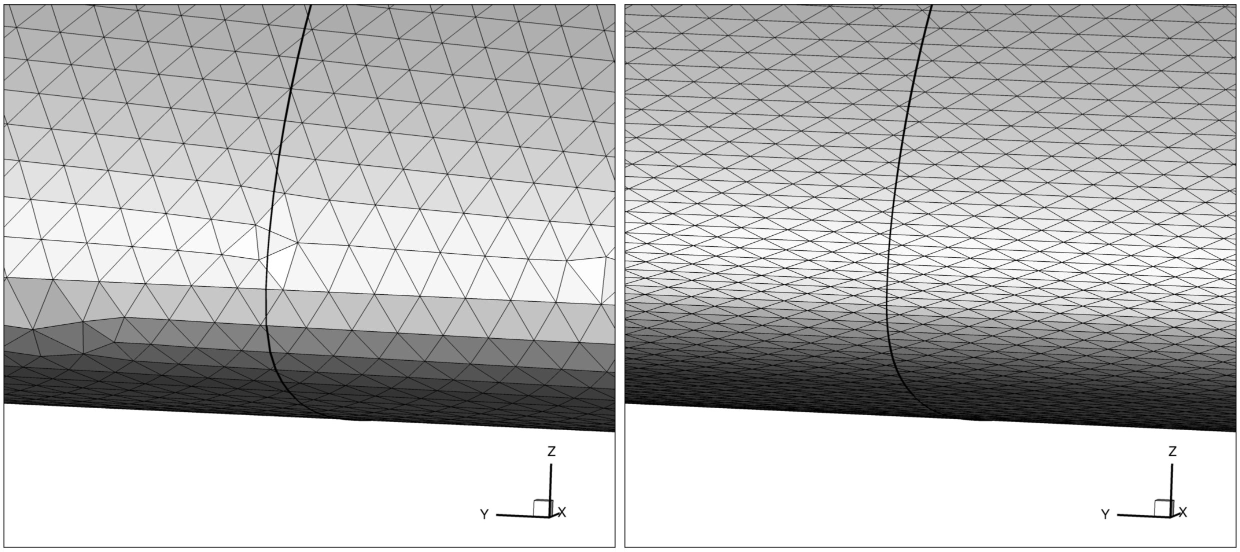

(a) Original Wing-LE Mesh (b) Stretched Wing-LE Mesh

Figure 20. Zoom into Wing Leading Edge at y = 95 inches.

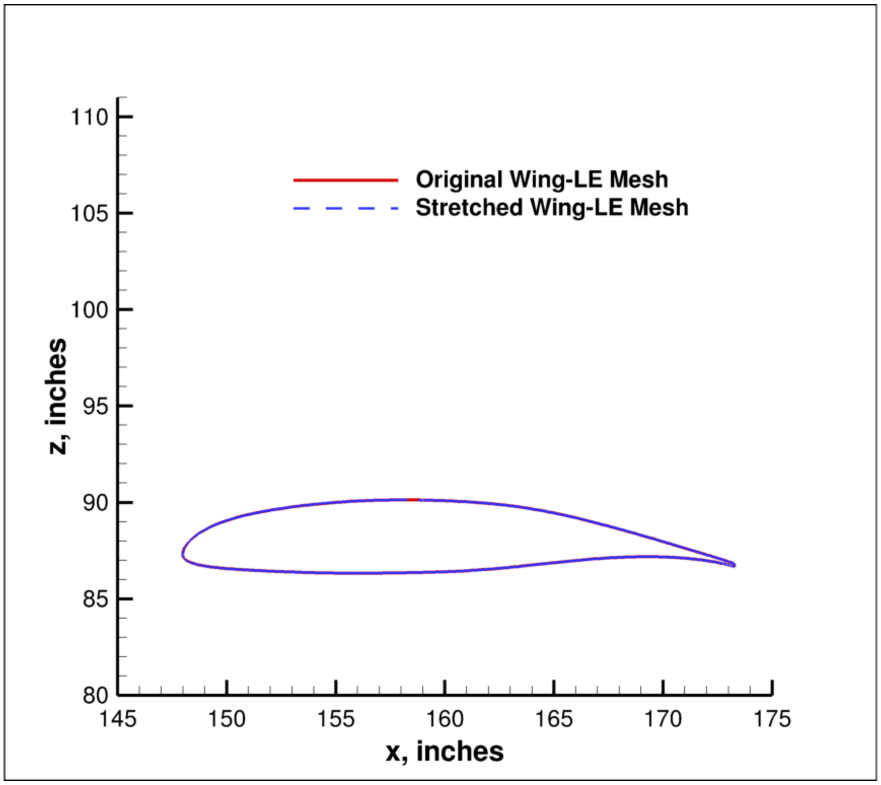

(a) Airfoil Comparison

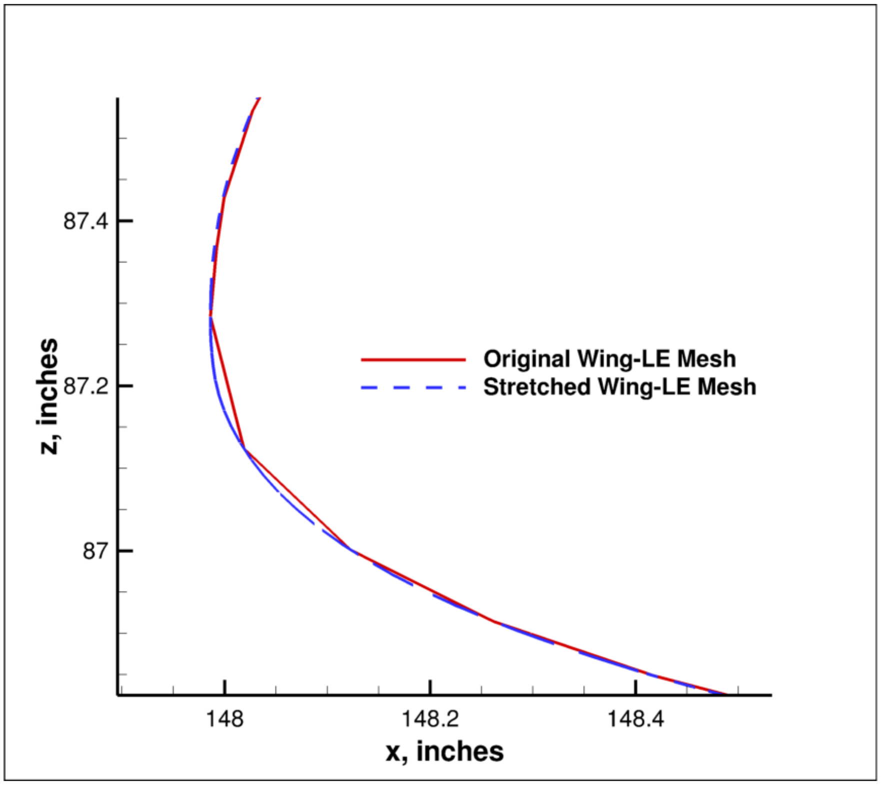

(b) Leading Edge Comparison

Figure 21. Comparison of the Airfoil at a Span of y = 95 inches.

Five mesh refinements were investigated to study the effect of cell stretching along the wing leading edge. Figure 22 shows the diagram of the designated source locations along the wing leading edge, which includes the tip (T), near the tip (B), midspan (M), near the root (A), and at the root (R). Table 2 shows the source size that ultimately determines the size of the surface triangle on the geometry. Table 3 shows the stretching value at each of the designated locations. The size is marked as NA if the designated location was not used, and the stretch column is marked as None for isotropic, unstretched cells.

A comparison of the surface meshes at the wing root, midspan, and wing tip leading edges are shown in Figures 23 to 25. The surface triangle size scaled with source size, such that a decrease in source size resulted in smaller surface triangles. The surface triangle size remained the same when the source size was unchanged during a mesh refinement, unless stretching was added to an unstretched source. In the first mesh refinement (Refine1), 5x stretching was added to the midspan location (Figure 24(b)), but nonstretched, isotropic surface triangles were kept at the wing root (Figure 23(b)) and the wing tip (Figure 25(b)). In the second mesh refinement (Refine2), the source size at the wing root and wing tip also remained the same, but the midspan stretching was increased to 10x (Figure 24(c)). In the third mesh refinement (Refine3), the source size at the wing root and wing tip also remained the same, but 2x stretching was added at the wing root (Figure 23(d)) and wing tip (Figure 25(d)), with 5x stretching from B to A (Figure 24(d)). In the fourth mesh refinement (Refine4), the wing root source size was reduced from 0.03 to 0.02. Also for the Refine4 mesh, the stretching was changed to 5x along the full wing leading edge, from the wing root to the wing tip (Figures 23(e), 24(e), and 25(e)). Finally, in the fifth mesh refinement (Refine5), the source size was reduced further to 0.01 at both the wing root (Figure 23(f)) and the wing tip (Figure 25(f)), but the fullspan 5x stretching was unchanged (Figures 23(f), 24(f), and 25(f)).

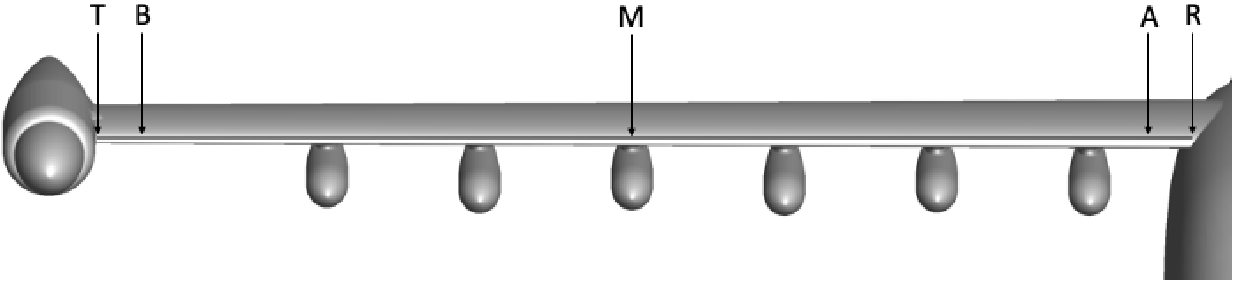

Figure 22. Diagram of Designated Source Locations along the Wing Leading Edge of the Cruise Configuration, No Flap Deflection.

Table 2. Wing Leading-Edge Source Sizes at the Designated Locations.

Mesh	*T*	*B*	*M*	*A*	*R*
Original	0.02	NA	NA	NA	0.03
Refine1	0.02	NA	0.03	NA	0.03
Refine2	0.02	NA	0.03	NA	0.03
Refine3	0.02	0.03	NA	0.03	0.03
Refine4	0.02	0.02	NA	0.02	0.02
Refine5	0.01	0.01	NA	0.01	0.01

Table 3. Wing Leading-Edge Source Stretching at the Designated Locations.

Mesh	*T*	*B*	*M*	*A*	*R*
Original	None	NA	NA	NA	None
Refine1	None	NA	5x	NA	None
Refine2	None	NA	10x	NA	None
Refine3	2x	5x	NA	5x	2x
Refine4	5x	5x	NA	5x	5x
Refine5	5x	5x	NA	5x	5x

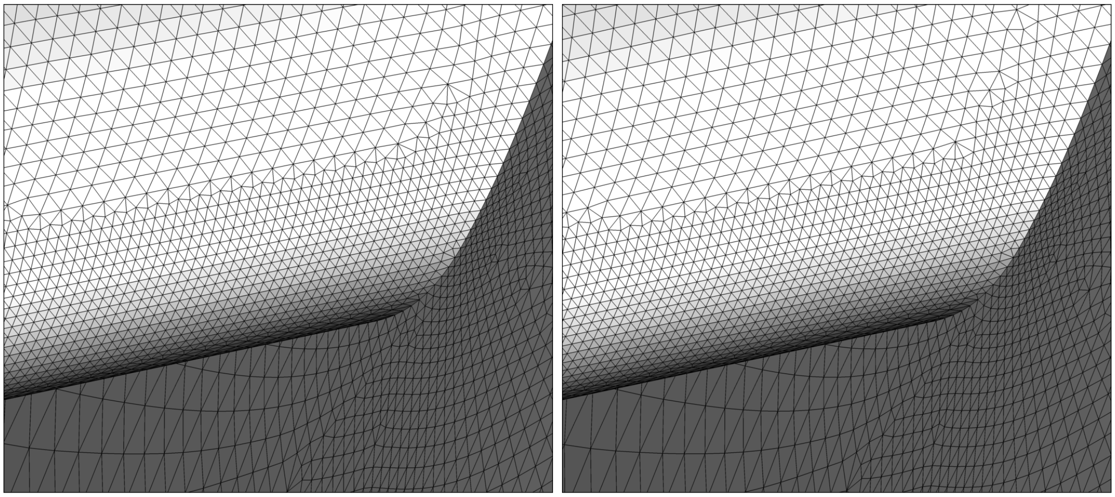

(a) Original Mesh

(b) Refine1 Mesh: Stretch 5x Midspan

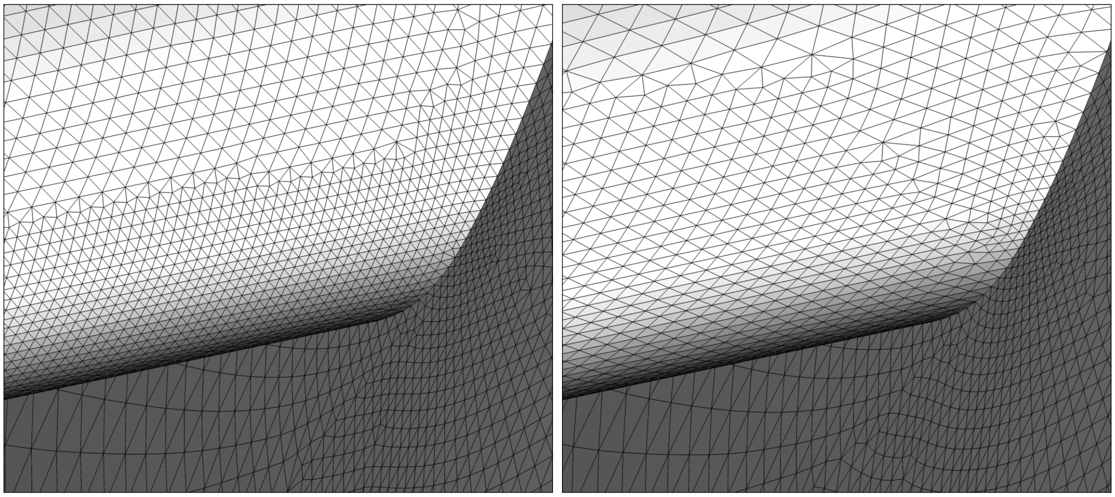

(c) Refine2 Mesh: Stretch 10x Midspan

(d) Refine3 Mesh: Stretch 5x Midspan, 2x Root, 2x Tip

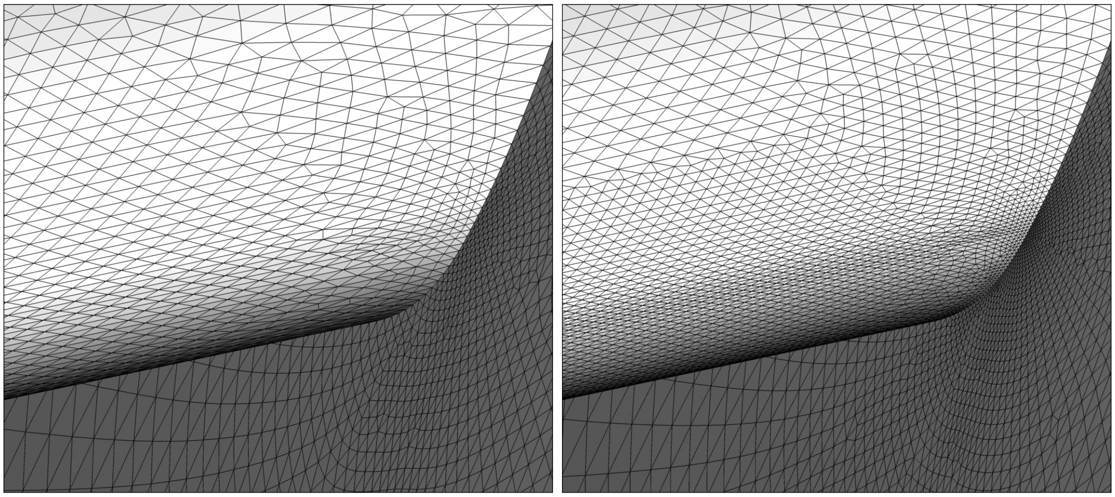

(e) Refine4 Mesh: Stretch 5x Root to Tip

(f) Refine5 Mesh: Stretch 5x Root to Tip, Half Size Cells

Figure 23. Comparison of Meshes at the Wing Root Leading Edge.

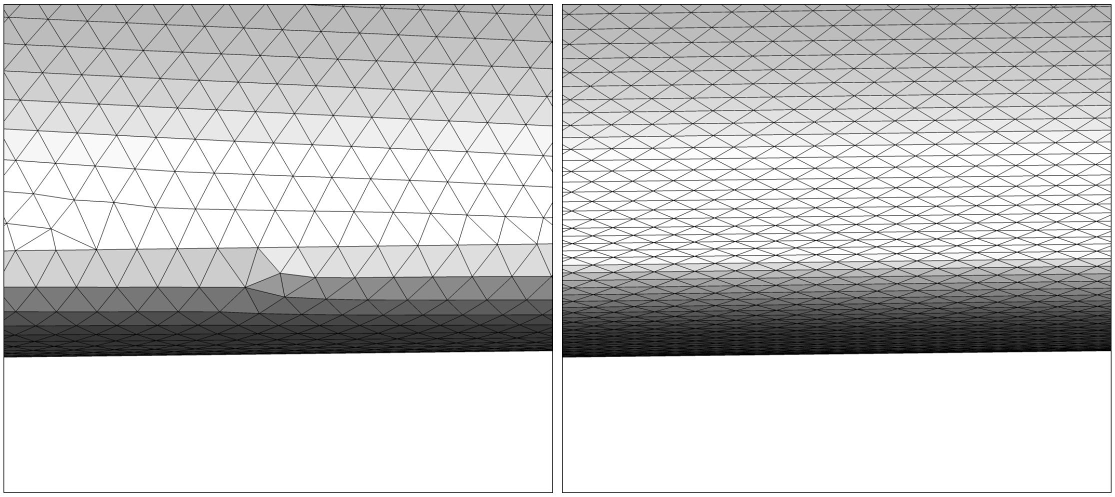

(a) Original Mesh

(b) Refine1 Mesh: Stretch 5x Midspan

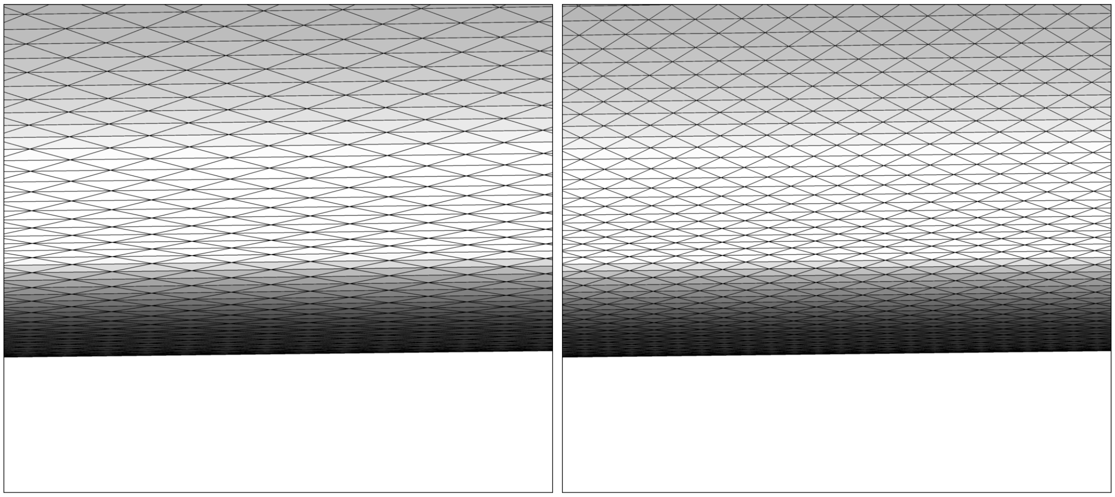

(c) Refine2 Mesh: Stretch 10x Midspan

(d) Refine3 Mesh: Stretch 5x Midspan, 2x Root, 2x Tip

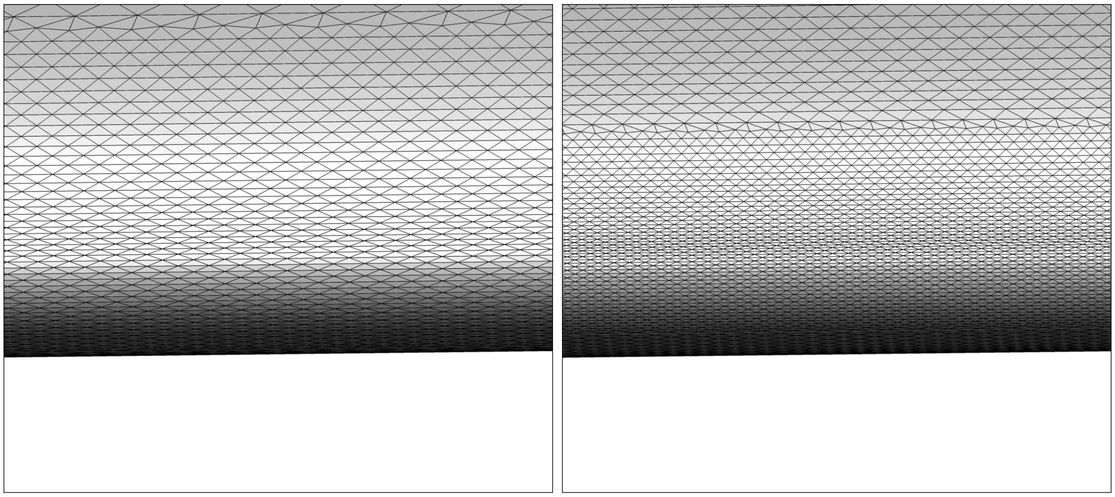

(e) Refine4 Mesh: Stretch 5x Root to Tip

(f) Refine5 Mesh: Stretch 5x Root to Tip, Half Size Cells

Figure 24. Comparison of Meshes at Midspan Leading Edge.

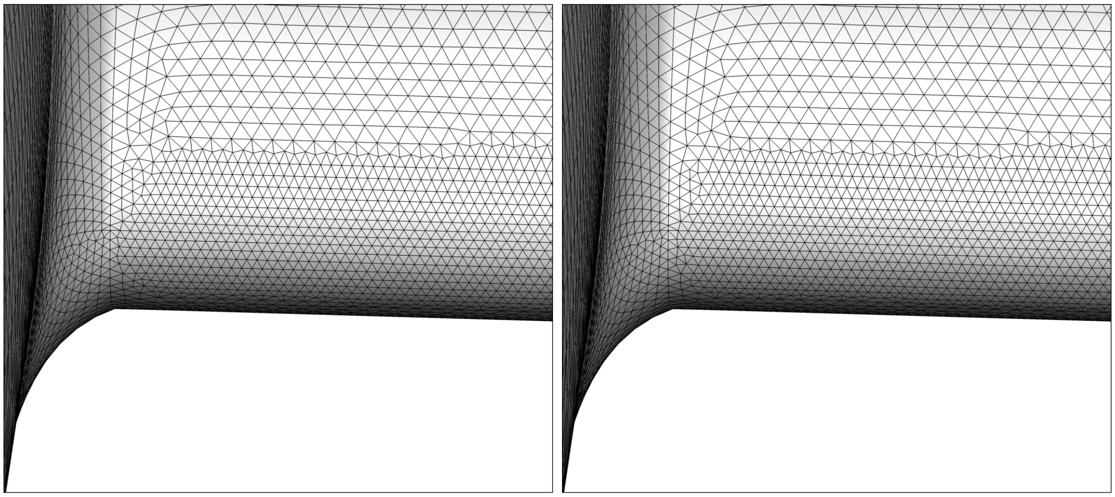

(a) Original Mesh

(b) Refine1 Mesh: Stretch 5x Midspan

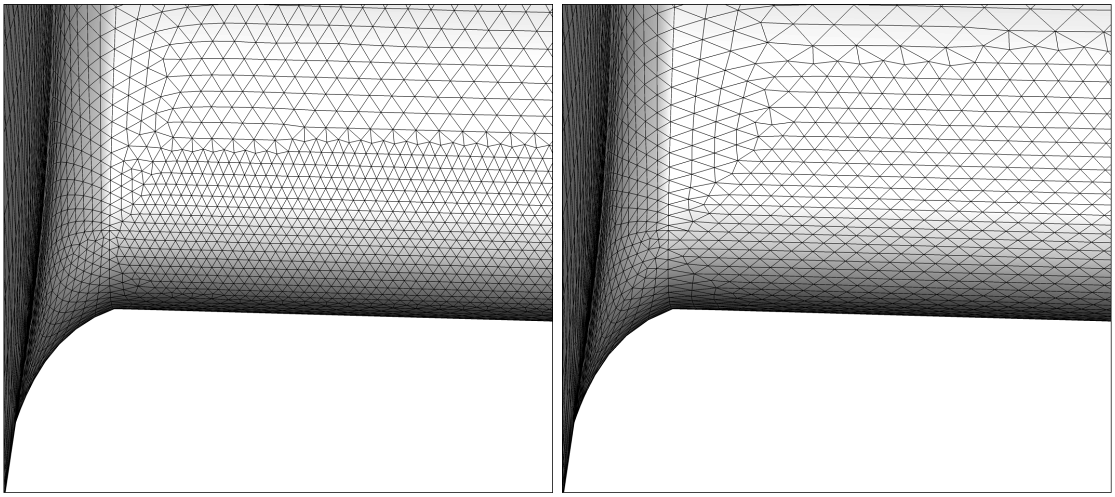

(c) Refine2 Mesh: Stretch 10x Midspan

(d) Refine3 Mesh: Stretch 5x Midspan, 2x Root, 2x Tip

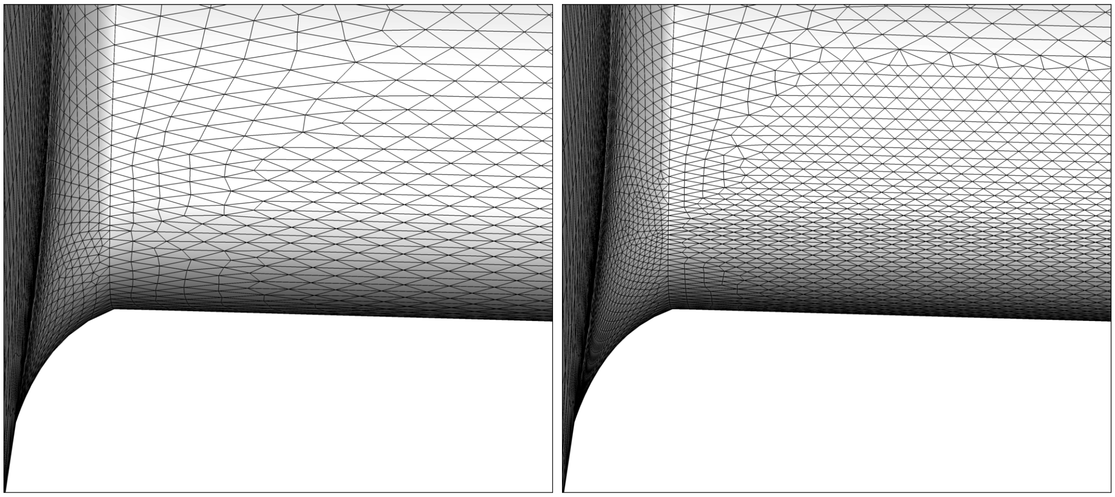

(e) Refine4 Mesh: Stretch 5x Root to Tip

(f) Refine5 Mesh: Stretch 5x Root to Tip, Half Size Cells

Figure 25. Comparison of Meshes at the Wing Tip Leading Edge.

Figure 26 shows the effect of grid changes along the leading edge, on lift coefficient, for the cruise configuration at $M = 0.233$. The Original Mesh had a much lower lift coefficient from $\alpha = 12°$ to $\alpha = 17°$ than all of the mesh refinements with various stretching along the wing leading edge. The lift was increased at both $\alpha = 15°$ and $\alpha = 17°$ for the Refine1 Mesh, with 5x stretching out the midspan location. At $\alpha = 17°$, the Refine2 Mesh (10x midspan stretching) produced more lift than the Original Mesh, but lower lift than the Refine1 Mesh (5x midspan stretching). Adding 2x stretching at the wing root and wing tip in Refine3 Mesh resulted in a slight increase in lift at $\alpha = 17°$, compared to Refine1 Mesh with equilateral triangles at the wing root and wing tip. The fourth mesh refinement, with 5x stretching from the wing root to wing tip, resulted in another slight increase in lift coefficient at $\alpha = 17°$. Finally, there was a significant increase in lift coefficient from the Refine5 Mesh, when compared to the Original Mesh, for angles of attack of $\alpha = 12°$ to $\alpha = 17°$. The combination of stretching the leading edge sources by a factor of 5 from the wing root to the wing tip, and reducing the size of the wing leading-edge cells increased the lift coefficient the most, for angles of attack from $\alpha = 12°$ to $\alpha = 17°$.

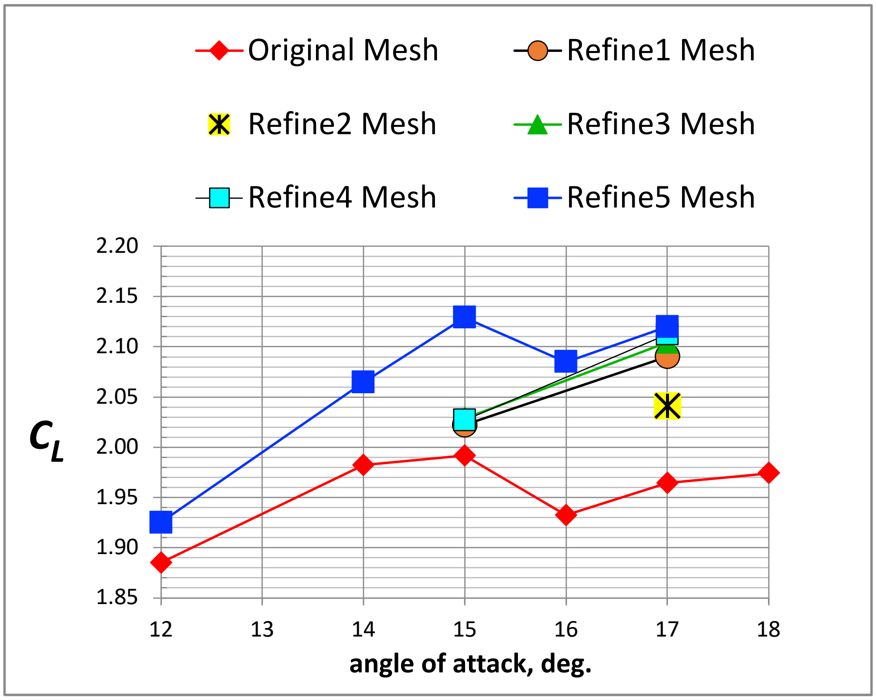

Figure 26. Effect of Grid Changes along the Wing Leading Edge, on Lift Coefficient for the Cruise Configuration at $M = 0.233$.

Three more grid refinements were investigated by determining the effect of the first cell height and the number of cells within the boundary layer on lift coefficient. The results of the grid changes in the boundary layer are shown in Figure 27. The Refine5 Mesh was used as the baseline, which had a $y^+_{cell} = 0.20$ and 96 tetrahedral cells, for 32 prism-like layers within the boundary layer. The first cell height was reduced from a value for a $y^+ = 0.20$ to $y^+ = 0.08$, with 96 cells in the boundary layer for the sixth mesh refinement (Refine6 Mesh). The number of cells in the boundary layer was reduced from 96 to 45, with a $y^+ = 0.20$ for the seventh mesh refinement (Refine7 Mesh). Finally, the first cell height was reduced from a value for a $y^+ = 0.20$ to $y^+ = 0.08$, and the number of cells in the boundary layer was reduced from 96 to 45 for the eighth mesh refinement (Refine8 Mesh).

There was a slight decrease in lift coefficient at $\alpha = 15°$ and $\alpha = 17°$ with the extremely small first cell height used in the Refine6 Mesh. The lift coefficient was decreased even more when the number of cells within the boundary layer was reduced to 45 (Refine7 Mesh), compared to the baseline Refine5 Mesh with 96 cells within the boundary layer. Reducing the number of cells within the boundary layer increased the grid size expansion rate normal to the surface, which resulted in a reduction of lift coefficient for both $\alpha = 15°$ and $\alpha = 17°$. Finally, reducing the first cell height from a $y^+ = 0.2$ to $y^+ = 0.08$ and reducing the number of cells within in boundary layer (Refine8 Mesh), resulted in further reductions of the lift coefficient compared to the rest of the meshes as the expansion rate of cell growth off the surface was further decreased by reducing the first cell height and reducing the number of cells within the boundary layer.

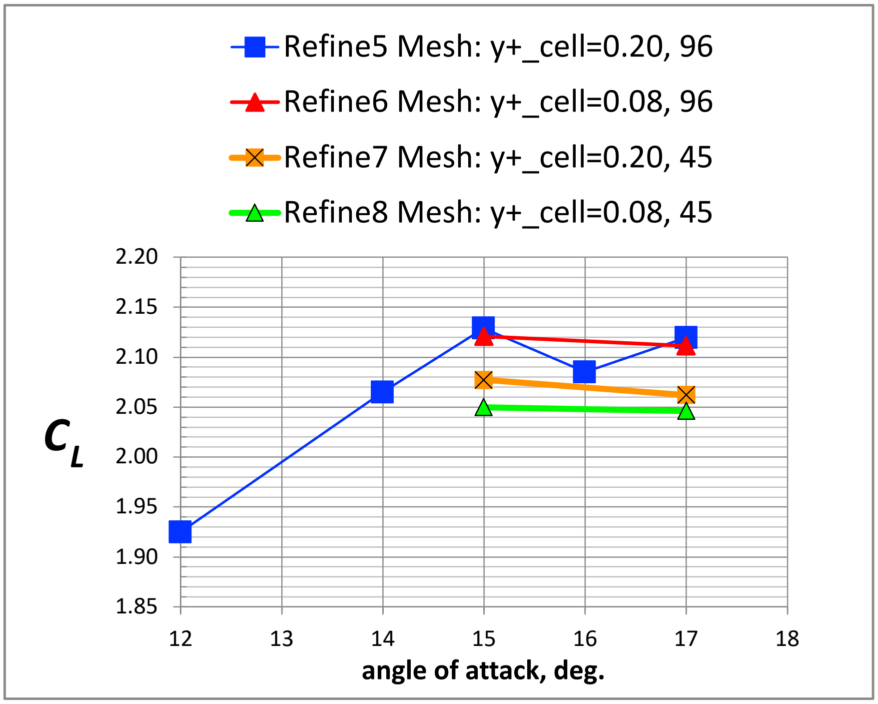

Figure 27. Effect of Grid Changes in the Boundary Layer, on Lift Coefficient for the Cruise Configuration at $M = 0.233$.

The authors proceeded with the Refine5 Mesh for the cruise configuration (no flap deflection) and finished solutions for the full angle of attack. The comparison of lift coefficient between the Original Mesh and the Refine5 Mesh is shown in Figure 28. This plot shows the effect of improved grid resolution on the lift coefficient for the full airplane, as well as component contributions to lift coefficient from the wing, fuselage and the combined component of nacelles, pylons and strakes (NPS). Similar comparisons are also shown in Figures 29-31, but with an expanded scale for the wing (Figure 29), the fuselage (Figure 30), and NPS (Figure 31). The Original Mesh has an unexpected shift in the lift curve at $\alpha = 8°$ because the leading-edge curvature is slightly faceted for this mesh, which becomes important at this angle of attack. The improved Refine5 Mesh, with a smoother leading-edge curvature, has a more continuous increasing lift curve slope up through $\alpha = 15°$. Most of the increased lift for the Refine5 Mesh comes from the wing (Figure 29), which was expected since this component was the focus of the grid study. The lift from the fuselage is different between the two meshes at $\alpha = 14°$ and $\alpha = 15°$ (Figure 30), as the smaller cell sizes at the wing root in the Refine5 Mesh have also reduced the cell size on the fuselage in this area and thus, impacted lift. The lift from the NPS has also increased with the Refine5 Mesh (Figure 31), but the scale is expanded so the effect on lift coefficient is much smaller than from the wing.

The same wing leading-edge stretching (5x from the wing root to the wing tip) and the reduced cell size were also used to generate the meshes for the takeoff (10° flap deflection) and landing (30° flap deflection) configurations.

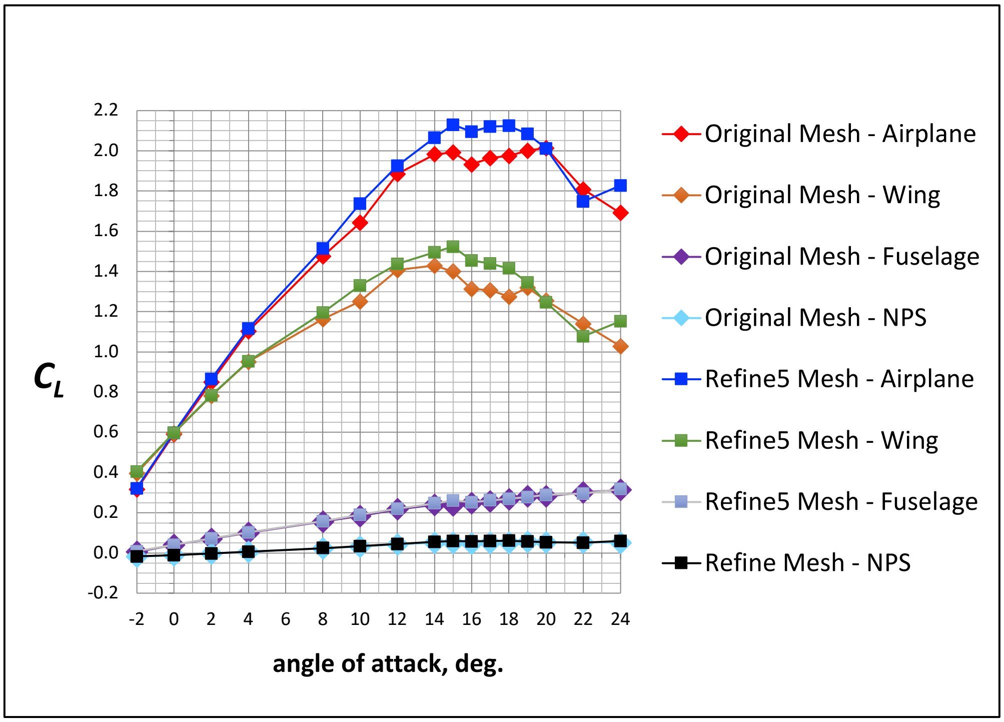

Figure 28. Effect of Improved Grid Resolution on Lift Coefficient between the Original and Refine5 Meshes, for the Cruise Configuration at $M = 0.233$.

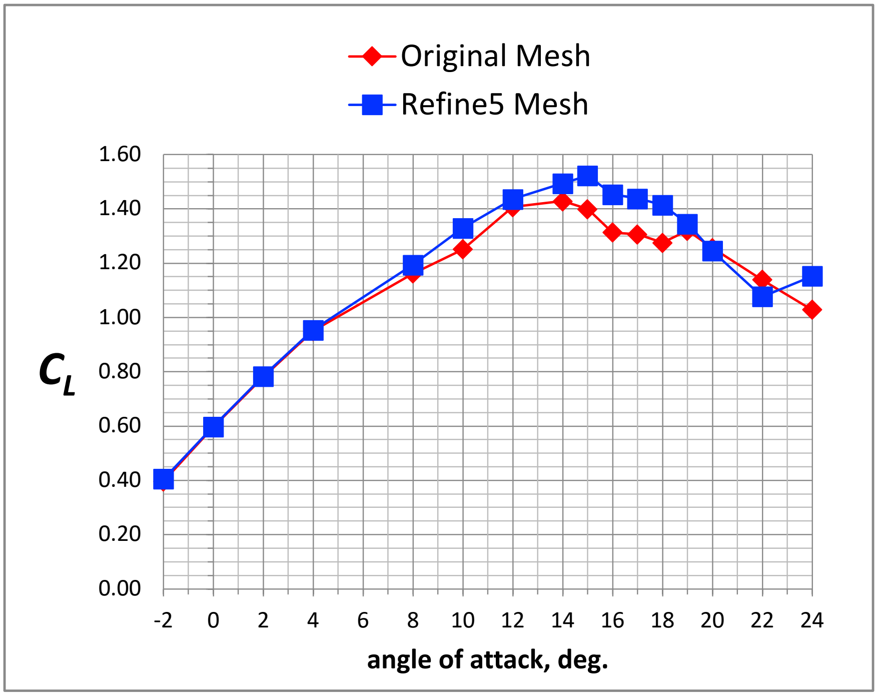

Figure 29. Effect of Improved Grid Resolution on Lift Coefficient for the Wing of the Cruise Configuration at $M = 0.233$.

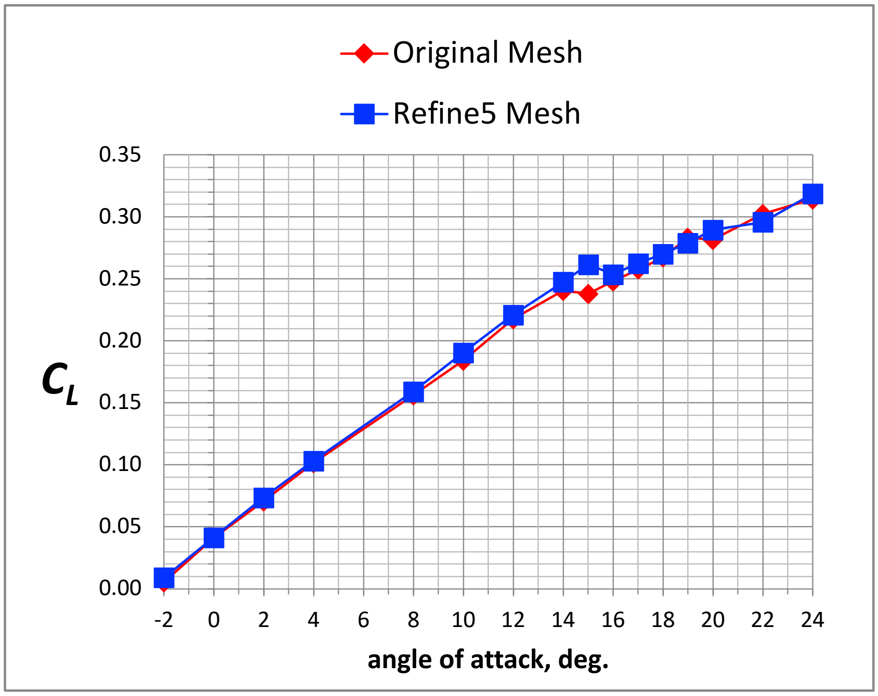

Figure 30. Effect of Improved Grid Resolution on Lift Coefficient for the Fuselage of the Cruise Configuration at $M = 0.233$.

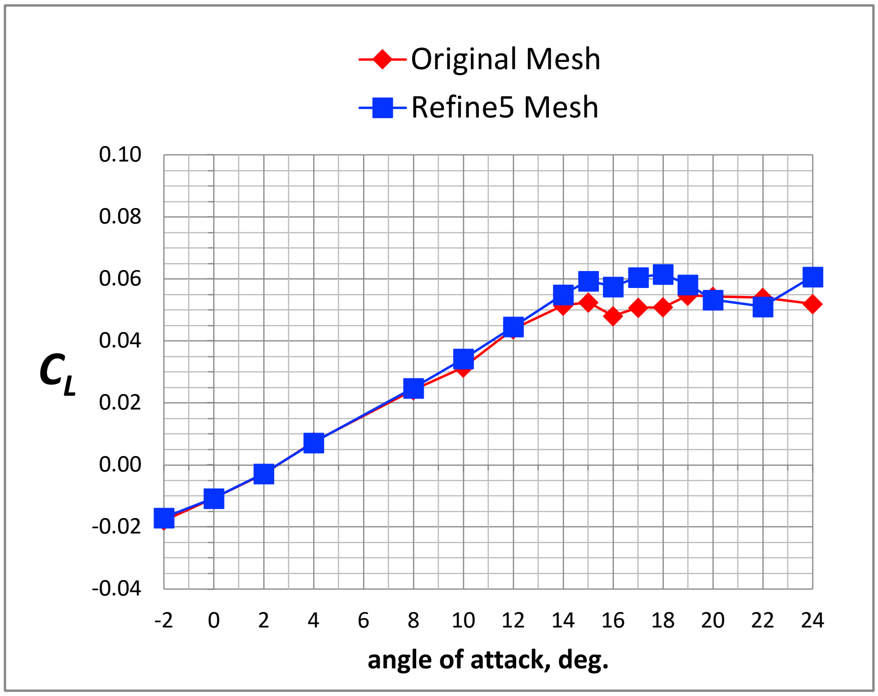

Figure 31. Effect of Improved Grid Resolution on Lift Coefficient for the NPS of the Cruise Configuration at $M = 0.233$.

2.8 Computational Flow Solver

The USM3D flow solver (Ref. [13]) is a tetrahedral cell-centered, finite volume Reynolds-averaged Navier-Stokes (RANS) method. The code version was usm3d.cvs20160902+rotorextensions. Each solution was started with local-time stepping, steady-state RANS method for up to 15,000 iterations and CFL number was typically ramped up from 1 to 50 over approximately 1,000 iterations. Then, each solution was continued with a global-time stepping, time-accurate RANS method until convergence or solution periodicity. The time-stepping scheme used for this work was the implicit Gauss-Seidel method. The spatial-differencing scheme of Euler fluxes used in this work was the Roe flux difference-splitting scheme. The Newton method (3-point backward differencing without pseudotime and up to 15 subiterations) was used for the time-accurate scheme. The code was run in first-order spatial accuracy until the residual dropped two orders of magnitude, at which point the code automatically switched to generate second-order, spatially-accurate solutions.

2.8.1 Turbulence Model Selection

The USM3D code has a variety of options for solving the flow equations and several turbulence models (Ref. [23]) for closure of the RANS equations. The Spalart-Allmaras (SA) turbulence model (Ref. [24]) with the Quadratic Constitutive Relation (QCR) (Ref. [25]) was used for all of the flow solutions. The QCR2000 version is implemented in USM3D but it is referred to as QCR within this document. The SA QCR turbulence model was mainly chosen for this work because the QCR option was created as an improvement to the standard SA model to better capture corner flows, which could potentially be beneficial for this configuration at the wing root fuselage junction.

2.8.2 Time Step

For USM3D nondimensionalization, the relationship for time step ($delta_t$) and the number of steps (N) to traverse a characteristic length (L_{char}) is shown in Equation 2. The distance a signal travels in one time step ($D_{t,char}$) is computed with Equation 3. For this work, a characteristic length of L_{char} = 25.56 inches was used. The solutions at each M were started with a $delta_t$ computed with a $D_{t,char}$ = 1 inch/step, and then smaller time steps were used to verify that the solution did not change. The time step settings for each Mach number are shown in Table 4.

$$delta_t = \frac{L_{char}}{N * M} \tag{2}$$

$$D_{t,char} = \frac{L_{char}}{N} \tag{3}$$

Table 4. Time Step For Each Mach Number and L_{char} = 25.56 inches.

Configuration	M	$D_{t,char}$	$delta_t$	N
Landing	0.139	1.00	7.18	25.56
Landing	0.139	0.50	3.59	51.12
Takeoff	0.149	1.00	6.72	25.56
Takeoff	0.149	0.50	3.36	51.12
Cruise	0.233	1.00	4.29	25.56
Cruise	0.233	0.25	1.07	102.24

For the takeoff configuration, the solutions were computed at $delta_t$ = 6.72 ($D_{t,char}$ = 1 inch/step) and then continued at $delta_t$ = 3.36 ($D_{t,char}$ = 0.5 inch/step) at three angles of attack. The averaged values of lift, drag and pitching moment coefficients are shown in Tables 5-7 and the time history plots of the force and moment coefficients are shown in Figures 32-34.

The force and moment coefficient history plot for $\alpha = 8°$ is shown in Figure 32. The time step was reduced at 60,000 iterations. There was a slight change in lift coefficient with change in time step, from C_L = 1.652 to C_L = 1.670 over the next 15,000 iterations. There was also a change in pitching moment coefficient from C_m = -0.759 to C_m = -0.734, that occurred once the lift coefficient began to converge for the smaller time step. There was a 14-count drag reduction with the change in time step, see Table 5.

The force and moment coefficient history plot for $\alpha = 10°$ is shown in Figure 33. The time step was reduced at 56,500 iterations. The average lift coefficient remained nearly the same for both time steps, C_L = 1.886 at 56,500 iterations and C_L = 1.888 at 94,000 iterations. The pitching moment coefficient had a slight increase from C_m = -0.989 to C_m = -0.969 with reduction in time step. There was a 9-count drag reduction with a smaller time step, see Table 6.

The force and moment coefficient history plot for $\alpha = 12°$ is shown in Figure 34. The time step was reduced at 65,000 iterations. There were very small impacts on with the reduction in time step. The average lift coefficient was C_L = 2.057 for $delta_t$ = 6.72 and C_L = 2.055 with the smaller time step ($delta_t$ = 3.36). The pitching moment coefficient was C_m = -1.246 for $delta_t$ = 6.72 and C_m = -1.249 for $delta_t$ = 3.36. There was a 4-count drag increase with the reduction in time step, see Table 7.

The results from the takeoff configuration did not give sufficient evidence that a smaller time step would significantly change the results of C_L, C_D, and C_m. Therefore, the time step of $delta_t$

= 6.72 ($D_{t,char}$ = 1 inch/step) was sufficient, and there was no reason to pay the extra cost of running the rest of the solutions at a smaller time step.

Table 5. Effect of Time Step on Lift, Drag and Pitching Moment Coefficients for the Takeoff Configuration with a 10° Flap Deflection at $M = 0.149$ and $\alpha = 8°$.

$delta_t$	$D_{t,char}$	C_L	C_D	C_m
6.72	1.0	1.652	0.1386	-0.759
3.36	0.5	1.670	0.1372	-0.734

Table 6. Effect of Time Step on Lift, Drag and Pitching Moment Coefficients for the Takeoff Configuration with a 10° Flap Deflection at $M = 0.149$ and $\alpha = 10°$.

$delta_t$	$D_{t,char}$	C_L	C_D	C_m
6.72	1.0	1.886	0.1699	-0.989
3.36	0.5	1.888	0.1690	-0.969

Table 7. Effect of Time Step on Lift, Drag and Pitching Moment Coefficients for the Takeoff Configuration with a 10° Flap Deflection at $M = 0.149$ and $\alpha = 12°$.

$delta_t$	$D_{t,char}$	C_L	C_D	C_m
6.72	1.0	2.057	0.1997	-1.246
3.36	0.5	2.055	0.2001	-1.249

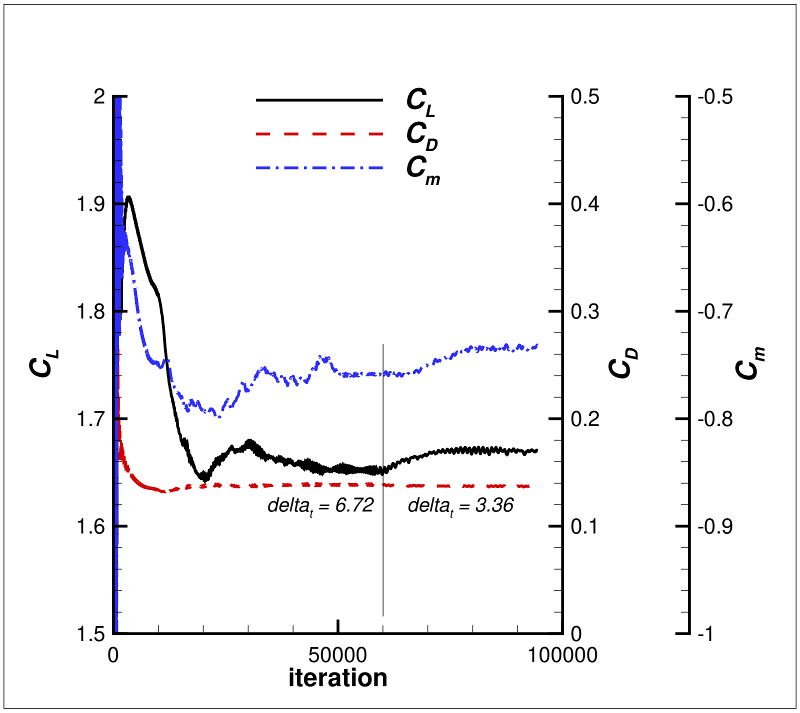

Figure 32. Effect of Time Step on Force and Moment Coefficients for the Takeoff Configuration with a 10° Flap Deflection at $M = 0.149$ and $\alpha = 8°$.

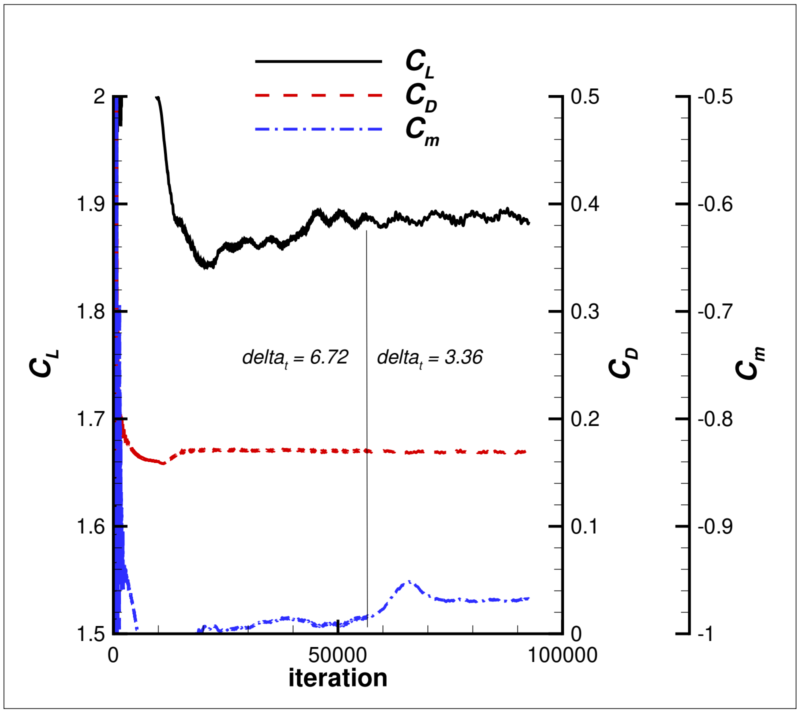

Figure 33. Effect of Time Step on Force and Moment Coefficients for the Takeoff Configuration with 10° Flap Deflection at $M = 0.149$ and $\alpha = 10°$.

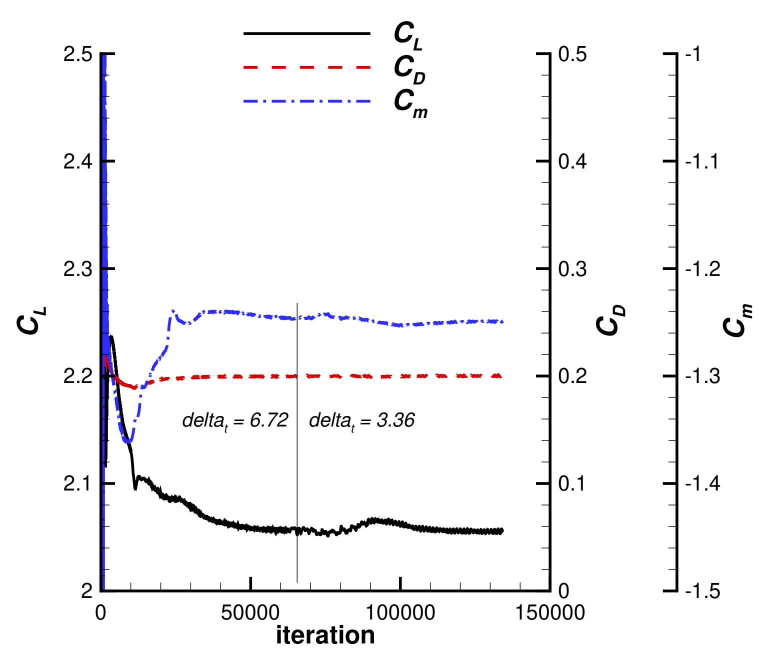

Figure 34. Effect of Time Step on Force and Moment Coefficients for the Takeoff Configuration with 10° Flap Deflection at $M = 0.149$ and $\alpha = 12°$.

For the cruise configuration, two separate solutions were computed with different time steps at $M = 0.233$ and $\alpha = 16°$. One solution had a time step of $delta_t = 4.29$ ($D_{t,char} = 1$ inch/step) and the second solution had a time step of $delta_t = 1.07$ ($D_{t,char} = 0.25$ inch/step). The averaged values of lift, drag and pitching moment coefficients for each solution are shown in Table 8. There was a 0.57 percent difference in lift coefficient, a 0.75 percent difference in drag coefficient, and a 0.40 percent difference in pitching moment coefficient between the two solutions with different time steps.

Table 8. Effect of Time Step on Lift, Drag and Pitching Moment Coefficients for the Cruise Configuration at $M = 0.233$ and $\alpha = 16°$.

$delta_t$	$D_{t,char}$	C_L	C_D	C_m
4.29	1.00	2.090	0.268	-1.978
1.07	0.25	2.102	0.266	-1.986

The convergence plots are shown in Figures 35 and 36. The solution with $delta_t = 4.29$ ($D_{t,char}$ = 1 inch/step) was computed to 60,000 iterations (to be certain of convergence), but the solution could have been stopped at 35,000 iterations (Figure 35(a)). The solution with $delta_t = 1.07$ ($D_{t,char} = 0.25$ inch/step) was computed to 80,000 iterations (Figure 36(b)). There is a larger amplitude for the oscillations of pitching moment coefficient with the smaller time step ($delta_t =$ 1.079), than with the larger time step ($delta_t = 4.29$). The drop in mean flow residuals ($r/r0$) were comparable (Figure 36), but the turbulence residuals ($tnu/tnu0$) for the solution with a smaller time step dropped four orders of magnitude (Fig. 36(b)), while the solution with the larger step dropped only two orders of magnitude (Fig. 36(a)).

Figure 37 shows the normalized U velocity contours for the two solutions with different time steps. As expected from the small differences in average force and moment coefficients, the contours are similar. There is slightly less inboard flow separation for the solution with the smaller time step ($delta_t = 1.07$), that corresponds to a slightly higher lift coefficient, than the solution with the larger time step ($delta_t = 4.29$).

These differences of less than 1 percent in C_L, C_D, and C_m between the solutions with different time steps did not justify computing the rest of the angles of attack at the smaller time step. Running solutions with smaller time steps generally use more resources. Therefore, the time step of $delta_t = 4.29$ ($D_{t,char} = 1$ inch/step) was sufficient and there was no reason to pay the extra cost of running the solutions with a smaller time step.

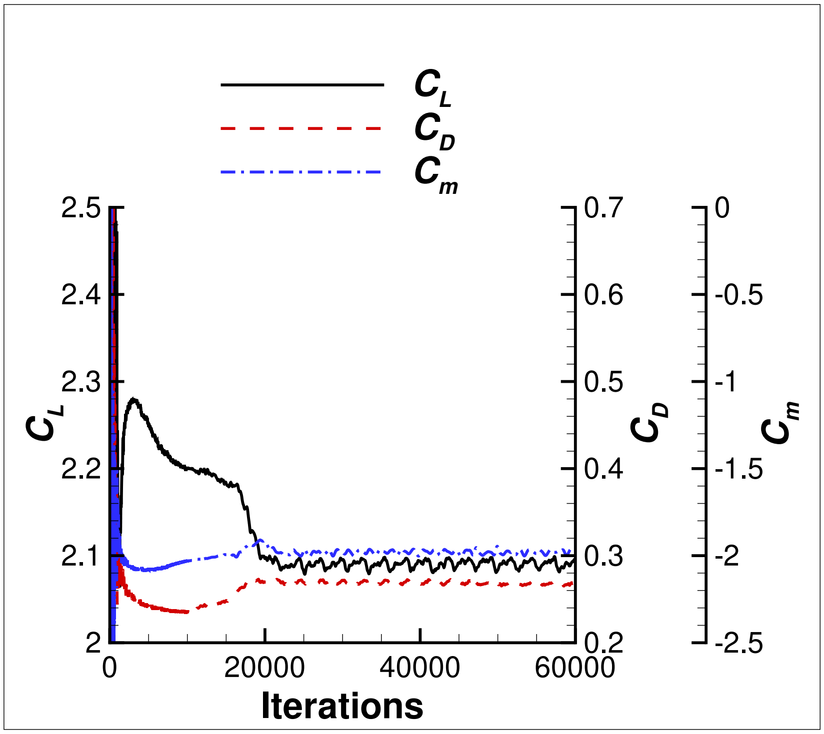

(a) $delta_t = 4.29$ ($D_{t,char} = 1$ inch/step)

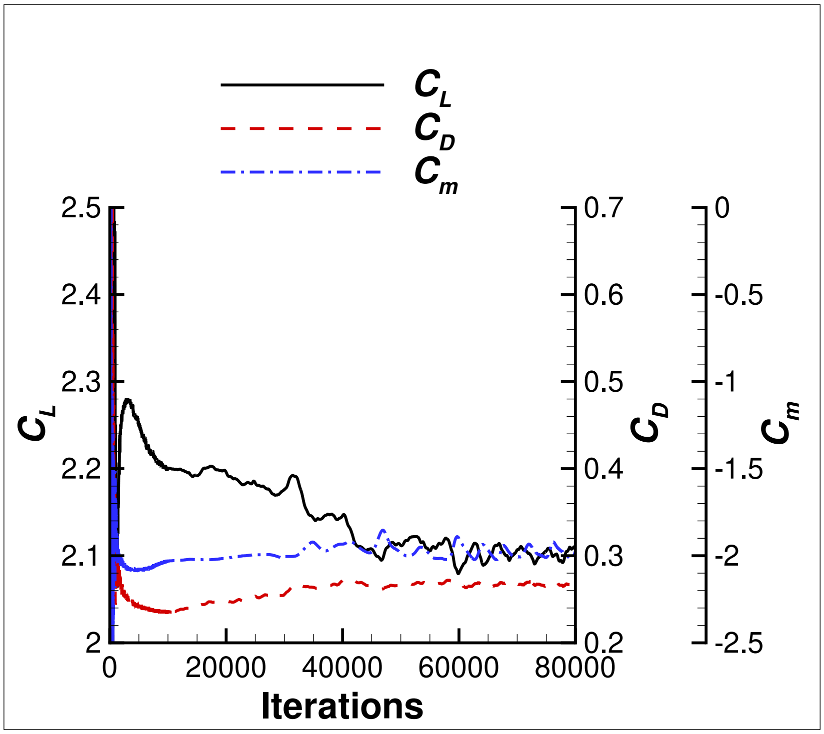

(b) $delta_t = 1.07$ ($D_{t,char} = 0.25$ inch/step)

Figure 35. Effect of Time Step on Forces and Moment Coefficients for the Cruise Configuration at $M = 0.233$ and $\alpha = 16°$.

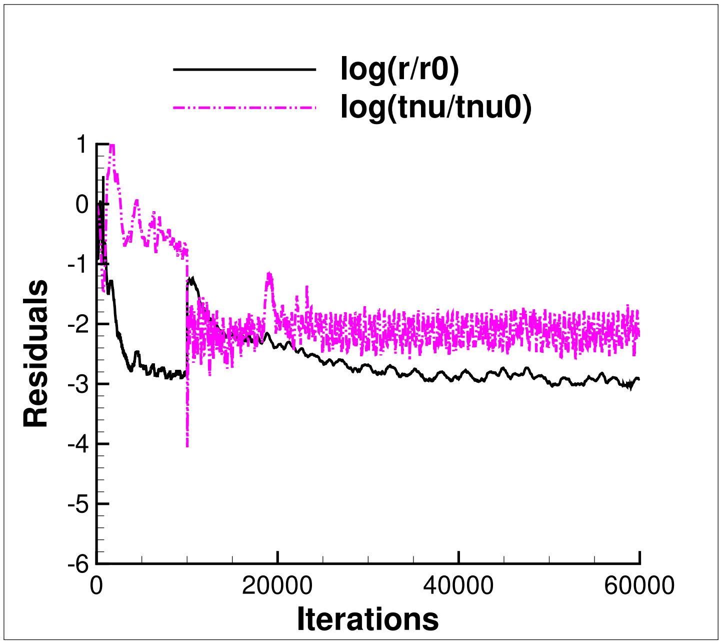

(a) $delta_t = 4.29$ ($D_{t,char} = 1$ inch/step)

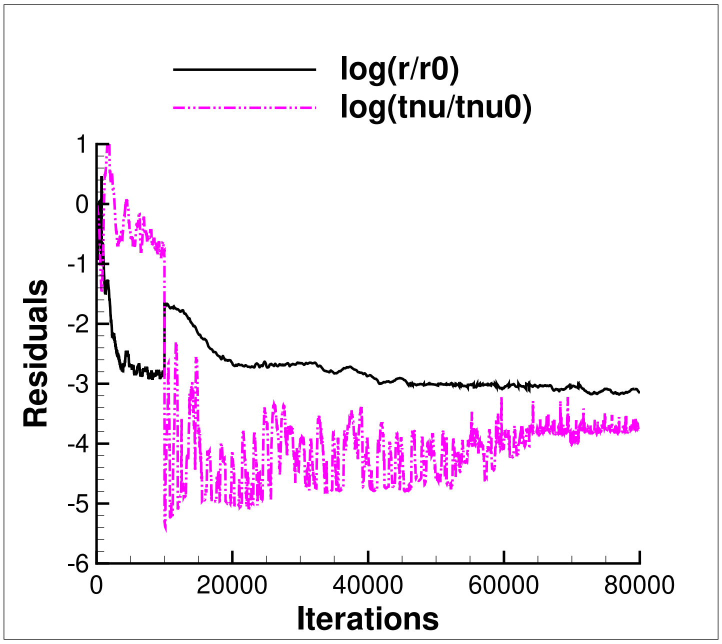

(b) $delta_t = 1.07$ ($D_{t,char} = 0.25$ inch/step)

Figure 36. Effect of Time Step on Residuals for the Cruise Configuration at $M = 0.233$ and $\alpha = 16°$.

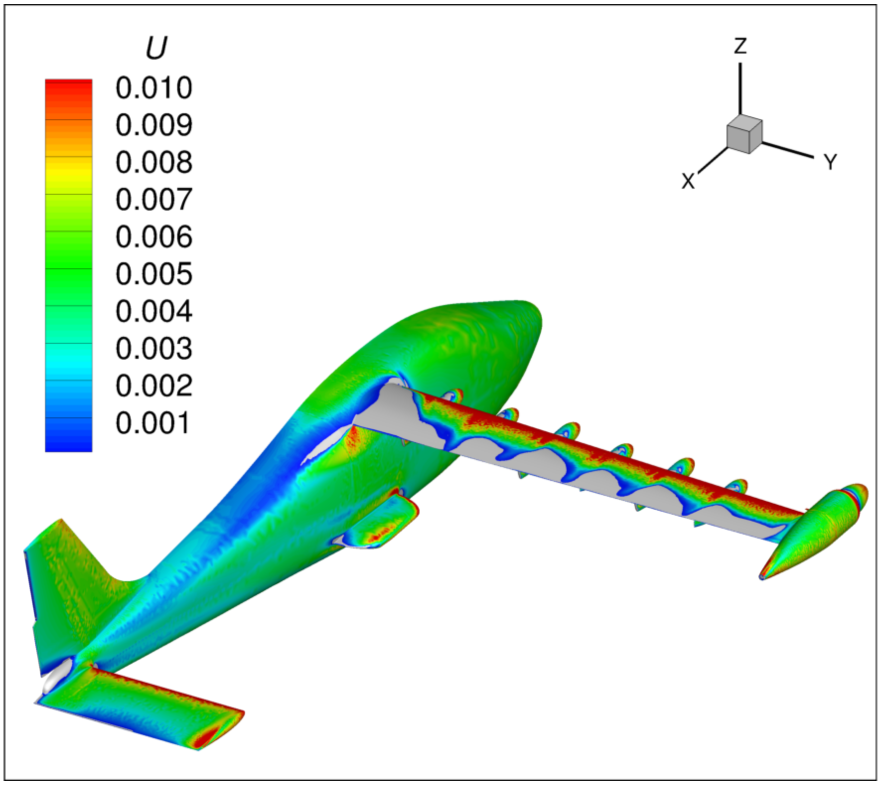

(a) $delta_t = 4.29$ ($D_{t,char} = 1$ inch/step)

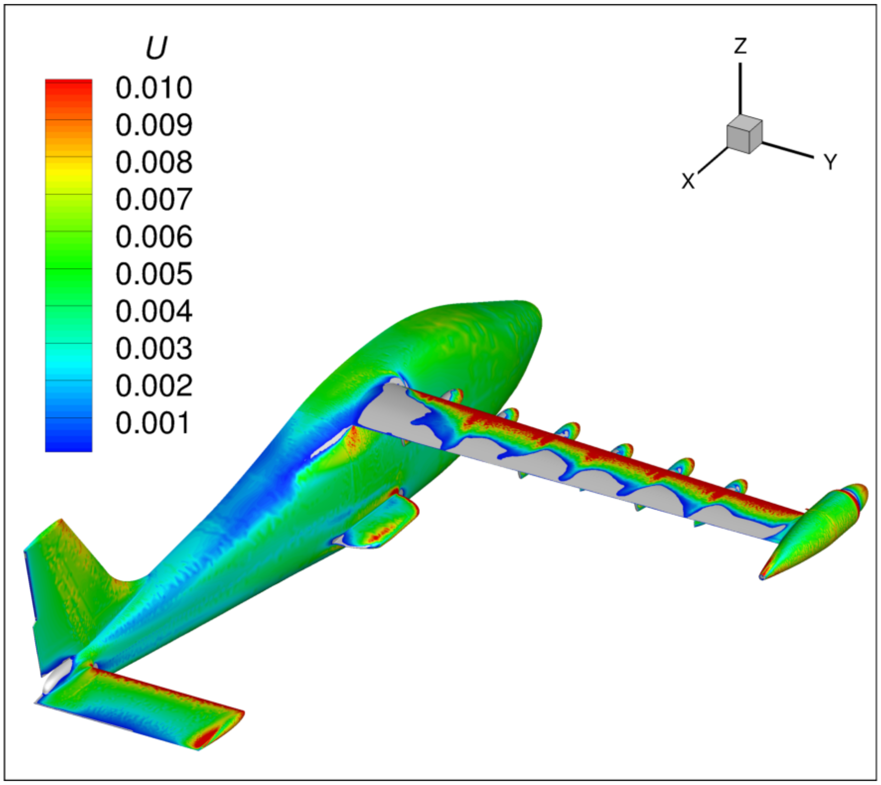

(b) $delta_t = 1.07$ ($D_{t,char} = 0.25$ inch/step)

Figure 37. Effect of Time Step on Normalized U Velocity for the Cruise Configuration at $M = 0.233$ and $\alpha = 16°$.

2.9 Convergence

The solution residuals and the force and moment coefficient histories for the cruise configuration, the takeoff configuration, and the landing configuration are shown in Appendices A to C, respectively. In general, it is easier to judge convergence when a solution is steady because the residuals are usually smooth, and the coefficients typically flatten out with a very small standard deviation from the average. However, judging the convergence of an unsteady problem requires engineering judgment in determining solution convergence and the averaging should be done over a reasonable period.

For steady problems, two main criteria were used to determine solution convergence; a drop in residual of two orders of magnitude and the convergence of force and moment coefficients to less than 0.5 percent change over a specified range of iterations. The coefficients were averaged over a range of 2,000 iterations. The standard deviation and the percent over range (POR) were also calculated for each coefficient over the specified range. The POR was calculated with Equation 4, where $C_{(N,max-(range))}$ and $C_{N,max}$ are the values of the coefficient at the first and last iterations of the range, respectively. The average value of a coefficient is computed with Equation 5.

$$POR = \left(\frac{C_{N,max} - C_{(N,max-(range))}}{C_{average}} \right) * 100 \tag{4}$$

$$C_{average} = \frac{1}{range} \sum_{j=N_{max}-range}^{N_{max}} (C_j) \tag{5}$$

Steady solutions are deemed converged when the POR values are less than 0.5. In the situation where the coefficient is approaching zero, the POR values may be larger than 0.5 percent because of the near zero average value of the coefficient in the denominator of Equation 4. These higher POR calculations when the average is near zero can be deceiving, and therefore, engineering judgment is used with the standard deviation to determine if properly converged with $POR > 0.5$. An example of force and moment convergence data for a steady case is shown in Table 9.

Table 9. Typical Convergence Data for a Steady Solution, the Cruise Configuration at $M = 0.233$, $\alpha = 0°$.

Coefficient	C_L	C_D	C_m
Average	0.5920E+00	0.4631E-01	0.6121E-01
Standard Deviation	0.2425E-04	0.2536E-05	0.9198E-04
POR	0.01	0.01	0.54

In this example for the cruise configuration at $M = 0.233$ and $\alpha = 0°$, the lift coefficient (C_L) and drag coefficient (C_D) have a POR of 0.01 percent, but the pitching moment coefficient (C_m) is 0.54 percent. A further look at the C_m average and standard deviation show that C_m is in fact converged. A grouping of plots used to evaluate convergence is shown in Figures 38-41. For this steady state solution example of the cruise configuration at $M = 0.233$ and $\alpha = 0°$, Figure 38 shows decreasing residuals of at least four orders of magnitude. The force and moment coefficients shown in Figure 39 indicate good convergence as well. A typical plot of the subiteration residual convergence is shown in Figure 40 and shows that for each time step, the mean flow and turbulence residuals are dropping four and five orders of magnitude, respectively. Finally, Figure 41 shows the normalized U velocity contours in the x direction, at the first cell above the surface. This figure shows fully attached flow on the full configuration because reversed flow, values less than 0, are removed from the plot and none of the shaded surface is showing. The normalized U velocity contours are computed by dividing the dimensional U velocity by the dimensional freestream speed of sound.

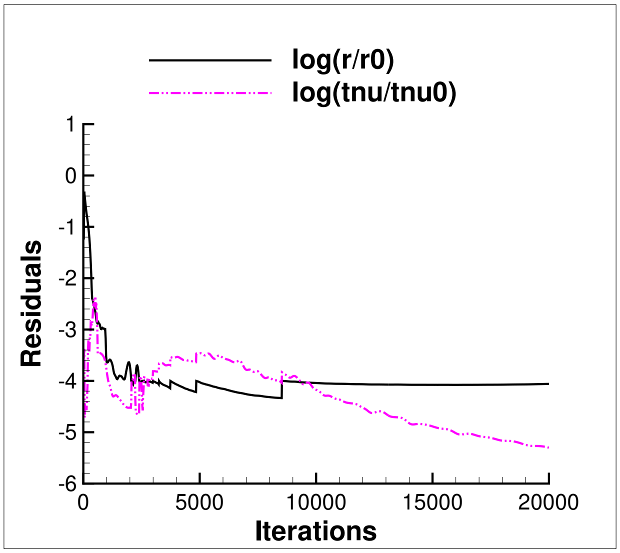

Figure 38. Convergence History Showing Residuals as a Function of Iteration for a Steady Solution on the Cruise Configuration at $M = 0.233$ and $\alpha = 0°$, No Cruise Power, and No High-Lift Blowing.

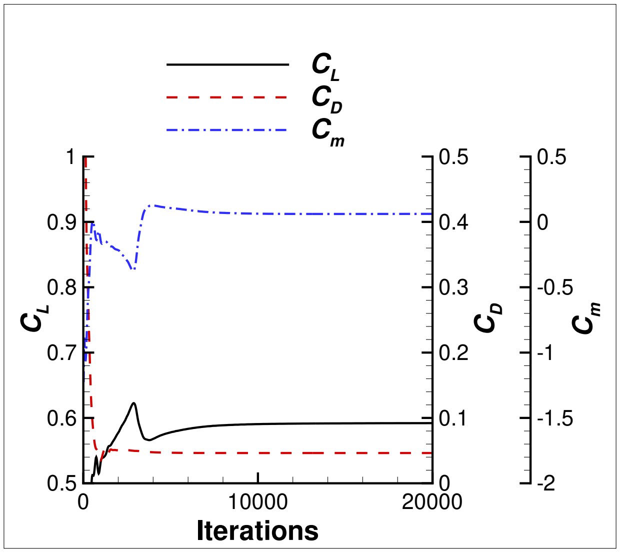

Figure 39. Convergence History Showing Force and Moment Coefficients as a Function of Iteration for a Steady Solution on the Cruise Configuration at $M = 0.233$ and $\alpha = 0°$, No Cruise Power, and No High-Lift Blowing.

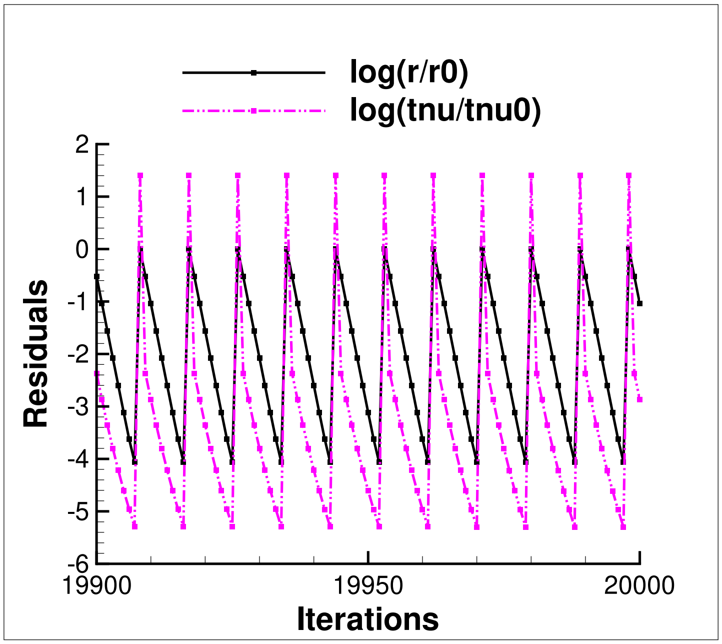

Figure 40. Convergence History Showing Subiteration Residuals as a Function of Iteration for a Steady Solution on the Cruise Configuration at $M = 0.233$ and $\alpha = 0°$, No Cruise Power, and No High-Lift Blowing.

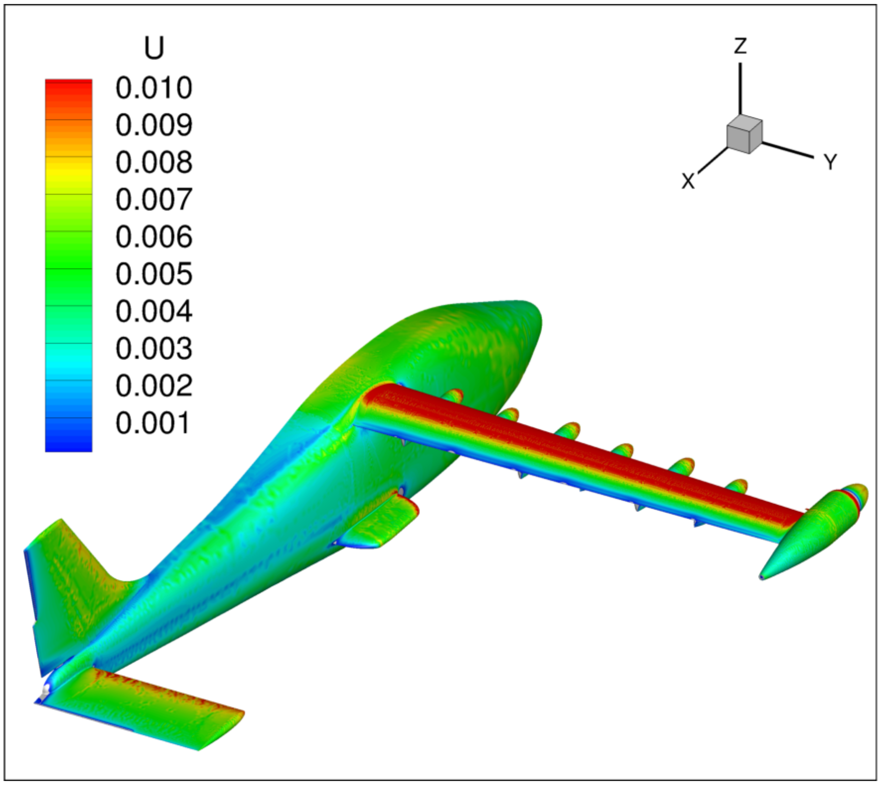

Figure 41. The Normalized U Velocity Contours for a Steady Solution on the Cruise Configuration at $M = 0.233$ and $\alpha = 0°$, No Cruise Power, and No High-Lift Blowing.

For unsteady problems, a drop in residuals of two orders of magnitude is preferable and periodicity in the force and moment coefficients is needed to compute a reasonable average of the coefficients. Unsteady flows with large regions of flow separation can prevent large or smooth decreases in the solution residuals.

An example of convergence data for an unsteady case, the cruise configuration at $M = 0.233$ and $\alpha = 12°$, is shown in Table 10 and the convergence history plots are shown in Figures 42-45. In this example, the C_L, C_D, and C_m all have POR that are less than 0.5 percent, see Table 10.

Table 10. Typical Convergence Data for an Unsteady Solution, the Cruise Configuration at $M = 0.233$ and $\alpha = 12°$.

Coefficient	C_L	C_D	C_m
Average	0.1925E+01	0.1643E+00	-0.1270E+01
Standard Deviation	0.1215E-02	0.2798E-03	0.8249E-03
POR	-0.12	-0.26	0.09

The mean flow residual dropped four orders of magnitude, but the turbulence residual did not drop smoothly like the solution with steady flow in the example in Figure 38, even though it has reached two orders of magnitude reduction, see Figure 42. The force and moment coefficients shown in Figure 43 indicate good convergence with little variance over 10,000 iterations. The subiteration residual convergence is shown in Figure 44 and indicates that the mean flow and turbulence residuals are dropping well over the specified subiterations at each time step. Finally, Figure 45 shows the normalized U velocity contours at the first cell above the surface and values less than 0 are cut from rendering. Therefore, the solution shows that the flow is separated from the aft portion of the wing since the gray surface of the configuration is visible along the wingspan. This flow separation is the reason why the turbulence residuals are not smoothly decreasing with iteration since the aft portion of the wing has separated flow.

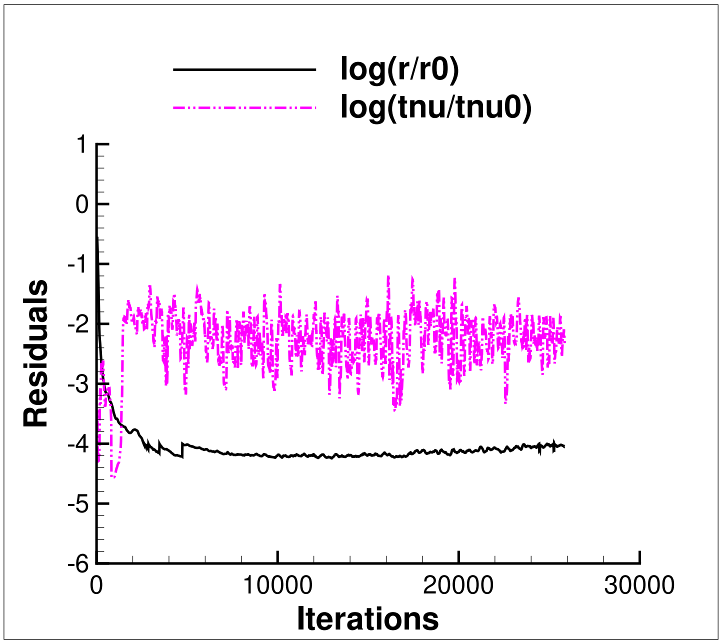

Figure 42. Convergence History Showing Residuals as a Function of Iteration for an Unsteady Solution on the Cruise Configuration at $M = 0.233$ and $\alpha = 12°$, No Cruise Power, and No High-Lift Blowing.

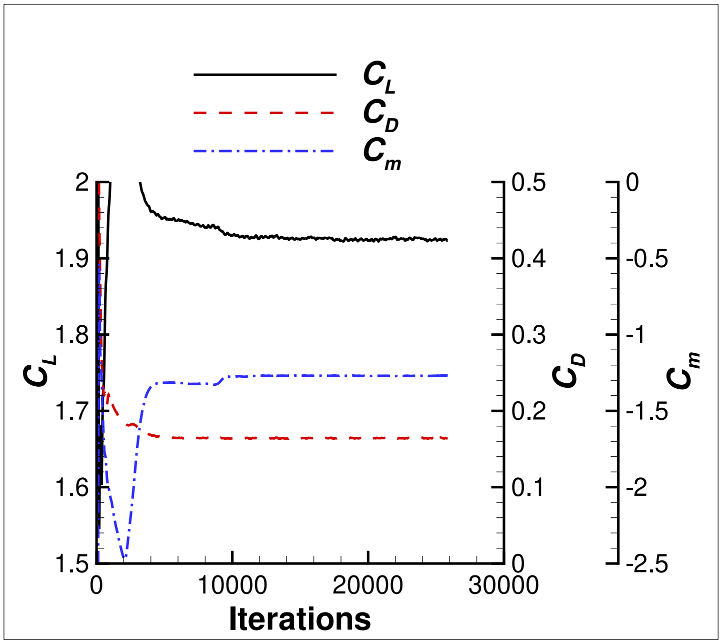

Figure 43. Convergence History Showing Force and Moment Coefficients as a Function of Iteration for an Unsteady Solution on the Cruise Configuration at $M = 0.233$ and $\alpha = 12°$, No Cruise Power, and No High-Lift Blowing.

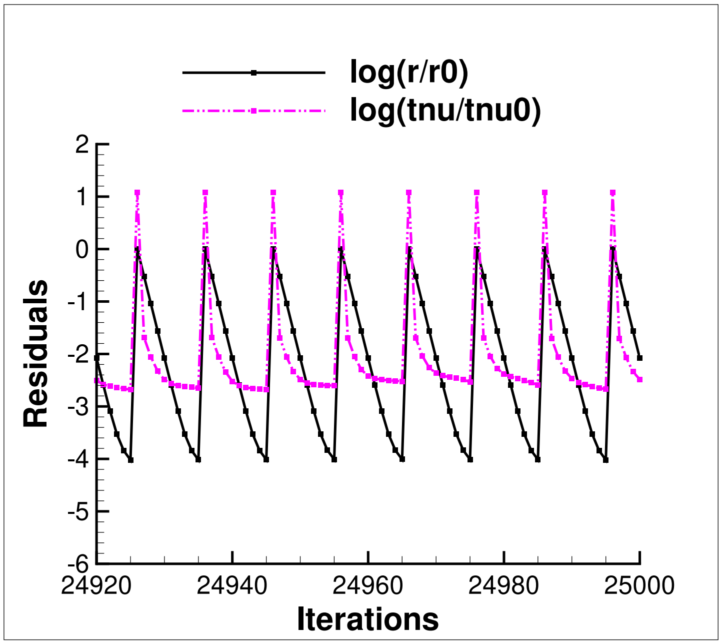

Figure 44. Convergence History Showing Subiteration Residuals as a Function of Iteration for an Unsteady Solution on the Cruise Configuration at $M = 0.233$ and $\alpha = 12°$, No Cruise Power, and No High-Lift Blowing.

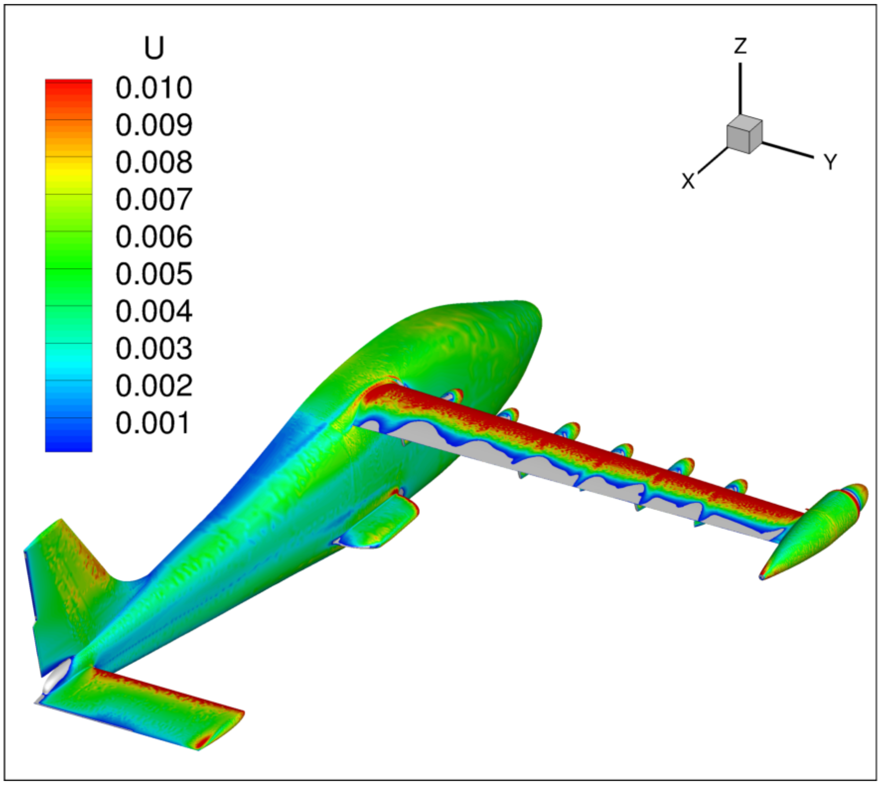

Figure 45. Normalized U Velocity Contours for an Unsteady Solution on the Cruise Configuration at $M = 0.233$ and $\alpha = 12°$, No Cruise Power, and No High-Lift Blowing.

2.10 Post Processing

Several reference values were used to compute the lift, drag and pitching moment coefficients. The reference length was the mean aerodynamic chord 25.56 inches and the reference span was 379.47 inches. The reference area was $S_{ref} = 9600\ in^2$, but $S_{ref} = 4800\ in^2$ was used to get fullspan coefficients from the semispan mesh. The moment reference point (x = 154.797 in., y = 0.0 in., z = 64.527 in.) is hidden within the airplane, but can be discerned from the intersection of the black, red, and blue lines in Figure 46.

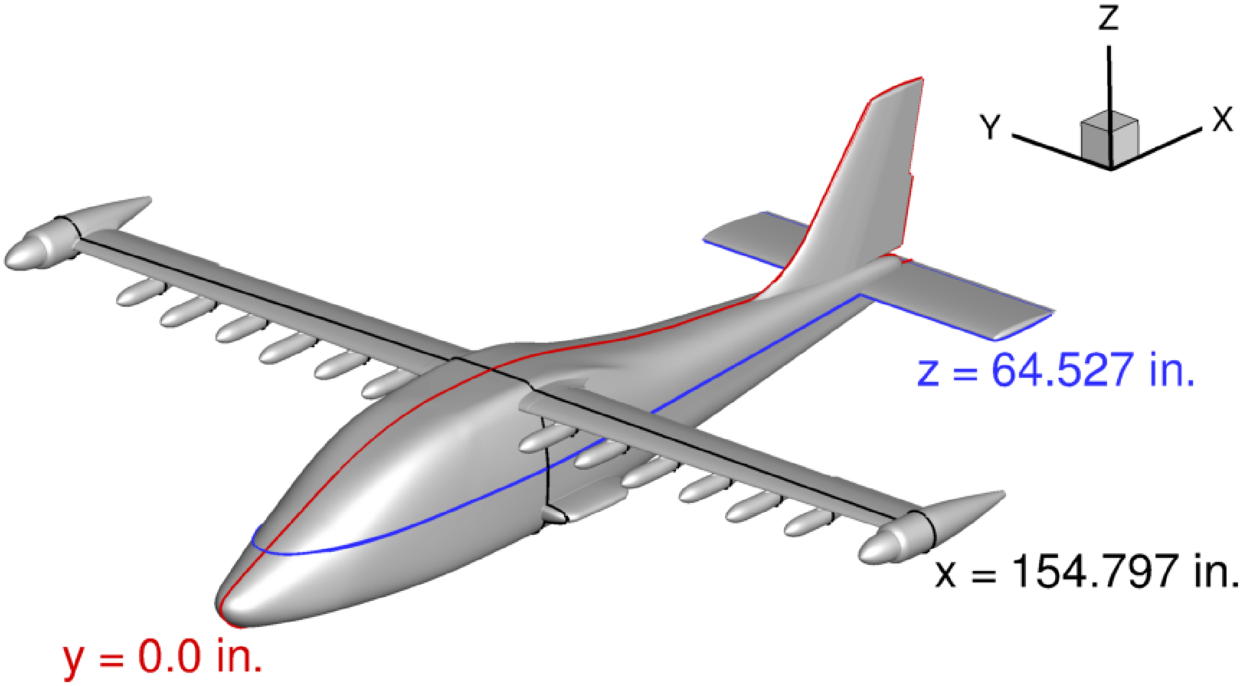

Figure 46. The X, Y and Z Planes that Intersect to Form the Moment Reference Center.

For each iteration, the USM3D code computes the total force and moment coefficients. If the user chooses, the component contributions to the force and moment coefficients are written to a file to track the convergence throughout the solution development. The Langley developed post-processing tool, USMC6, was used to extract data from the solution. The USMC6 utility (Ref. [15]) is capable of computing the force and moment coefficients on the basis of individual components. The tet2tec utility was used to extract data from the tetrahedral volume solution and write it into a Tecplot format with a variety of variables.

3 Results

This paper documents the performance of the X-57 Maxwell at three flight conditions for the unblown wing and the unpowered cruise propeller. The cruise configuration had no flap deflection and solutions were computed at $M = 0.233$ (150 KTAS at an altitude of 8,000 feet) for this geometry. The landing configuration, with a 30° flap deflection, was computed at $M = 0.139$ (91.3 KTAS at an altitude of 2,500 feet). The takeoff configuration, with a 10° flap deflection, was computed at $M = 0.149$ (97.5 KTAS at an altitude of 2,500 feet). These configurations have the preliminary fuselage that was designed in OpenVSP (VSP fuselage) and used at NASA Langley for the first three years of the X-57 program.

3.1 Results for the Cruise Configuration

The airplane lift coefficient and the component contributions to lift for the cruise configuration are shown in Figure 47 and the airplane drag coefficient is shown in Figure 48. The lift to drag ratio (L/D) is often used to characterize the efficiency of an airplane and the airplane's maximum range would occur at the maximum L/D. The L/D as a function of angle of attack and lift coefficient are shown in Figure 49. The skin friction coefficient contours at each angle of attack are shown in Figures 50-61. Regions of flow separation can be visualized as areas of dark blue contours where the value of skin friction is zero. The pressure coefficient contours, with black lines showing surface streamlines, at several angles of attack are shown in Figures 62-73. The semispan data were mirrored to the left side of the airplane in the figures showing pressure coefficient contours.

The computed cruise lift coefficient for the X-57 Maxwell airplane is $C_L = 0.7516$, as estimated for an airplane weight of 3,000 lbs, flying at an altitude of 8,000 feet and a Mach number of $M = 0.233$. Based on the results in Figure 47, a $C_L = 0.7516$ occurs at the cruise angle of attack of $\alpha = 1.15°$. The computed drag coefficient at $\alpha = 1.15°$ is $C_D = 0.05275$, see Figure 48(b). Using the cruise angle of attack of $\alpha = 1.15°$ in Figure 49(a), or the $C_L = 0.7516$ in Figure 49(b), the cruise lift to drag ratio can be determined as $L/D = 14.14$. This computed L/D on the computationally smooth X-57 airplane would be reduced somewhat in comparison to the real X-57 Maxwell airplane with rivets, gaps and steps, but it provides an estimate for the potential L/D at cruise. This potential L/D at cruise for the all-electric X-57 Maxwell airplane is about 50 percent higher, or more efficient than the baseline Tecnam P2006T airplane, while offering the additional environmental advantage of zero emissions. The maximum computed lift to drag ratio for the cruise configuration across the range of angle of attack is $L/D_{max} = 15.8$ at $\alpha = 4°$.

The maximum lift coefficient ($C_{L,max}$) for the unpowered and unblown cruise configuration was $C_{L,max} = 2.13$ at $\alpha = 15°$. As expected, the largest contribution to lift is from the wing (Figure 47(a)). The lift contribution from the wing increases from $\alpha = -2°$ to $\alpha = 15°$. There is a small region of fullspan flow separation along the aft portion of the wing for $\alpha = 8°$ (Figure 50). The flow separation region moves upstream and the area increases as angle of attack increases to $\alpha = 15°$ (Figures 51-54). The fullspan flow separation along the aft portion of the wing is also visible in Figures 62-66, where the streamlines indicate recirculating flow downstream of the nacelles, and the area of flow separation increases as the angle of attack increases.

The first drop in lift occurs on the wing at $\alpha = 16°$, which results from a large region of flow separation at the wing root, see Figures 55, when compared to attached flow at the wing root in Figures 50-54. The wingroot flow separation region is also visible in Figure 67 where black lines coalesce into thick dividing streamlines that are slanted from the wingroot leading edge to the trailing edge, downstream of the second nacelle (from the centerline). These streamlines divide the attached flow and the separated flow regions at the wing root.

At $\alpha = 18°$, another region of flow separation forms between the third and fourth high-lift nacelles from the centerline (Figures 57 and 69), but there is only a slight decrease in lift (Figure 47) as the flow separation has not yet moved forward to the wing leading edge. At $\alpha = 20°$, there is a larger decrease in lift on the wing (and airplane) as yet another flow separation region forms between the fifth and sixth high-lift nacelles from the centerline (Figures 59 and 71), and both flow separation regions move forward to the wing leading edge. At $\alpha = 22°$, there is another large decrease in lift on the wing (and airplane) as two more flow separation regions form, one between the second and third high-lift nacelles from the centerline and outboard of the last high-lift nacelle

(Figures 60 and 72). Finally, at $\alpha = 24°$, there is an increase in lift on the wing (and airplane) as the flow separation patterns change on the wing upper surface (Figure 61 and 73).

The stabilator and fuselage have a small contribution to lift that increases with increasing angle of attack, see Figure 47. The vertical tail (vtail), tip nacelle, and high-lift nacelles, pylons, and strakes (NPS) have minimal contribution to the lift coefficient. The lift coefficient without the contribution of the stabilator ($C_{L,airplane}$ - $C_{L,stabilator}$) is shown in Figure 47(b). The lift from stabilator increases until $\alpha = 20°$. At $\alpha = 22°$, there is a loss of lift on the stabilator (Figure 47(b)) as the flow separation on the stabilator moves forward to the leading edge (Figure 60), which is in contrast to some attached flow on the stabilator at $\alpha = 20°$ (Figure 59). At $\alpha = 24°$ (Figure 61), the stabilator remains stalled and there is a slight loss in lift from additional inboard flow separation the stabilator.

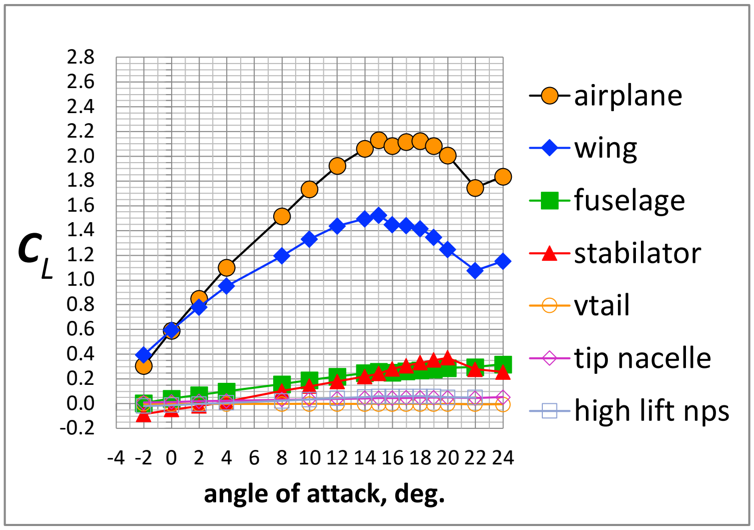

(a) Component Contributions to Lift

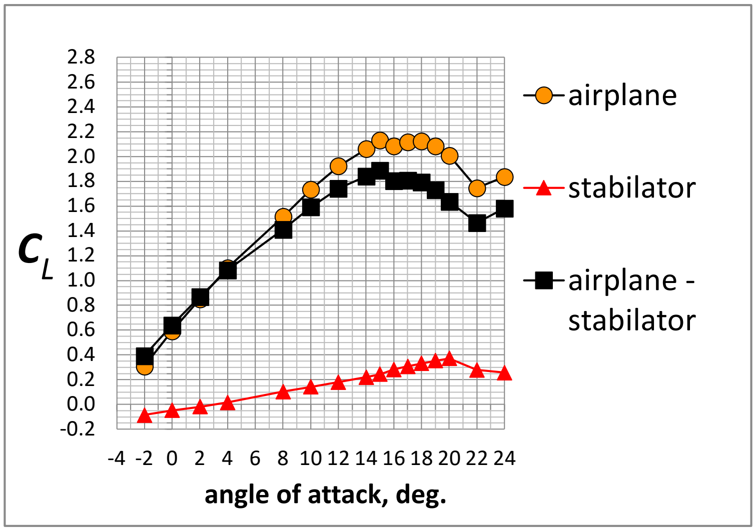

(b) Effect of Stabilator on Lift

Figure 47. Lift Coefficient as a Function of Angle of Attack for the Cruise Configuration at $M = 0.233$.

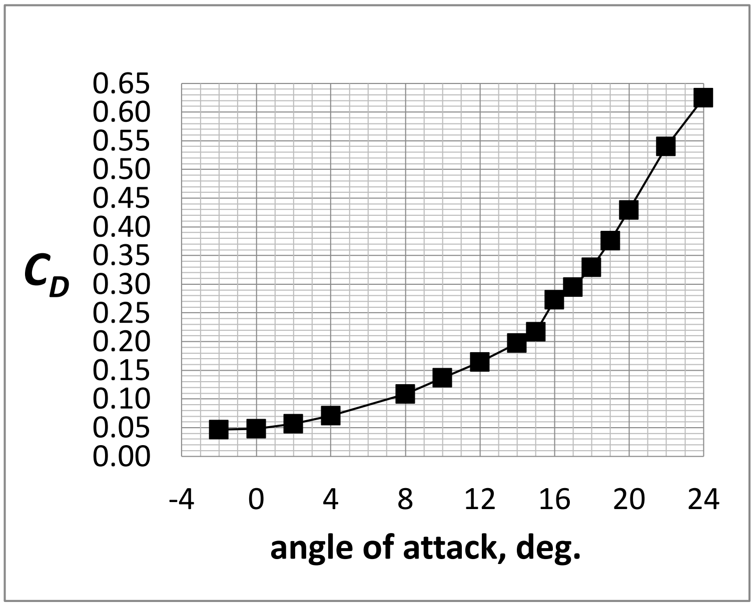

(a) Full Angle of Attack Range

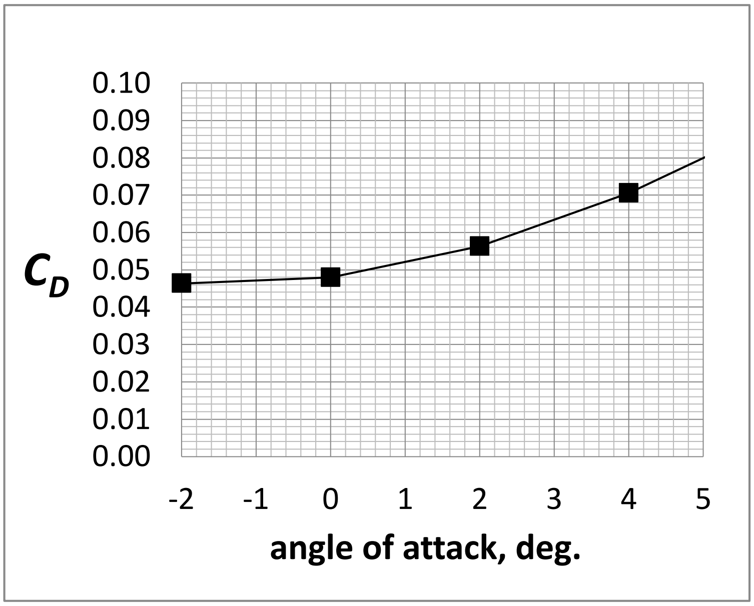

(b) Limited Angle of Attack Range

Figure 48. Airplane Drag Coefficient as a Function of Angle of Attack for the Cruise Configuration at $M = 0.233$.

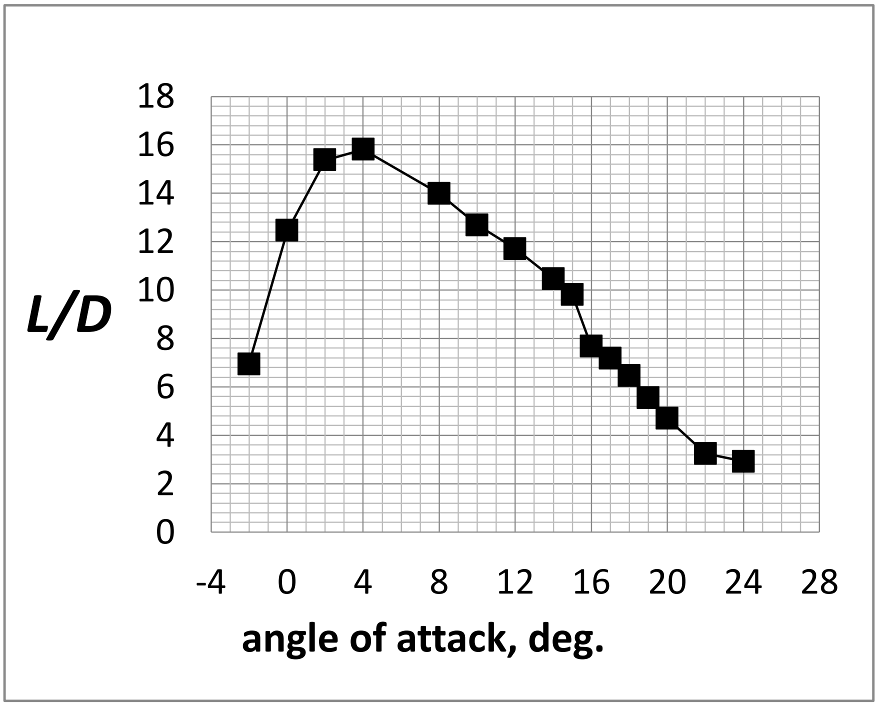

(a) Lift to Drag Ratio as a Function of Angle of Attack

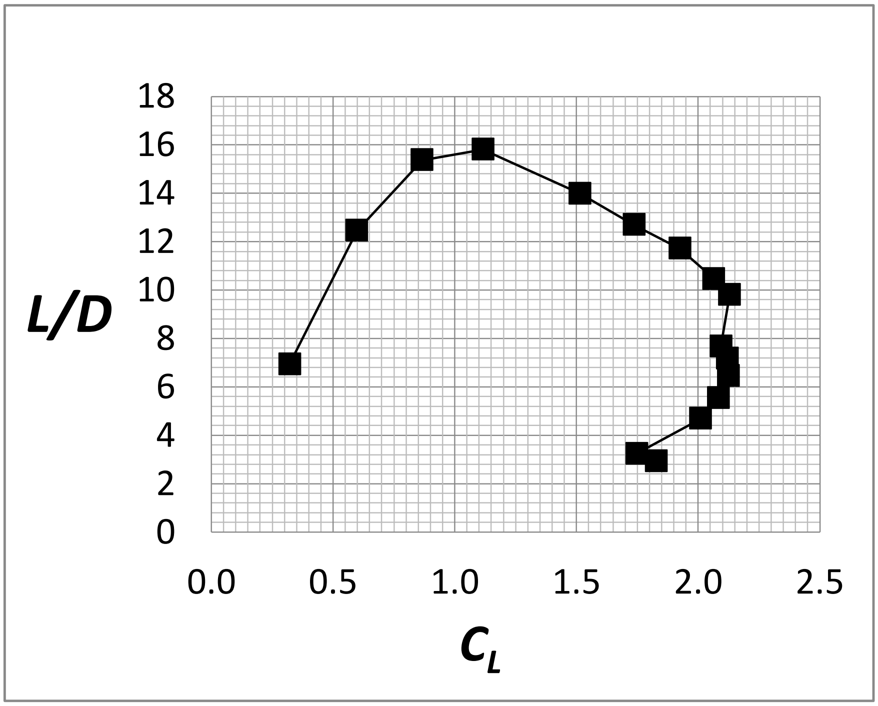

(b) Lift to Drag Ratio as a Function of Lift Coefficient

Figure 49. The Lift to Drag Ratio for the Cruise Configuration at $M = 0.233$.

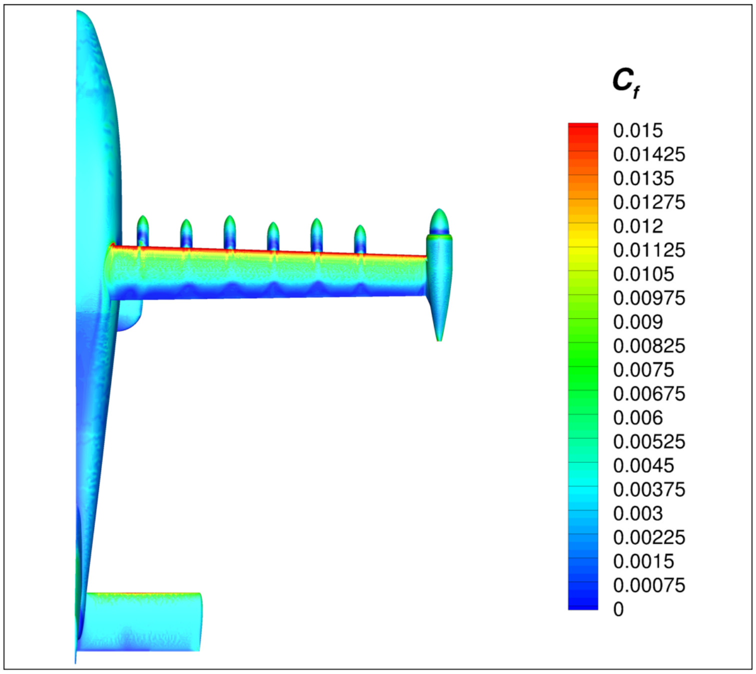

Figure 50. Skin Friction Coefficient Contours for the Cruise Configuration at $M = 0.233$ and $\alpha = 8°$.

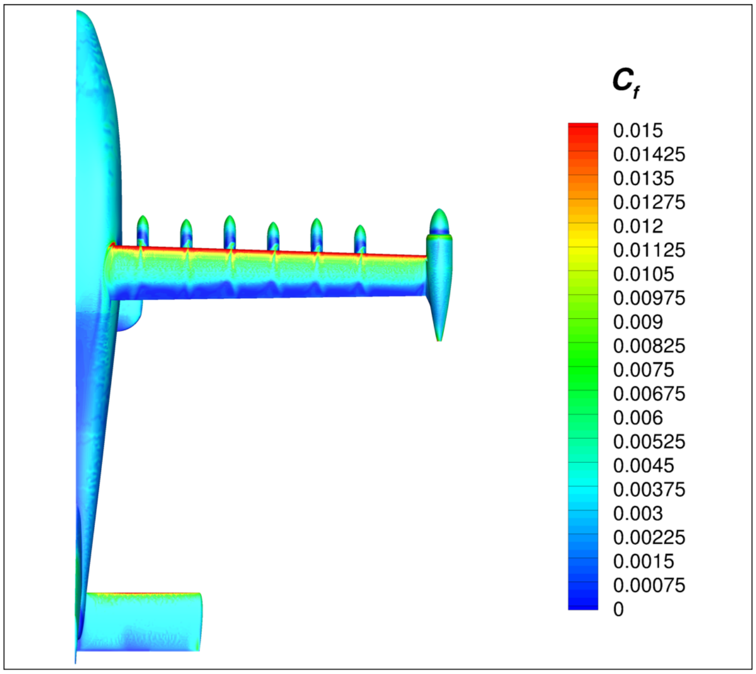

Figure 51. Skin Friction Coefficient Contours for the Cruise Configuration at $M = 0.233$ and $\alpha = 10°$.

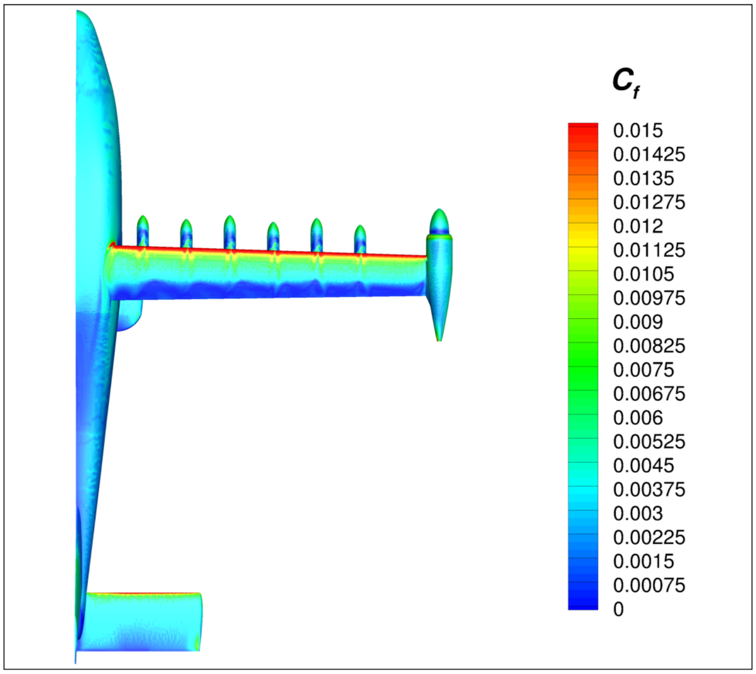

Figure 52. Skin Friction Coefficient Contours for the Cruise Configuration at $M = 0.233$ and $\alpha = 12°$.

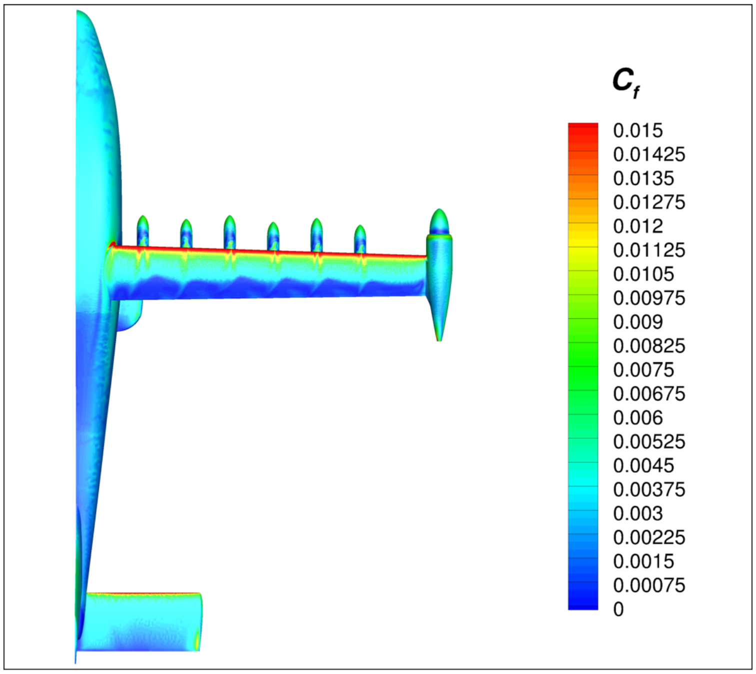

Figure 53. Skin Friction Coefficient Contours for the Cruise Configuration at $M = 0.233$ and $\alpha = 14°$.

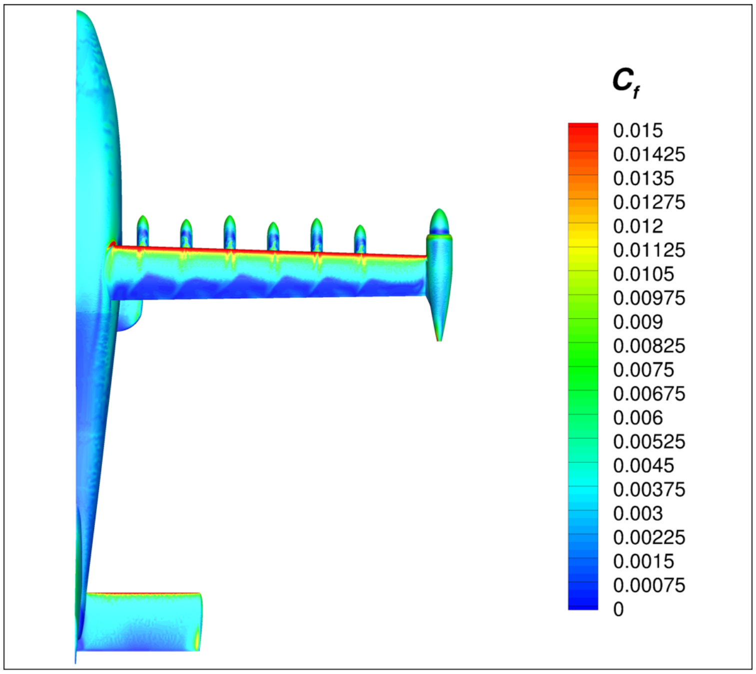

Figure 54. Skin Friction Coefficient Contours for the Cruise Configuration at $M = 0.233$ and $\alpha = 15°$.

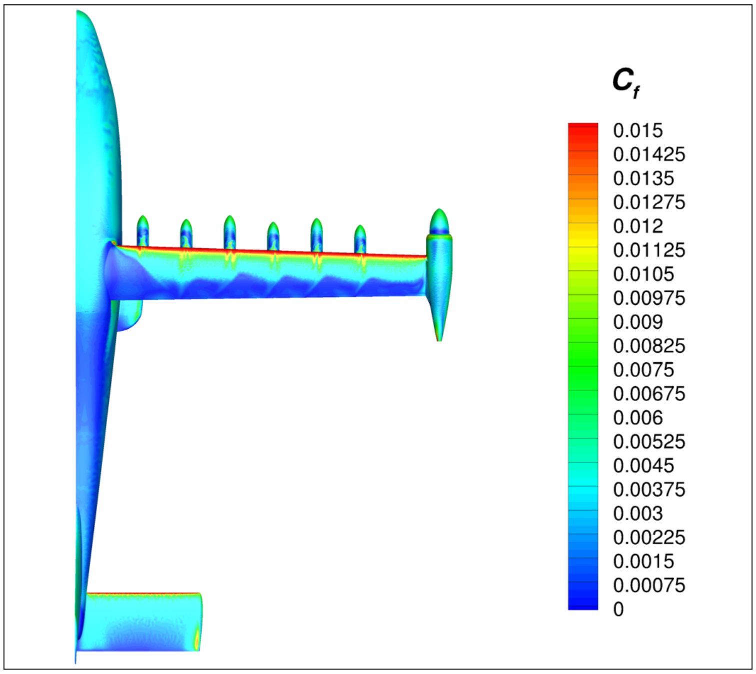

Figure 55. Skin Friction Coefficient Contours for the Cruise Configuration at $M = 0.233$ and $\alpha = 16°$.

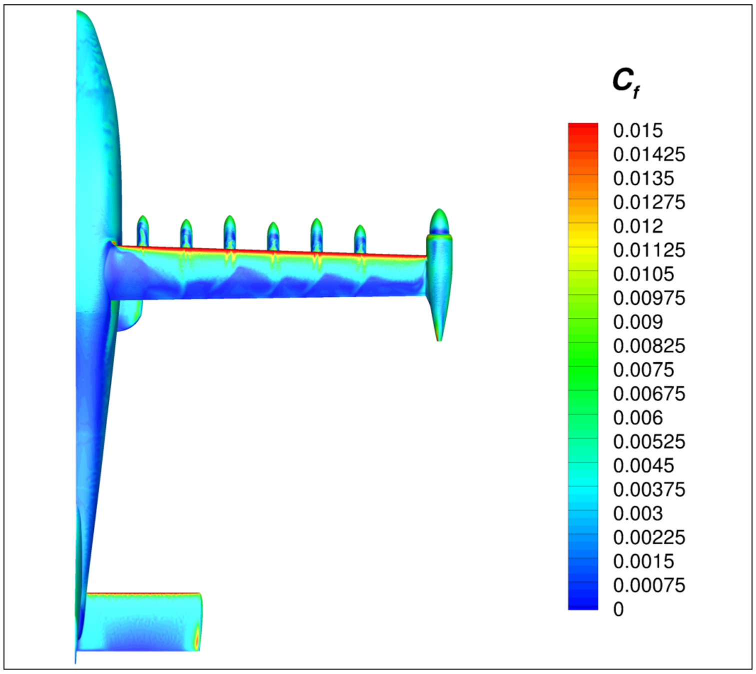

Figure 56. Skin Friction Coefficient Contours for the Cruise Configuration at $M = 0.233$ and $\alpha = 17°$.

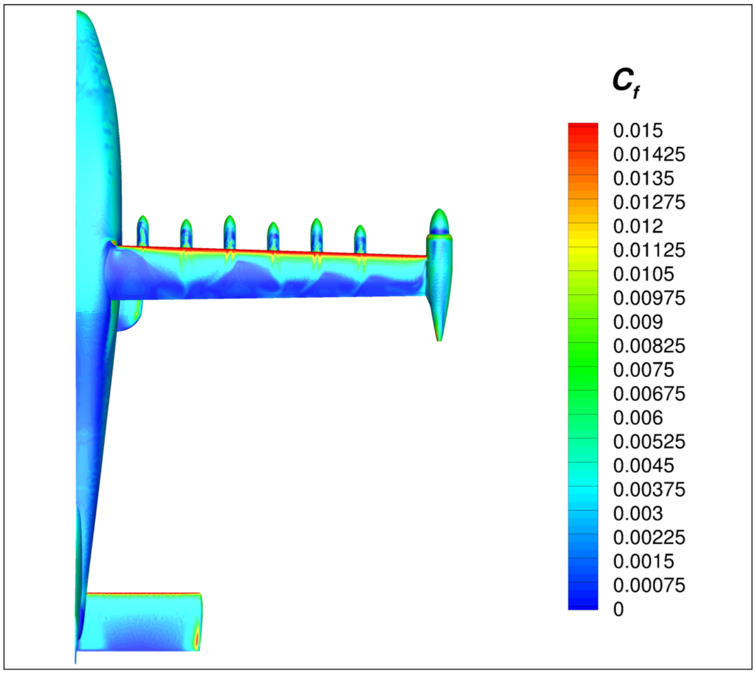

Figure 57. Skin Friction Coefficient Contours for the Cruise Configuration at $M = 0.233$ and $\alpha = 18°$.

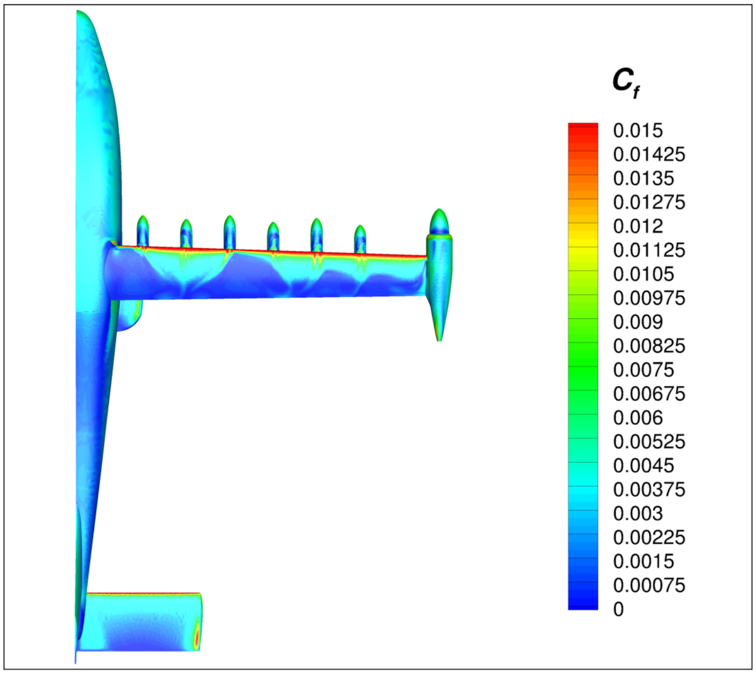

Figure 58. Skin Friction Coefficient Contours for the Cruise Configuration at $M = 0.233$ and $\alpha = 19°$.

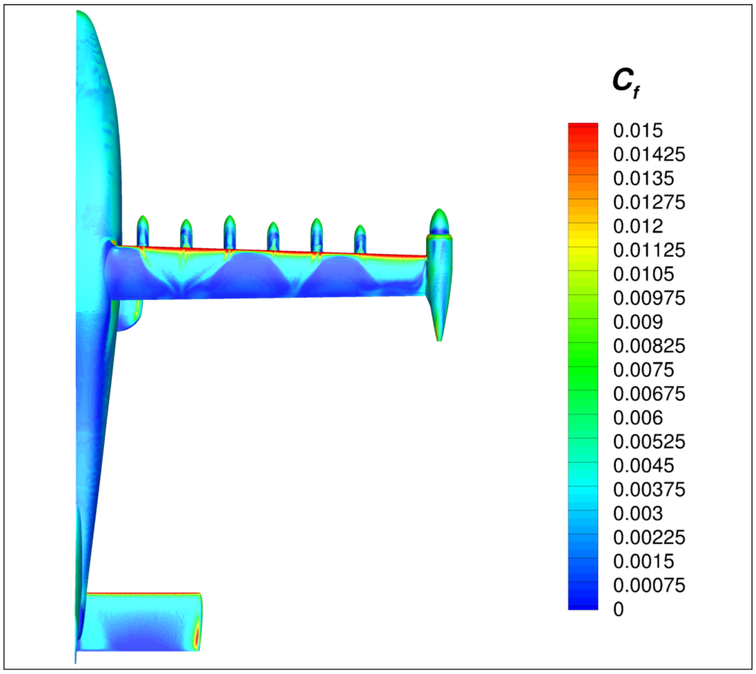

Figure 59. Skin Friction Coefficient Contours for the Cruise Configuration at $M = 0.233$ and $\alpha = 20°$.

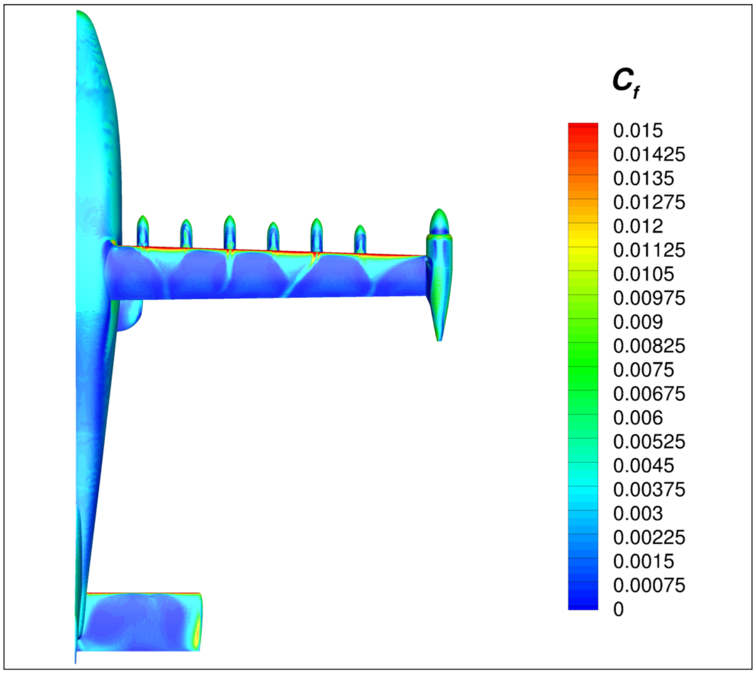

Figure 60. Skin Friction Coefficient Contours for the Cruise Configuration at $M = 0.233$ and $\alpha = 22°$.

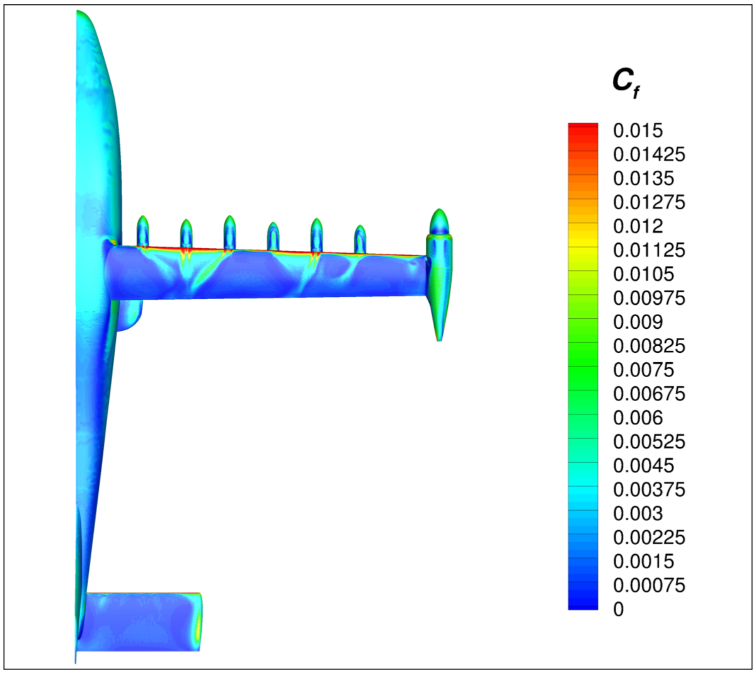

Figure 61. Skin Friction Coefficient Contours for the Cruise Configuration at $M = 0.233$ and $\alpha = 24°$.

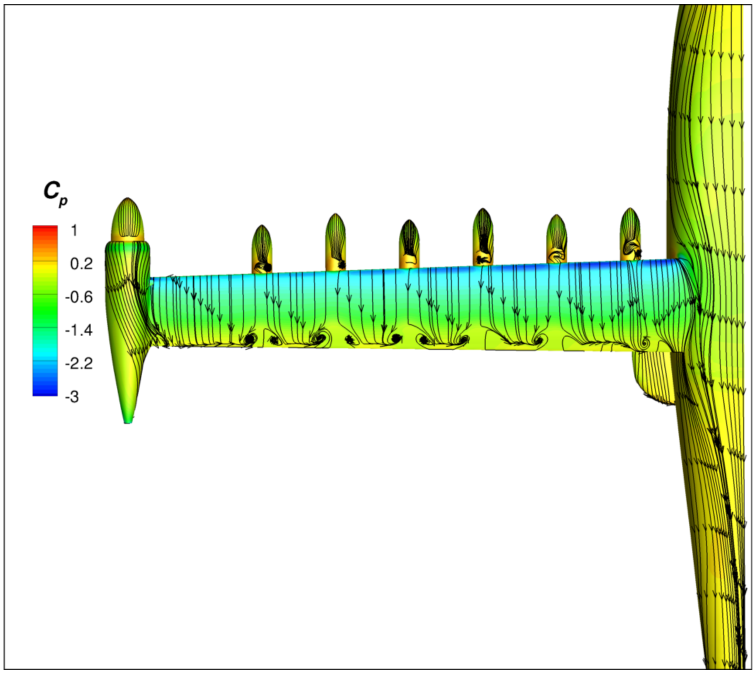

Figure 62. Streamlines and Pressure Coefficient Contours for the Cruise Configuration at $M = 0.233$ and $\alpha = 8°$.

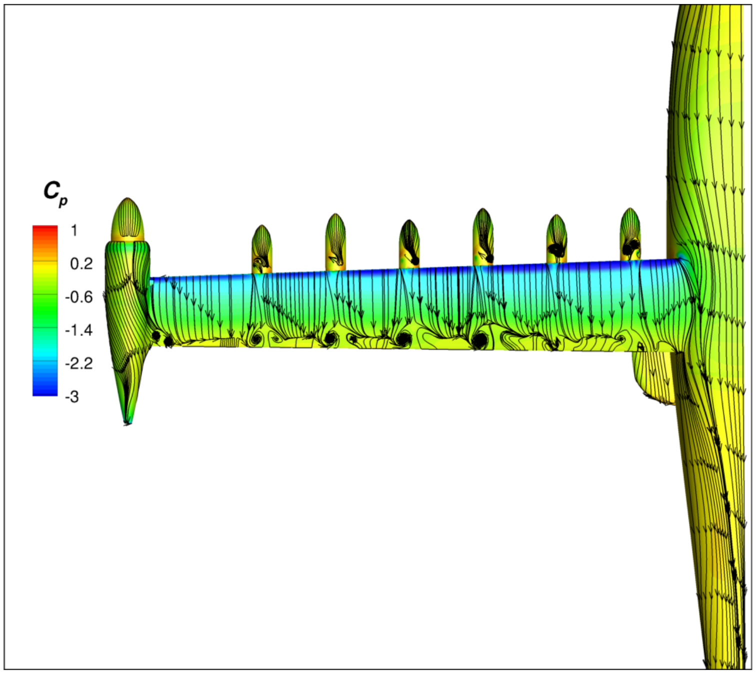

Figure 63. Streamlines and Pressure Coefficient Contours for the Cruise Configuration at $M = 0.233$ and $\alpha = 10°$.

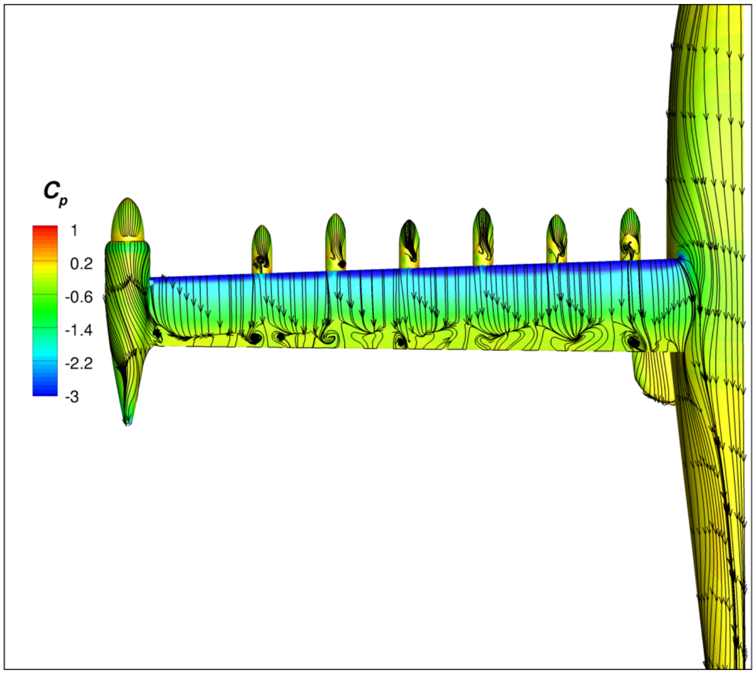

Figure 64. Streamlines and Pressure Coefficient Contours for the Cruise Configuration at $M = 0.233$ and $\alpha = 12°$.

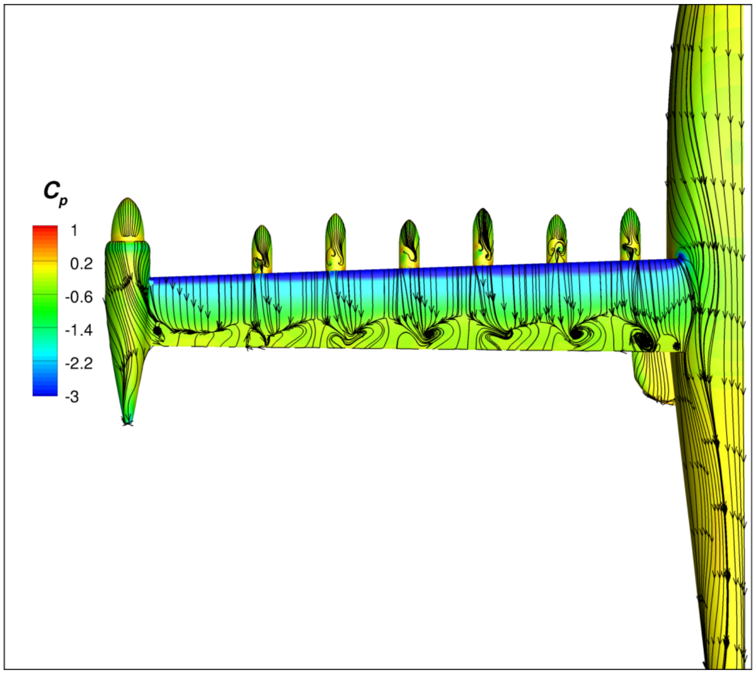

Figure 65. Streamlines and Pressure Coefficient Contours for the Cruise Configuration at $M = 0.233$ and $\alpha = 14°$.

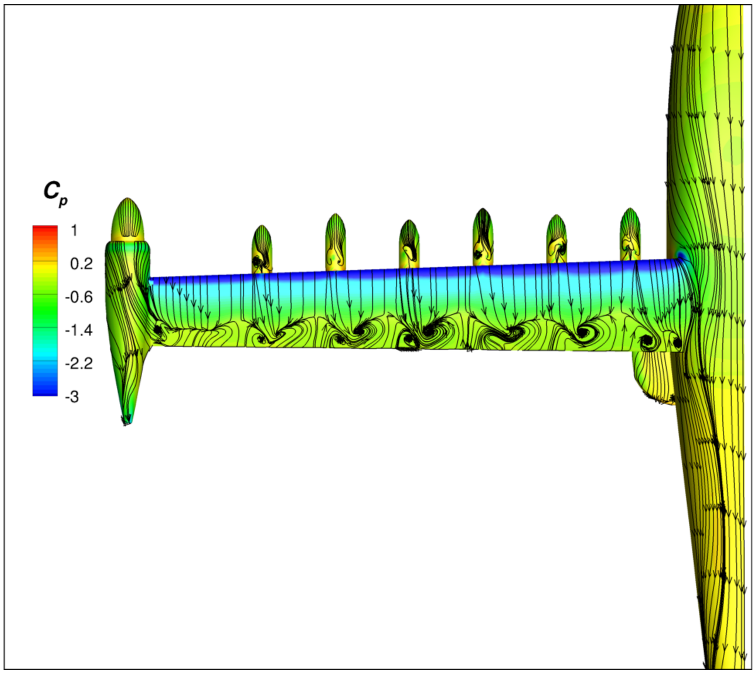

Figure 66. Streamlines and Pressure Coefficient Contours for the Cruise Configuration at $M = 0.233$ and $\alpha = 15°$.

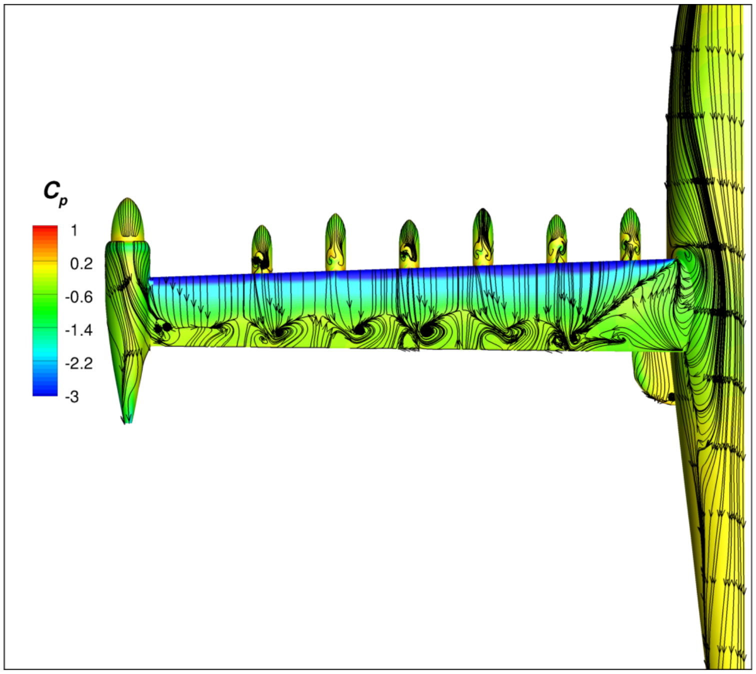

Figure 67. Streamlines and Pressure Coefficient Contours for the Cruise Configuration at $M = 0.233$ and $\alpha = 16°$.

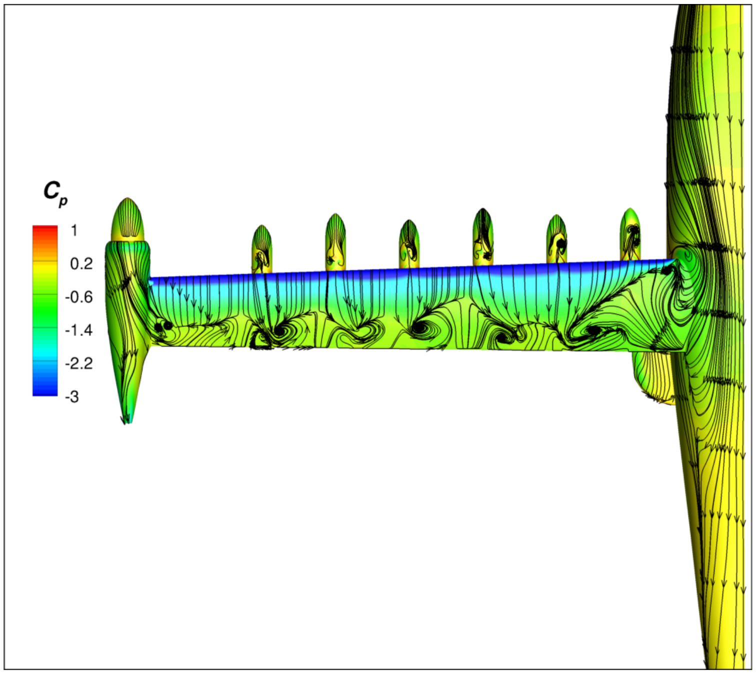

Figure 68. Streamlines and Pressure Coefficient Contours for the Cruise Configuration at $M = 0.233$ and $\alpha = 17°$.

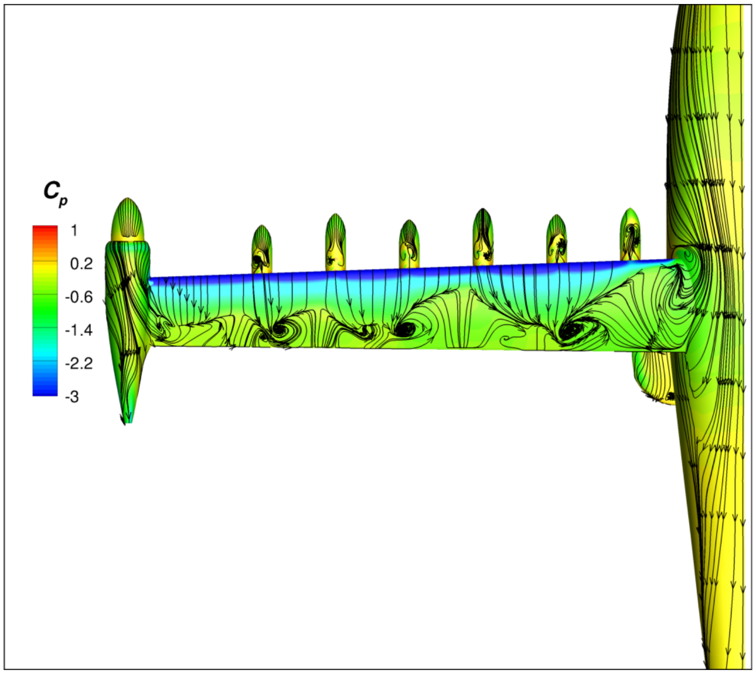

Figure 69. Streamlines and Pressure Coefficient Contours for the Cruise Configuration at $M = 0.233$ and $\alpha = 18°$.

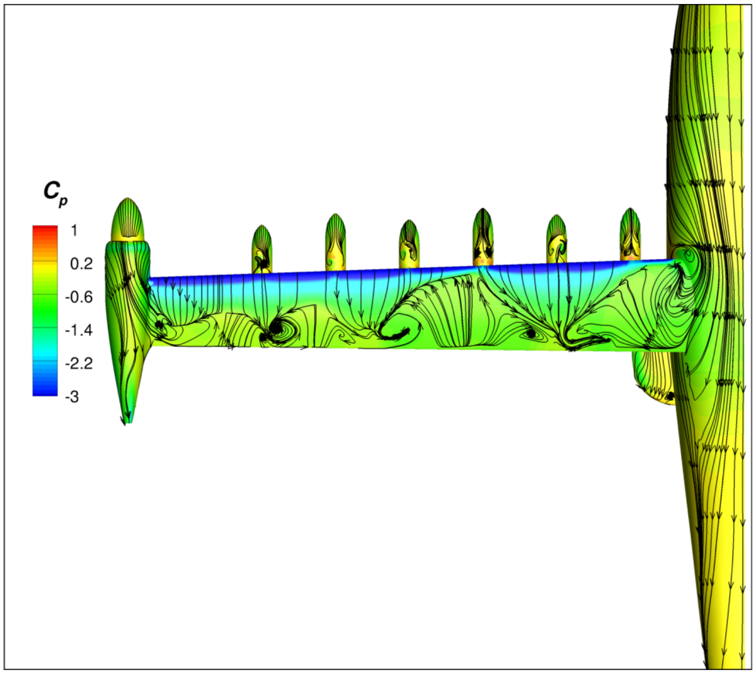

Figure 70. Streamlines and Pressure Coefficient Contours for the Cruise Configuration at $M = 0.233$ and $\alpha = 19°$.

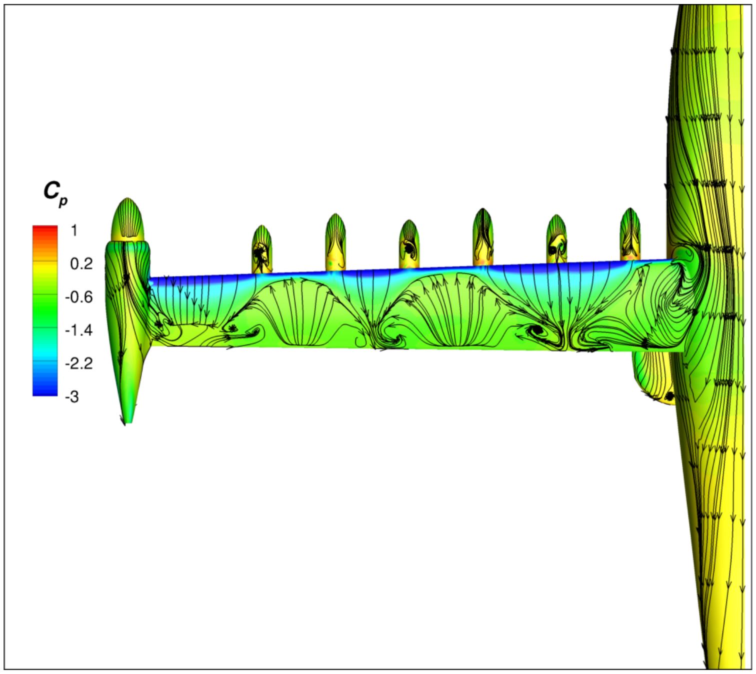

Figure 71. Streamlines and Pressure Coefficient Contours for the Cruise Configuration at $M = 0.233$ and $\alpha = 20°$.

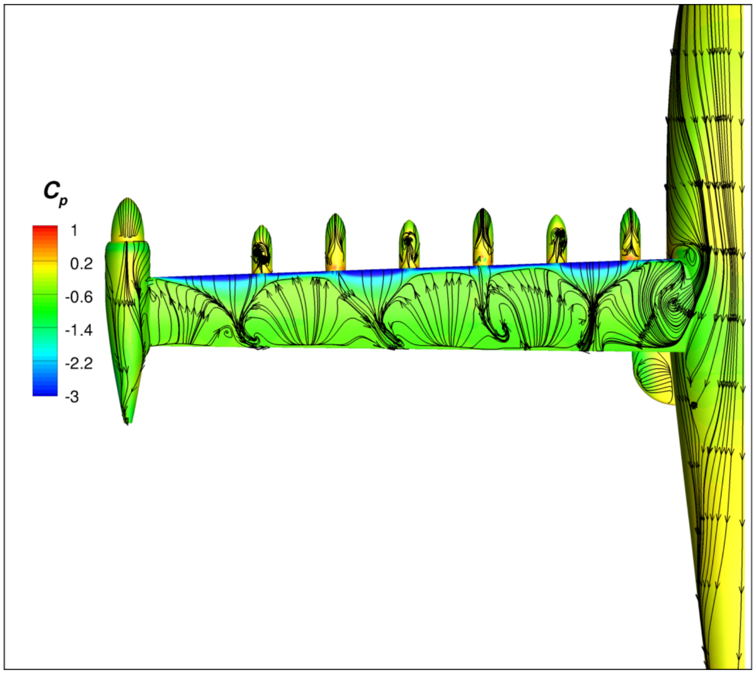

Figure 72. Streamlines and Pressure Coefficient Contours for the Cruise Configuration at $M = 0.233$ and $\alpha = 22°$.

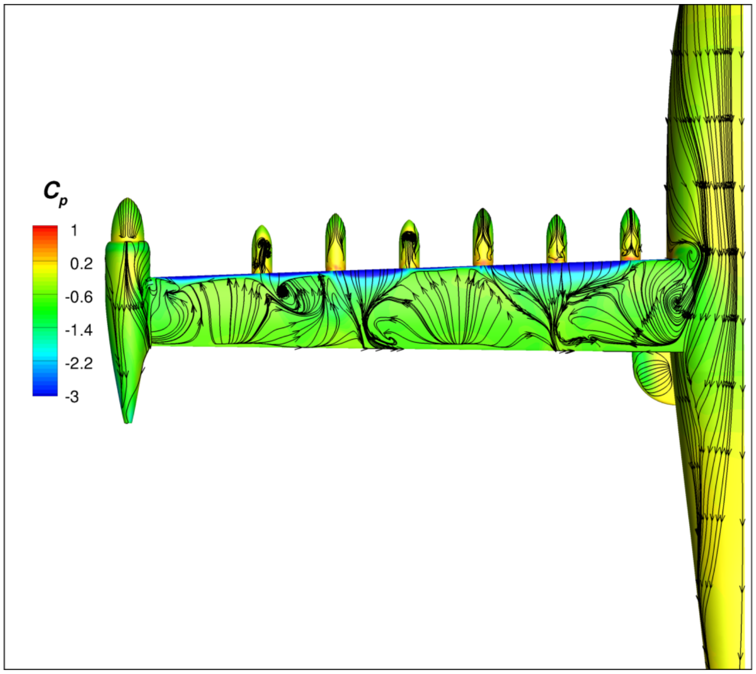

Figure 73. Streamlines and Pressure Coefficient Contours for the Cruise Configuration at $M = 0.233$ and $\alpha = 24°$.

3.1.1 Code Comparisons for the Cruise Configuration

In this section, the results from USM3D are compared with results from LAVA and STAR-CCM+ in Ref. [12]. The maximum lift coefficient for the unpowered and unblown cruise configuration as computed with USM3D was $C_{L,max} = 2.13$ at $\alpha = 15°$. The LAVA codes predicts $C_{L,max} = 2.34$ at $\alpha = 19°$ and STAR-CCM+ predicts $C_{L,max} = 2.32$ at $\alpha = 17°$. The USM3D lift coefficient matches LAVA and STAR-CCM+ for $\alpha < 16°$. The USM3D code predicts wing stall at $\alpha = 16°$ and a corresponding drop in lift as the flow separation at the wing root moves forward to the wing leading edge (compare Figure 67 to Figure 66).

When the wing root flow separation was discovered and the USM3D solutions were compared with results from LAVA and STAR-CCM+, the differences in flow separation prompted the authors to interrogate the geometry definition used with each code. A geometry difference was discovered at the wing root for USM3D, as compared to the geometry used in STAR-CCM+ and LAVA, see Figure 74. The fuselage in the USM3D solutions has a more gradual slope from the centerline to the wing root (Figure 74(a)), while the geometry for STAR-CCM+ and LAVA had a fuselage that is flat for a wider distance from the centerline, with a steeper slope into the wing root (Figure 74(b)). In Figure 74(b), the fuselage geometry used with STAR-CCM+ and LAVA is shown in gray, and is superimposed over the fuselage geometry used with USM3D (shown in blue). The USM3D used the OpenVSP fuselage geometry, while the STAR-CCM+ and LAVA codes used the scaled-up CAD geometry of a wind tunnel model. The difference in the location of the fuselage and wing root intersection is about 1.37 inches in the y direction and 1.08 inches in the z direction, at the axial station of 157.3 inches, see Figure 74(c). The geometry difference appears to mainly have an impact on the comparison of lift coefficient at high angles of attack.

The only pressure coefficient contours and streamlines for LAVA and STAR-CCM+ on the cruise configuration are for $\alpha = 8°$ in Figure 6(a) of Ref. [12]. The USM3D contours in Figure 62 show similar streamline patterns with flow separation in very small triangular-shaped regions far downstream of the high-lift nacelles. The lift coefficients for the three codes compare well for the cruise configuration $M = 0.233$ and $\alpha = 8°$; USM3D is $C_L = 1.514$, LAVA is C_L =1.569, and STAR-CCM+ is $C_L = 1.570$.

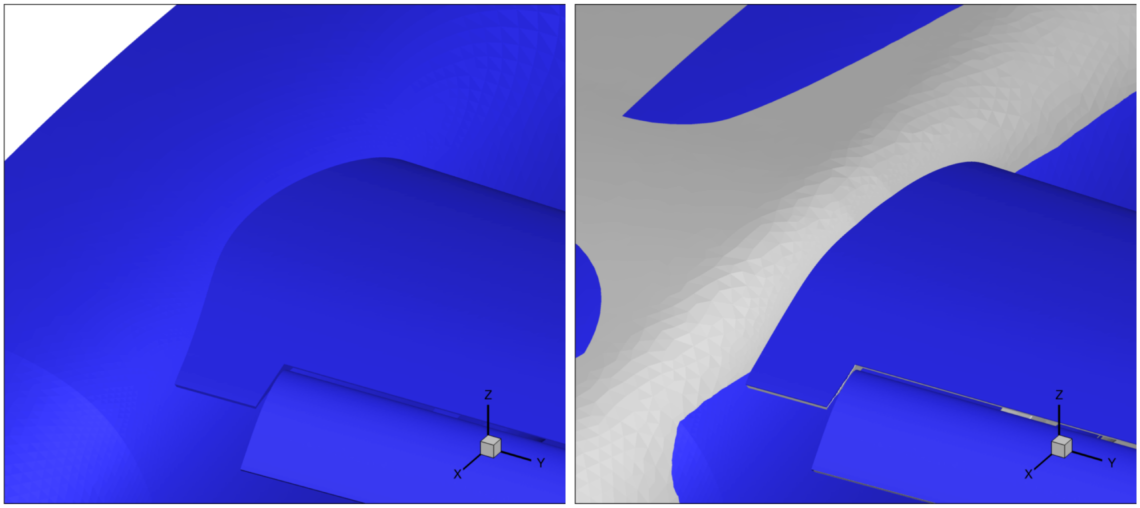

(a) USM3D Geometry (b) STAR-CCM+ Geometry in Gray

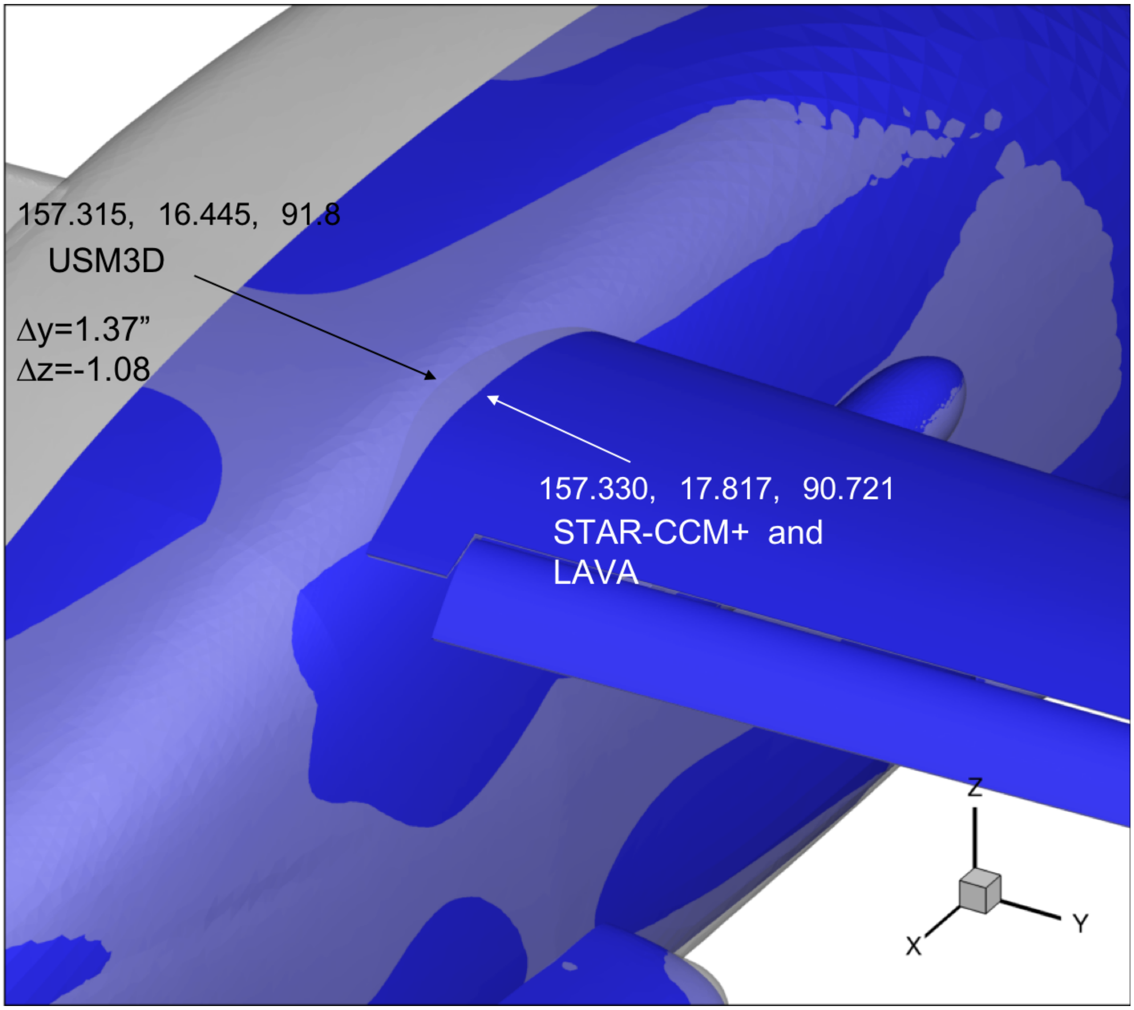

(c) USM3D Geometry shown in Blue and STAR-CCM+ Geometry shown in Gray

Figure 74. Differences in the Geometry at the Wing Root for USM3D and STAR-CCM+.

3.2 Results for the Takeoff Configuration, 10° Flap Deflection

The airplane lift coefficient and the component contributions to lift for the takeoff configuration are shown in Figure 75. The maximum lift coefficient for the unpowered and unblown takeoff configuration was $C_{L,max} = 2.21$ at $\alpha = 16^\circ$. The airplane lift coefficient was $C_L = 2.16$ at $\alpha = 13^\circ$, but lift dropped at $\alpha = 14^\circ$ due to a drop in lift on the wing. The airplane lift coefficient increased back to $C_{L,max} = 2.21$ at $\alpha = 16^\circ$ because the lift continued to increase on the stabilator and fuselage. As expected, the largest contribution to lift is from the wing. There is a shift upward in the wing lift curve when the flap, nacelles, pylons, strakes, wing-tip nacelle and vortex generator are added to the wing (wing flap nps tn vg). The lift from the flap is nearly constant, with a very slight increase from 0.08 to 0.09 over the range of angle of attack. The fuselage has a small contribution to lift that increases with increasing angle of attack up through $\alpha = 22^\circ$. The stabilator has a small contribution to lift that increases with increasing angle of attack up to $\alpha = 20^\circ$, but lift drops at $\alpha = 22^\circ$ as the flow separation on the stabilator moves forward to the leading edge.

There was an atypical change in lift-curve slope at $\alpha = 8^\circ$, that can be explained by the change in flow separation on the wing. The pressure coefficient contours, with black lines showing surface streamlines, are shown in Figures 76-87 for the takeoff configuration at $M = 0.149$ (94 KEAS) from $\alpha = -2^\circ$ to $\alpha = 22^\circ$. For $\alpha < 6^\circ$, the streamlines indicate attached flow over the full upper surface of the wing, see Figures 76 to 78. At $\alpha = 8^\circ$, the streamlines indicate triangular-shaped regions of flow separation downstream of each high-lift nacelle, see Figure 79. The lift continues to increase as angle of attack increases to $\alpha = 12^\circ$ even though the flow separation regions get slightly larger, see Figures 80 to 82. At $\alpha = 14^\circ$, there is a large region of flow separation at the wing root, see Figure 83 and a drop in wing lift, see Figure 75. The lift of the wing is approximately constant for $\alpha = 14^\circ$ to $\alpha = 16^\circ$ but the whole airplane lift increases due to lift on the stabilator and fuselage increasing. At $\alpha = 18^\circ$ (Figure 85), the airplane and wing lift decreases as two new regions of flow separation occur on the wing; outboard of the last high-lift nacelle, and also between the first two high-lift nacelles from the centerline. With the exception of the fuselage, the lift coefficient continues to decrease with increasing angle of attack from $\alpha = 18^\circ$ to $\alpha = 22^\circ$ as the flow separation increases, see Figures 85 to 87.

The flow separation regions discussed above are also visible as dark blue regions in the skin friction coefficient contours, shown at angles of attack from $\alpha = -2^\circ$ to $\alpha = 22^\circ$ in Figures 88-99. The contours on the stabilator are now visible and mostly cyan in color, indicating attached flow up through $\alpha = 20^\circ$ and Figure 75 shows the lift from the stabilator increasing up through an angle of attack of $\alpha = 20^\circ$. At $\alpha = 22^\circ$, there is a decrease in lift and the skin friction contours on the stabilator are dark blue over most of the upper surface, except the outboard tip, as full chord flow separation occurs.

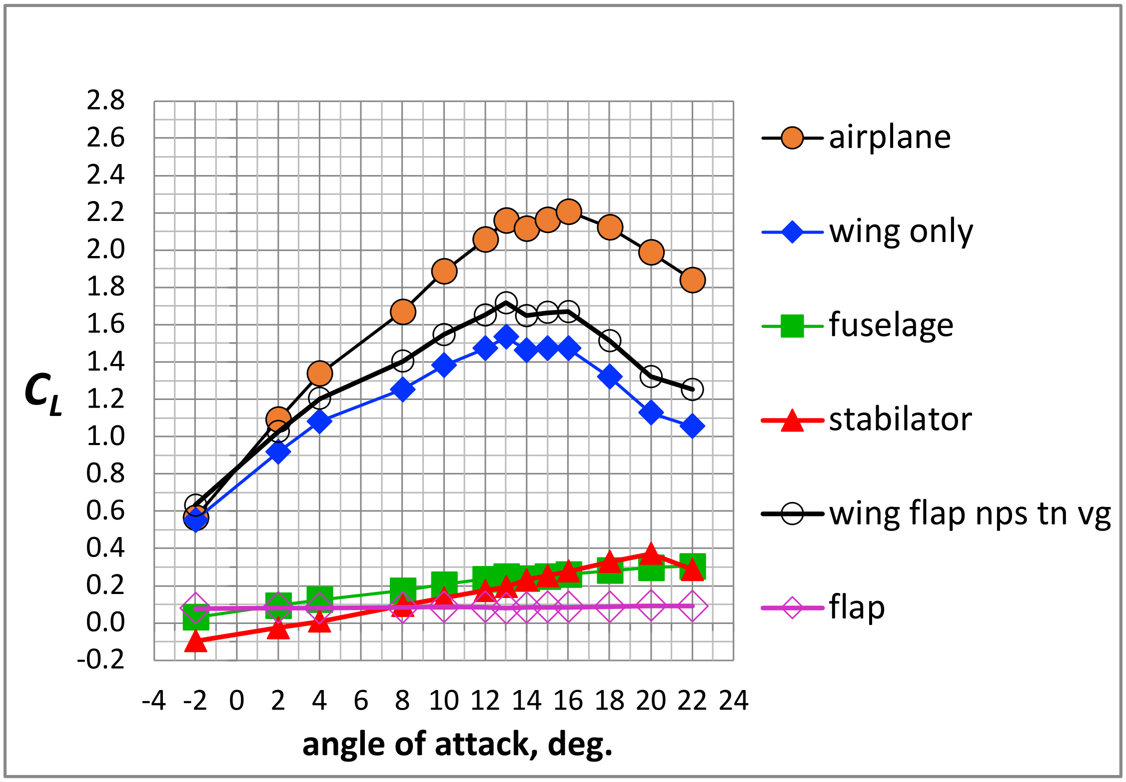

Figure 75. The Effect of Angle of Attack on Airplane Lift Coefficient and Component Contributions to C_L for the Takeoff Configuration with a 10° Flap Deflection at $M = 0.149$.

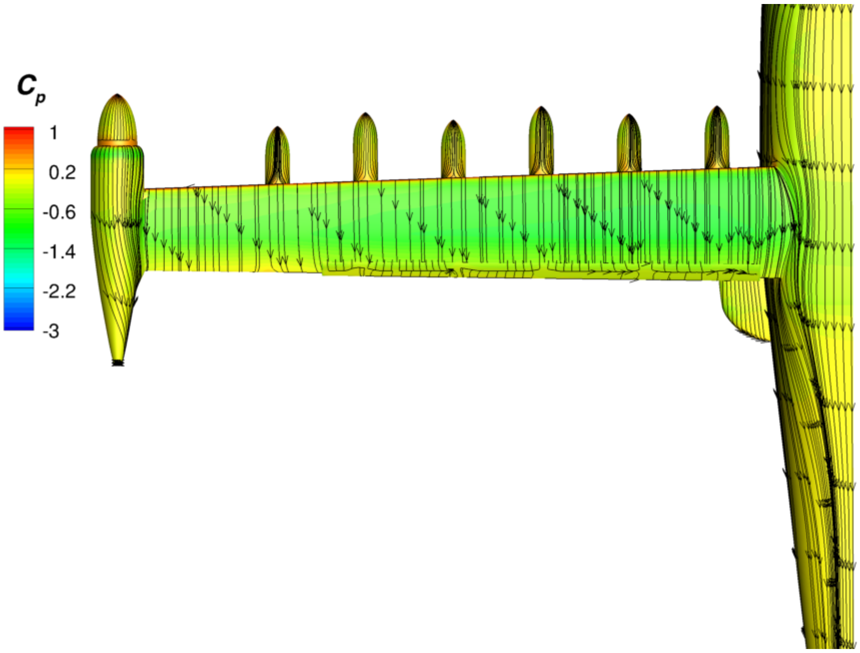

Figure 76. Streamlines and Pressure Coefficient Contours for the Takeoff Configuration with a 10° Flap Deflection at $M = 0.149$ and $\alpha = -2°$.

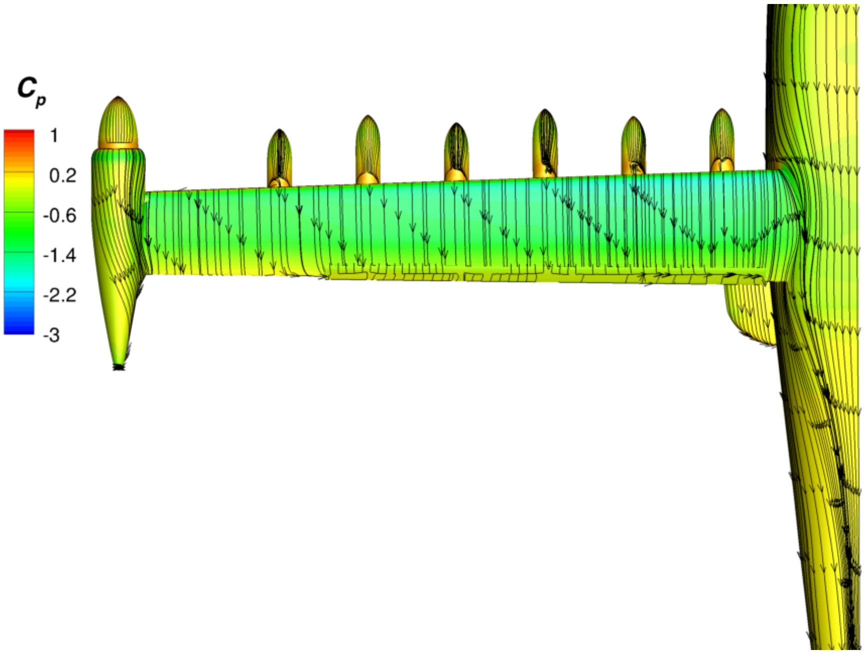

Figure 77. Streamlines and Pressure Coefficient Contours for the Takeoff Configuration with a 10° Flap Deflection at $M = 0.149$ and $\alpha = 2°$.

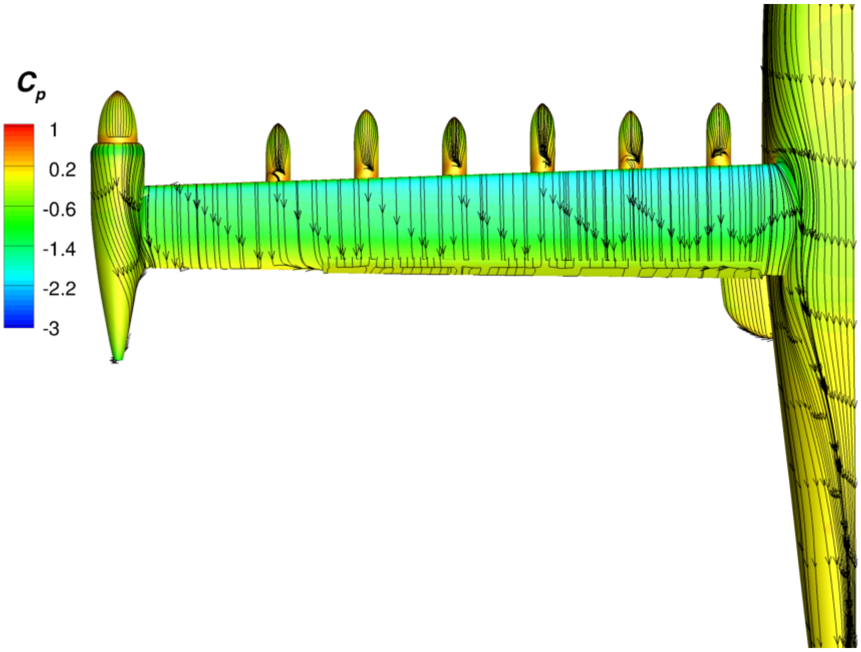

Figure 78. Streamlines and Pressure Coefficient Contours for the Takeoff Configuration with a 10° Flap Deflection at $M = 0.149$ and $\alpha = 4°$.

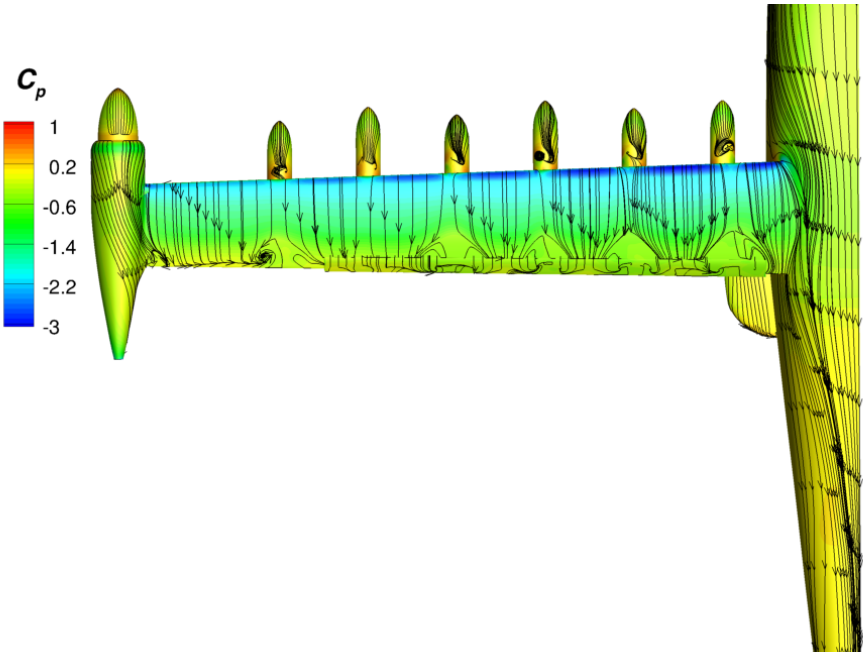

Figure 79. Streamlines and Pressure Coefficient Contours for the Takeoff Configuration with a 10° Flap Deflection at $M = 0.149$ and $\alpha = 8°$.

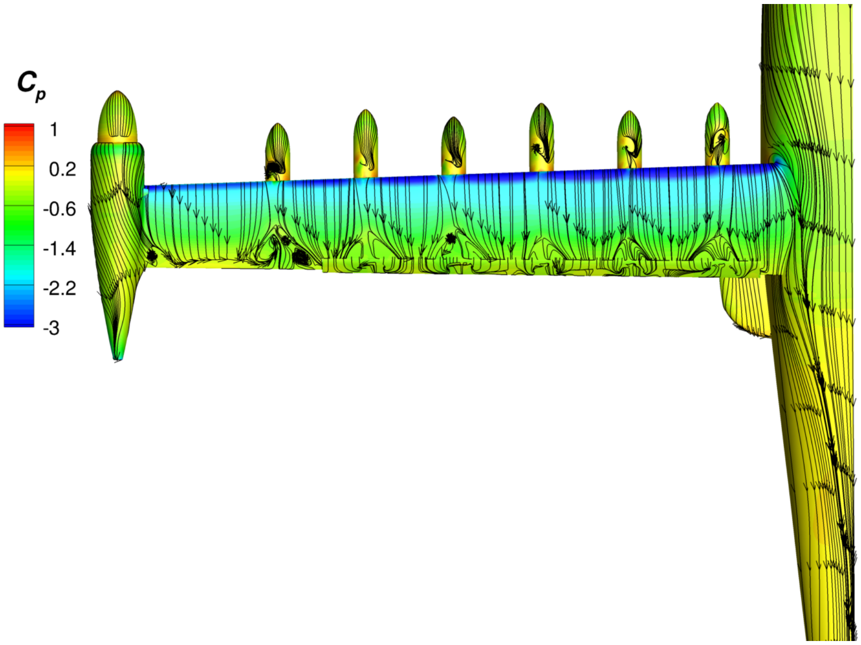

Figure 80. Streamlines and Pressure Coefficient Contours for the Takeoff Configuration with a 10° Flap Deflection at $M = 0.149$ and $\alpha = 10°$.

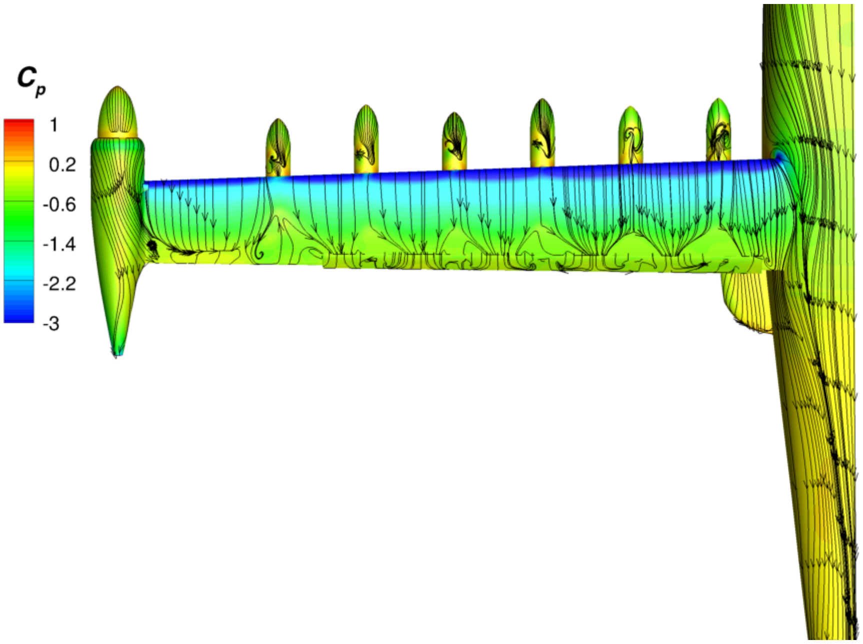

Figure 81. Streamlines and Pressure Coefficient Contours for the Takeoff Configuration with a 10° Flap Deflection at $M = 0.149$ and $\alpha = 12°$.

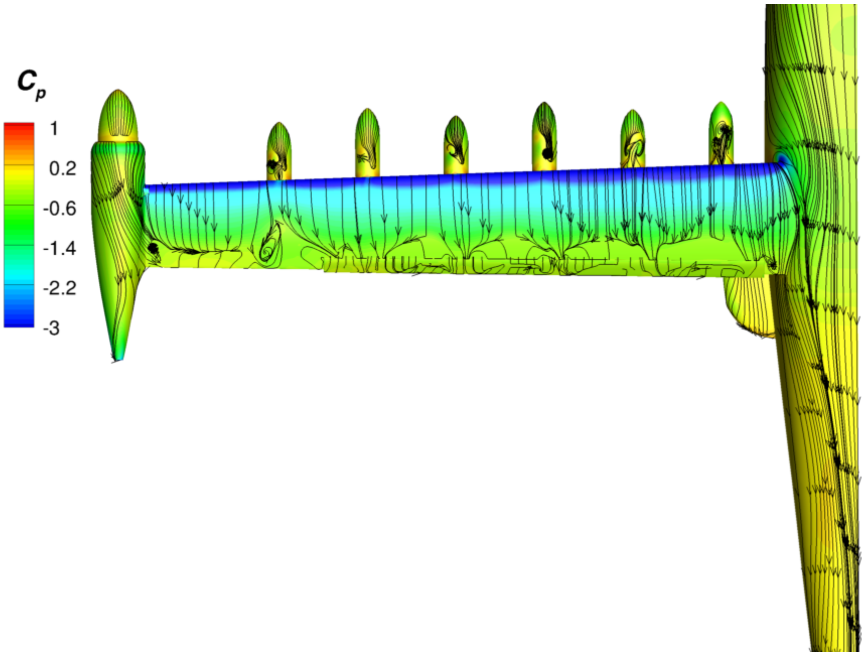

Figure 82. Streamlines and Pressure Coefficient Contours for the Takeoff Configuration with a 10° Flap Deflection at $M = 0.149$ and $\alpha = 13°$.

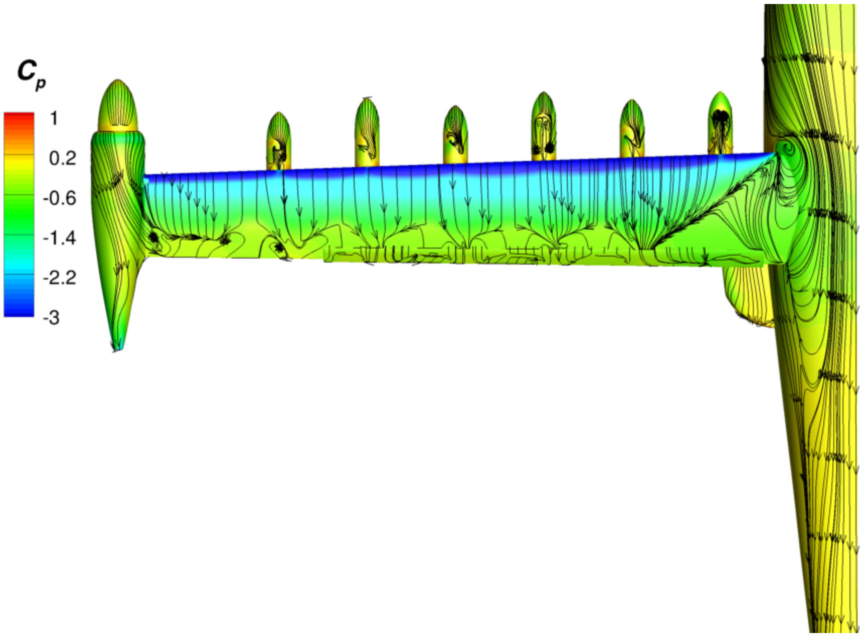

Figure 83. Streamlines and Pressure Coefficient Contours for the Takeoff Configuration with a 10° Flap Deflection at $M = 0.149$ and $\alpha = 14°$.

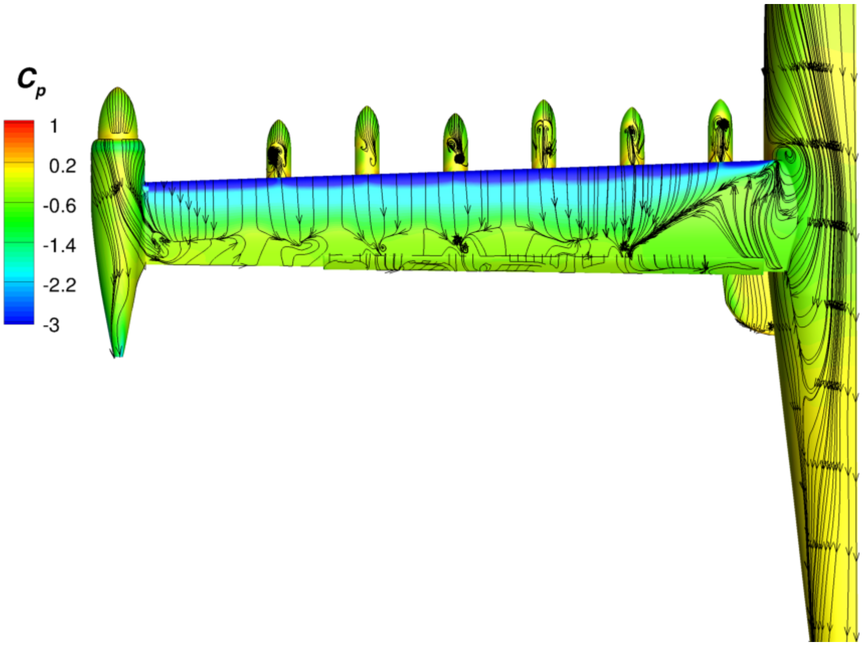

Figure 84. Streamlines and Pressure Coefficient Contours for the Takeoff Configuration with a 10° Flap Deflection at $M = 0.149$ and $\alpha = 16°$.

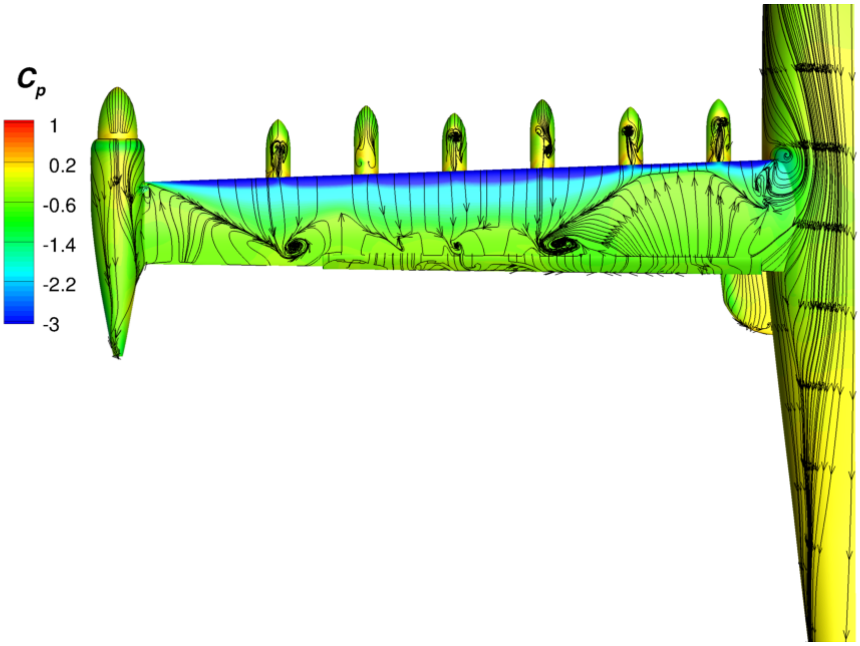

Figure 85. Streamlines and Pressure Coefficient Contours for the Takeoff Configuration with a 10° Flap Deflection at $M = 0.149$ and $\alpha = 18°$.

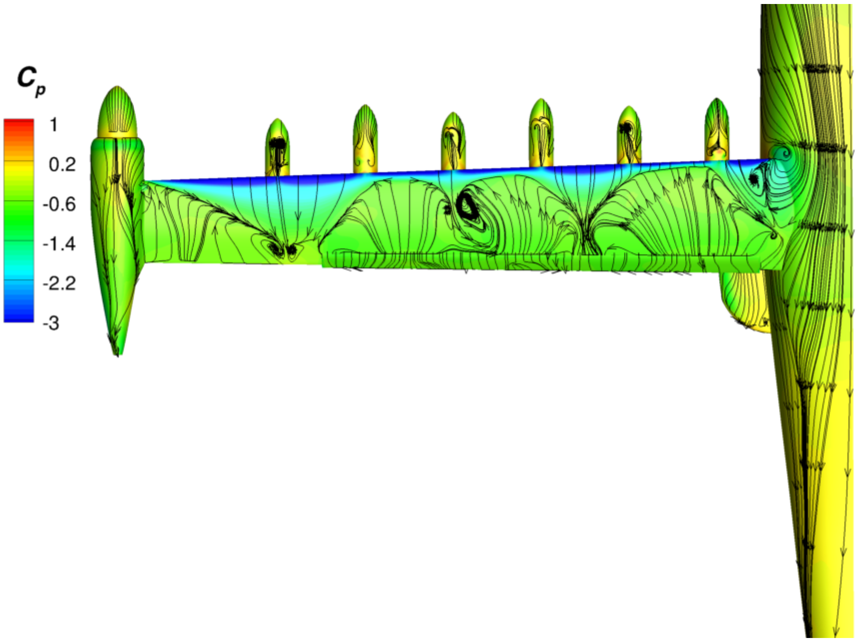

Figure 86. Streamlines and Pressure Coefficient Contours for the Takeoff Configuration with a 10° Flap Deflection at $M = 0.149$ and $\alpha = 20°$.

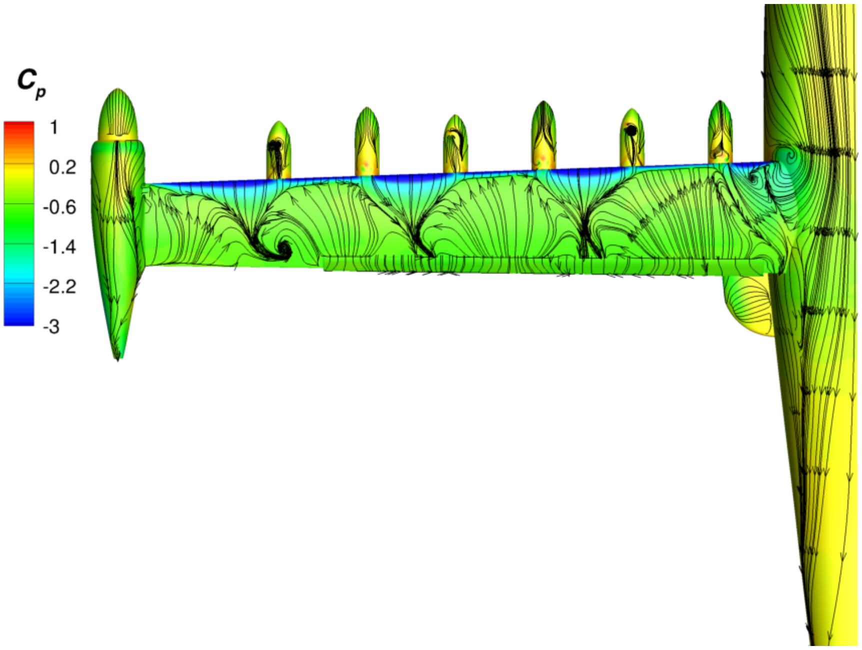

Figure 87. Streamlines and Pressure Coefficient Contours for the Takeoff Configuration with a 10° Flap Deflection at $M = 0.149$ and $\alpha = 22°$.

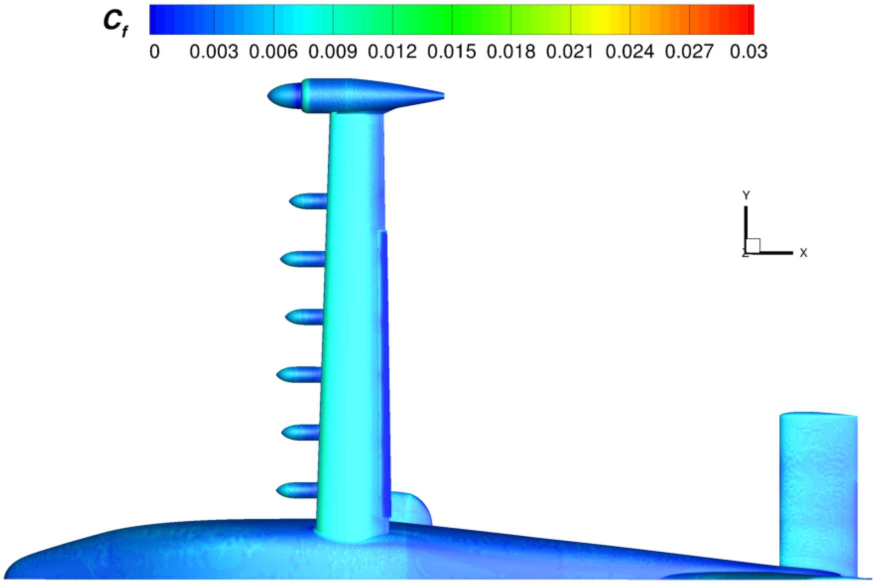

Figure 88. Skin Friction Coefficient Contours for the Takeoff Configuration with a 10° Flap Deflection at $M = 0.149$ and $\alpha = -2°$.

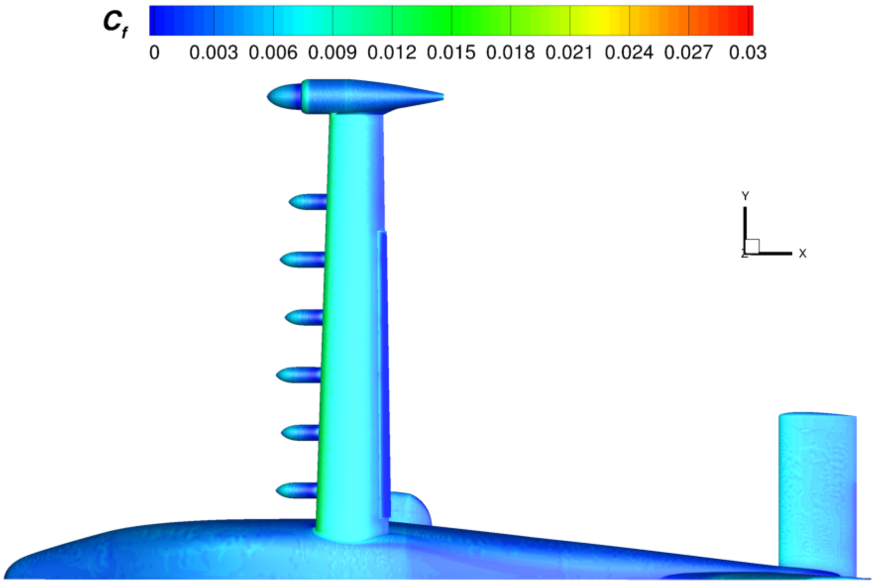

Figure 89. Skin Friction Coefficient Contours for the Takeoff Configuration with a 10° Flap Deflection at $M = 0.149$ and $\alpha = 2°$.

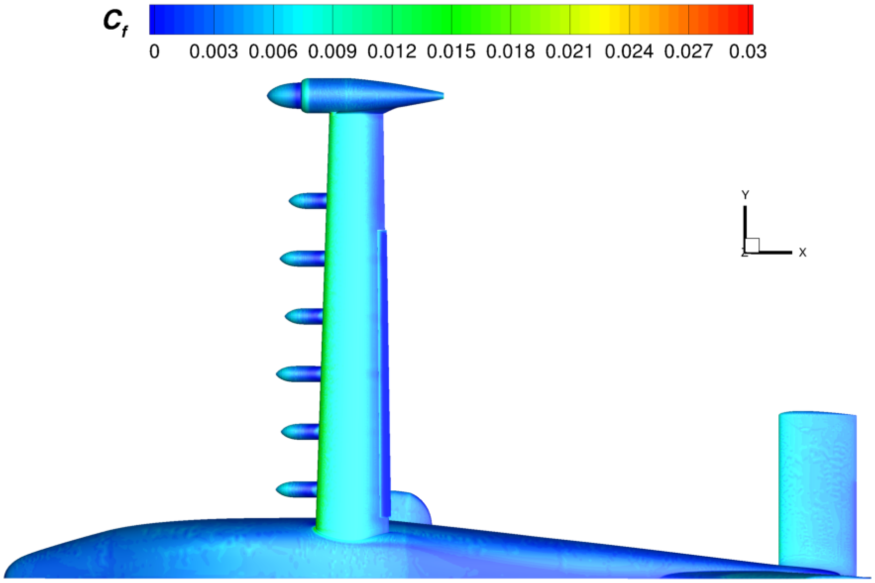

Figure 90. Skin Friction Coefficient Contours for the Takeoff Configuration with a 10° Flap Deflection at $M = 0.149$ and $\alpha = 4°$.

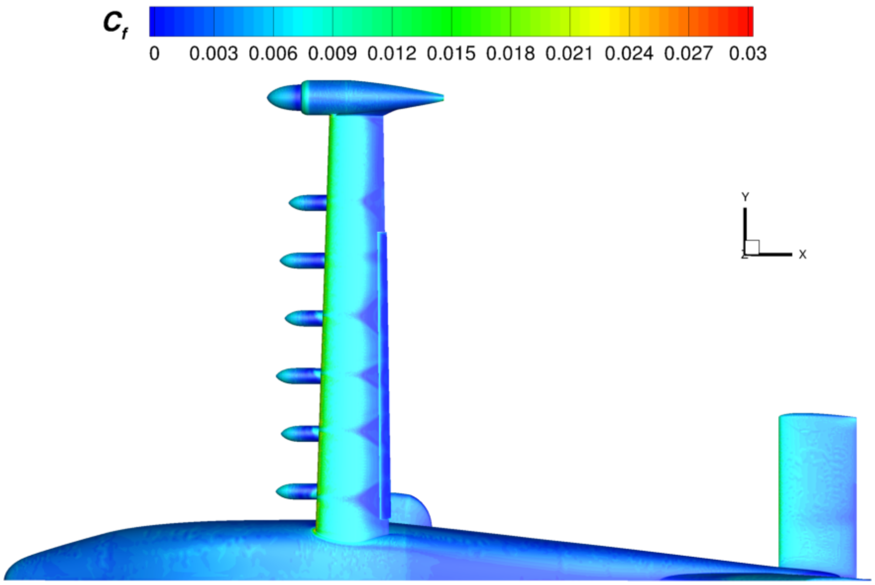

Figure 91. Skin Friction Coefficient Contours for the Takeoff Configuration with a 10° Flap Deflection at $M = 0.149$ and $\alpha = 8°$.

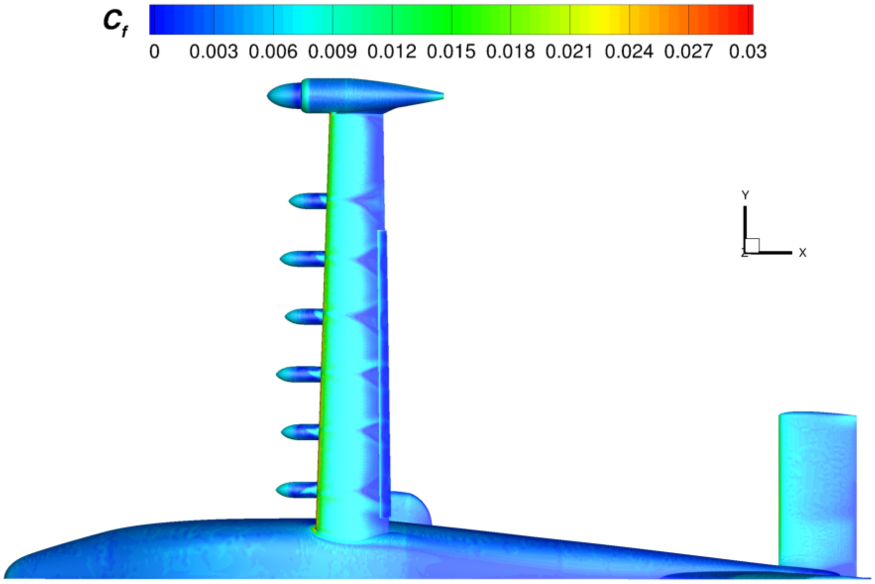

Figure 92. Skin Friction Coefficient Contours for the Takeoff Configuration with a 10° Flap Deflection at $M = 0.149$ and $\alpha = 10°$.

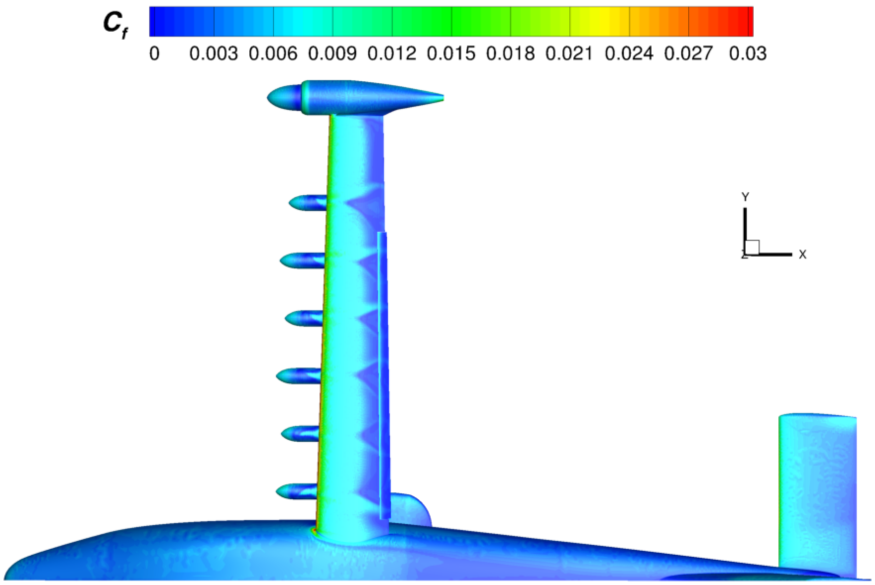

Figure 93. Skin Friction Coefficient Contours for the Takeoff Configuration with a 10° Flap Deflection at $M = 0.149$ and $\alpha = 12°$.

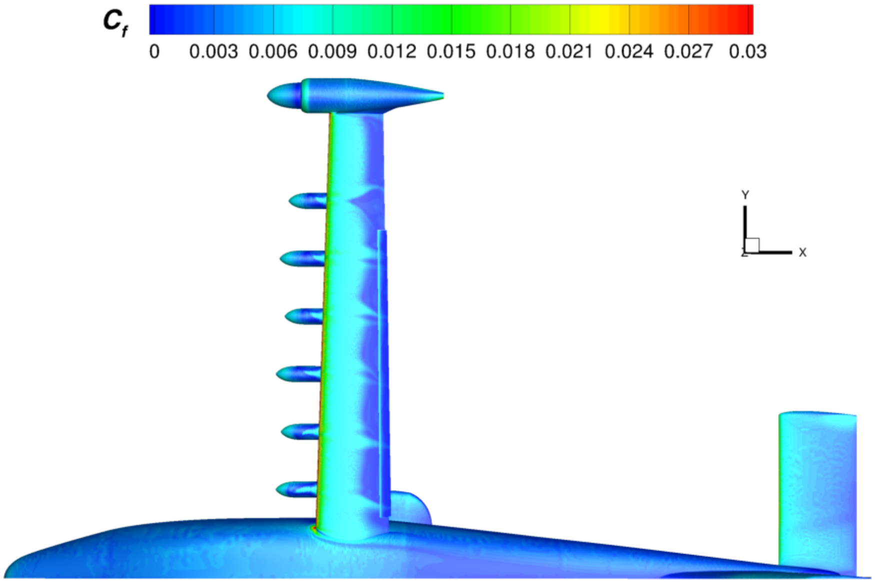

Figure 94. Skin Friction Coefficient Contours for the Takeoff Configuration with a 10° Flap Deflection at $M = 0.149$ and $\alpha = 13°$.

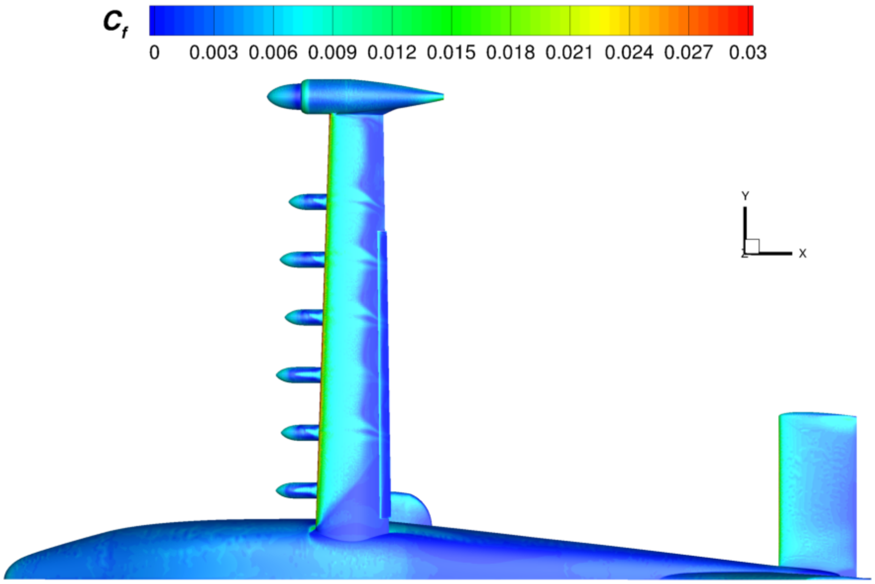

Figure 95. Skin Friction Coefficient Contours for the Takeoff Configuration with a 10° Flap Deflection at $M = 0.149$ and $\alpha = 14°$.

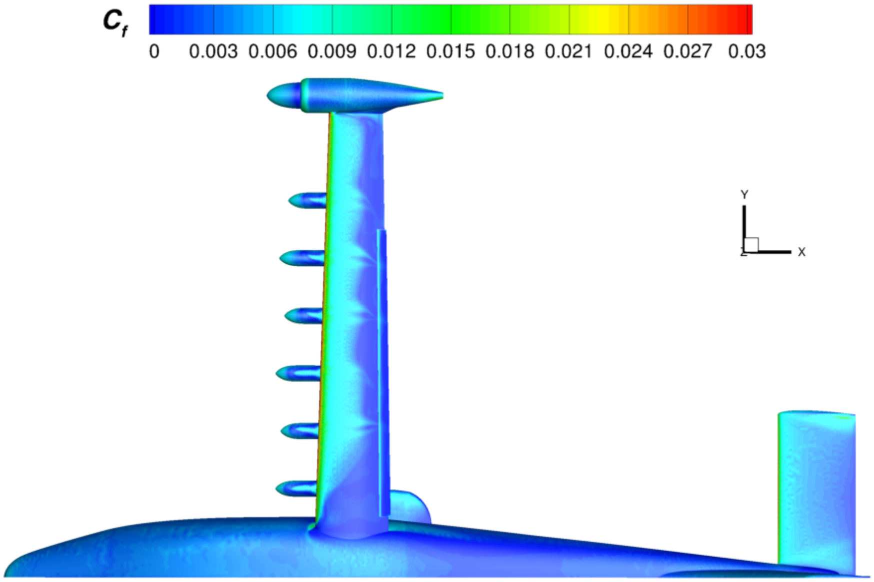

Figure 96. Skin Friction Coefficient Contours for the Takeoff Configuration with a 10° Flap Deflection at $M = 0.149$ and $\alpha = 16°$.

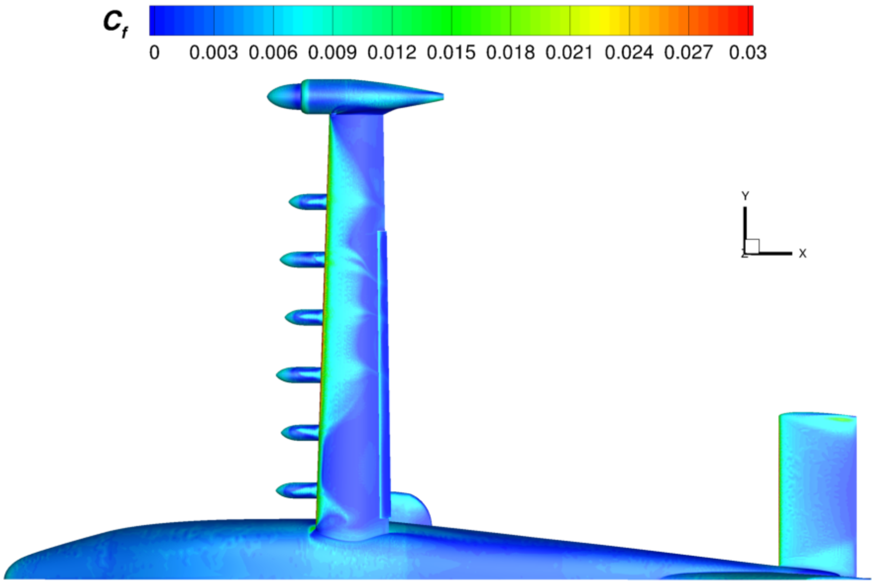

Figure 97. Skin Friction Coefficient Contours for the Takeoff Configuration with a 10° Flap Deflection at $M = 0.149$ and $\alpha = 18°$.

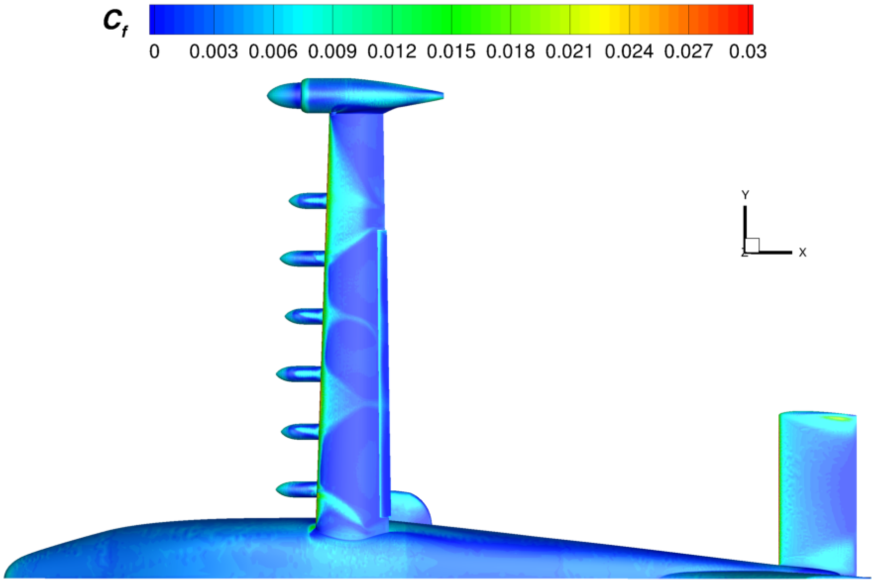

Figure 98. Skin Friction Coefficient Contours for the Takeoff Configuration with a 10° Flap Deflection at $M = 0.149$ and $\alpha = 20°$.

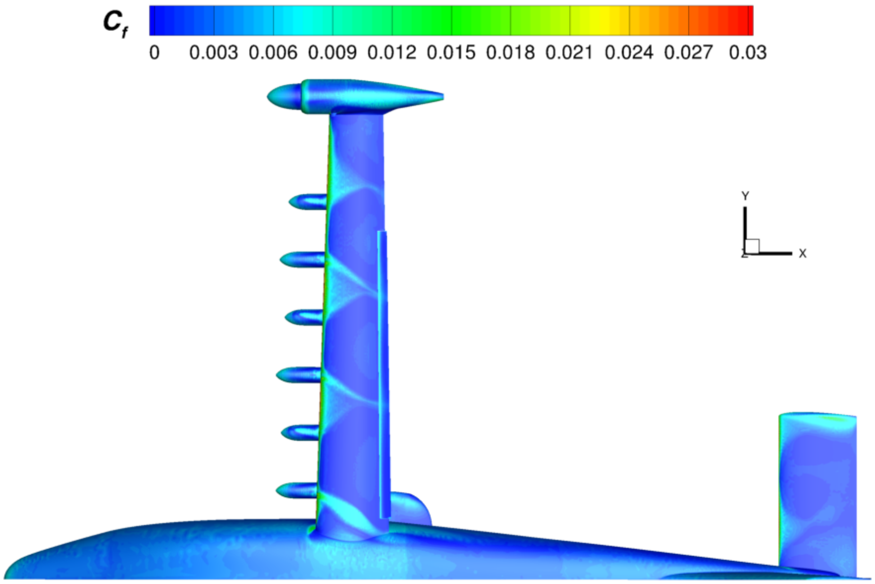

Figure 99. Skin Friction Coefficient Contours for the Takeoff Configuration with a 10° Flap Deflection at $M = 0.149$ and $\alpha = 22°$.

To further discuss the change in lift-curve slope at $\alpha = 8°$ shown in Figure 75, notice how the triangular-shaped flow separation regions start developing at $\alpha = 8°$ and are aligned downstream of the centerline of the high-lift nacelles in Figure 91, compared to Figure 90. The authors hypothesized that vortices were shedding off the high-lift nacelles and were interacting with the boundary layer, which resulted in flow separation.

To investigate if a mesh refinement would impact the lift coefficient and flow separation patterns, the cell size on the high-lift nacelles, pylons and strakes (NPS) were reduced. The nacelle source sizes were reduced from 0.1 at the nose and 0.3 at the maximum diameter, to 0.05 at the nose and 0.1 at the maximum diameter. The strakes and pylon source sizes were reduced from 0.15 to 0.1. The NPS-refined mesh increased surface triangle count by 152,064, which was an additional 25,344 triangles for each high-lift nacelle, pylon and strake. The solutions were recomputed for the takeoff configuration at $M = 0.149$ for $\alpha = 8°$, $\alpha = 10°$, and $\alpha = 14°$ using the NPS-refined mesh.

The effects of NPS refinement on lift coefficient and on skin friction coefficient contours for $\alpha = 8°$ are shown in Figures 100 and 101. The lift coefficient did increase slightly by 0.085 with NPS mesh refinement, as some of the triangular-shaped flow separation regions were reduced downstream of nacelles 7, 8, and 10. However, the flow separation downstream of nacelle 9 looks slightly larger, while the flow downstream of nacelles 11 and 12 appear unaffected.

The effects of NPS refinement on lift coefficient and on skin friction coefficient contours for $\alpha = 10°$ are shown in Figures 102 and 103. The lift coefficient was lower with the grid refinement, but only by approximately 0.02. The flow separation regions appear to be larger downstream of nacelles 9, 11, and 12 with mesh refinement, but appear smaller downstream of nacelles 7 and 10.

The effects of NPS refinement on lift coefficient and on skin friction coefficient contours for $\alpha = 14°$ are shown in Figures 104 and 105. The lift coefficient was the same with and without the NPS mesh refinement and the flow separation patterns are similar. The triangular-shaped flow separation pattern downstream of nacelle 12 is slightly larger and more aligned with the nacelle centerline for the mesh with NPS refinement. The NPS mesh refinement had no impact on the large flow separation region at the wing root.

The results from the NPS mesh refinement were inconclusive. The results did not indicate the NPS mesh refinement would greatly change the lift coefficient and therefore, further angles of attack were not recomputed with the NPS-refined mesh.

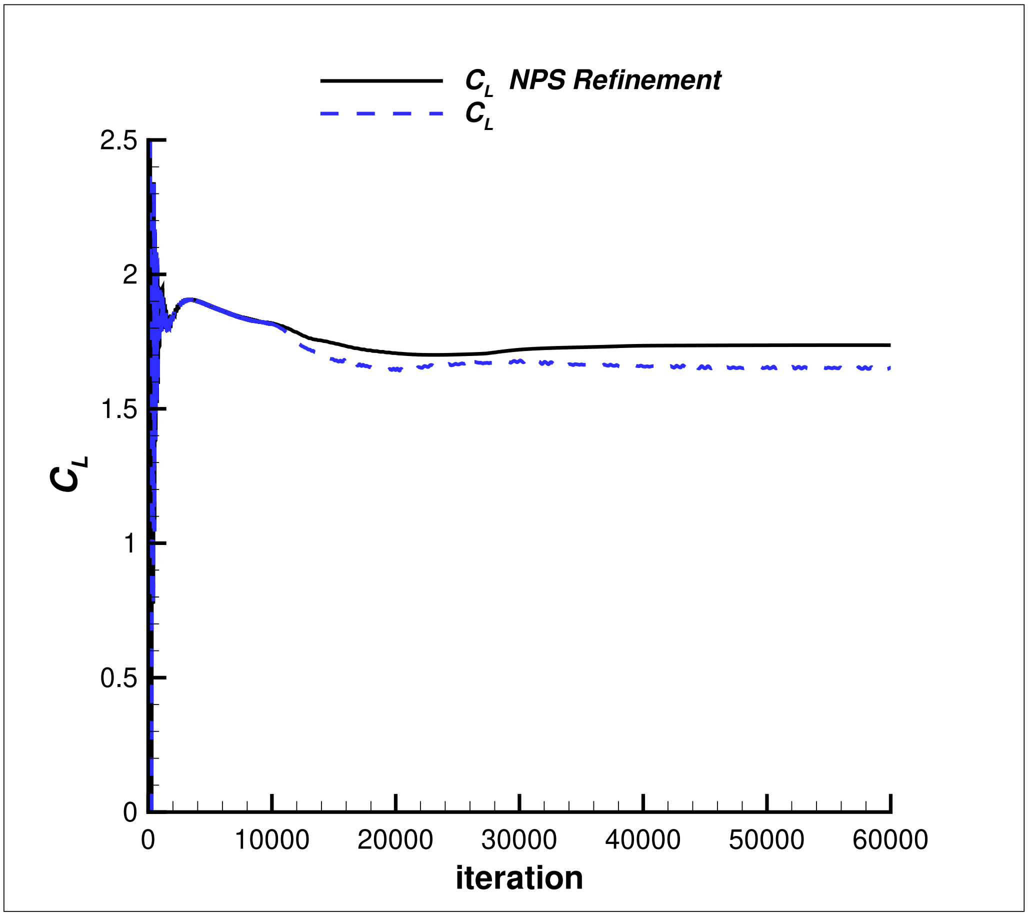

Figure 100. Effect of NPS Mesh Refinement on C_L for the Takeoff Configuration with a 10° Flap Deflection at $M = 0.149$ and $\alpha = 8°$.

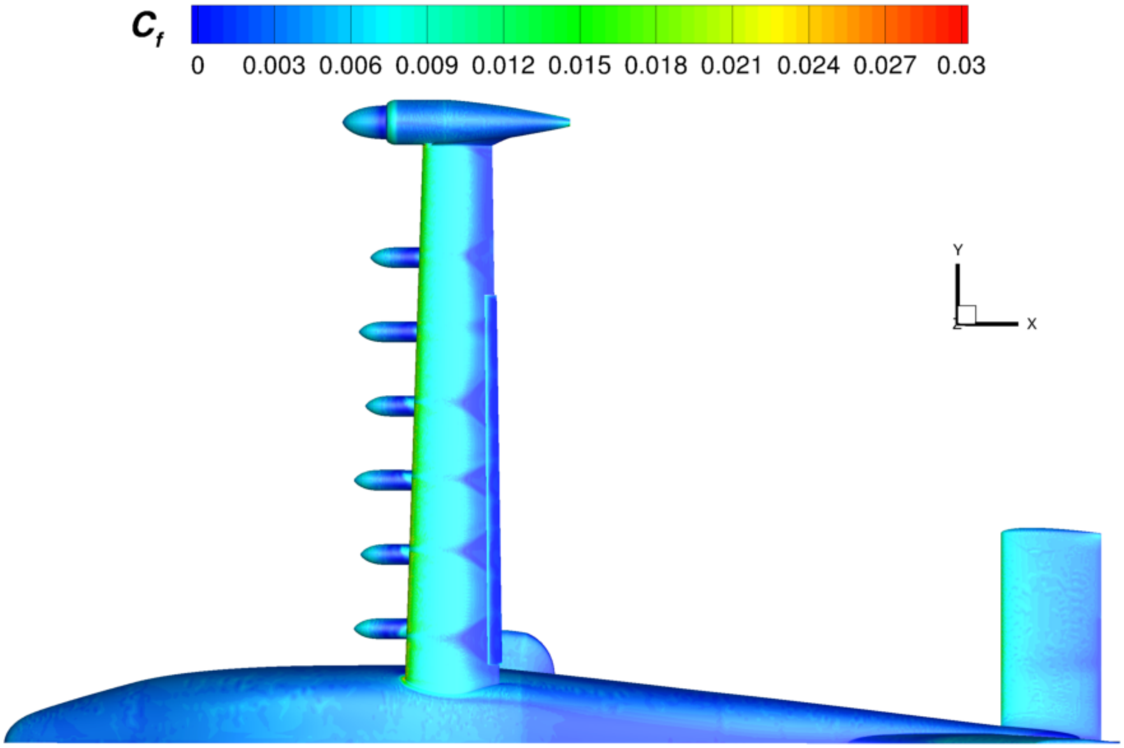

(a) Baseline Mesh

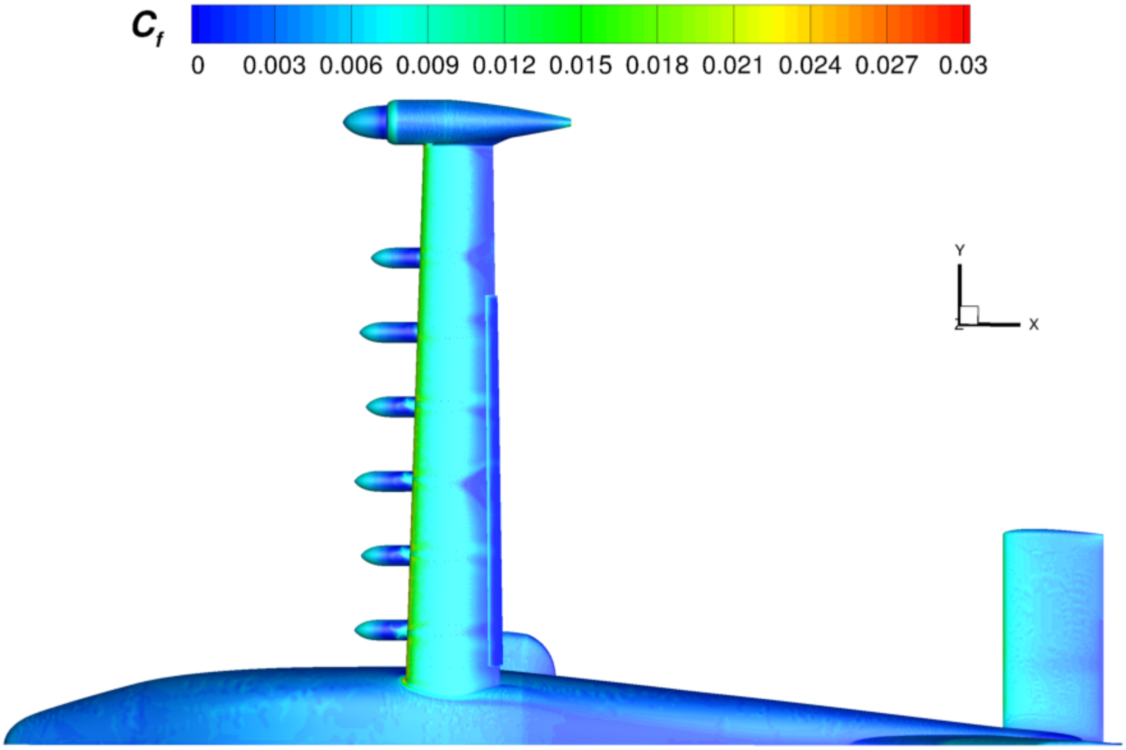

(b) NPS Mesh Refinement

Figure 101. Effect of NPS Mesh Refinement on Skin Friction Coefficient Contours for the Takeoff Configuration with a 10° Flap Deflection at $M = 0.149$ and $\alpha = 8°$.

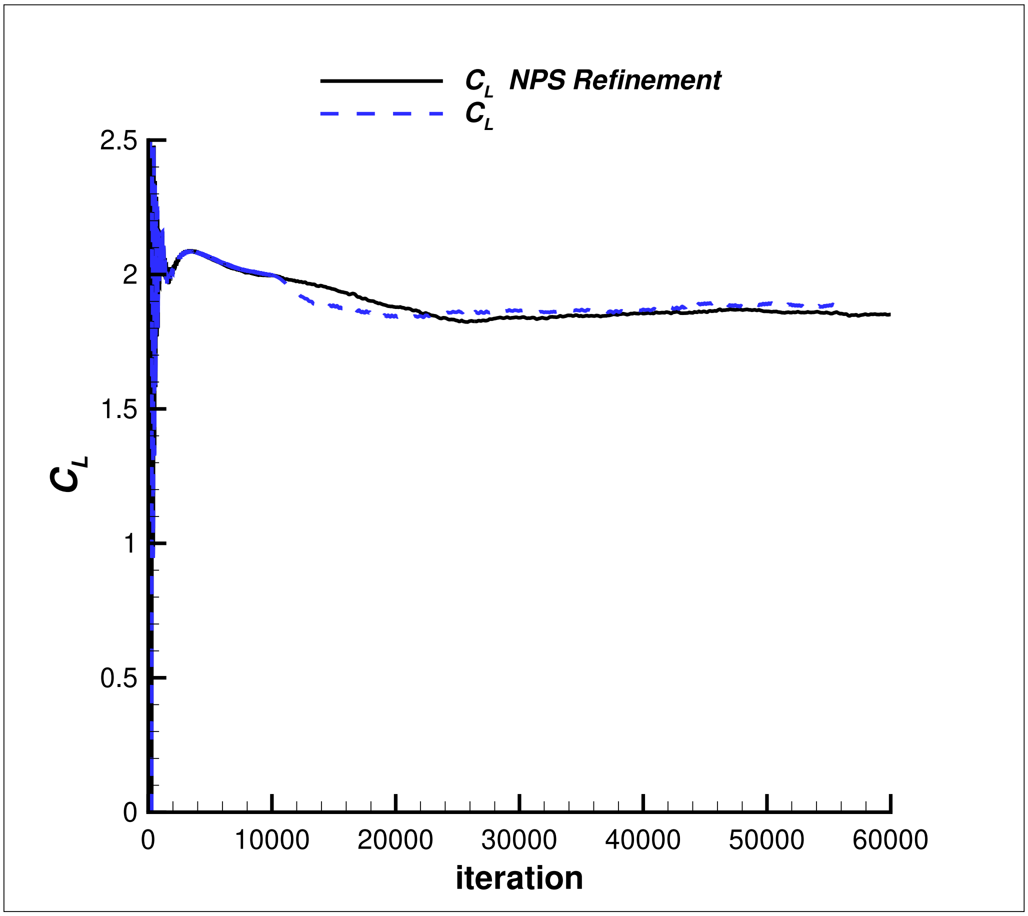

Figure 102. Effect of NPS Mesh Refinement on C_L for the Takeoff Configuration with a 10° Flap Deflection at $M = 0.149$ and $\alpha = 10°$.

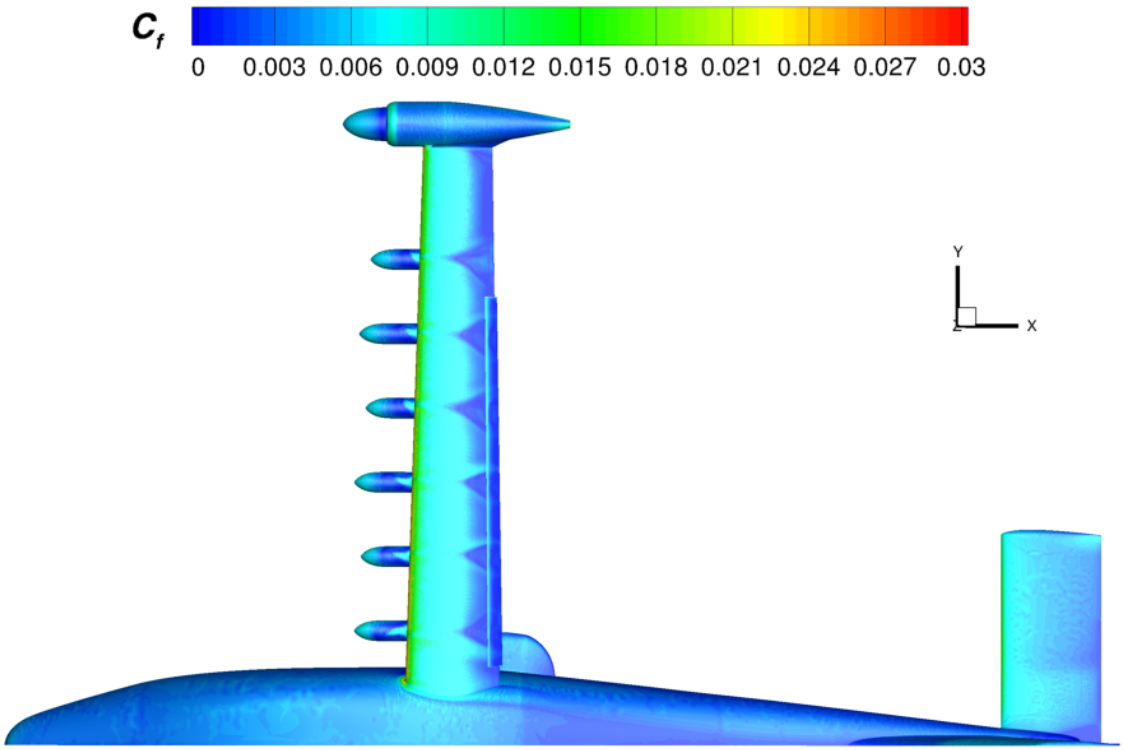

(a) Baseline Mesh

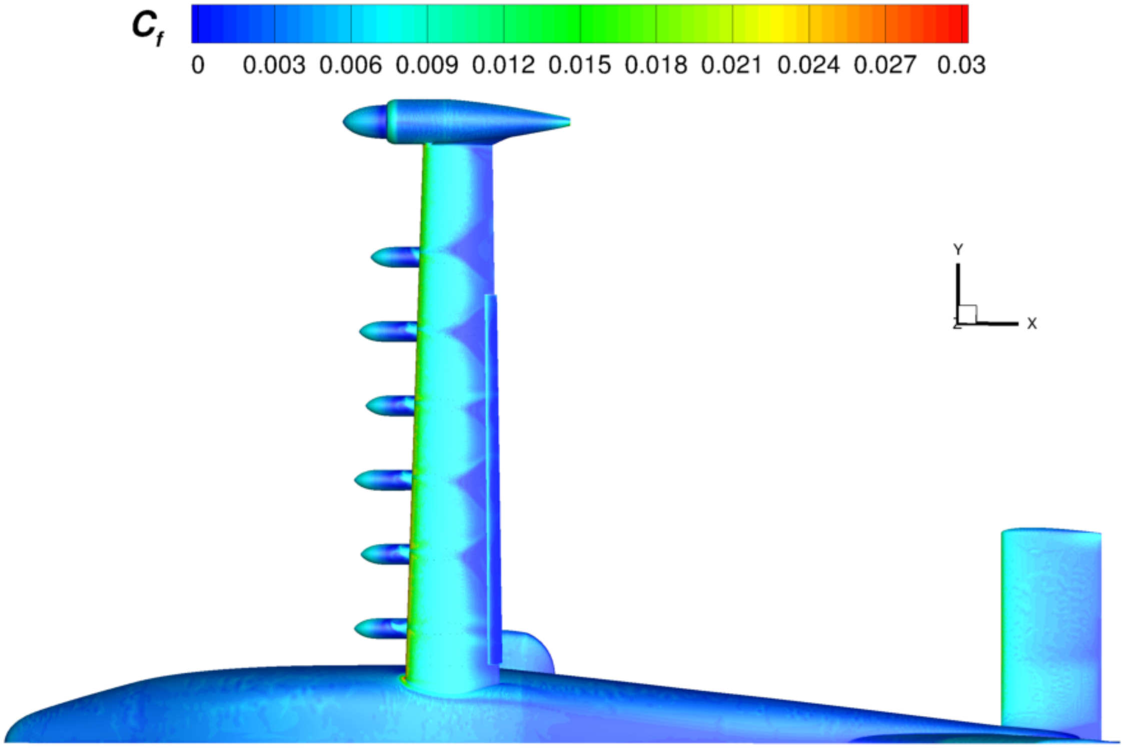

(b) NPS Mesh Refinement

Figure 103. Effect of NPS Mesh Refinement on Skin Friction Coefficient Contours for the Takeoff Configuration with a 10° Flap Deflection at $M = 0.149$ and $\alpha = 10°$.

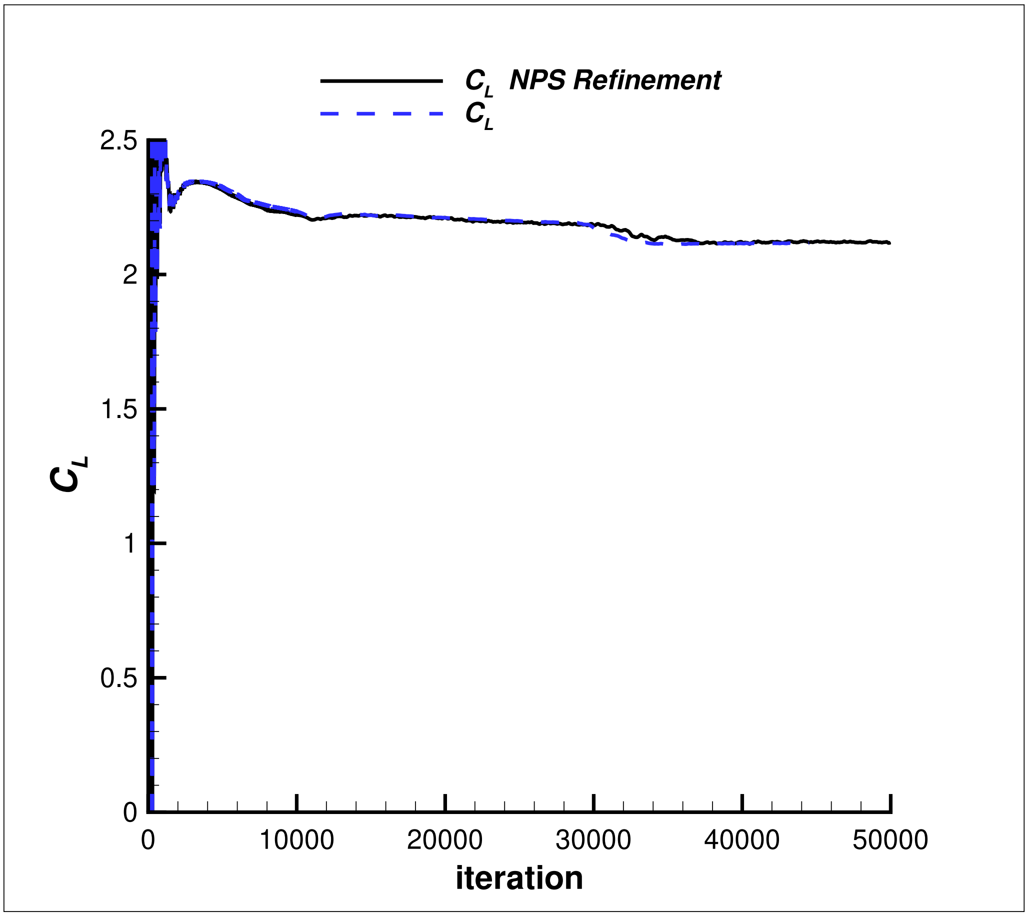

Figure 104. Effect of NPS Mesh Refinement on C_L for the Takeoff Configuration with a 10° Flap Deflection at $M = 0.149$ and $\alpha = 14°$.

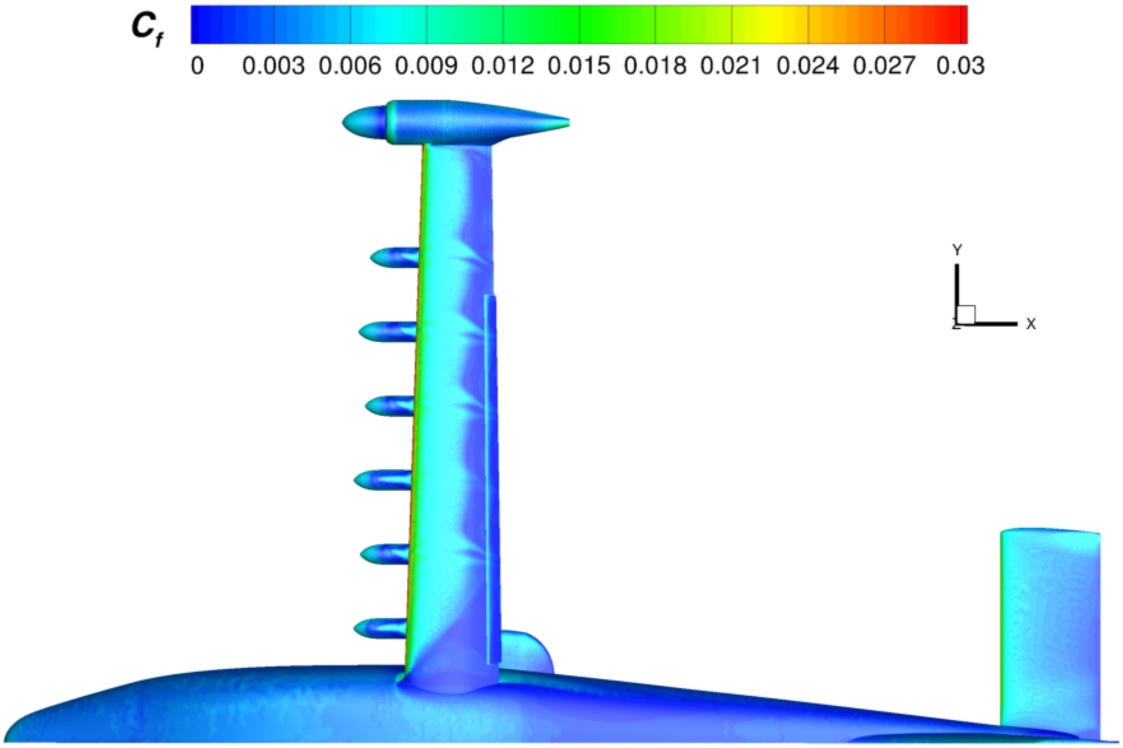

(a) Baseline Mesh

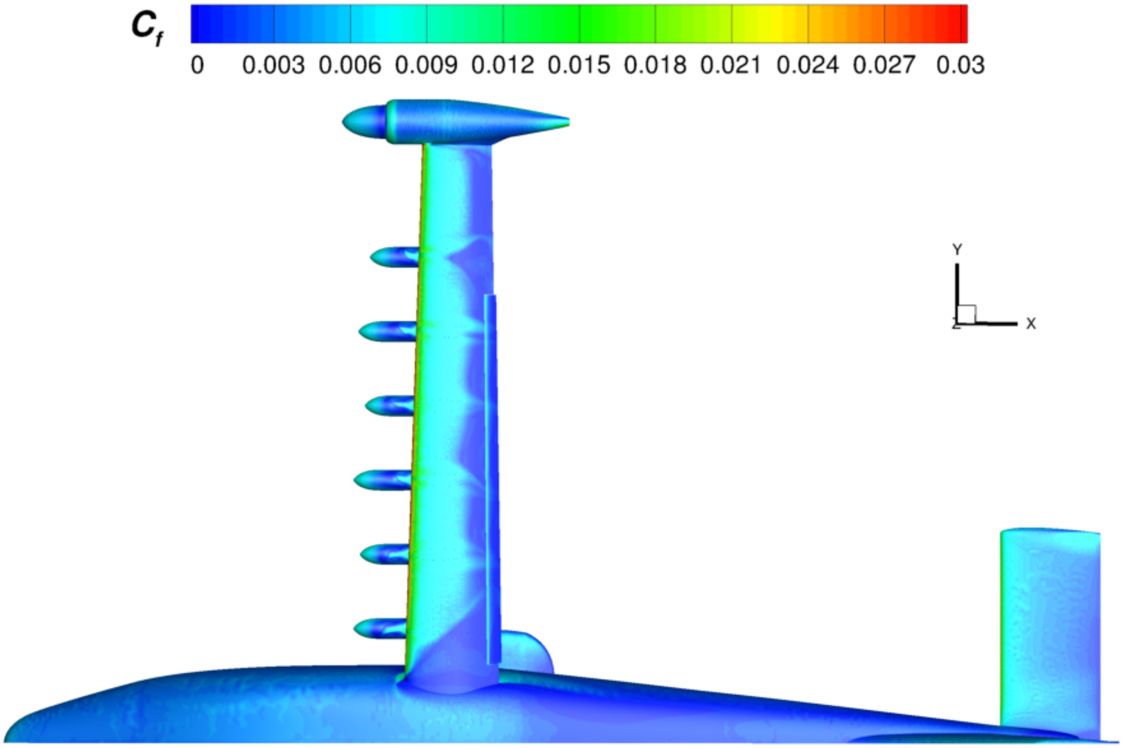

(b) NPS Mesh Refinement

Figure 105. Effect of NPS Mesh Refinement on Skin Friction Coefficient Contours for the Takeoff Configuration with a 10° Flap Deflection at $M = 0.149$ and $\alpha = 14°$.

3.2.1 Code Comparisons for the Takeoff Configuration with a 10° Flap Deflection

The $C_{L,max}$ computed with USM3D for the takeoff configuration (10° flap deflection) was $C_{L,max} = 2.21$ at $\alpha = 16°$. The LAVA code predicted a $C_{L,max} = 2.53$ at $\alpha = 18°$ and the STAR-CCM+ code predicted $C_{L,max} = 2.48$ at $\alpha = 16°$ (Ref. [12]).

The only pressure coefficient contours and streamlines for LAVA and STAR-CCM+ on the takeoff configuration, are for $\alpha = 8°$ in Figure 6(b) of Ref. [12]. The lift coefficients at $\alpha = 8°$ are $C_L = 1.670$ (USM3D), $C_L = 1.836$ (LAVA), and $C_L = 1.865$ (STAR-CCM+). The lift is lower for USM3D than LAVA and STAR-CCM+ due to more flow separation. The USM3D contours in Figure 79 show flow separation in triangular-shaped regions downstream of all of the high-lift nacelles, except the fifth from the centerline. The LAVA and STAR-CCM+ codes only have flow separation downstream of the outer most high-lift nacelle, with LAVA predicting slightly more flow separation than STAR-CCM+ (Ref. [12]).

3.3 Results for the Landing Configuration, 30° Flap Deflection

The airplane lift coefficient and the component contributions to lift for the landing configuration are shown in Figure 106. The maximum lift coefficient for the unpowered and unblown landing configuration was $C_{L,max} = 2.58$ at $\alpha = 10°$ and $\alpha = 14°$. The airplane lift coefficient dropped at $\alpha = 11°$ due to a drop in lift on the wing, but then airplane lift coefficient increased back to $C_L = 2.58$ at $\alpha = 14°$ because the lift continued to increase on the stabilator and fuselage even though wing lift plateaued. As expected, the largest contribution to lift from a single component is from the wing alone. There is a shift upward in the lift curve when the flap, nacelles, pylons, strakes, tip nacelle and vortex generator are added to the wing (wing flap nps tn vg). The stabilator has a negative lift coefficient for $\alpha < 6°$. There is a small contribution to lift from the stabilator that increases with increasing angle of attack up to $\alpha = 20°$, after which lift decreases. The small contribution to lift from the fuselage increases with angle of attack, except for a small drop in lift from $\alpha = 10°$ to $\alpha = 11°$ that is explained by viewing the pressure coefficient contours.

The pressure coefficient contours, with black lines showing surface streamlines, are shown for the landing configuration at $M = 0.139$ (88 KEAS) from $\alpha = -2°$ (Figure 107) to $\alpha = 24°$ (Figure 123). The angle of attack where flow separation first moves forward to the leading edge at the wing root fuselage intersection, is at $\alpha = 11°$ (Figure 113), and is also the first drop in lift on the wing and airplane with increasing angle of attack (Figure 106). The airplane lift coefficient increases with increasing angle of attack from $\alpha = 11°$ to $\alpha = 14°$, but then there is another drop in lift at $\alpha = 15°$. There is a big difference in the flow separation patterns between $\alpha = 14°$ and $\alpha = 15°$ as the flow separation near the fuselage moves forward to the wing leading edge, between the first two inboard high-lift nacelles (Figure 117). As angle of attack is increased to $\alpha = 17°$, another large region of flow separation moves forward to the wing leading edge, this time far outboard at the wing-tip nacelle, see Figure 119. The airplane lift continues to drop as the flow continues to separate from the wing upper surface with increasing angle of attack to $\alpha = 24°$, see Figures 120 to 123.

The skin friction coefficient contours at angles of attack from $\alpha = -2°$ to $\alpha = 24°$ are shown in Figures 124-138, respectively. The flow separation regions discussed above are also visible as dark blue contours in these skin friction coefficient plots, which are included because they show the stabilator. The lift on the stabilator is increasing over the range of angle of attack from $\alpha = -2°$ to $\alpha = 20°$, and the value of skin friction coefficient ranges from 0.003 to 0.009 on the upper surface of the stabilator. The stabilator stalls with full chord flow separation on the upper surface at $\alpha = 24°$, shown in Figure 138. The values of skin friction coefficient over the whole upper surface of the stabilator are zero, indicating separated flow, except at the outboard tip.

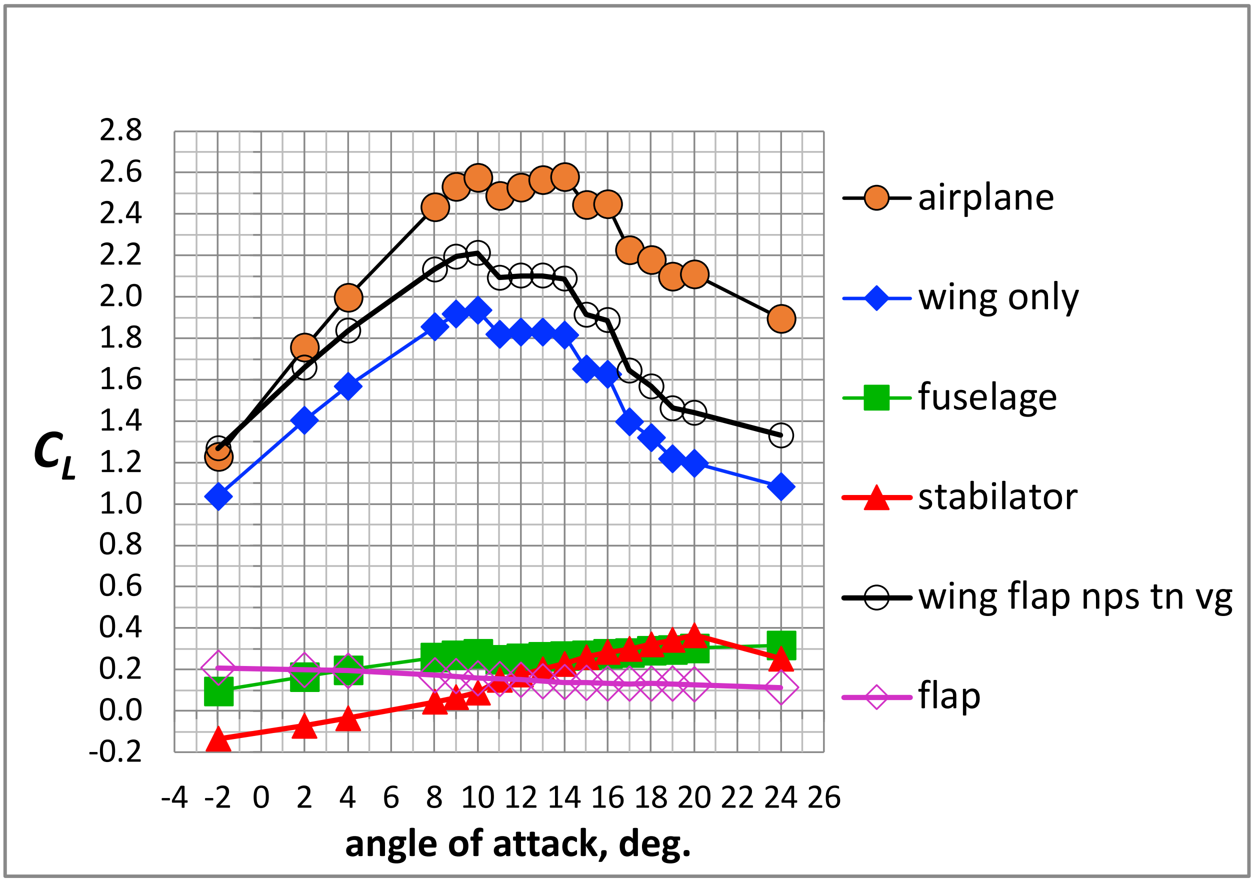

Figure 106. The Effect of Angle of Attack on Airplane C_L and Component Contributions to C_L for the Landing Configuration with a 30° Flap Deflection at $M = 0.139$.

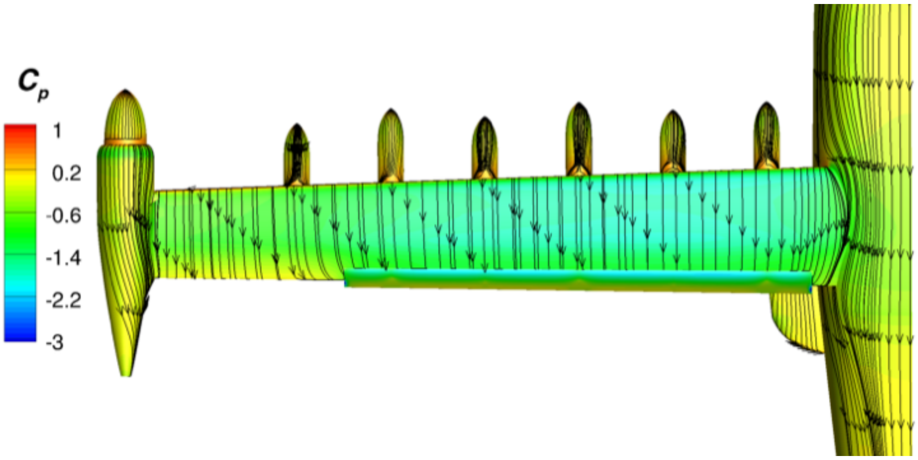

Figure 107. Streamlines and Pressure Coefficient Contours for the Landing Configuration with a 30° Flap Deflection at $M = 0.139$ and $\alpha = -2°$.

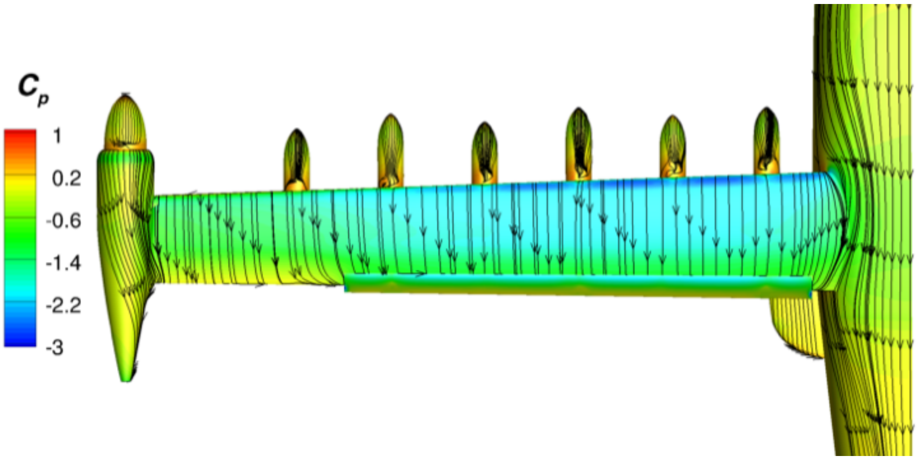

Figure 108. Streamlines and Pressure Coefficient Contours for the Landing Configuration with a 30° Flap Deflection at $M = 0.139$ and $\alpha = 2°$.

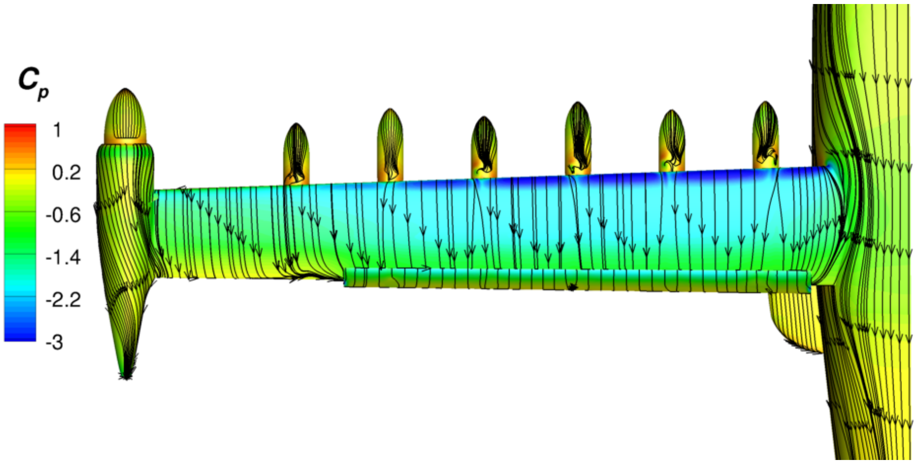

Figure 109. Streamlines and Pressure Coefficient Contours for the Landing Configuration with a 30° Flap Deflection at $M = 0.139$ and $\alpha = 4°$.

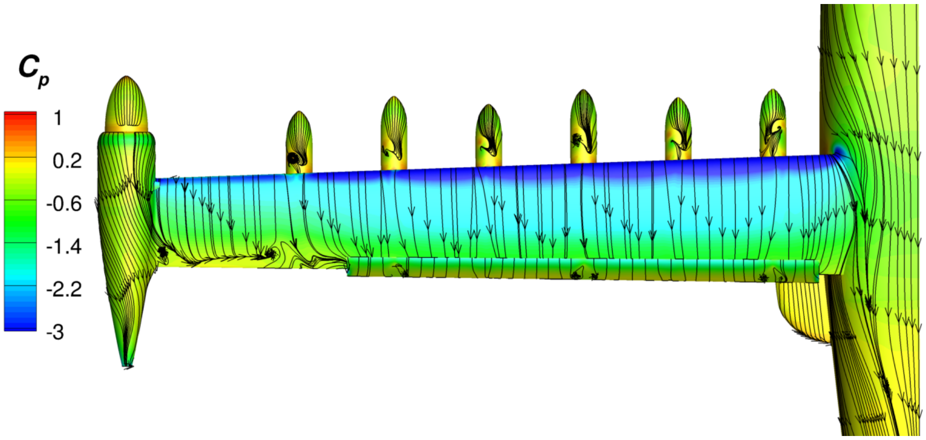

Figure 110. Streamlines and Pressure Coefficient Contours for the Landing Configuration with a 30° Flap Deflection at $M = 0.139$ and $\alpha = 8°$.

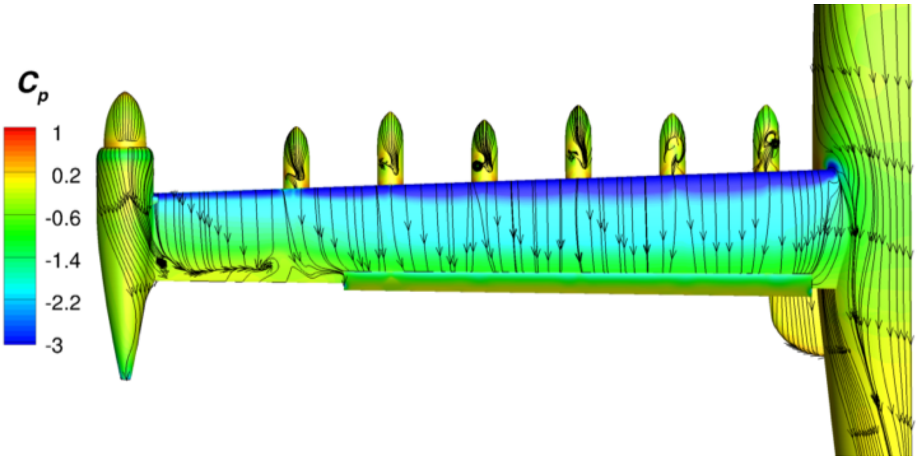

Figure 111. Streamlines and Pressure Coefficient Contours for the Landing Configuration with a 30° Flap Deflection at $M = 0.139$ and $\alpha = 9°$.

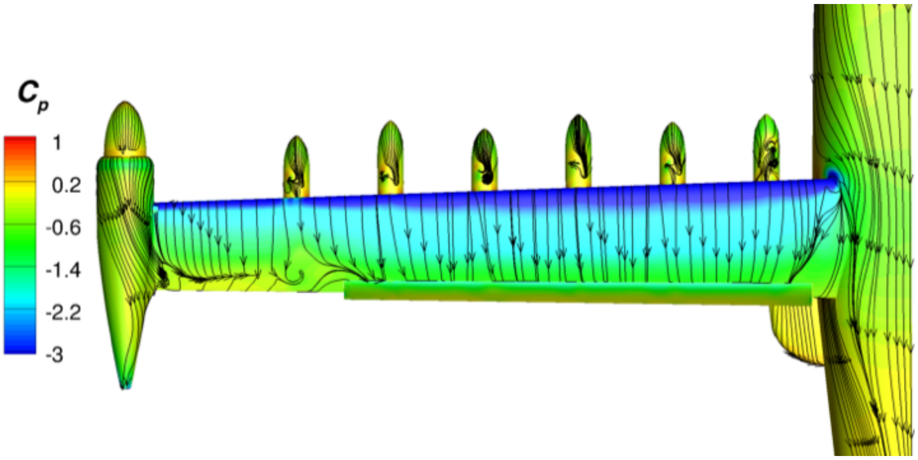

Figure 112. Streamlines and Pressure Coefficient Contours for the Landing Configuration with a 30° Flap Deflection at $M = 0.139$ and $\alpha = 10°$.

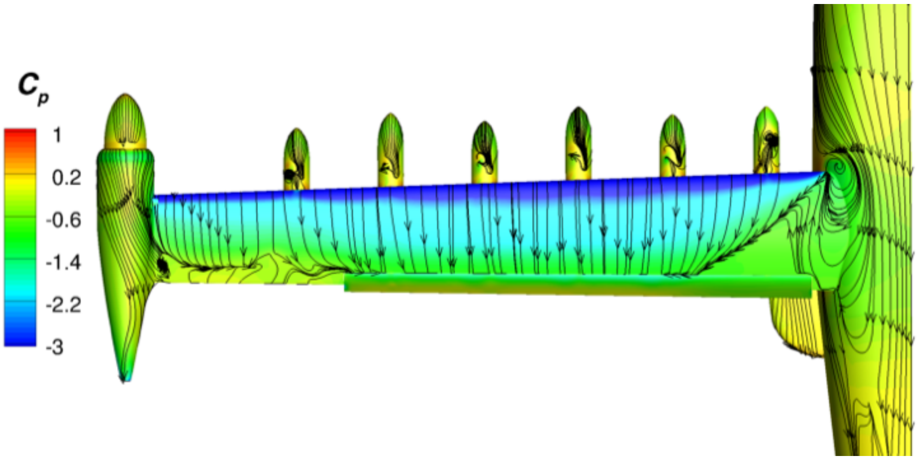

Figure 113. Streamlines and Pressure Coefficient Contours for the Landing Configuration with a 30° Flap Deflection at $M = 0.139$ and $\alpha = 11°$.

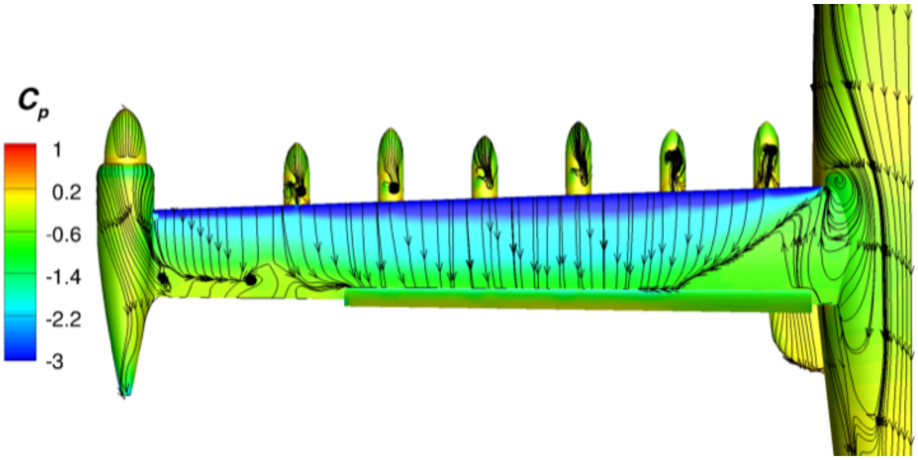

Figure 114. Streamlines and Pressure Coefficient Contours for the Landing Configuration with a 30° Flap Deflection at $M = 0.139$ and $\alpha = 12°$.

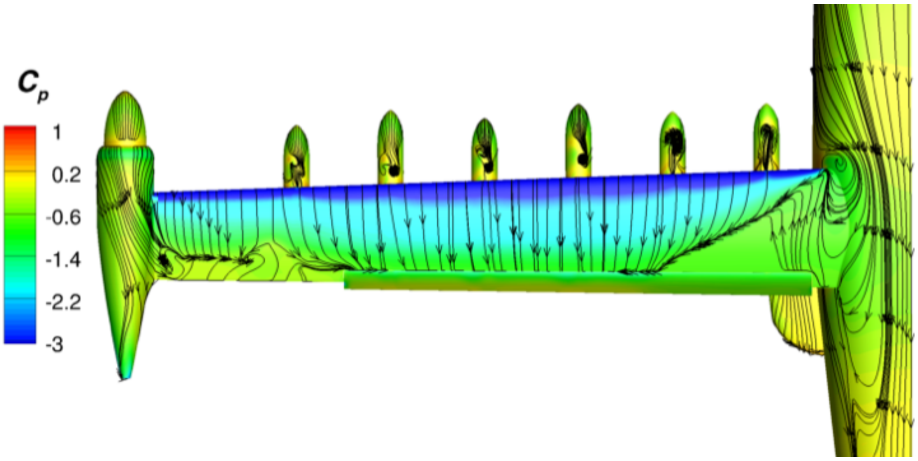

Figure 115. Streamlines and Pressure Coefficient Contours for the Landing Configuration with a 30° Flap Deflection at $M = 0.139$ and $\alpha = 13°$.

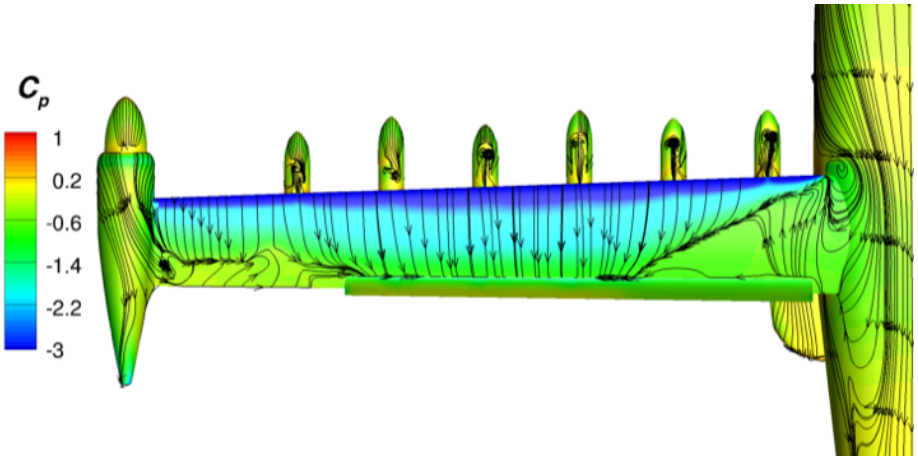

Figure 116. Streamlines and Pressure Coefficient Contours for the Landing Configuration with a 30° Flap Deflection at $M = 0.139$ and $\alpha = 14°$.

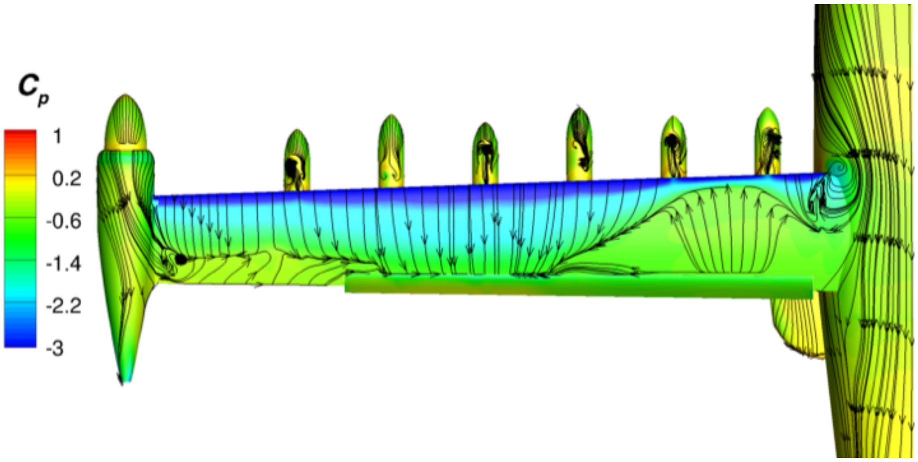

Figure 117. Streamlines and Pressure Coefficient Contours for the Landing Configuration with a 30° Flap Deflection at $M = 0.139$ and $\alpha = 15°$.

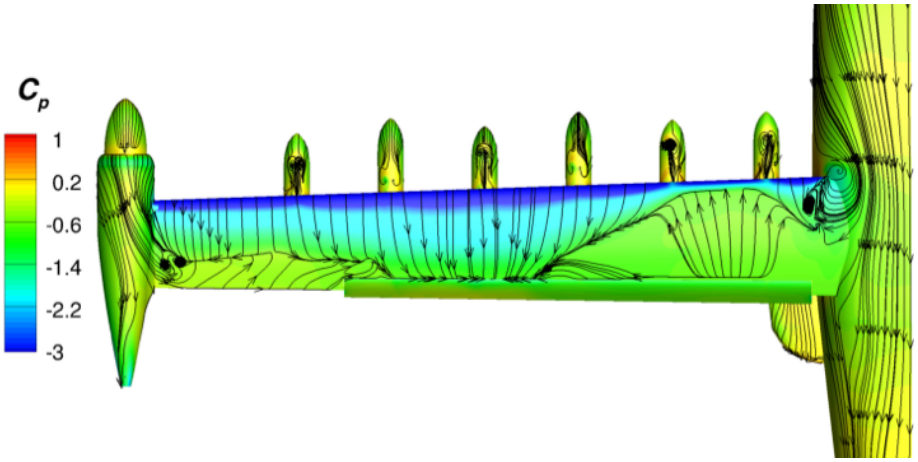

Figure 118. Streamlines and Pressure Coefficient Contours for the Landing Configuration with a 30° Flap Deflection at $M = 0.139$ and $\alpha = 16°$.

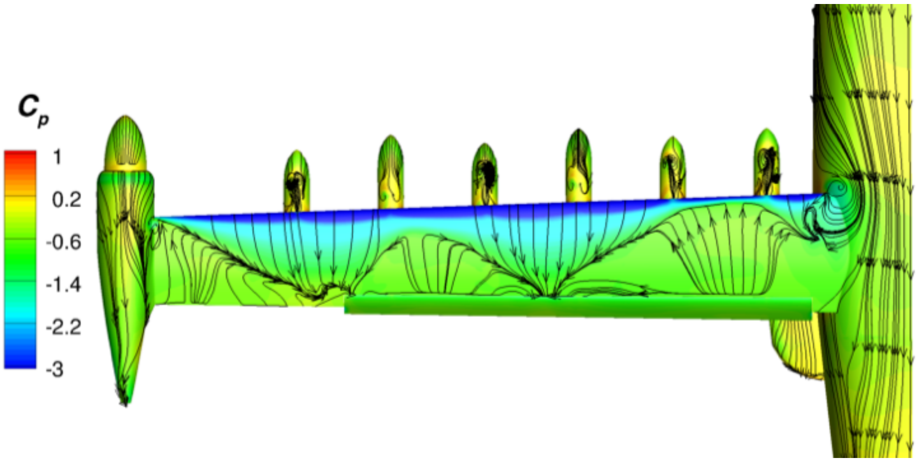

Figure 119. Streamlines and Pressure Coefficient Contours for the Landing Configuration with a 30° Flap Deflection at $M = 0.139$ and $\alpha = 17°$.

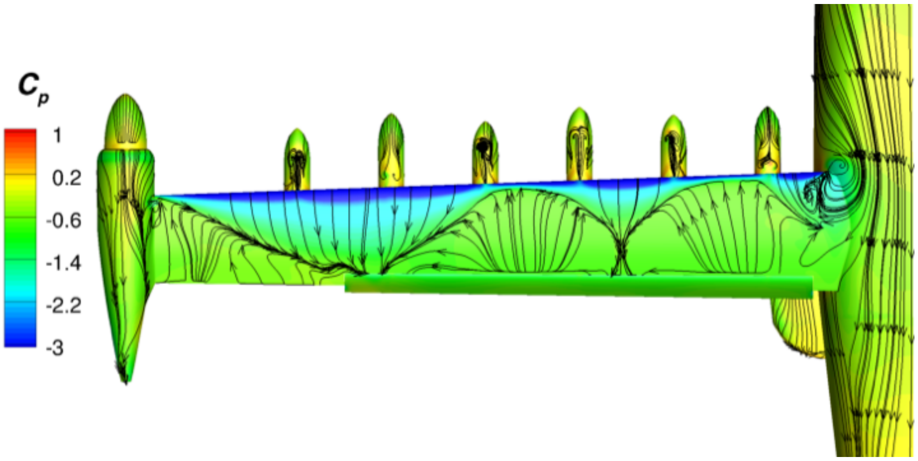

Figure 120. Streamlines and Pressure Coefficient Contours for the Landing Configuration with a 30° Flap Deflection at $M = 0.139$ and $\alpha = 18°$.

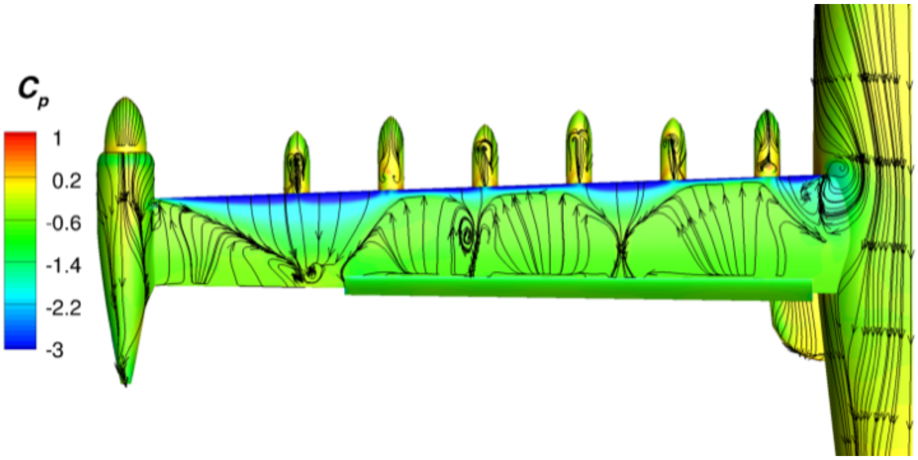

Figure 121. Streamlines and Pressure Coefficient Contours for the Landing Configuration with a 30° Flap Deflection at $M = 0.139$ and $\alpha = 19°$.

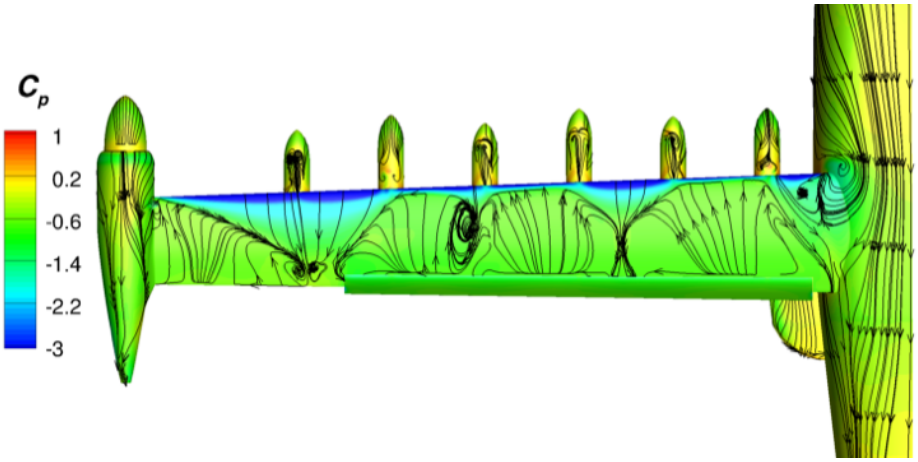

Figure 122. Streamlines and Pressure Coefficient Contours for the Landing Configuration with a 30° Flap Deflection at $M = 0.139$ and $\alpha = 20°$.

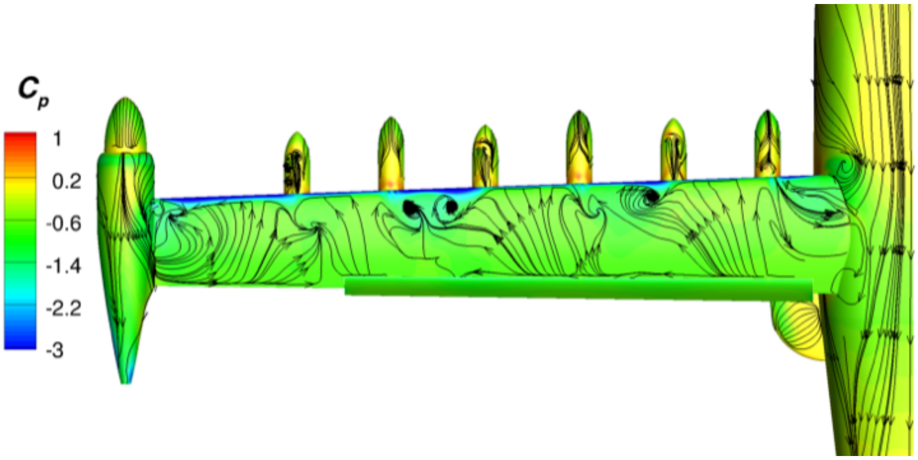

Figure 123. Streamlines and Pressure Coefficient Contours for the Landing Configuration with a 30° Flap Deflection at $M = 0.139$ and $\alpha = 24°$.

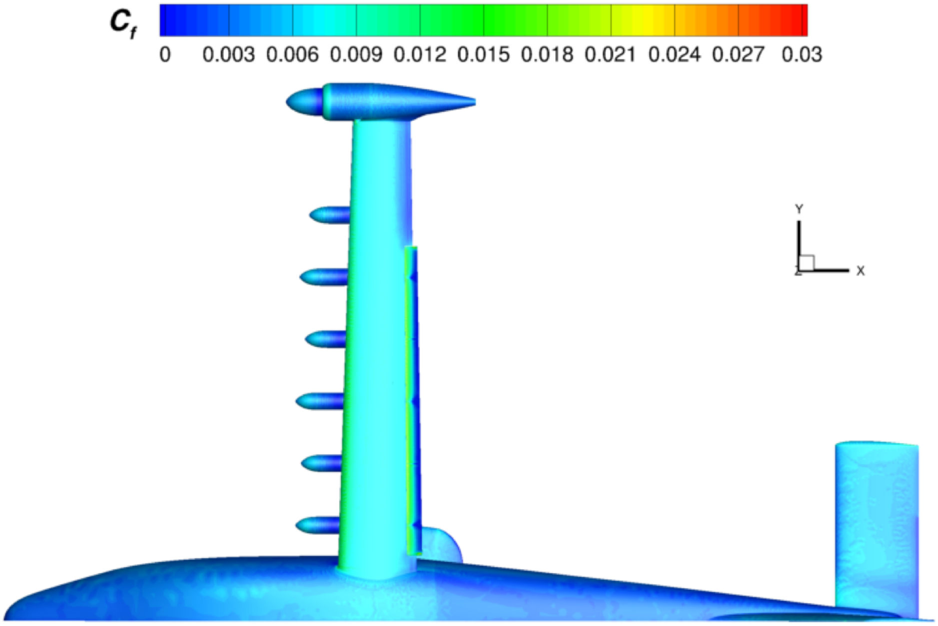

Figure 124. Skin Friction Coefficient Contours for the Landing Configuration with a 30° Flap Deflection at $M = 0.139$ and $\alpha = -2°$.

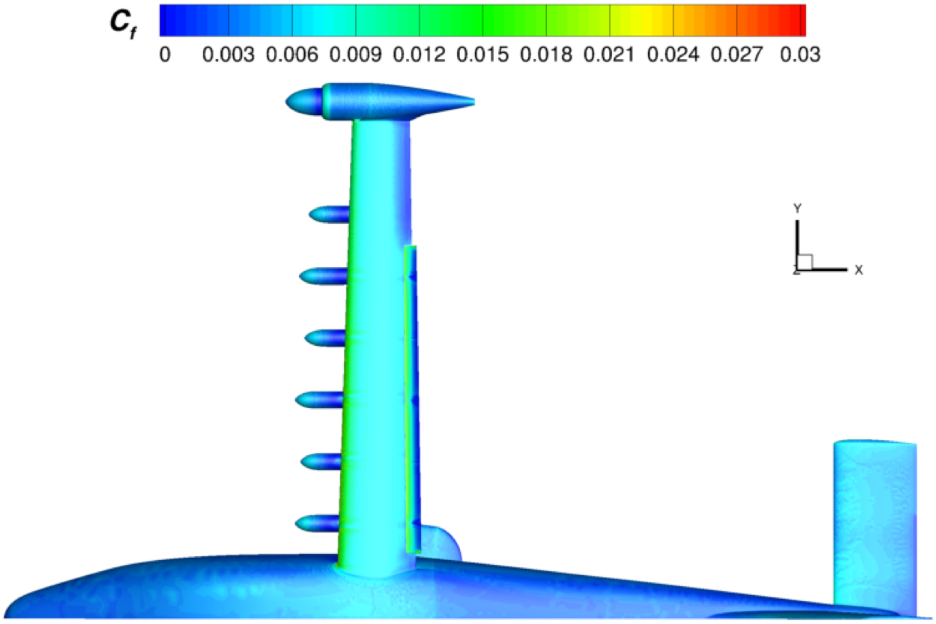

Figure 125. Skin Friction Coefficient Contours for the Landing Configuration with a 30° Flap Deflection at $M = 0.139$ and $\alpha = 2°$.

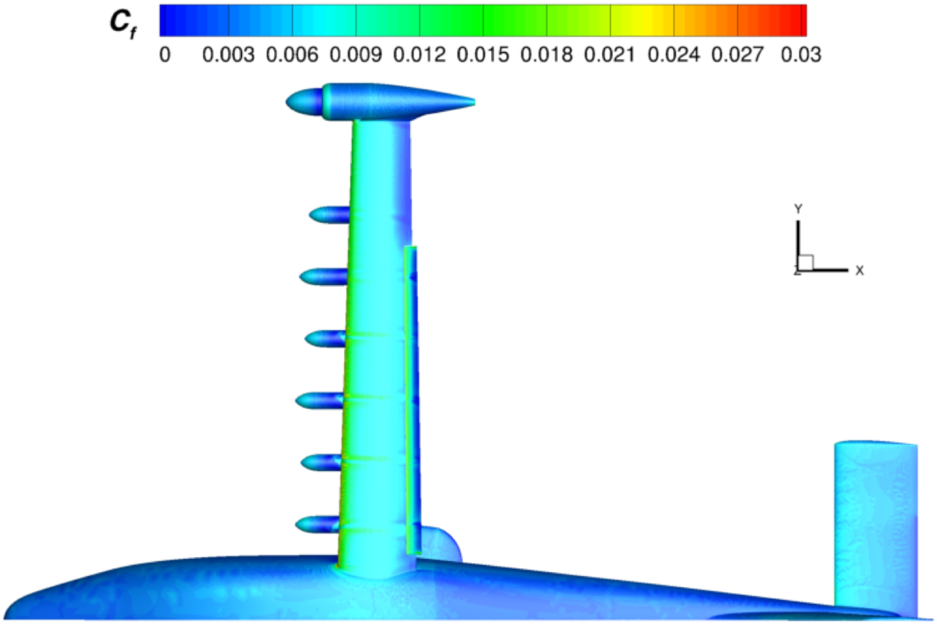

Figure 126. Skin Friction Coefficient Contours for the Landing Configuration with a 30° Flap Deflection at $M = 0.139$ and $\alpha = 4°$.

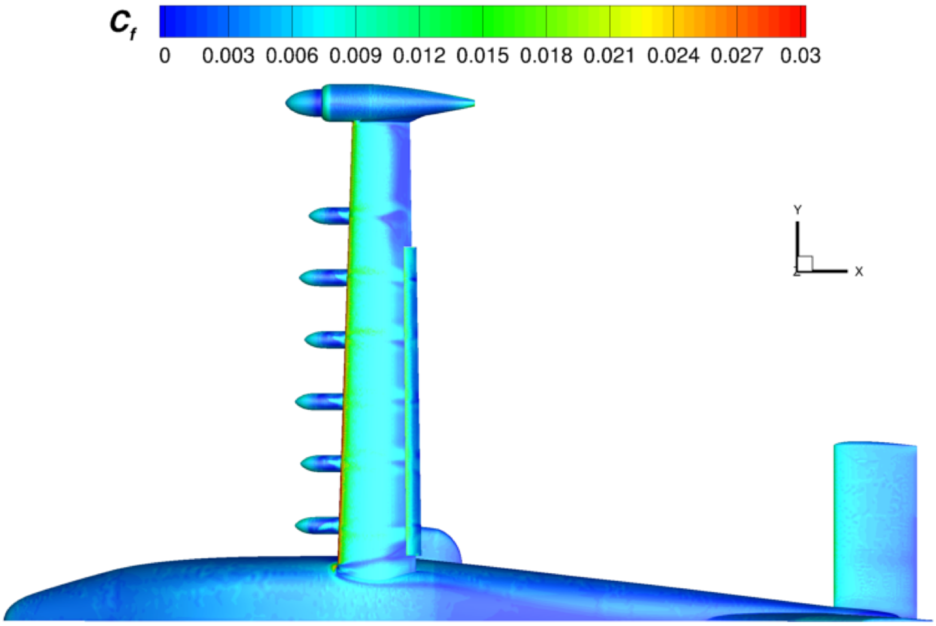

Figure 127. Skin Friction Coefficient Contours for the Landing Configuration with a 30° Flap Deflection at $M = 0.139$ and $\alpha = 10°$.

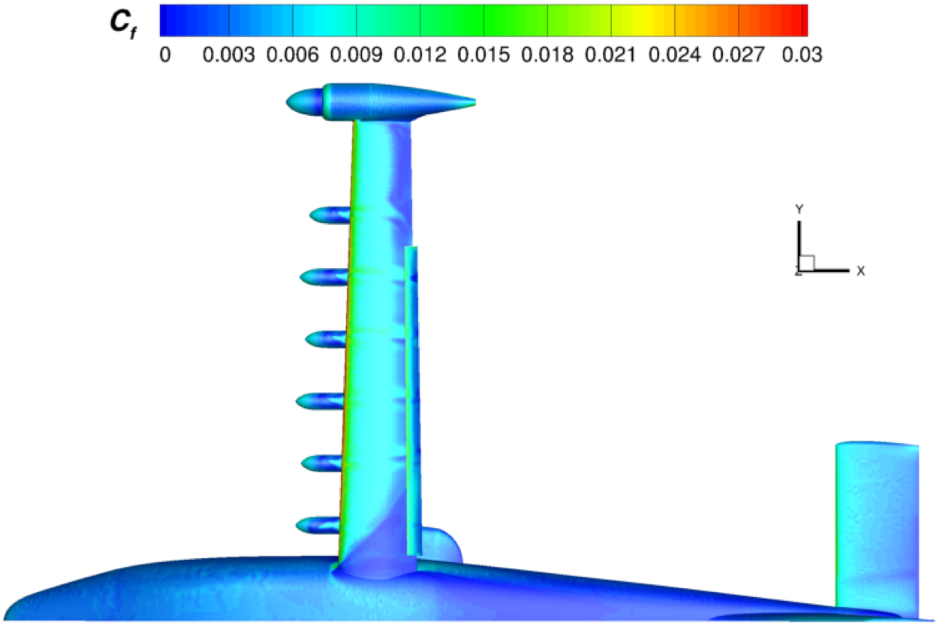

Figure 128. Skin Friction Coefficient Contours for the Landing Configuration with a 30° Flap Deflection at $M = 0.139$ and $\alpha = 11°$.

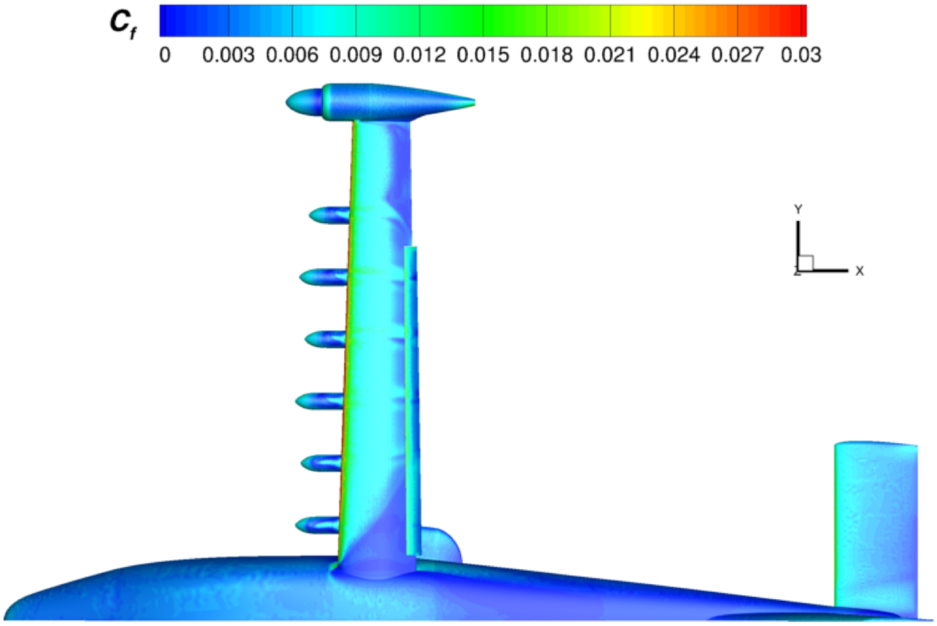

Figure 129. Skin Friction Coefficient Contours for the Landing Configuration with a 30° Flap Deflection at $M = 0.139$ and $\alpha = 12°$.

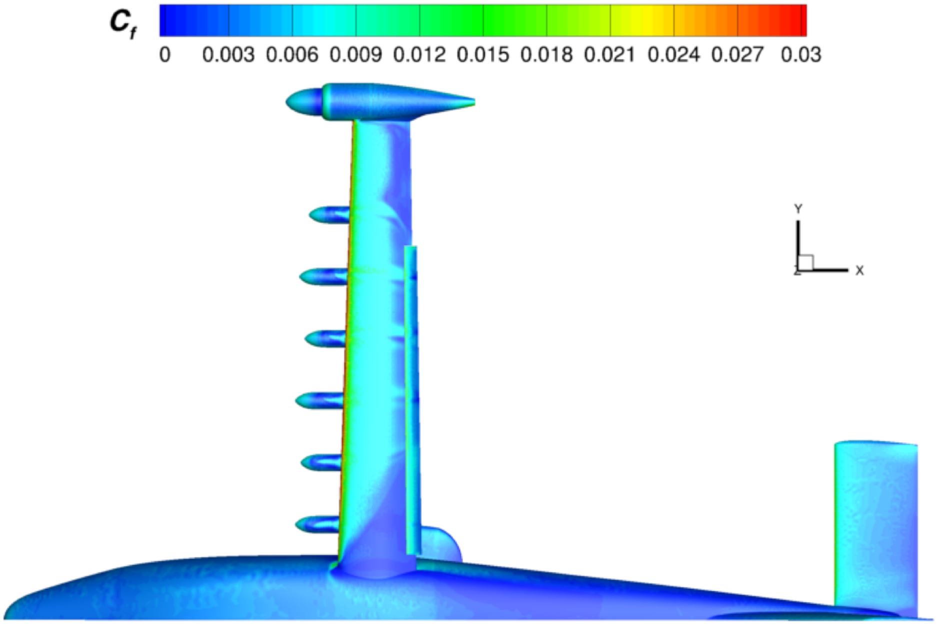

Figure 130. Skin Friction Coefficient Contours for the Landing Configuration with a 30° Flap Deflection at $M = 0.139$ and $\alpha = 13°$.

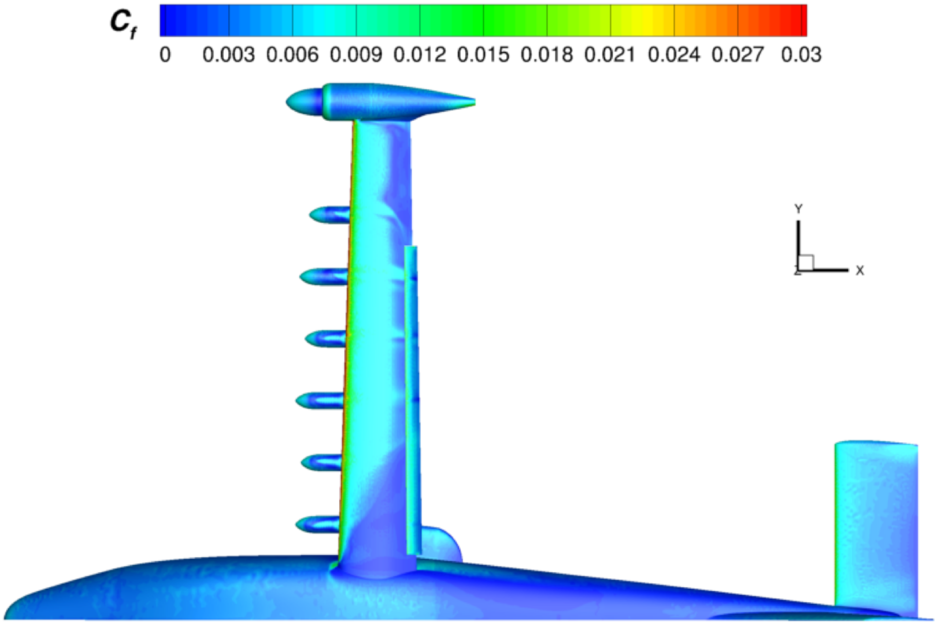

Figure 131. Skin Friction Coefficient Contours for the Landing Configuration with a 30° Flap Deflection at $M = 0.139$ and $\alpha = 14°$.

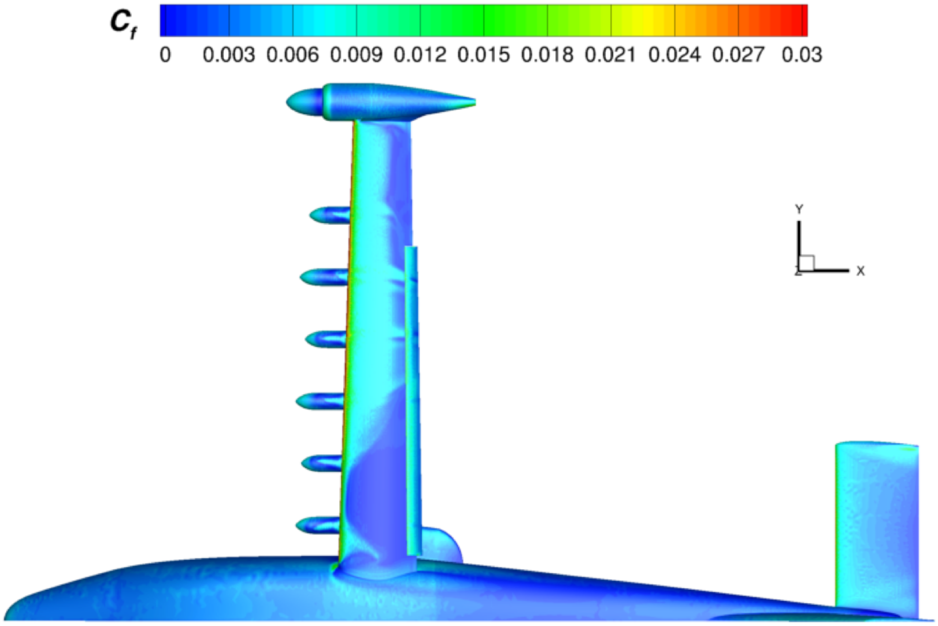

Figure 132. Skin Friction Coefficient Contours for the Landing Configuration with a 30° Flap Deflection at $M = 0.139$ and $\alpha = 15°$.

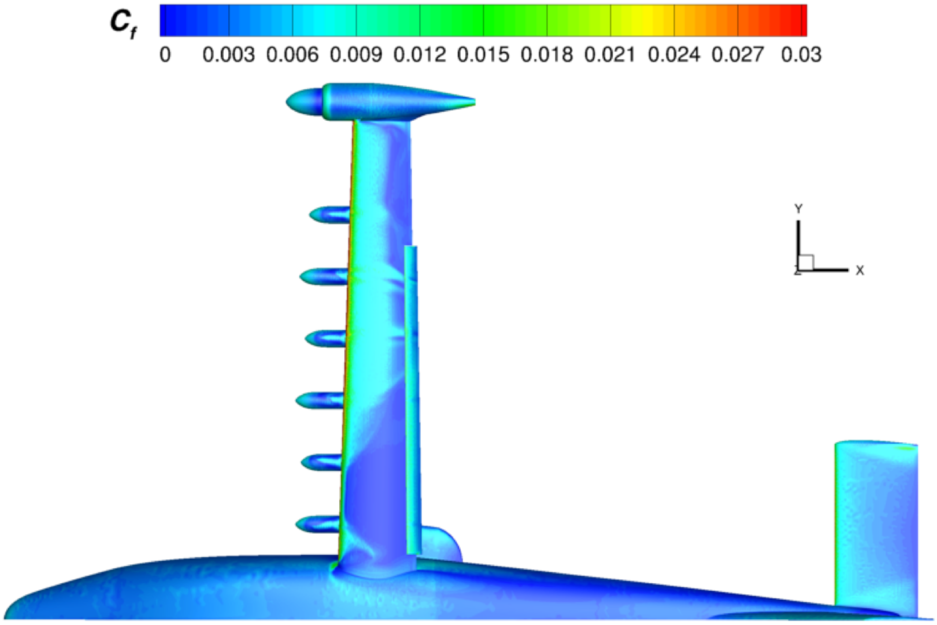

Figure 133. Skin Friction Coefficient Contours for the Landing Configuration with a 30° Flap Deflection at $M = 0.139$ and $\alpha = 16°$.

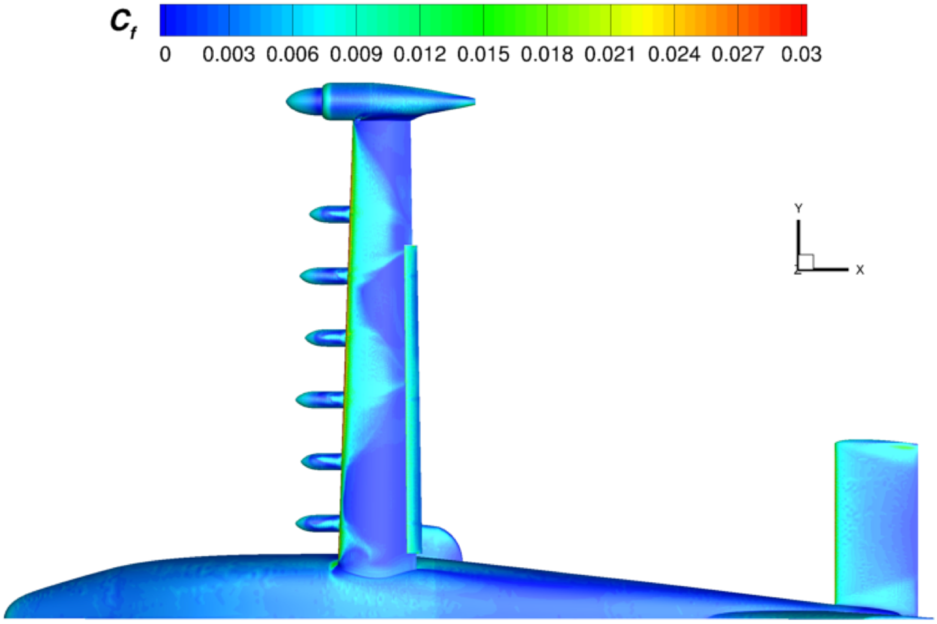

Figure 134. Skin Friction Coefficient Contours for the Landing Configuration with a 30° Flap Deflection at $M = 0.139$ and $\alpha = 17°$.

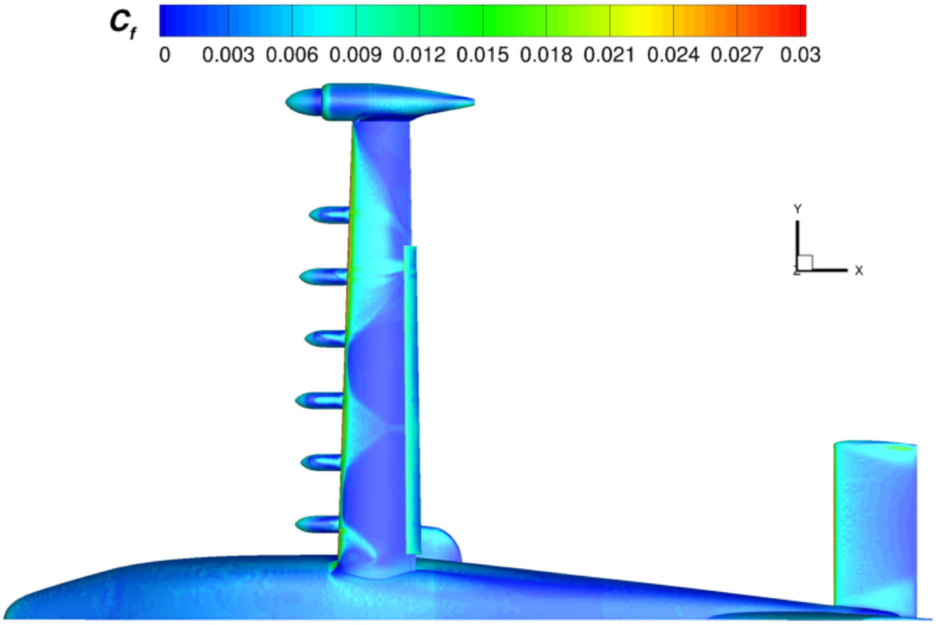

Figure 135. Skin Friction Coefficient Contours for the Landing Configuration with a 30° Flap Deflection at $M = 0.139$ and $\alpha = 18°$.

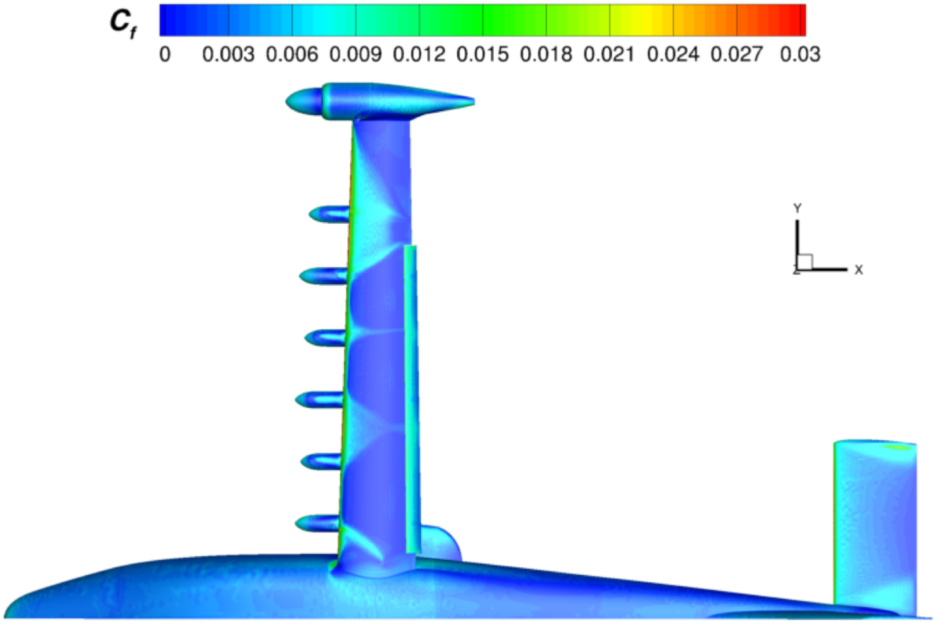

Figure 136. Skin Friction Coefficient Contours for the Landing Configuration with a 30° Flap Deflection at $M = 0.139$ and $\alpha = 19°$.

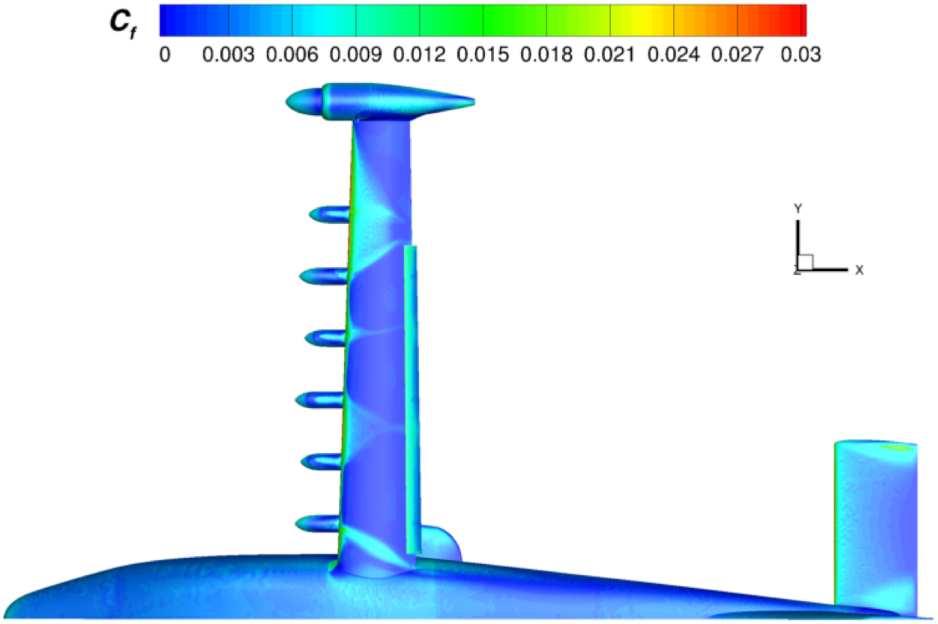

Figure 137. Skin Friction Coefficient Contours for the Landing Configuration with a 30° Flap Deflection at $M = 0.139$ and $\alpha = 20°$.

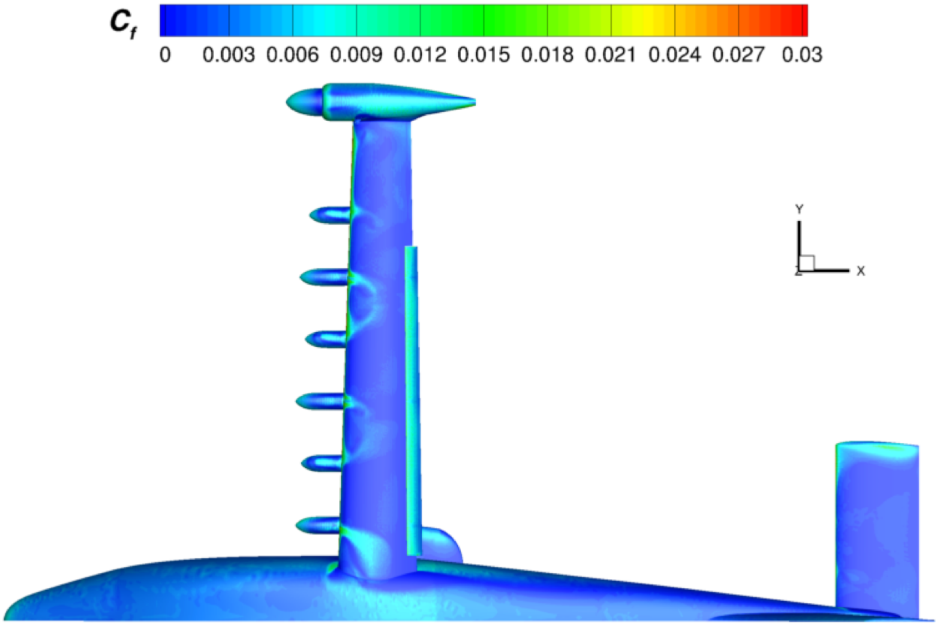

Figure 138. Skin Friction Coefficient Contours for the Landing Configuration with a 30° Flap Deflection at $M = 0.139$ and $\alpha = 24°$.

3.3.1 Code Comparisons for the Landing Configuration with a 30° Flap Deflection

The USM3D lift coefficient compares well with LAVA and STAR-CCM+ for the landing configuration up to $\alpha < 11^\circ$. The lift coefficients at $\alpha = 10^\circ$ are $C_L = 2.597$ (USM3D), $C_L = 2.688$ (LAVA), and $C_L = 2.6440$ (STAR-CCM+). The large difference in lift at $\alpha = 11^\circ$ is a result of the geometry difference at the fuselage wing root region. The USM3D code has a large region of flow separation that extends forward to the wing leading edge at $\alpha = 11^\circ$, see Figure 113. The flow separation remains in place up through $\alpha = 14^\circ$, then shifts outboard, between the first two high-lift nacelles from the centerline, at higher angles of attack. The STAR-CCM+ and LAVA codes do not predict wing root flow separation at $\alpha = 14^\circ$, although the STAR-CCM+ solution does have some flow separation downstream of the first two inboard nacelles that is not present in the LAVA solution, see Figure 7(b) in Ref. [12].

The maximum lift coefficient computed with USM3D was $C_{L,max} = 2.579$ at $\alpha = 10^\circ$, then the lift decreased at 11°, and then increased back to $C_{L,max} = 2.582$ at $\alpha = 14^\circ$. The LAVA code predicted $C_{L,max} = 3.031$ at $\alpha = 14^\circ$ and the STAR-CCM+ code predicted $C_{L,max} = 2.877$ at $\alpha = 14^\circ$, as seen in Figure 5 of Ref. [12]. The surface pressure coefficient contours (with black streamlines) for LAVA and STAR-CCM+ at $\alpha = 14^\circ$ are shown in Figure 7(b) of Ref. [12], and the USM3D contours are shown in Figure 116. As expected from the C_L values at $\alpha = 14^\circ$ for each of the codes, USM3D predicted the most flow separation at the wing root, followed by STAR-CCM+, with LAVA showing no wing root flow separation at this condition. All three codes predicted flow separation in the aileron region.

All three codes indicate large regions of flow separation at $\alpha = 18^\circ$; the pressure coefficient contours are shown in Figure 120 for USM3D and in Figure 7(c) of Ref. [12] for LAVA and STAR-CCM+. The USM3D and STAR-CCM+ codes predict two large regions of flow separation that extend forward to the wing leading edge between the first four high-lift nacelles from the centerline, but the LAVA code has just one large region of flow separation between the first two high-lift nacelles from the centerline. All three codes predict flow separation in the aileron region.

3.4 Effect of Flap Deflection and Airspeed

The effect of flap deflection and airspeed on drag, lift and pitching moment coefficients is shown in Figures 139-141, respectively. There is a slight increase in drag coefficient over the range of angles of attack for the takeoff configuration with a 10° flap deflection, as compared to the cruise configuration with no flap deflection, see Figure 139. There is a large increase in drag coefficient over the range of angles of attack for the landing configuration with a 30° flap deflection, as compared to the cruise and the takeoff configurations. There is a shift to increased drag in the drag curve at $\alpha = 16^\circ$ for the cruise configuration with 0° flap, at $\alpha = 14^\circ$ for the takeoff configuration with 10° flap, and at $\alpha = 11^\circ$ for the landing configuration with 30° flap, due to the wing root flow separation that moves upstream to the wing root leading edge at each of the angles of attack for each configuration. The wing root flow separation at $\alpha = 16^\circ$ for the cruise configuration, at $\alpha = 14^\circ$ for the takeoff configuration, and at $\alpha = 11^\circ$ for the landing configuration are shown in Figures 55, 95, and 128, respectively.

The lift coefficient increased with increasing flap deflection and note that there is the typical shift in $C_{L,max}$ to lower angles of attack with increasing flap deflection, see Figure 140. As expected, there is a significant increase in lift for the landing configuration with the 30° flap deflection and a smaller increase in lift for the takeoff configuration with the smaller, 10° flap deflection, as compared to the cruise configuration. As previously discussed, the lift-curve slope changed slightly at $\alpha = 8^\circ$ for the takeoff configuration, and there is less lift than expected. To discuss this further, comparing with the more continuous lift-curve slopes for the cruise and the landing configurations, the wing contribution to lift is plotted in Figure 142. These data show that the slope change at $\alpha = 8°$ for the takeoff configuration occurs from lower lift on the wing than the projected slope of the curve from $\alpha = -2°$ to $\alpha = 4°$.

To understand what is different for the takeoff wing when angle of attack is increased from $\alpha = 4°$ and $\alpha = 8°$, the pressure coefficient contours, combined with black streamlines, were plotted for each configuration in Figures 143 to 145. The normalized U velocity contours in the wing-flap region are shown in Figures 146-148, with velocities less than zero cut from view such that reversed, separated flow regions would be obvious by seeing the gray surface of the geometry. Additionally, the pressure coefficient and Mach contours at a span location of y = 80.34 in. at $\alpha = 4°$ are shown in Figures 149-151, and at $\alpha = 8°$ are shown in Figures 152-154 for the cruise, takeoff, and landing configurations, respectively. The centerline of nacelle 9 is located at y = 80.34 inches.

For the cruise configuration, the flow is mostly fully attached on the upper wing surface for $\alpha = 4°$, with very small regions of separated flow downstream of the high-lift nacelles, at the wing trailing edge, see Figure 146(a). The regions of flow separation downstream of each of the high-lift nacelles gets larger with increasing angle of attack to $\alpha = 8°$, see Figures 143(b) and 146(b). The flow separation downstream of nacelle 9 for the cruise configuration at $\alpha = 8°$ is visible as $M = 0$ in the Mach contours shown in Figure 152(b), but the flow is nearly fully attached to the upper wing surface at $\alpha = 4°$ shown in Figure 149(b).

For the takeoff configuration with the 10° flap deflection, the streamlines indicate that the flow is fully attached to the upper surface of the main wing at $\alpha = 4°$ (Figure 144(a)), but the flap has separated flow (Figure 147(a)). The separated flow region along the aft portion of the flap can also be visualized as dark blue Mach contours just above the flap near the trailing edge in Figure 150(b). At $\alpha = 8°$, triangular-shaped flow separation patterns form downstream of all but one of the high-lift nacelles, Figure 144(b). Figure 147(b) shows larger regions of flow separation on the flap and also regions of attached flow to the flap trailing edge at $\alpha = 8°$, which is different than the flow separation on the flap at $\alpha = 4°$ (Figure 147(a)). The flow separation on both the main element and the flap along the centerline of nacelle 9 at $\alpha = 8°$ is also visible in the Mach contours shown in Figure 153(b), but the flow is fully attached to the upper wing surface at $\alpha = 4°$ shown in Figure 150(b).

Finally, the streamlines on pressure coefficient contours are shown in Figure 145 for the landing configuration with the 30° flap deflection. The streamlines indicate fully attached flow to the upper surface of the wing and the flap for both angles of attack, except for the aileron region at $\alpha = 8°$. The normalized U velocity contours in Figure 148(b) do indicate three small regions of flow separation on the flap, one of which is downstream of nacelle 9 and is therefore, also visible in Figure 154(b). However, without the large triangular-shaped flow separation regions on the wing downstream of the high-lift nacelles, the lift coefficient continues to increase at the expected slope up through $\alpha = 10°$ (Figure 140). Therefore, the triangular-shaped flow separation regions that form downstream of the high-lift nacelles for the landing configuration appear to be the culprit for the change in lift-curve slope, and the slightly lower lift than expected from the takeoff configuration for $\alpha > 4°$.

The effect of flap deflection angle on pitching moment for the full airplane is shown in Figure 141 and the component contributions to C_m are shown in Figures 155-157. The comparison of airplane pitching moment coefficient is comparable for no flap deflection and 10° flap deflection, except at $\alpha = 20°$. This difference in pitching moment at $\alpha = 20°$ for the whole airplane is a consequence of the wing contributions to C_m (Figure 155(b)), as the C_m for the fuselage (Figure 156(b)) and the stabilator (Figure 157(a)) are the same for the cruise and takeoff configurations. The comparison of normalized U velocity contours on the cruise and takeoff configurations at $\alpha = 20°$ is shown in

Figure 158 and there appears to be more attached flow on the wing for the cruise configuration (Figure 158(a)), than on the wing of the takeoff configuration (Figure 158(b)). The contribution to lift from the wing is shown in Figure 142, which confirms that the takeoff wing is generating less lift at $\alpha = 20°$. Therefore, the airplane pitching moment for the takeoff configuration is less negative, compared to the cruise configuration.

The full aircraft landing configuration (30° flap deflection) has a less negative pitching moment for angles of attack $\alpha < 10°$, and a more negative pitching moment for 11° to 15° angles of attack, than the cruise and takeoff configurations (Figure 141). The component contributions to pitching moment coefficient (Figures 155-157) and pressure coefficient contours can be used to explain the effects of angle of attack on pitching moment coefficients for the landing configuration.

The contribution to C_m from the stabilator for the landing configuration is only different than the cruise and takeoff configurations for $\alpha < 10°$. Figures 159-164 shows the Mach contours at a span location of y = 40 inches for various angles of attack for the landing configuration. The downwash from the wing and flap impacts the stabilator for $\alpha = 8°$ (Figure 159) and $\alpha = 10°$ (Figure 160). However, for $\alpha > 10°$, the wake flow from the wing and flap does not impact the stabilator, see Figures 161 to 164. Therefore, the C_m for the landing configuration is only different than the cruise and takeoff configurations for $\alpha < 10°$ because the downwash is impacting the stabilator. As a check on this deduction, a comparison of the Mach contours for a span location of y = 40 inches is shown at $\alpha = 8°$ for all three configurations (see Figures 165-167) and the pressure coefficient contours support the deduction that the downwash impacts the stabilator for the landing configuration, but the wake is well above the stabilator for the cruise and takeoff configurations. Finally, there is a change in pitching moment slope for $\alpha > 20°$ due to full chord stall on the stabilator, as shown in Figure 164.

The contribution to C_m from the fuselage is shown in Figure 156(b). The $C_{m,fuselage}$ is the same for the three configurations up to $\alpha = 10°$. There is a shift in the $C_{m,fuselage}$ curve at $\alpha = 16°$ for the cruise configuration, at $\alpha = 14°$ for the takeoff configuration, and at $\alpha = 11°$ for the landing configuration. This shift and change in slope for $C_{m,fuselage}$ occurs at these angles of attack due to the wing root flow separation that also impacts the fuselage, as discussed previously in Figures 55, 95, and 128.

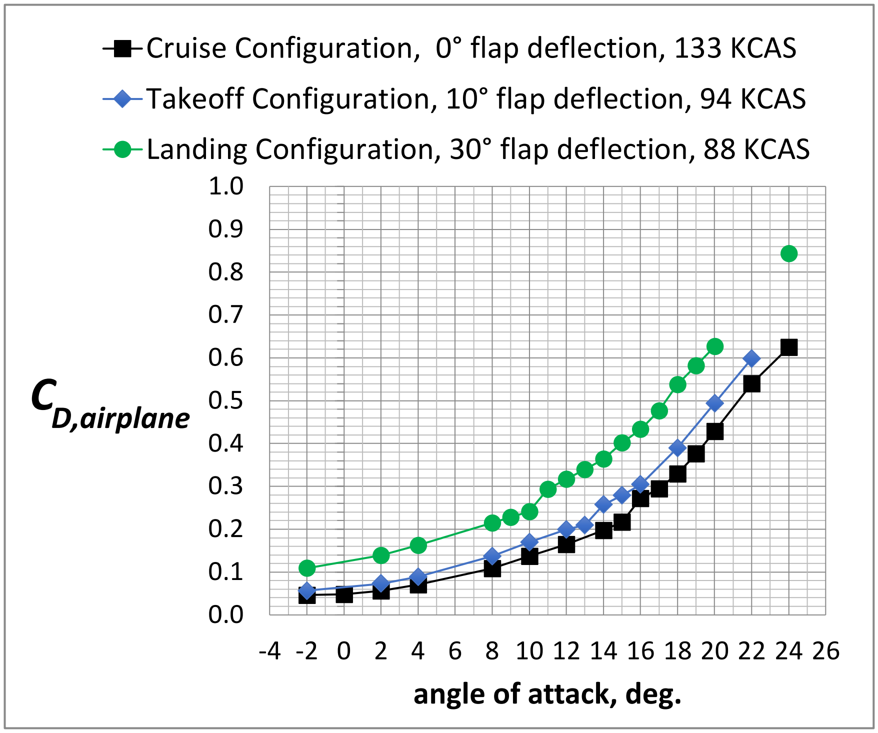

Figure 139. Effect of Flap Deflection and Airspeed on Airplane Drag Coefficient.

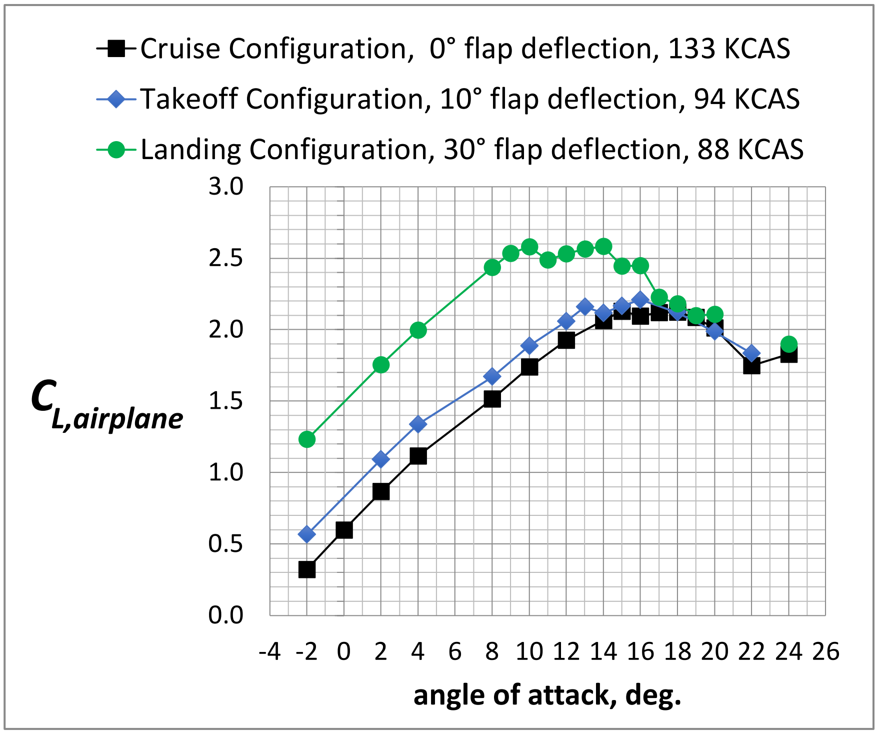

Figure 140. Effect of Flap Deflection and Airspeed on Airplane Lift Coefficient.

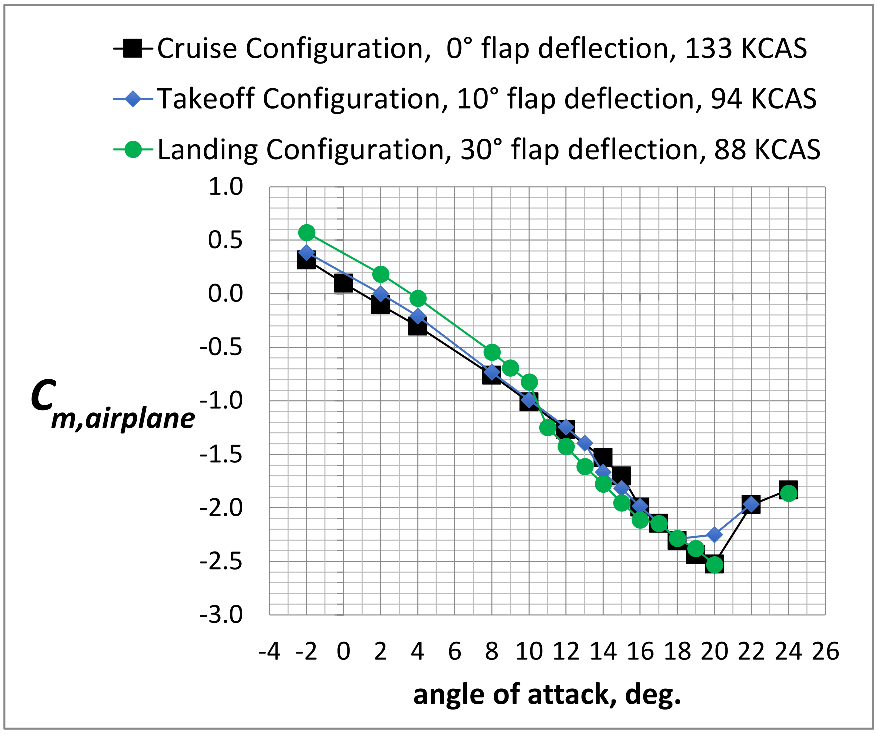

Figure 141. Effect of Flap Deflection and Airspeed on Airplane Pitching Moment Coefficient.

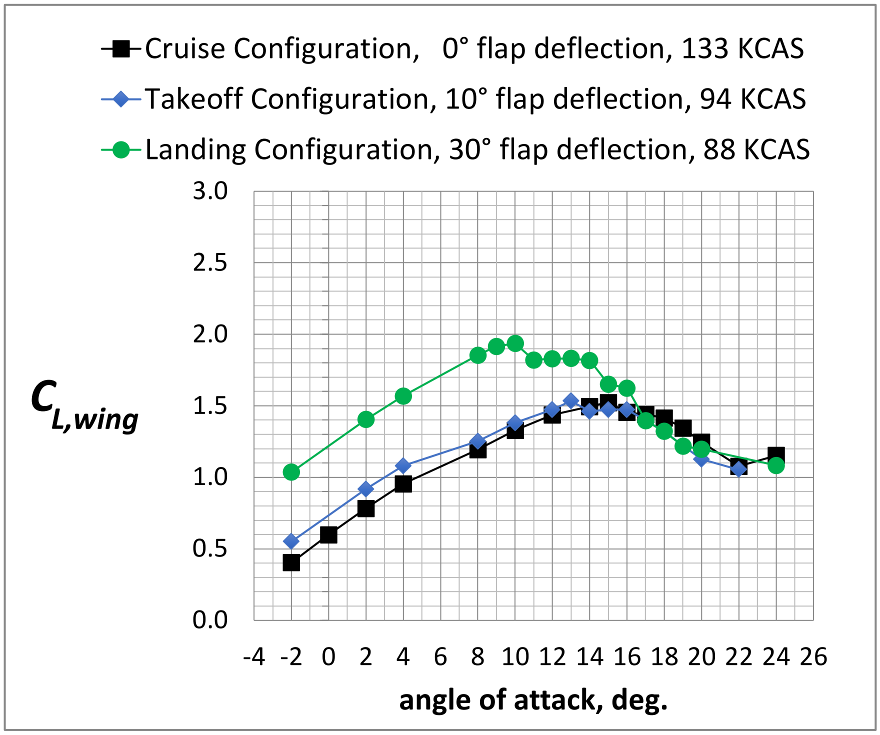

Figure 142. The Effect of Angle of Attack on Wing Lift Coefficient.

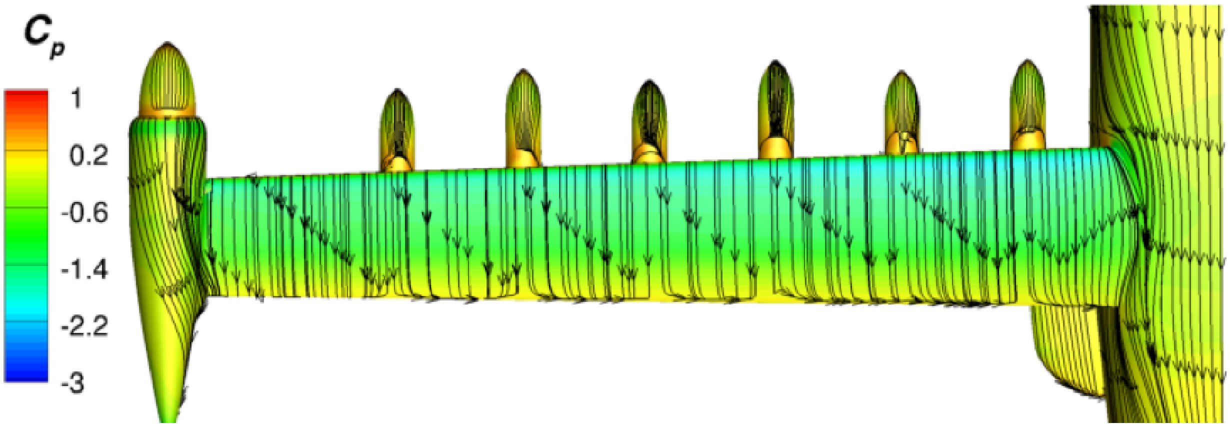

(a) $\alpha = 4°$

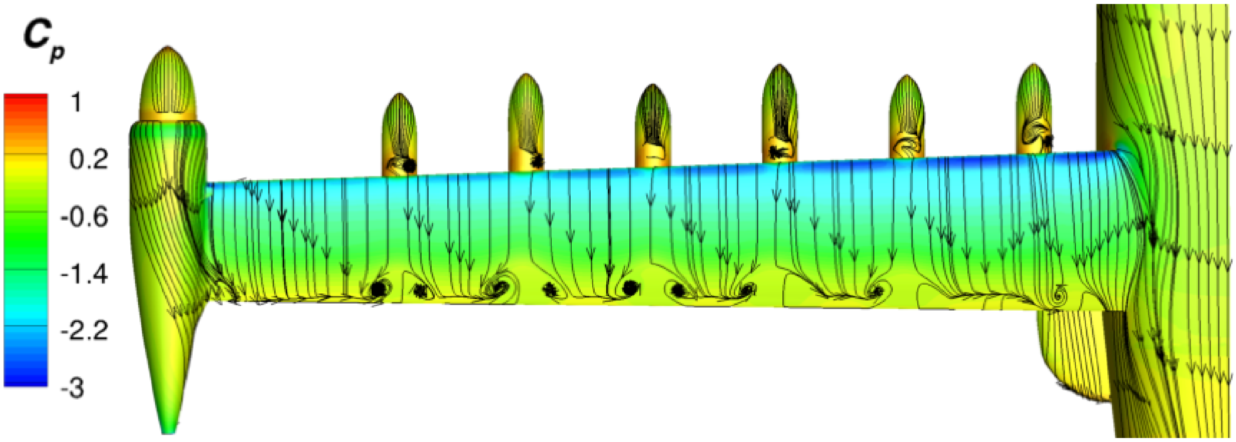

(b) $\alpha = 8°$

Figure 143. Comparison of C_p Contours and Streamlines between $\alpha = 4°$ and $\alpha = 8°$ for the Cruise Configuration at $M = 0.233$.

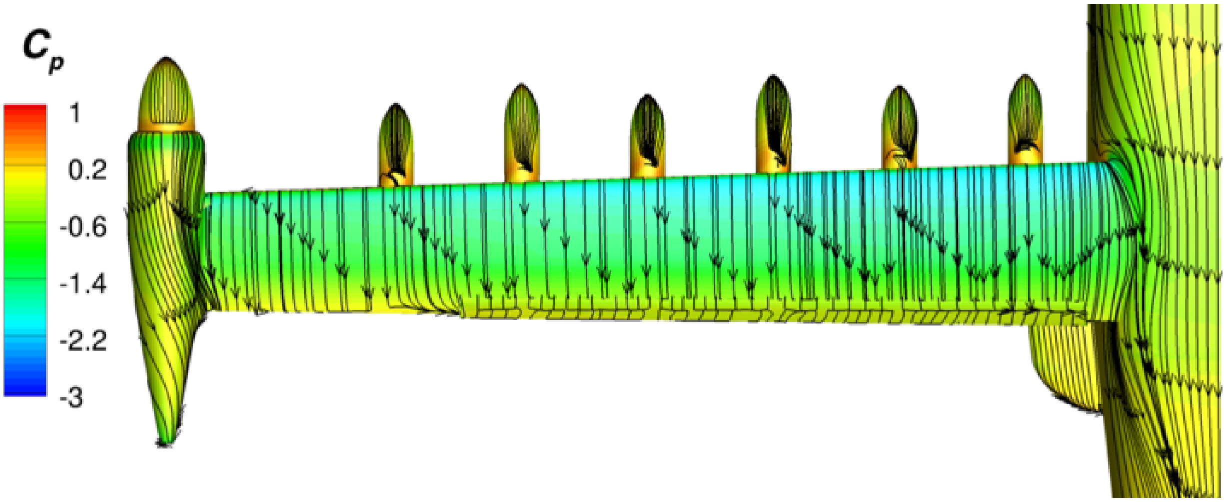

(a) $\alpha = 4°$

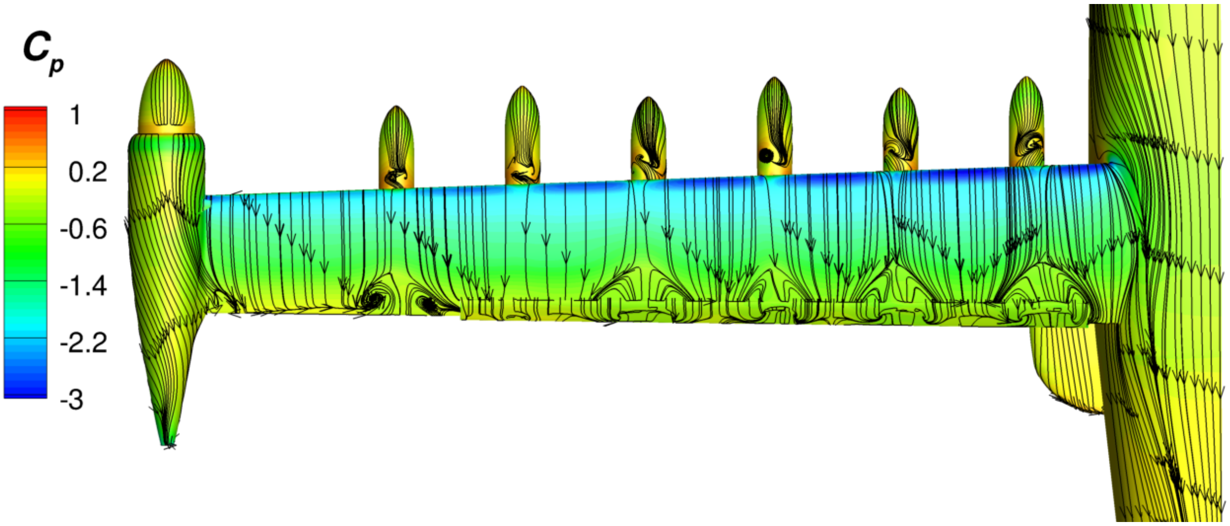

(b) $\alpha = 8°$

Figure 144. Comparison of C_p Contours and Streamlines between $\alpha = 4°$ and $\alpha = 8°$ for the Takeoff Configuration with a 10° Flap Deflection at $M = 0.149$.

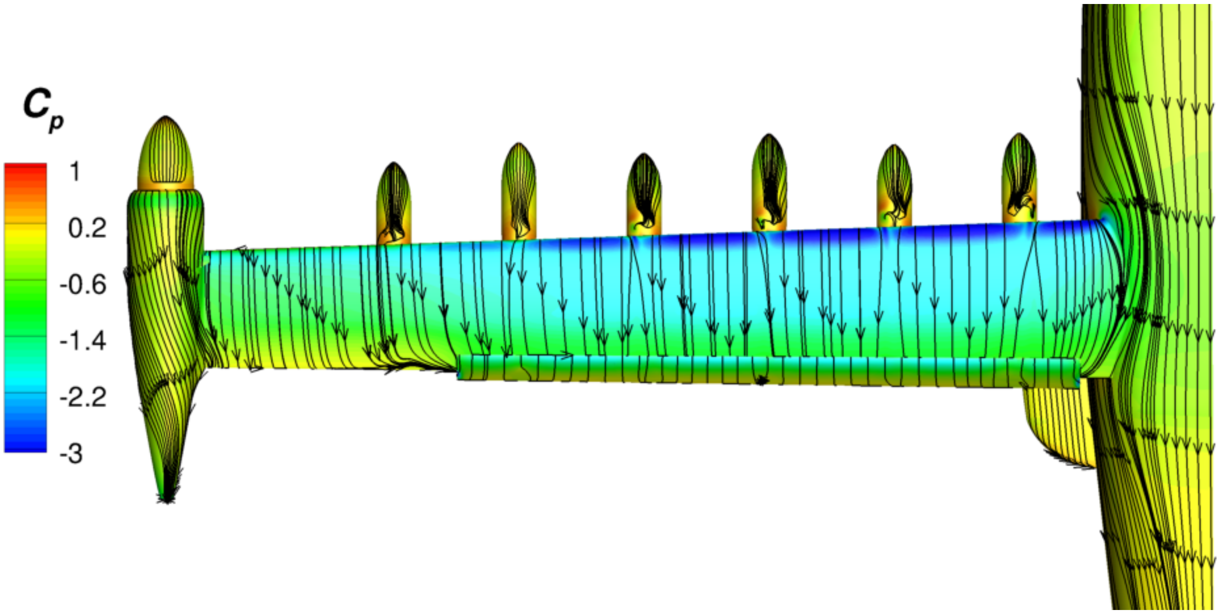

(a) α = 4°

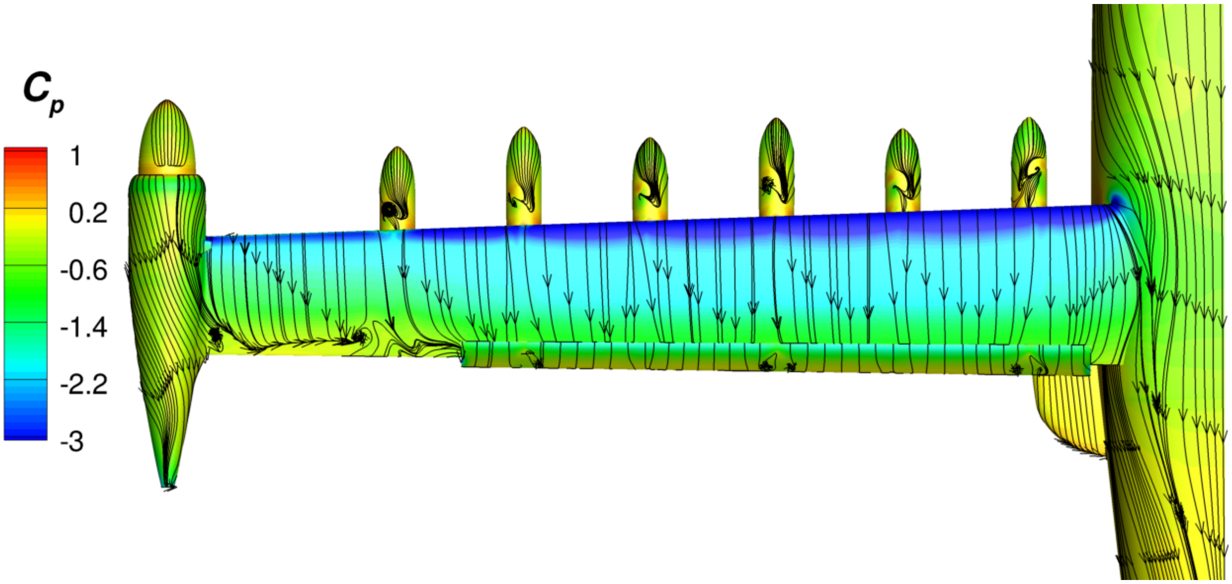

(b) α = 8°

Figure 145. Comparison of C_p Contours and Streamlines between $\alpha = 4°$ and $\alpha = 8°$ for the Landing Configuration with a 30° Flap Deflection at $M = 0.139$.

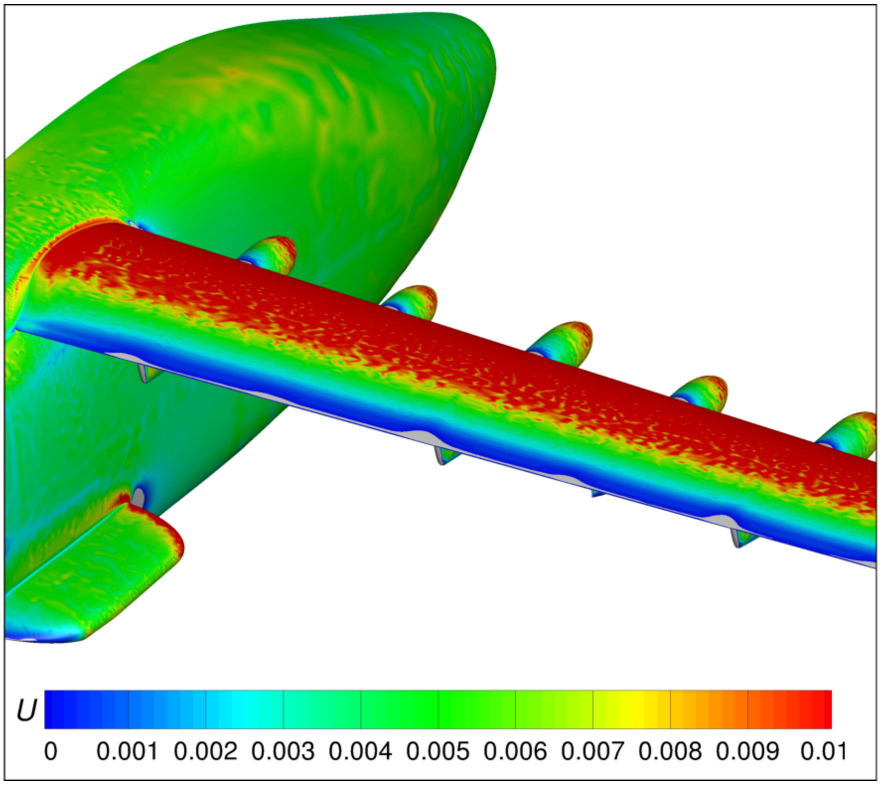

(a) $\alpha = 4°$

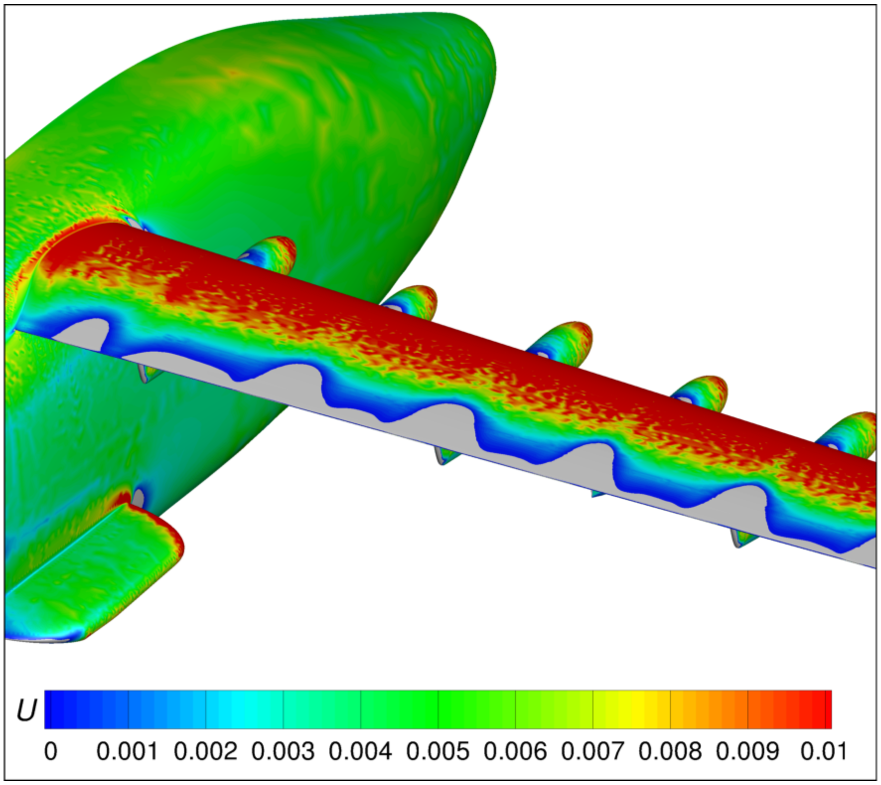

(b) $\alpha = 8°$

Figure 146. Comparison of Normalized U Velocity Contours between $\alpha = 4°$ and $\alpha = 8°$ for the Cruise Configuration.

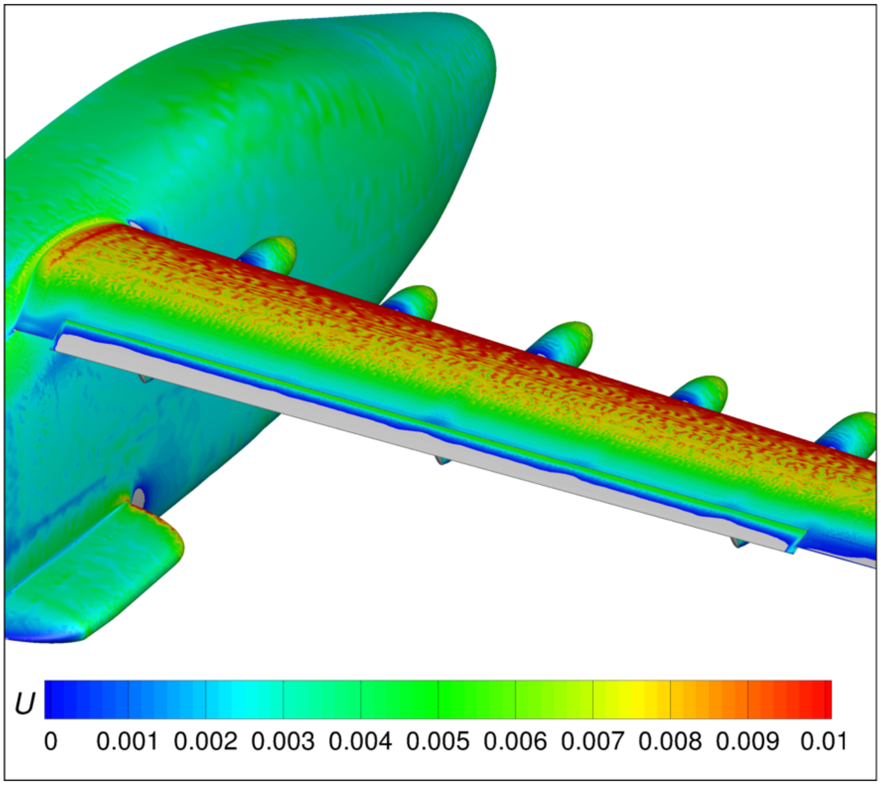

(a) $\alpha = 4^\circ$

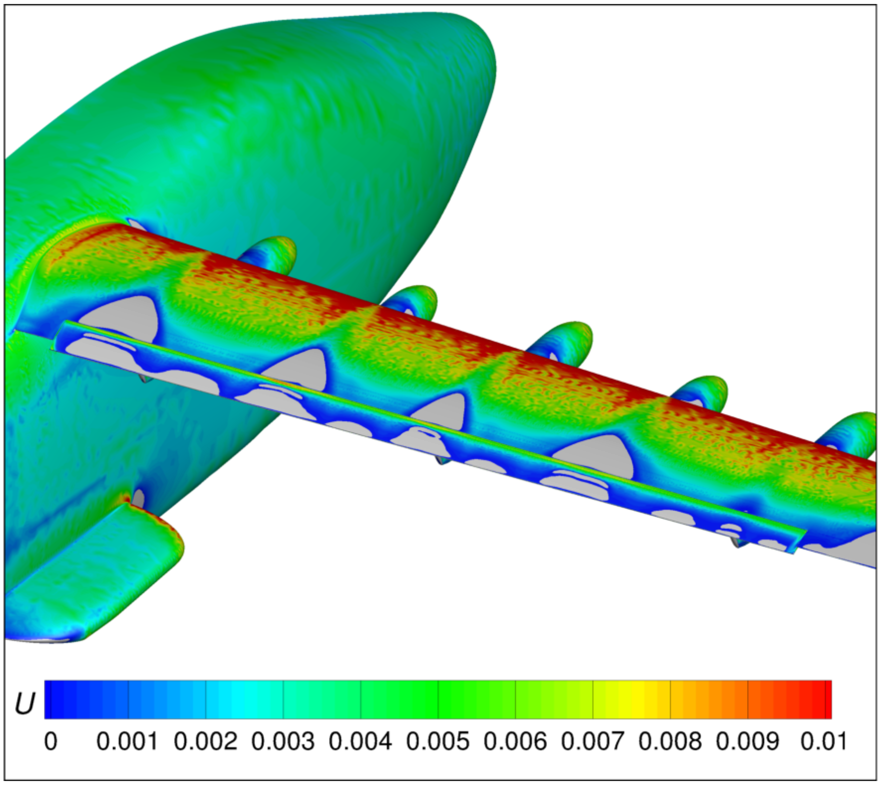

(b) $\alpha = 8^\circ$

Figure 147. Comparison of Normalized U Velocity Contours between $\alpha = 4^\circ$ and $\alpha = 8^\circ$ for the Takeoff Configuration.

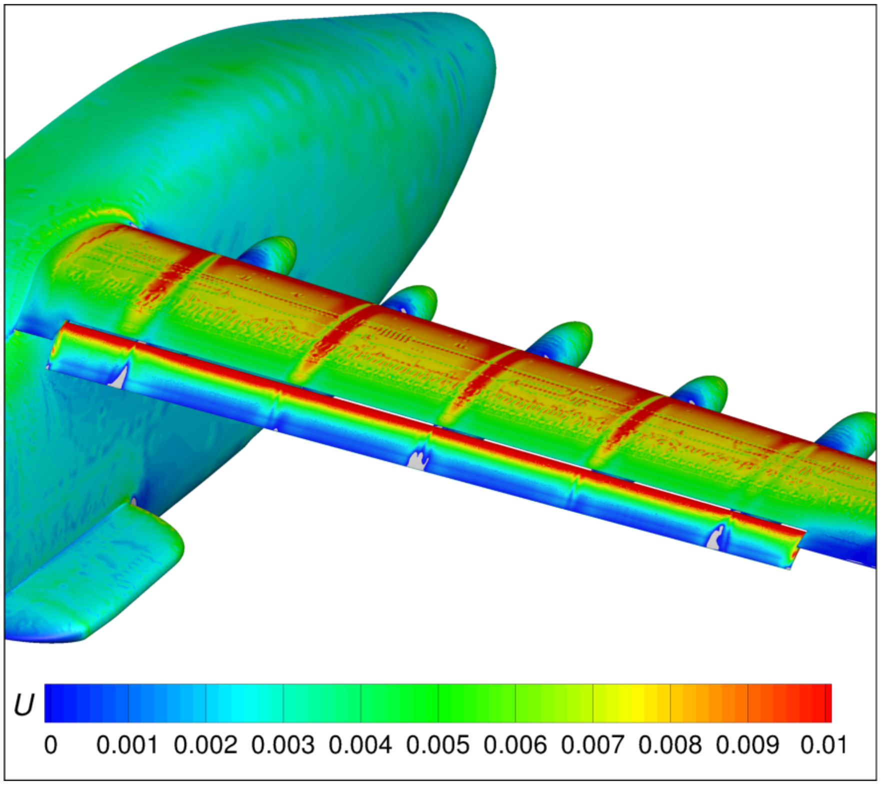

(a) $\alpha = 4^\circ$

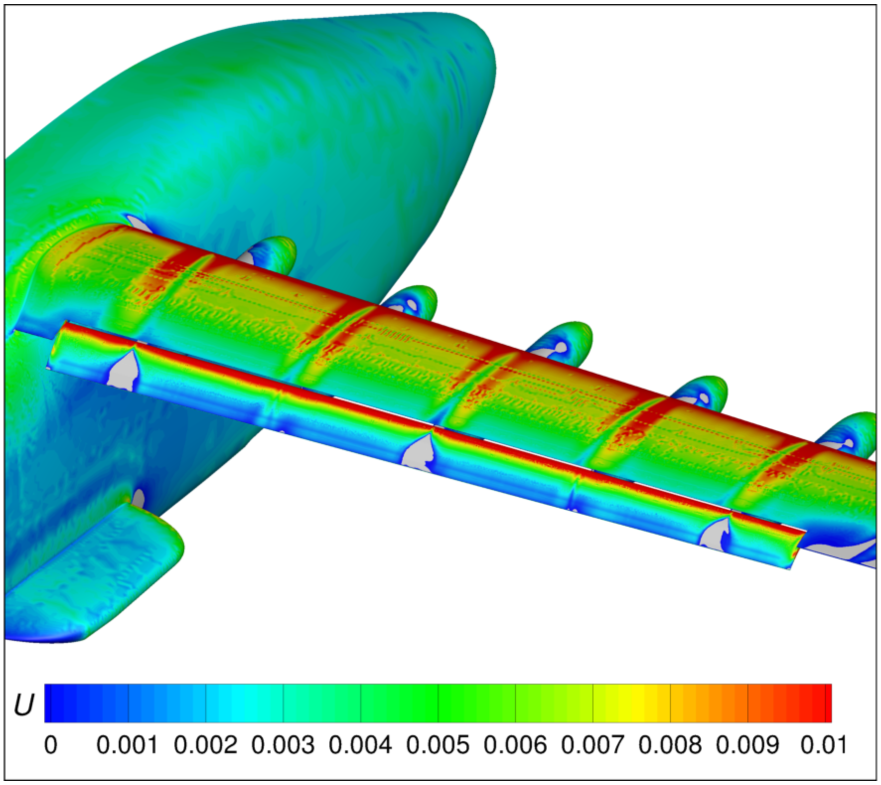

(b) $\alpha = 8^\circ$

Figure 148. Comparison of Normalized U Velocity Contours between $\alpha = 4^\circ$ and $\alpha = 8^\circ$ for the Landing Configuration.

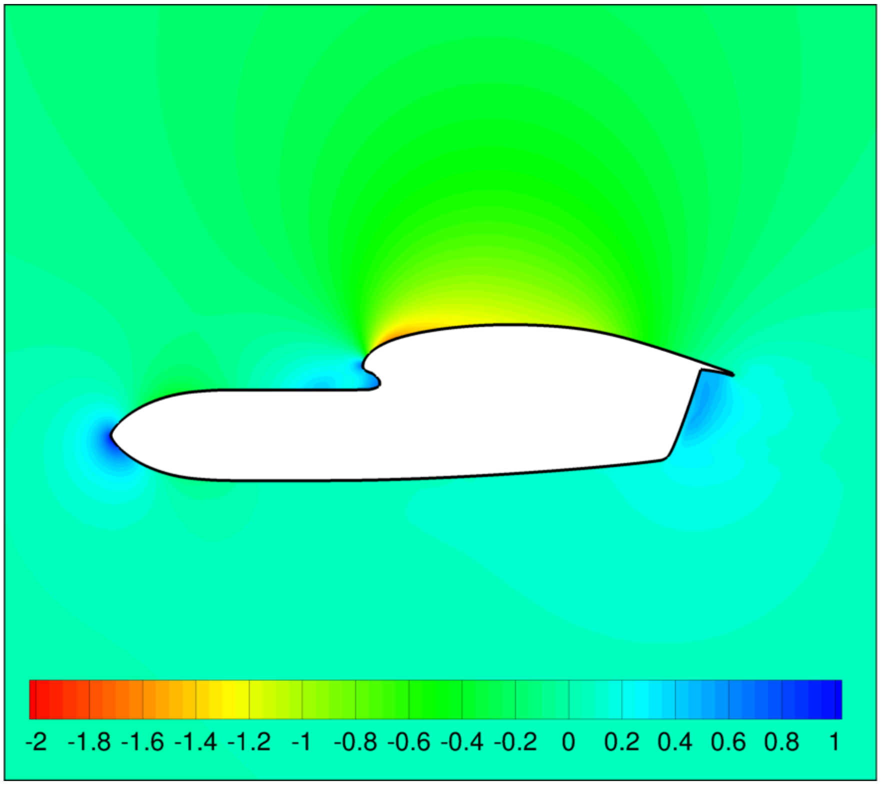

(a) C_p Contours

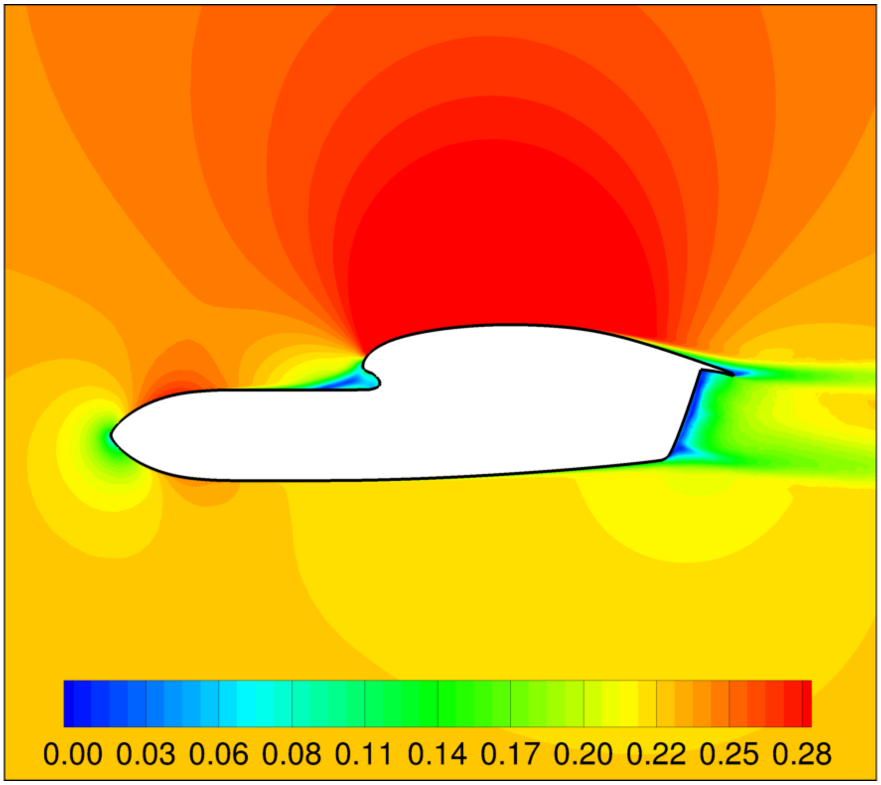

(b) $Mach$ Contours

Figure 149. Pressure Coefficient and Mach Contours at a Span Location of y = 80.34 in. for the Cruise Configuration at $\alpha = 4°$.

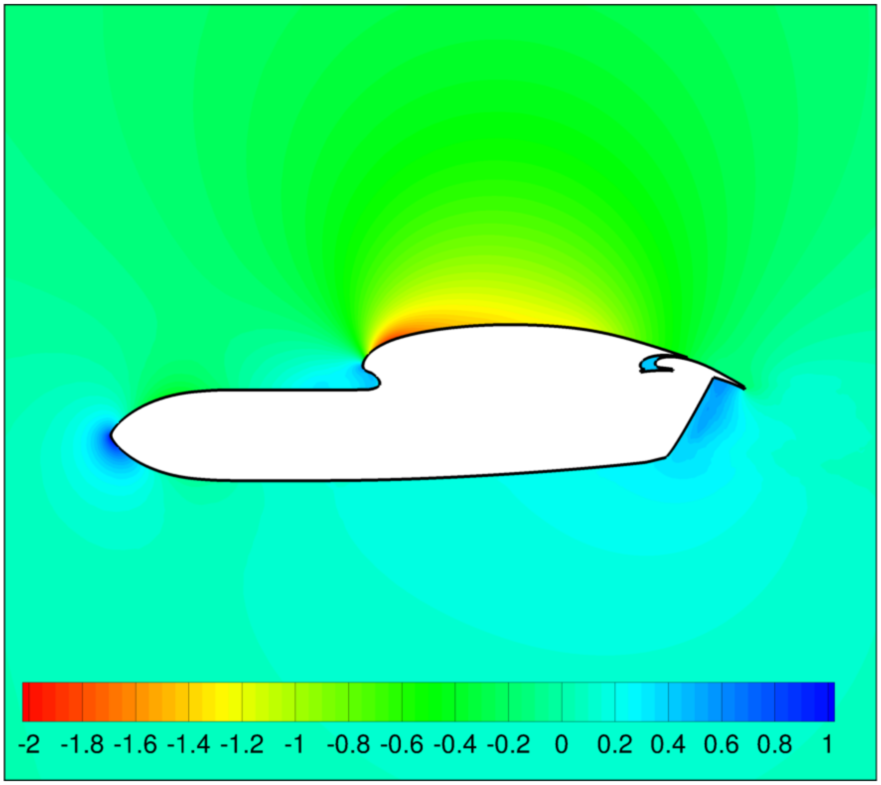

(a) C_p Contours

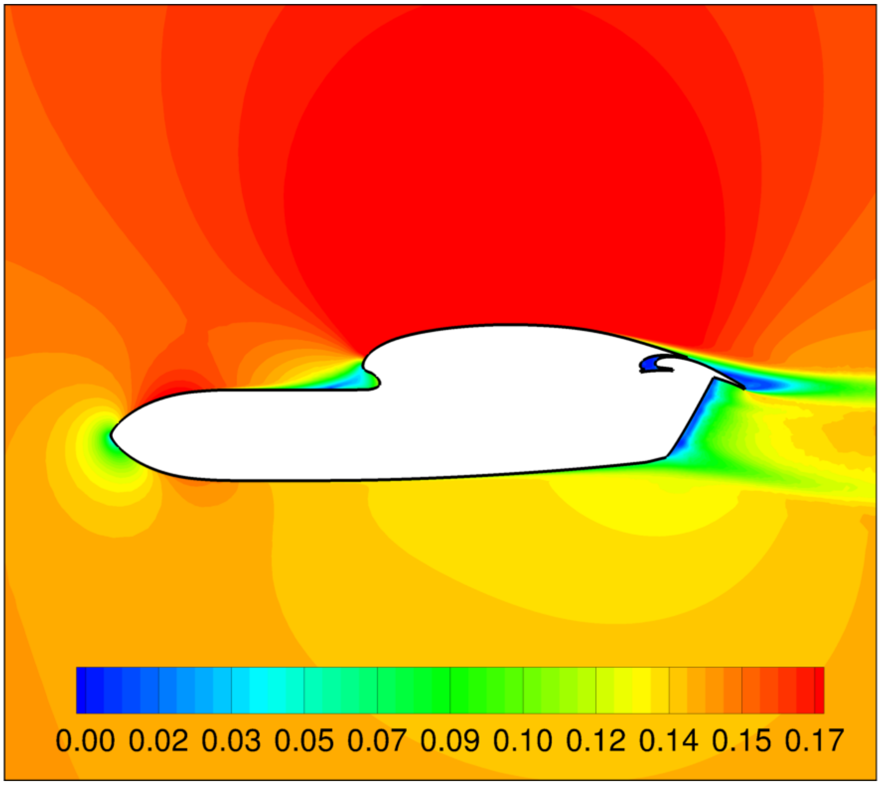

(b) $Mach$ Contours

Figure 150. Pressure Coefficient and Mach Contours at a Span Location of y = 80.34 in. for the Takeoff Configuration at $\alpha = 4°$.

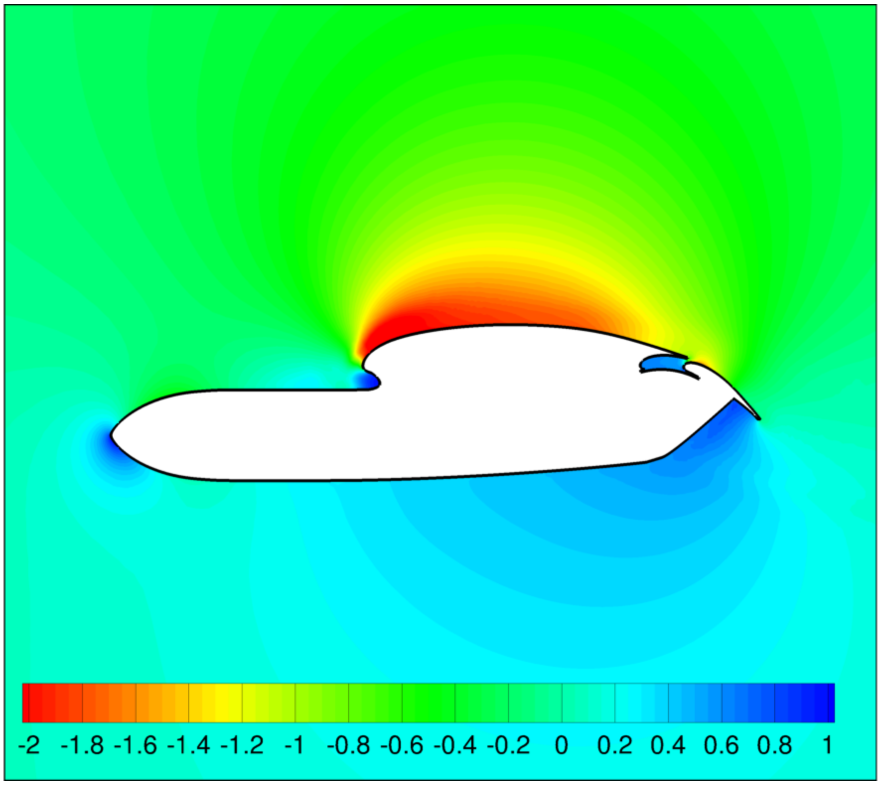

(a) C_p Contours

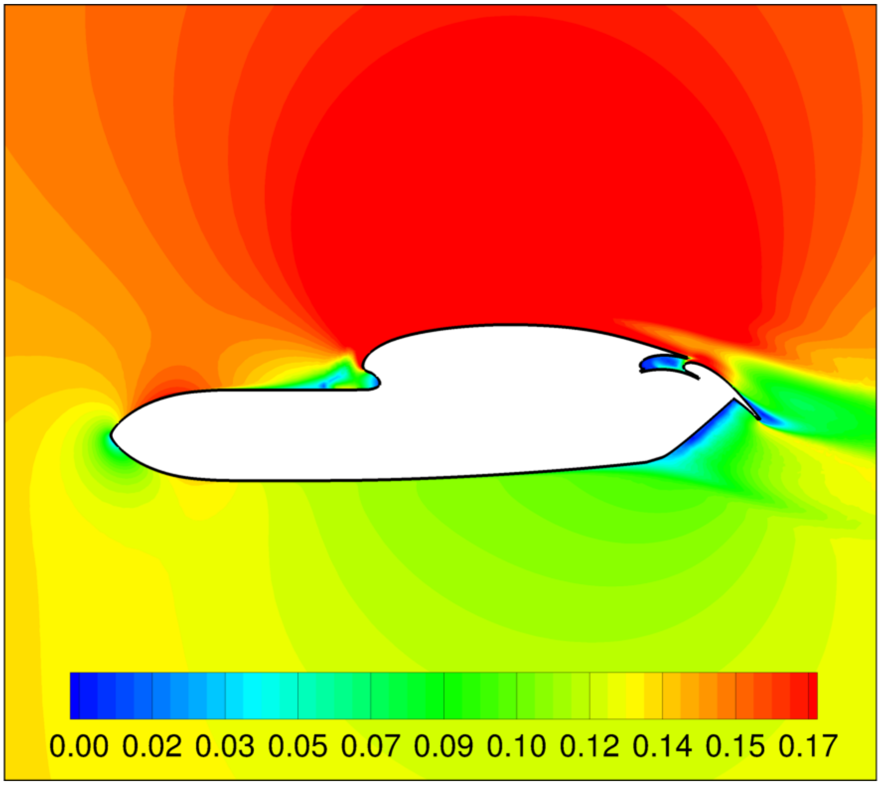

(b) $Mach$ Contours

Figure 151. Pressure Coefficient and Mach Contours at a Span Location of y = 80.34 in. for the Landing Configuration at $\alpha = 4°$.

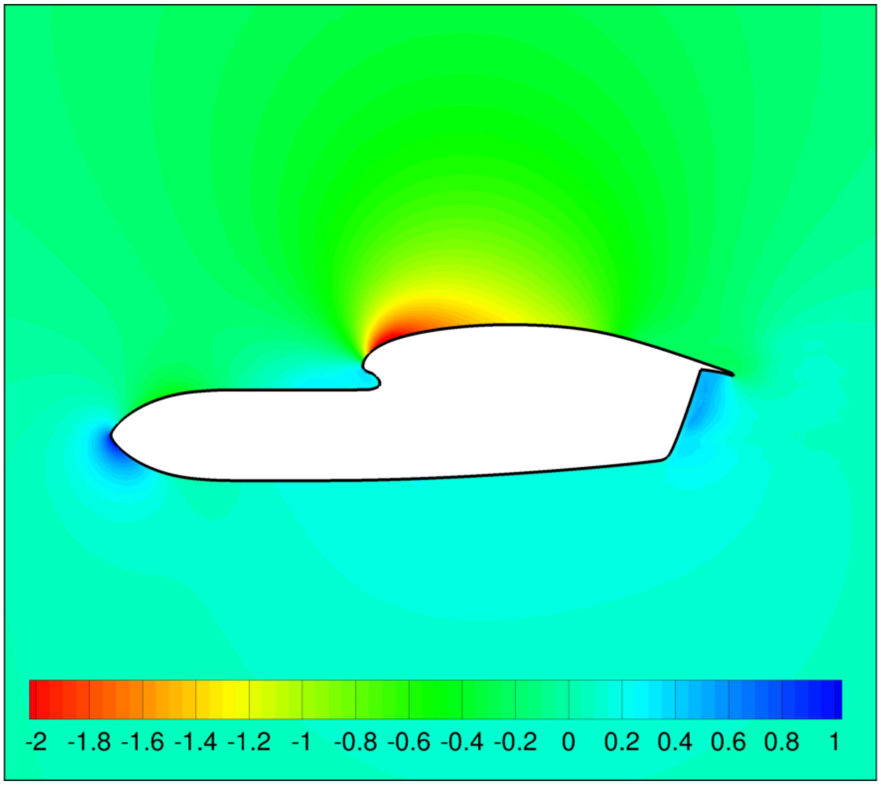

(a) C_p Contours

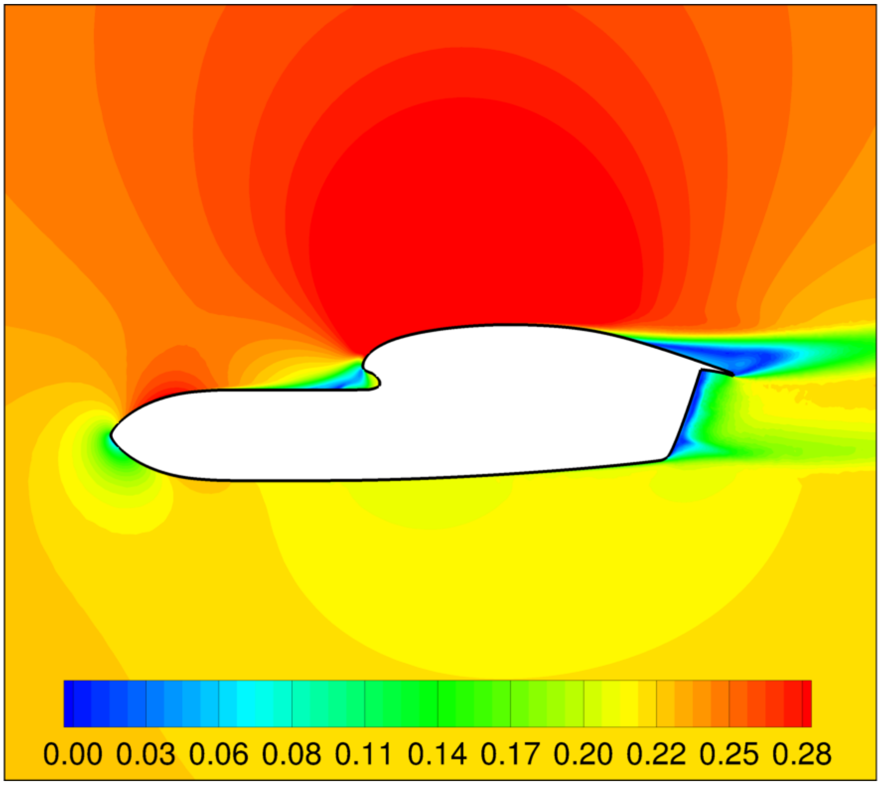

(b) $Mach$ Contours

Figure 152. Pressure Coefficient and Mach Contours at a Span Location of y = 80.34 in. for the Cruise Configuration at $\alpha = 8°$.

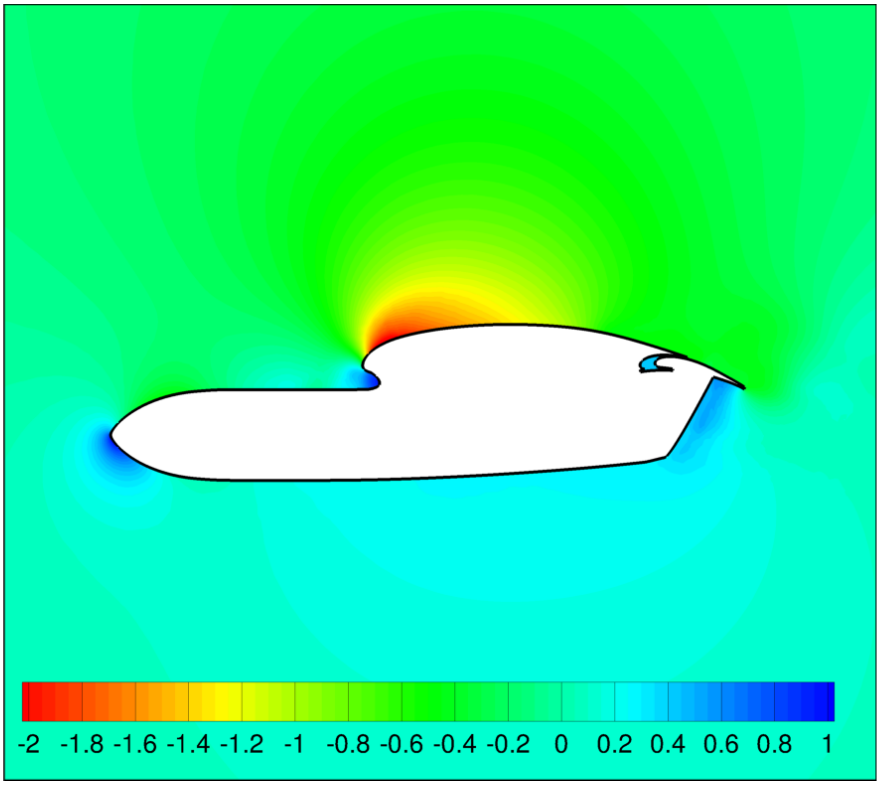

(a) C_p Contours

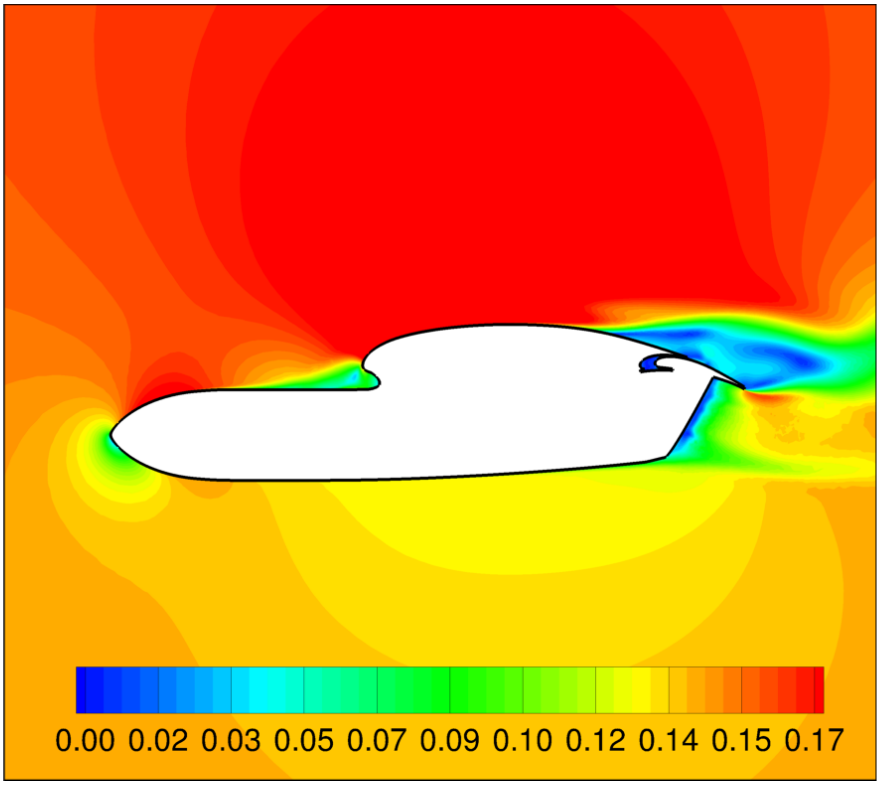

(b) $Mach$ Contours

Figure 153. Pressure Coefficient and Mach Contours at Span Location of y = 80.34 in. for the Takeoff Configuration at $\alpha = 8°$.

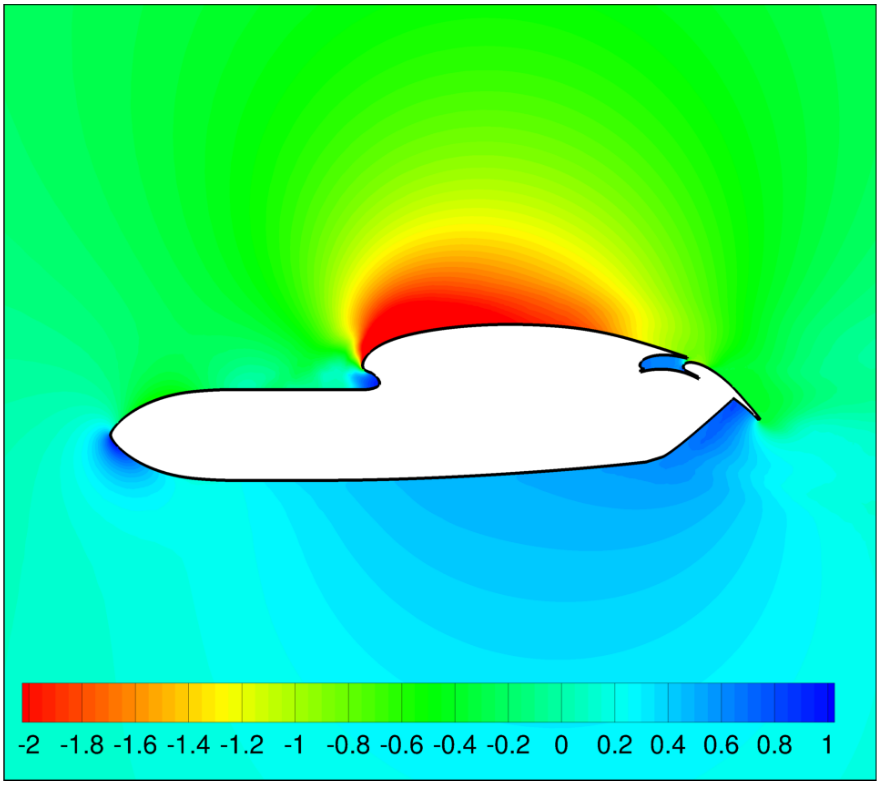

(a) C_p Contours

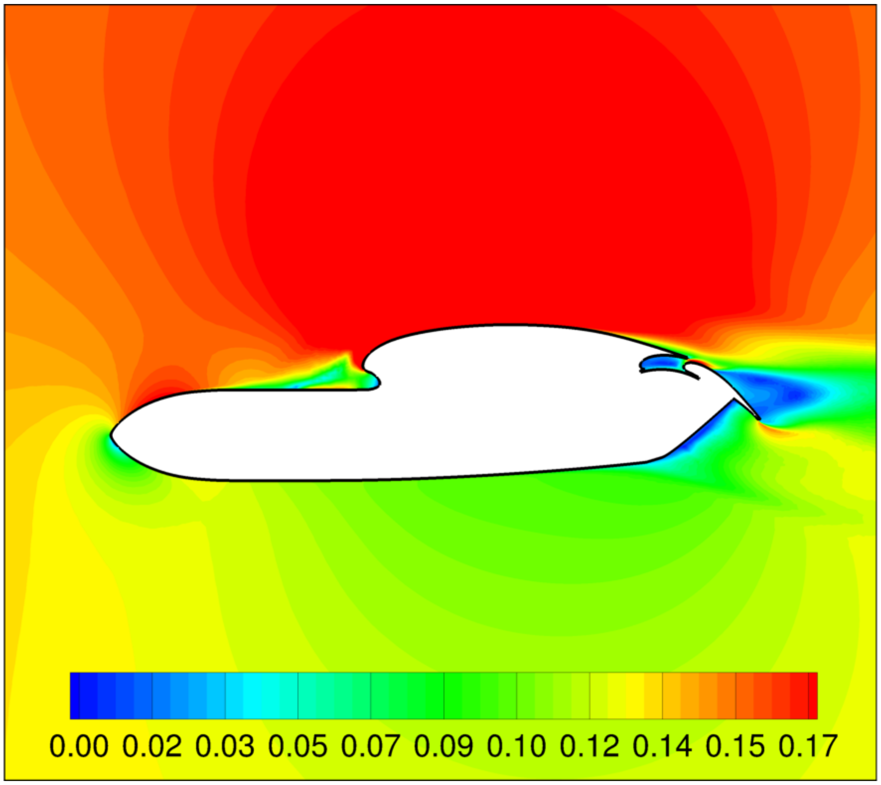

(b) $Mach$ Contours

Figure 154. Pressure Coefficient and Mach Contours at a Span Location of y = 80.34 in. for the Landing Configuration at $\alpha = 8°$.

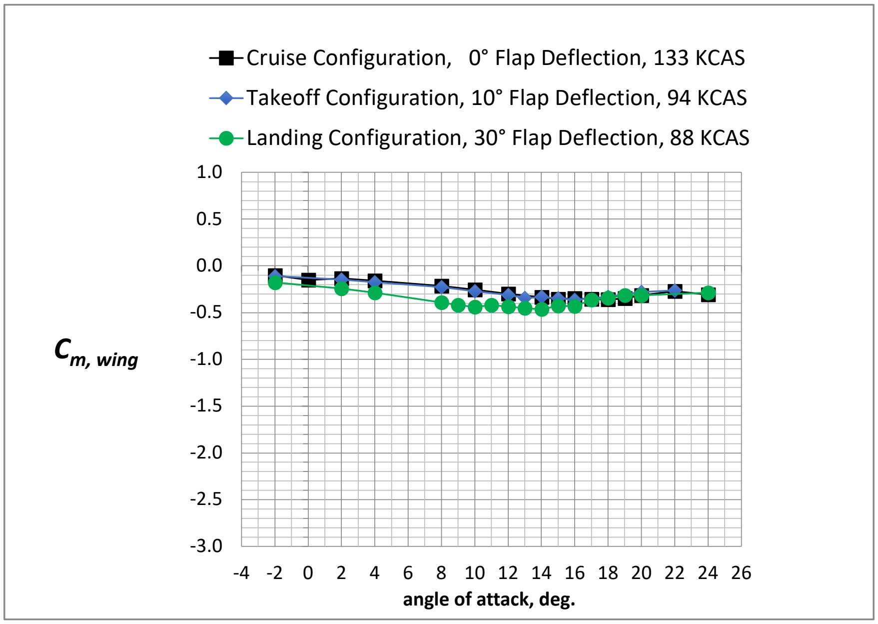

(a) Wing

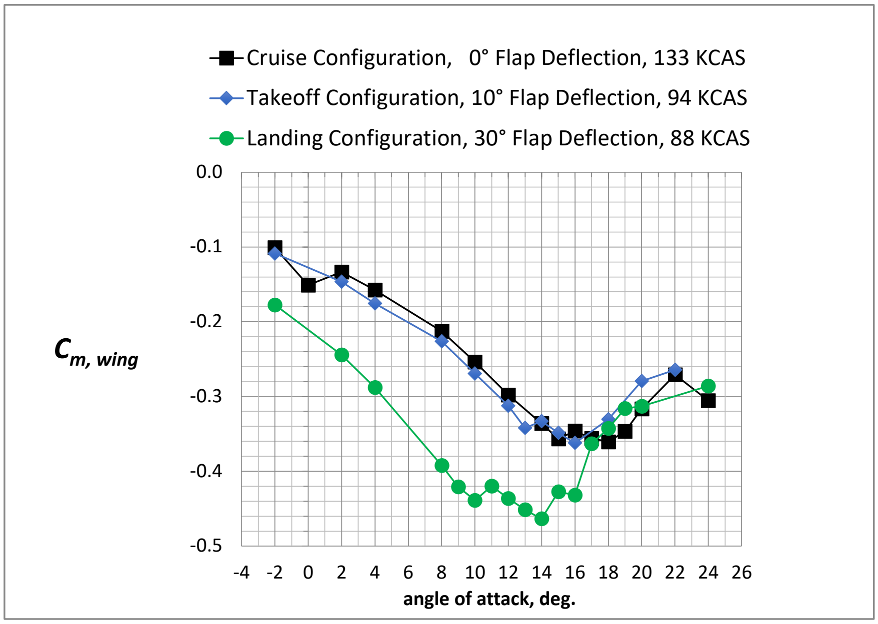

(b) Wing, Expanded Scale

Figure 155. The Effect of Flap Deflection and Airspeed on the Wing Contribution to Pitching Moment Coefficient.

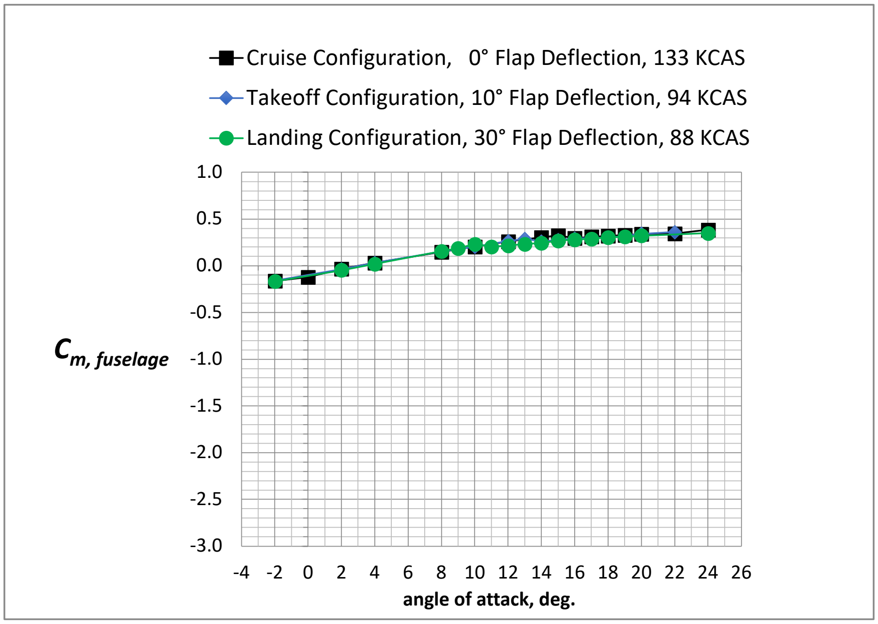

(a) Fuselage

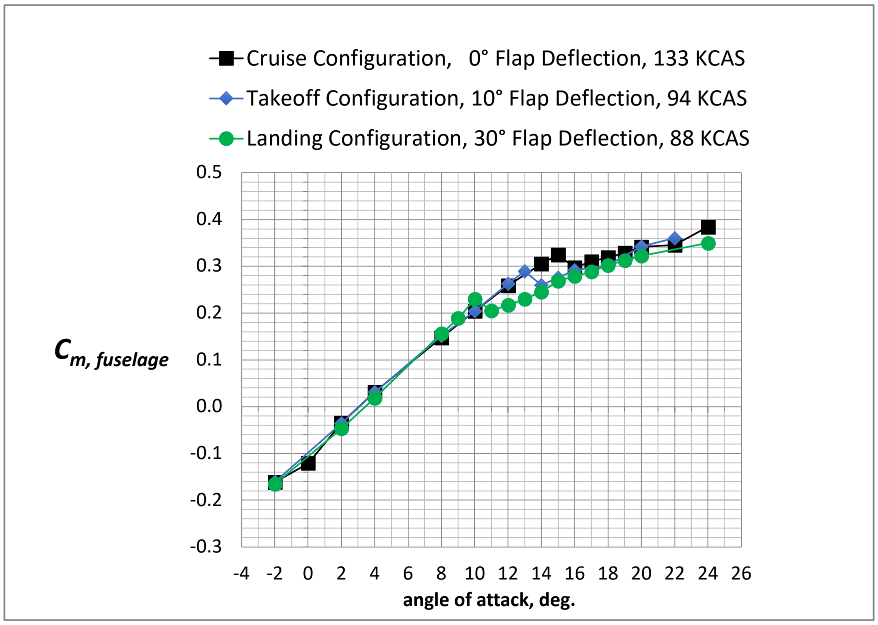

(b) Fuselage, Expanded Scale

Figure 156. The Effect of Flap Deflection and Airspeed on the Fuselage Contribution to Pitching Moment Coefficient.

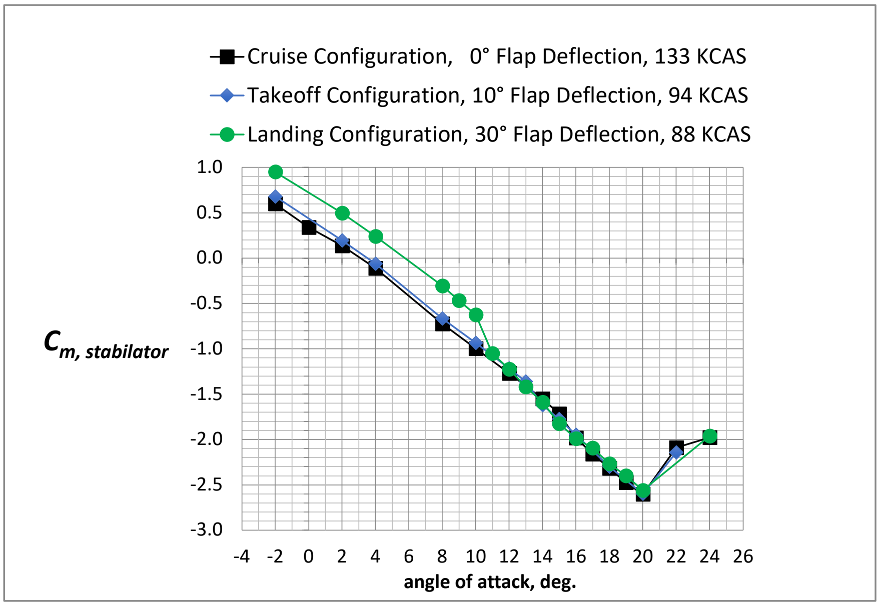

(a) Stabilator

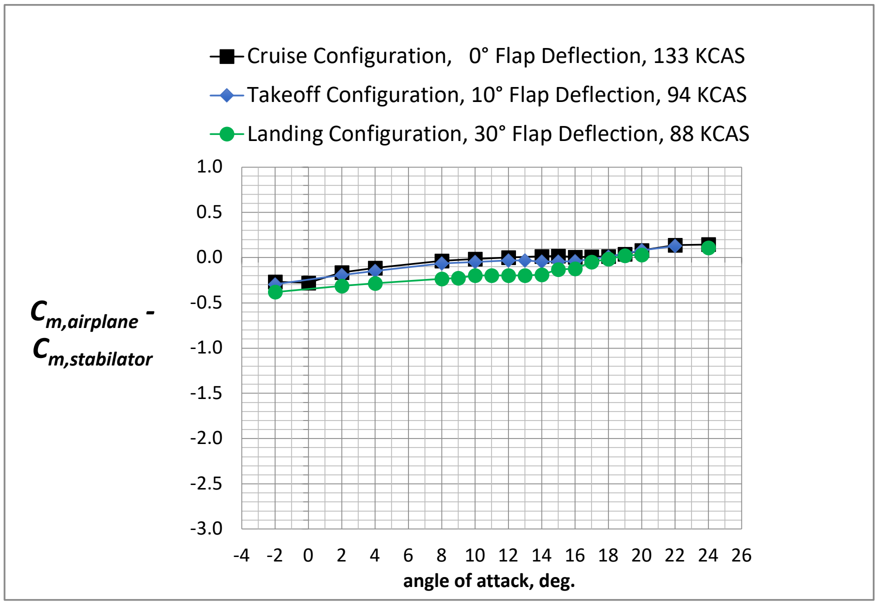

(b) Airplane without the Stabilator Contribution

Figure 157. The Effect of Flap Deflection and Airspeed on the Stabilator Contribution to Pitching Moment Coefficient and on the Airplane Pitching Moment Coefficient without the Contribution from the Stabilator.

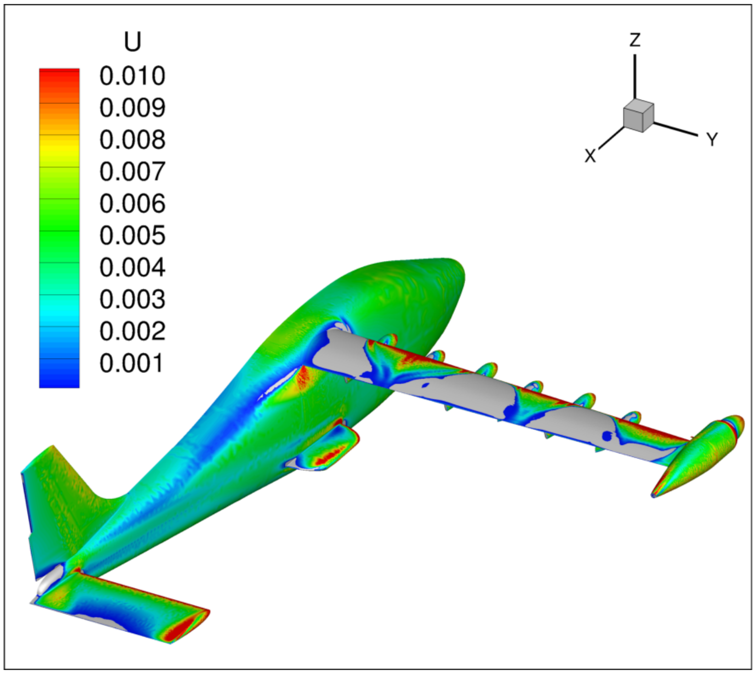

(a) Cruise Configuration at $M = 0.233$ (133 KCAS)

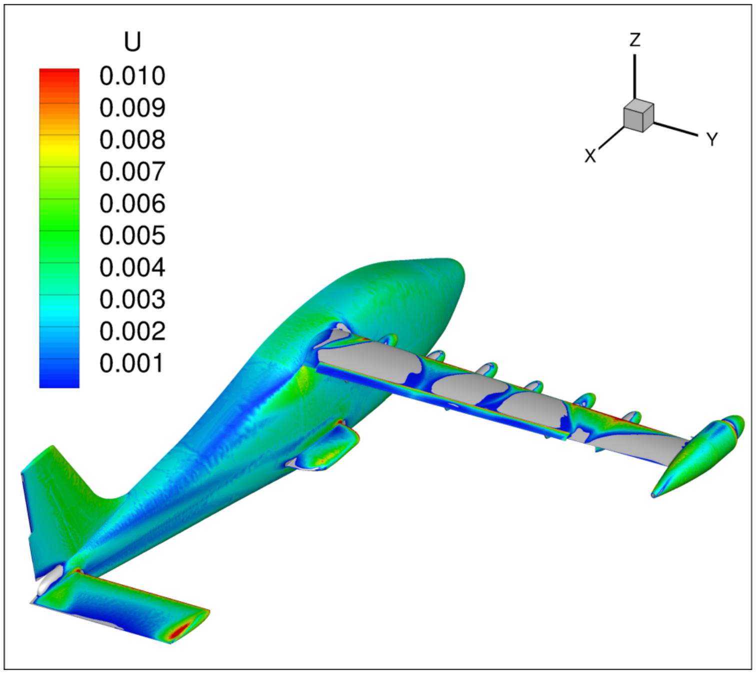

(b) Takeoff Configuration at $M = 0.149$ (94 KCAS)

Figure 158. Comparison of Normalized U Velocity Contours on the Cruise Configuration and the Takeoff Configuration with a 10° Flap Deflection at $\alpha = 20°$.

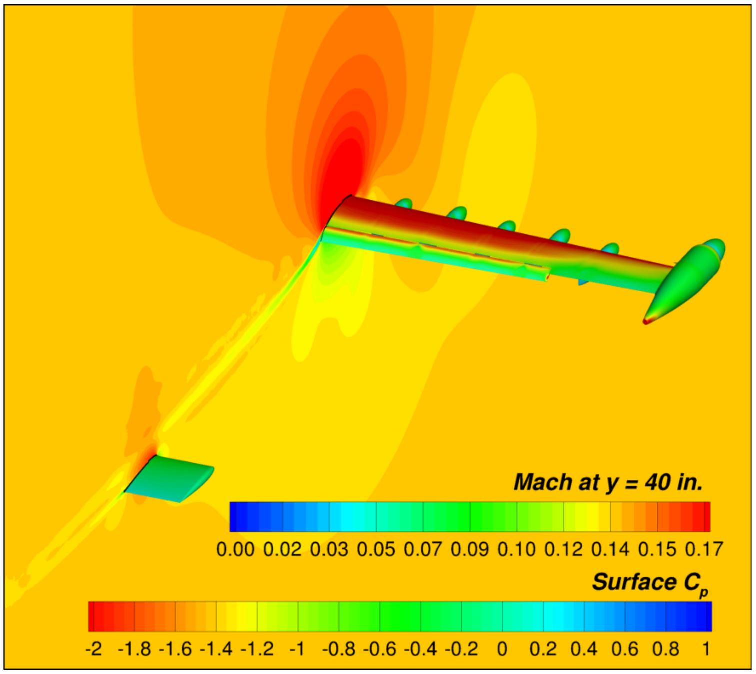

Figure 159. Mach Contours at y = 40 inches and Surface Pressure Coefficient Contours on the Landing Configuration with a 30° Flap Deflection at $M = 0.139$ and $\alpha = 8°$.

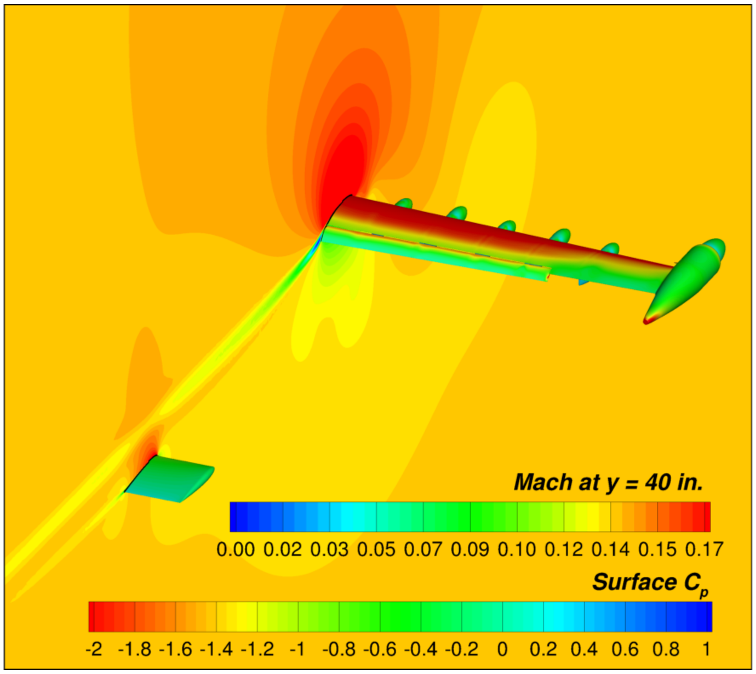

Figure 160. Mach Contours at y = 40 inches and Surface Pressure Coefficient Contours on the Landing Configuration with a 30° Flap Deflection at $M = 0.139$ and $\alpha = 10°$.

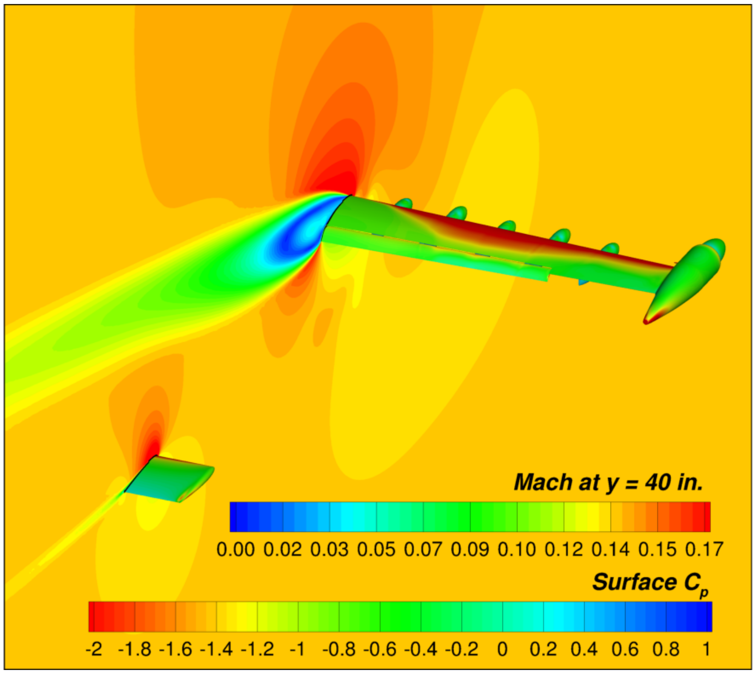

Figure 161. Mach Contours at y = 40 inches and Surface Pressure Coefficient Contours on the Landing Configuration with a 30° Flap Deflection at $M = 0.139$ and $\alpha = 15°$.

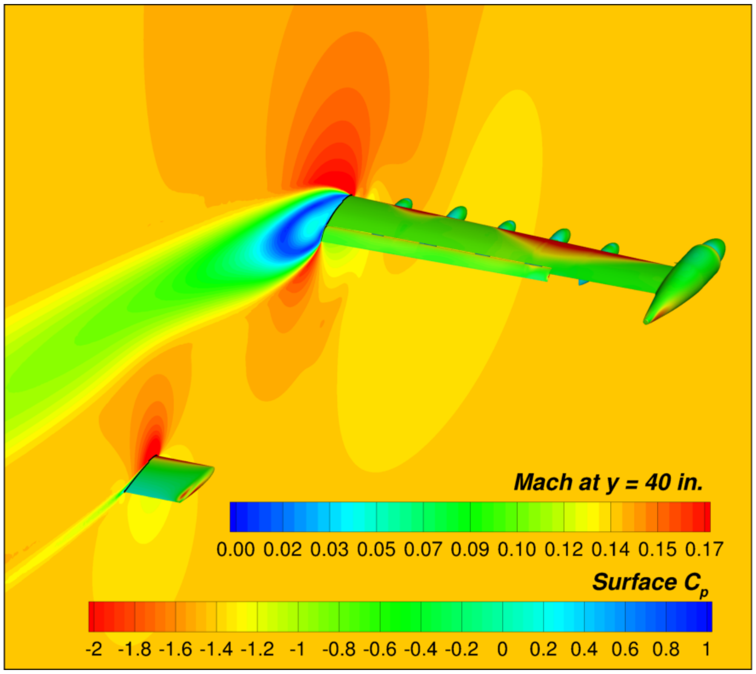

Figure 162. Mach Contours at y = 40 inches and Surface Pressure Coefficient Contours on the Landing Configuration with a 30° Flap Deflection at $M = 0.139$ and $\alpha = 18°$.

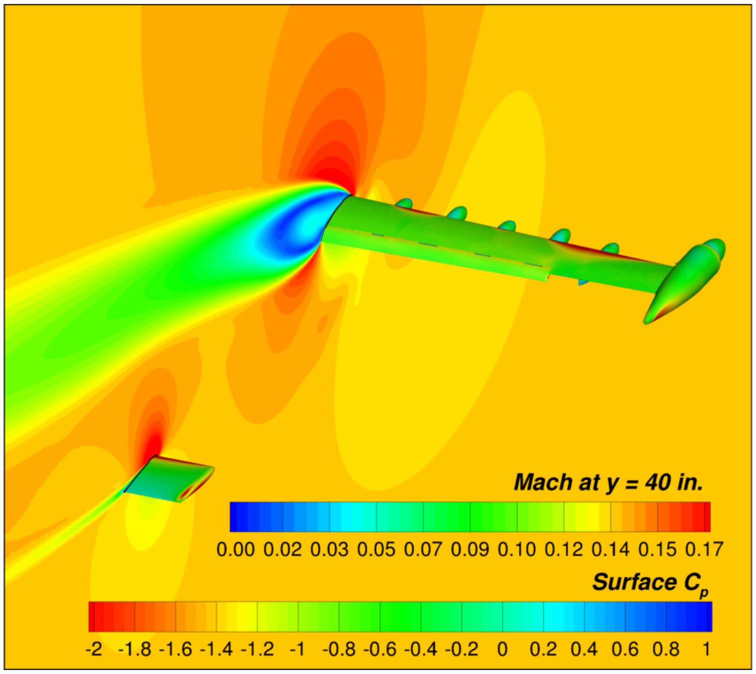

Figure 163. Mach Contours at y = 40 inches and Surface Pressure Coefficient Contours on the Landing Configuration with a 30° Flap Deflection at $M = 0.139$ and $\alpha = 20°$.

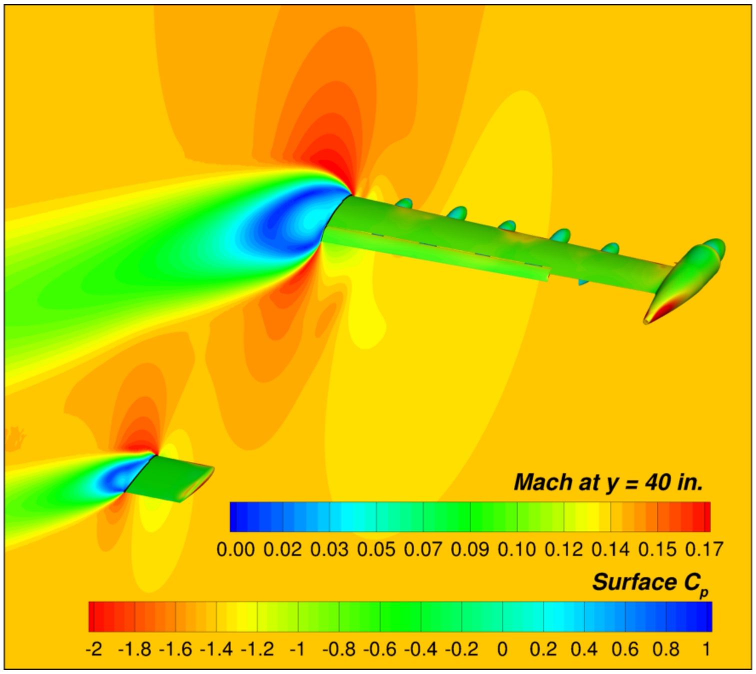

Figure 164. Mach Contours at y = 40 inches and Surface Pressure Coefficient Contours on the Landing Configuration with a 30° Flap Deflection at $M = 0.139$ and $\alpha = 24°$.

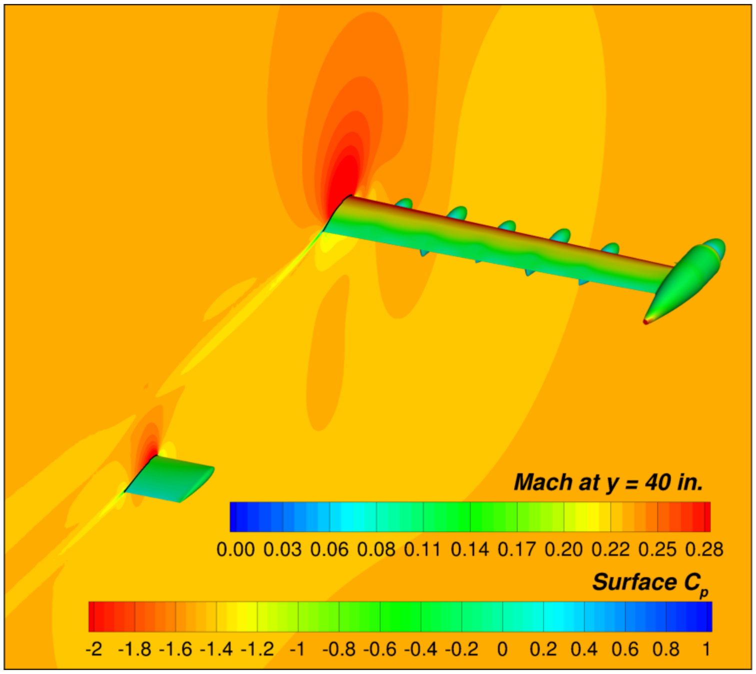

Figure 165. Mach Contours at y = 40 inches and Surface Pressure Coefficient Contours on the Cruise Configuration with No Flap Deflection at $\alpha = 8°$.

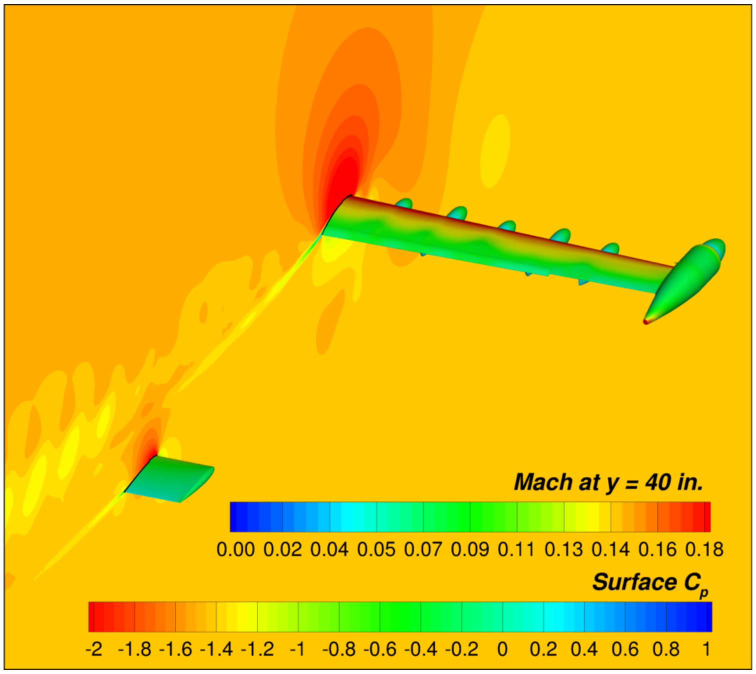

Figure 166. Mach Contours at y = 40 inches and Surface Pressure Coefficient Contours on the Takeoff Configuration with a 10° Flap Deflection at $\alpha = 8°$.

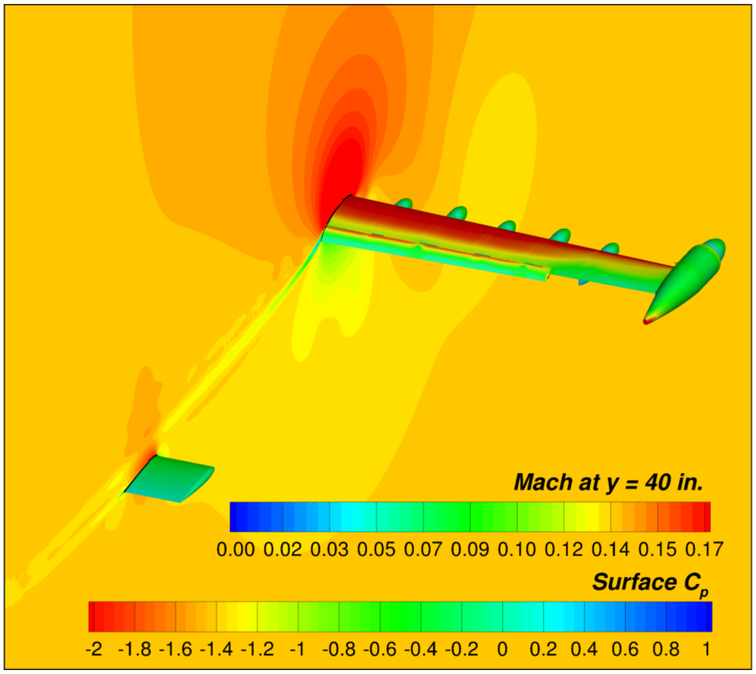

Figure 167. Mach Contours at y = 40 inches and Surface Pressure Coefficient Contours on the Landing Configuration with a 30° Flap Deflection at $\alpha = 8°$.

4 Conclusions

The X-57 Maxwell is an all-electric airplane that implements a distributed electric propulsion system to demonstrate that high-efficiency electric propulsion can be integrated with aerodynamics to increase the performance of an airplane. To this end, distributed electric fans were installed on the wing to provide increased flow over the wing at the low takeoff and landing speeds of the X-57 Maxwell. The low-speed lift augmentation allows for a reduction in wing area for cruise optimization. The wing area of the X-57 Maxwell was reduced to 42 percent of the wing area of the baseline aircraft, a Tecnam P2006T. With this reduced wing area and the electric propulsion system, it is estimated that the X-57 Maxwell will cruise on less than one-third the total energy compared to the baseline aircraft. To meet the cruise performance goal at a Mach number of 0.233 (150 KTAS) and at an altitude of 8000 feet, the X-57 Maxwell has a cruise lift coefficient of 0.7516 and needs to have a cruise drag coefficient of 0.05423 or less.

Three primary configurations were investigated in this study; a cruise configuration with all control surfaces neutral, a takeoff configuration with a 10° flap deflection, and a landing configuration with a 30° flap deflection. The USM3D computational solver was used to investigate the performance of these three preliminary X-57 configurations, without the distributed electric propulsion high-lift system operating. The unpowered X-57 airplane performance is of interest to quantify if the X-57 Maxwell can meet the cruise drag performance goal, and to document the lift performance of the very small wing at takeoff and landing conditions. At the cruise lift coefficient of 0.7516, the computed drag coefficient is 0.05275. This computed drag is less than the drag coefficient of 0.05423 that is required to meet the X-57 airplane performance goal. However, the computational airplane is a completely smooth geometry and does not account for protuberance drag, nor the drag from steps and gaps in the actual X-57 airplane. Therefore, based upon the CFD drag calculation there is a 10-percent margin to account for some of the differences between the as-built metal fuselage and empennage construction, and the smooth computational geometry. The computed cruise drag also does not account for an induced drag reduction due to the wing-tip propellers and a drag reduction due to laminar flow achieved on the wing.

The conditions for the cruise configuration were a flight unit Reynolds number of 1.32E+06, an altitude of 8000 feet, a Mach number of 0.233 (133 KEAS, 150 KTAS), and angles of attack from $-2°$ to 24°. The maximum lift coefficient for the cruise configuration was $C_{L,max} = 2.13$ at $\alpha = 15°$. The lift coefficient dropped at $\alpha = 16°$ due to wing root flow separation. However, the airplane lift coefficient increased back to $C_L = 2.12$ at $\alpha = 18°$ because the lift continued to increase on the stabilator and fuselage. The computed lift to drag ratio was $L/D_{max} = 14.14$ at the cruise lift coefficient of $C_L = 0.7516$, and the maximum computed lift to drag ratio was $L/D_{max} = 15.8$.

The conditions for the takeoff configuration with a 10° flap were a flight unit Reynolds number of 0.986E+06 per foot, an altitude of 2500 feet, a Mach number of 0.149 (94 KEAS, 97.5 KTAS), and angles of attack from $-2°$ to 22°. The airplane lift coefficient for the takeoff configuration was $C_L = 2.16$ at $\alpha = 13°$, but lift dropped at $\alpha = 14°$ due to wing root flow separation. Then the airplane lift coefficient increased back to $C_{L,max} = 2.21$ at $\alpha = 16°$ because the lift continued to increase on the stabilator and fuselage.

The conditions for the landing configuration with a 30° flap deflection were a flight unit Reynolds number of 0.922E+06 per foot, an altitude of 2500 feet, a Mach number of 0.139 (88 KEAS, 91.3 KTAS), and angles of attack from $-2°$ to 24°. The maximum lift coefficient for the landing configuration was $C_{L,max} = 2.58$ at $\alpha = 10°$ and at $\alpha = 14°$. The airplane lift coefficient dropped at $\alpha = 11°$ due to wing root flow separation, but then airplane lift coefficient increased back to $C_L = 2.58$ at $\alpha = 14°$ because the lift continued to increase on the stabilator and fuselage even though wing lift plateaued. Based on the unpowered maximum lift coefficient of 2.58 for the 30° flap deflection, along with computations of the distributed electric propulsion lift augmentation (not shown in this paper), the X-57 Maxwell airplane will meet its powered landing goal of a maximum lift coefficient of 4.0.

The USM3D results were compared to results from LAVA and STAR-CCM+ solutions published in Ref. [12]. The lift coefficients for the three codes compared well for the cruise configuration at an angle of attack of 8°; USM3D is $C_L = 1.514$, LAVA is $C_L =$1.569, and STAR-CCM+ is $C_L = 1.570$. All three codes predicted similar streamline patterns with small, triangular-shaped, flow separation regions downstream of the high-lift nacelles. The USM3D lift coefficient for the takeoff configuration was $C_L =$1.670 at $\alpha = 8°$, which was lower than LAVA ($C_L =$1.836) and STAR-CCM+ ($C_L = 1.865$) due to the triangular-shaped flow separation regions that were present on the wing downstream of all but one high-lift nacelle. There was only one region of flow separation downstream of the furthest outboard high-lift nacelle in the LAVA and STAR-CCM+ solutions. Finally, the USM3D lift coefficient compared well with LAVA and STAR-CCM+ for the landing configuration up to $\alpha = 10°$. The lift coefficients at $\alpha = 10°$ were $C_L = 2.579$ (USM3D), $C_L = 2.688$ (LAVA), and $C_L = 2.6440$ (STAR-CCM+). The large difference in lift at $\alpha = 11°$ is a result of the difference between the geometry at the fuselage-wing-root region, since the LAVA and STAR-CCM+ codes used a scaled up version of a wind tunnel model that was different at the wing root than the VSP geometry used for the USM3D solutions.

References

1. Borer, N. K.; Patterson, M. D.; Viken, J. K.; Moore, M. D.; Clarke, S.; Redifer, M. E.; Christie, R. J.; Stoll, A., Dubois, A.; Bevirt, J.; and Gibson, A. R., Foster, T. J.; and Osterkamp, P. G.: Multidimensional Design and Performance of the NASA SCEPTOR Distributed Electric Propulsion Flight Demonstrator. AIAA 2016-3920, June 2016.

2. Patterson, M. D.; Derlaga, J. M.; and Borer, N. K.: High-Lift Propeller System Configuration Selection for NASA's SCEPTOR Distributed Electric Propulsion Flight Demonstrator. 16th AIAA Aviation Technology, Integration, and Operations Conference. AIAA 2016-3922, June 2016.

3. Borer, N. K.; Patterson, M. D.; Derlaga, J. M.; Litherland, B. L.; Deere, K. A.; and Stoll, A.: Flight Performance Maneuver Planning for NASA's X-57 "Maxwell" Flight Demonstrator-Part 1: Power-off Glides. AIAA Aviation 2019 Forum. AIAA 2019-2855, June 2019.

4. Borer, N. K.; Patterson, M. D.; Derlaga, J. M.; Litherland, B. L.; Deere, K. A.; and Stoll, A.: Comparison of Mixed-Order Aero-Propulsive Performance Predictions for Distributed Electric Propulsion Configurations. Invited paper for AIAA Transformational Flight Program Committee. AIAA 2016-3981, June 2016.

5. Borer, N. K.; Derlaga, J. M.; Deere, K. A.; Carter, M. B.; Viken, S. A.; Patterson, M. D.; Litherland, B. L.; and Stoll, A.: Comparison of Aero-Propulsive Performance Predictions for Distributed Electric Propulsion Configurations. Invited paper for AIAA Transformational Flight Program Committee. AIAA 2017-0209, January 2017.

6. Viken, J. K.; Viken, S. A.; Deere, K. A.; and Carter, M. B.; Design of the Cruise and Flap Airfoil for the X-57 Maxwell Distributed Electric Propulsion Aircraft. Aviation Forum 2017, 35th AIAA Applied Aerodynamics Conference, AIAA 2017-3922, June 2017.

7. Deere, K. A.; Viken, J. K.; Viken, S. A.; Carter, M. B.; Wiese, M. R.; and Farr, N. L.: Computational Analysis of a Wing Designed for the X-57 Distributed Electric Propulsion Aircraft. Aviation Forum 2017, 35th AIAA Applied Aerodynamics Conference, AIAA 2017-3923, June 2017.

8. Deere, K. A.; Viken, S. A.; Carter, M. B.; Viken, J. K.; Derlaga, J. M.; and Stoll, A.: Comparison of High-Fidelity Computational Tools for Wing Design of a Distributed Electric Propulsion Aircraft. Aviation Forum 2017, 35th AIAA Applied Aerodynamics Conference, AIAA 2017-3925, June 2017.

9. Deere, K. A.; Viken, S. A.; Carter, M. B.; Viken, J. K.; Wiese, M. R.; and Farr, N. L.: Computational Analysis of Powered Lift Augmentation for the LEAPTech Distributed Electric Propulsion Wing. Aviation Forum 2017, 35th AIAA Applied Aerodynamics Conference, AIAA 2017-3921, June 2017.

10. Deere, K. A.; Viken, J. K.; Viken, S. A.; Carter, M. B.; Cox, D.; Wiese, M. R.; and Farr, N. L.: Computational Component Build-up for the X-57 Distributed Electric Propulsion Aircraft. SciTech AIAA, AIAA 2018-1275, January 2018.

11. van der Meer, S.; and Veldhuis, L.: Numerical Assessment of Directional Stability and Control with Tip-mounted Propellers. Master's Thesis at the Delft University of Technology, January 24, 2020.

12. Yoo, S. Y.; and Duensing, J. C.: Computational Analysis of the External Aerodynamics of the Unpowered X-57 Mod-III Aircraft. Aviation Forum 2019, AIAA 2019-3698, June 2019.

13. Frink, N. T.; Pirzadeh, S. Z.; Parikh, P. C.; Pandya, M. J.; and Bhat, M. K.: The NASA Tetrahedral Unstructured Software System. The Aeronautical Journal, Vol. 104, No. 1040, October 2000, pp. 491–499.

14. Samareh, J.: GridTool: A Surface Modeling and Grid Generation Tool. Proceedings of the Workshop on Surface Modeling, Grid Generation, and Related Issues in CFD Solutions, NASA CP–3291, May 9–11, 1995.

15. Pao, S. P.: USMC6-TetrUSS Grid and Solution Cutter: A Brief Users' Guide. Version 4, NASA Langley Research Center. October 2008.

16. Helden Aerospace Inc.: https://heldenaero.com/heldenmesh/.

17. Ratnayake, N. A.; Krist, S. E.; Ghaffari, F.; and Ahmed, V.: Unstructured Grid Development for the Space Launch System Liftoff and Transition Lineloads Computational Analysis. AIAA SciTech Forum, AIAA2020-0672, January 2020.

18. Hahn, A.: Open Vehicle Sketch Pad Aircraft Modeling Strategies. 51st AIAA Aerospace Sciences Meeting including the New Horizons Forum and Aerospace Exposition. 2013.

19. Belben, J. B.; McDonald, R. A..: Enabling Rapid Conceptual Design Using Geometry-Based Multi-Fidelity Models in VSP. 51st AIAA Aerospace Sciences Meeting, AIAA2013-0328, January 2013.

20. Pirzadeh, S.: Unstructured Viscous Grid Generation by Advancing Layers Method. AIAA Journal, Vol. 32, No. 8, pp. 1735–1737, August 1994.

21. Pirzadeh, S.: Structured Background Grids for Generation of Unstructured Grids by Advancing Front Method. AIAA Journal, Vol. 31, No. 2, pp. 257–265, February 1993.

22. https://hiliftpw.larc.nasa.gov/Workshop2/GriddingGuidelines-HiLiftPW2-v2.pdf. March 2013.

23. Abdol-Hamid, K. S.; Frink, N. T.; Deere, K. A.; and Pandya, M. J.: Propulsion Simulations Using Advanced Turbulence Models with the Unstructured-Grid CFD Tool, TetrUSS. AIAA 2004-0714, January 2004.

24. Spalart, P. R.; and Allmaras, S. R.: A One-Equation Turbulence Model for Aerodynamic Flows. Recherché, No. 1, 1994, pp. 5-21.

25. Spalart, P. R.: "Strategies for Turbulence Modeling and Simulation," International Journal of Heat and Fluid Flow, Vol. 21, 2000, pp. 252-263.

Appendix A

Convergence: Cruise Configuration

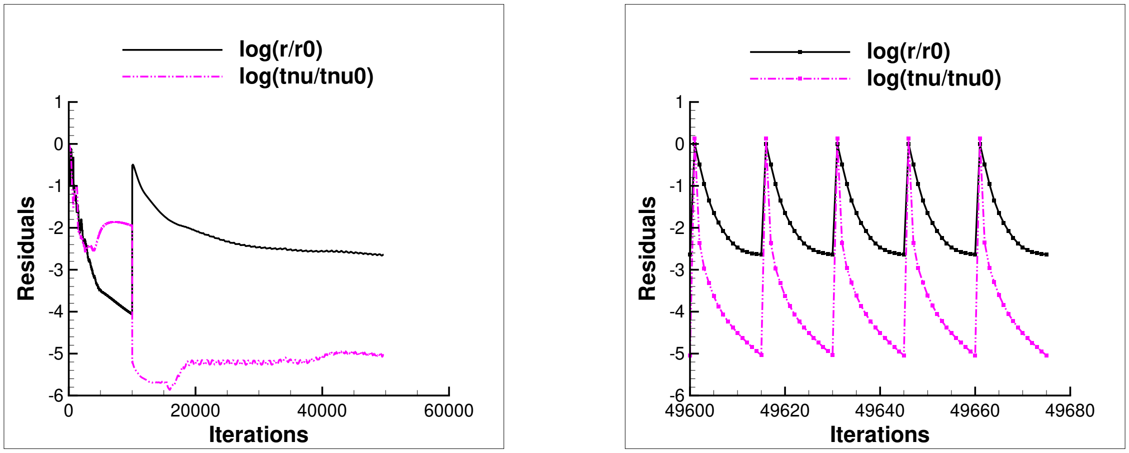

(a) Residuals (b) SubIterations Residuals

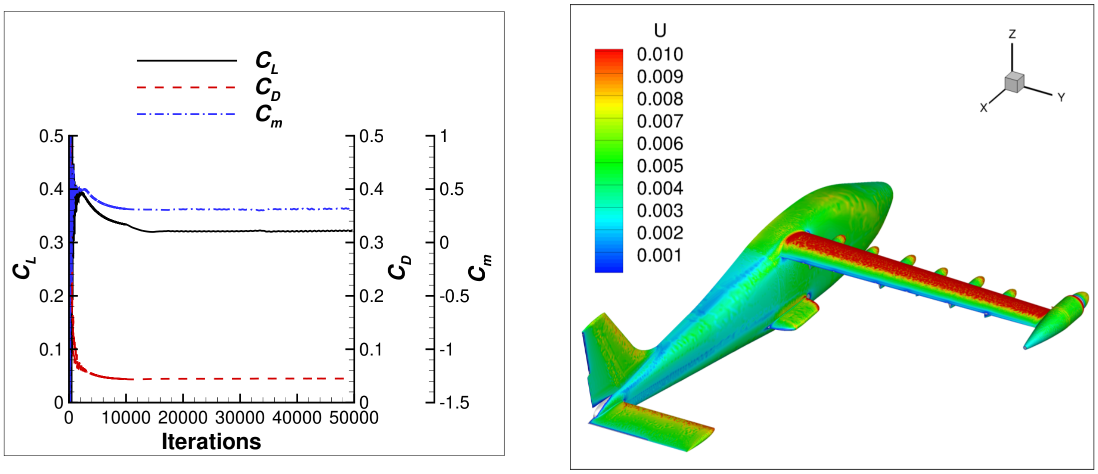

(c) Force and Moment Coefficients (d) Normalized U Velocity Contours

Figure A168. The Convergence History Data and Normalized U Velocity Contours for the Cruise Configuration at $M = 0.233$ and $\alpha = -2°$, No Cruise Power, and No High-Lift Blowing.

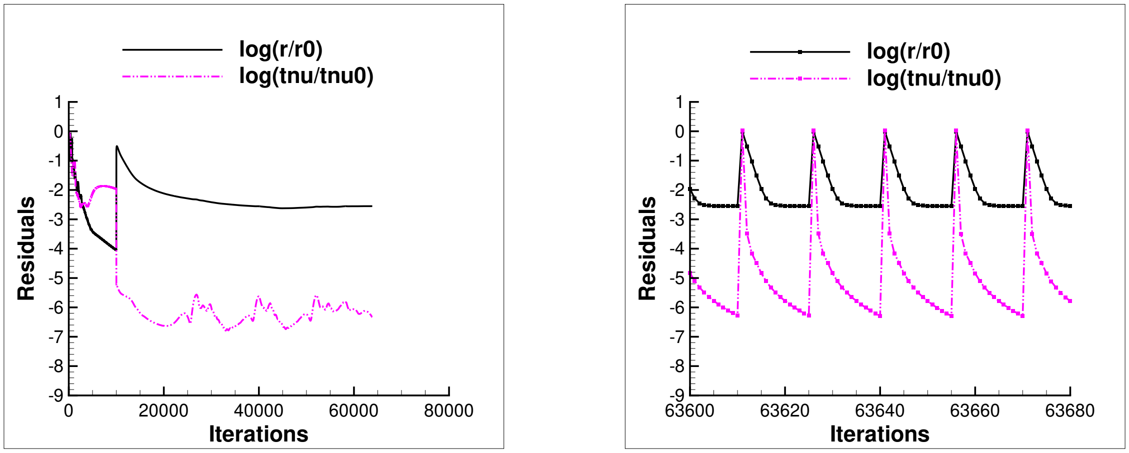

(a) Residuals (b) SubIterations Residuals

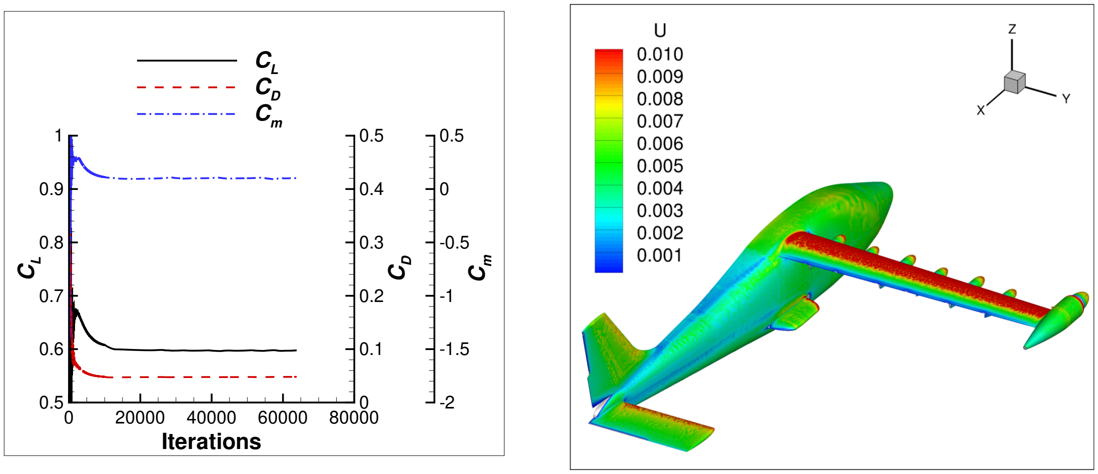

(c) Force and Moment Coefficients (d) Normalized U Velocity Contours

Figure A169. The Convergence History Data and Normalized U Velocity Contours for the Cruise Configuration at $M = 0.233$ and $\alpha = 0°$, No Cruise Power, and No High-Lift Blowing.

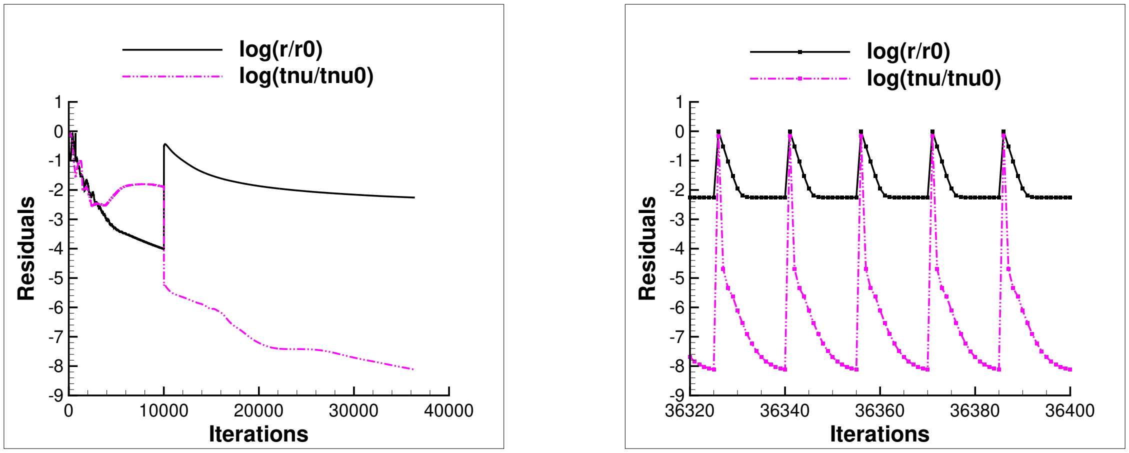

(a) Residuals

(b) SubIterations Residuals

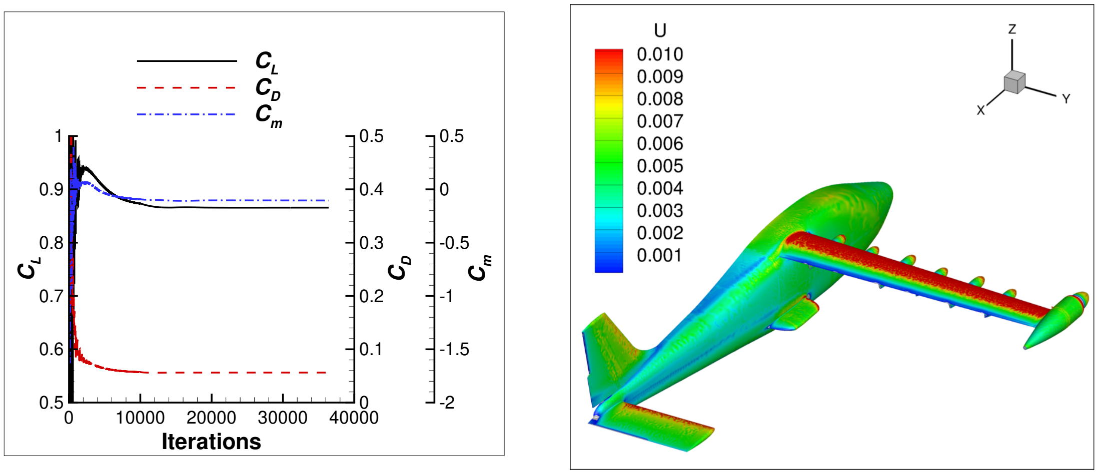

(c) Force and Moment Coefficients

(d) Normalized U Velocity Contours

Figure A170. The Convergence History Data and Normalized U Velocity Contours for the Cruise Configuration at $M = 0.233$ and $\alpha = 2°$, No Cruise Power, and No High-Lift Blowing.

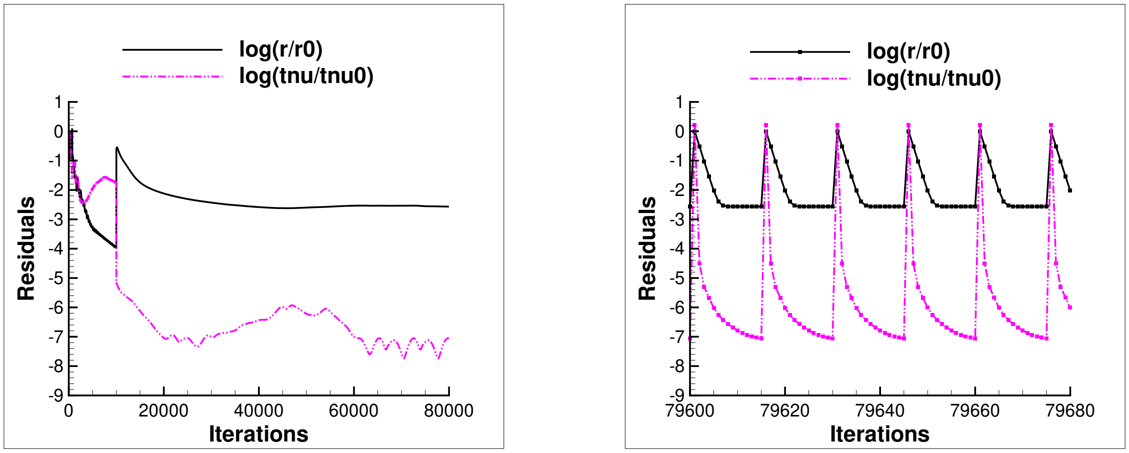

(a) Residuals

(b) SubIterations Residuals

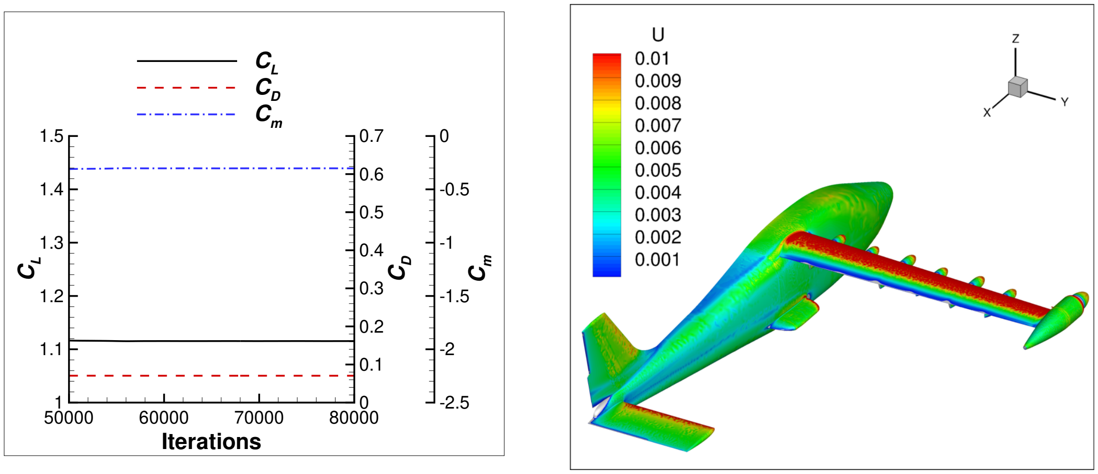

(c) Force and Moment Coefficients

(d) Normalized U Velocity Contours

Figure A171. The Convergence History Data and Normalized U Velocity Contours for the Cruise Configuration at $M = 0.233$ and $\alpha = 4°$, No Cruise Power, and No High-Lift Blowing.

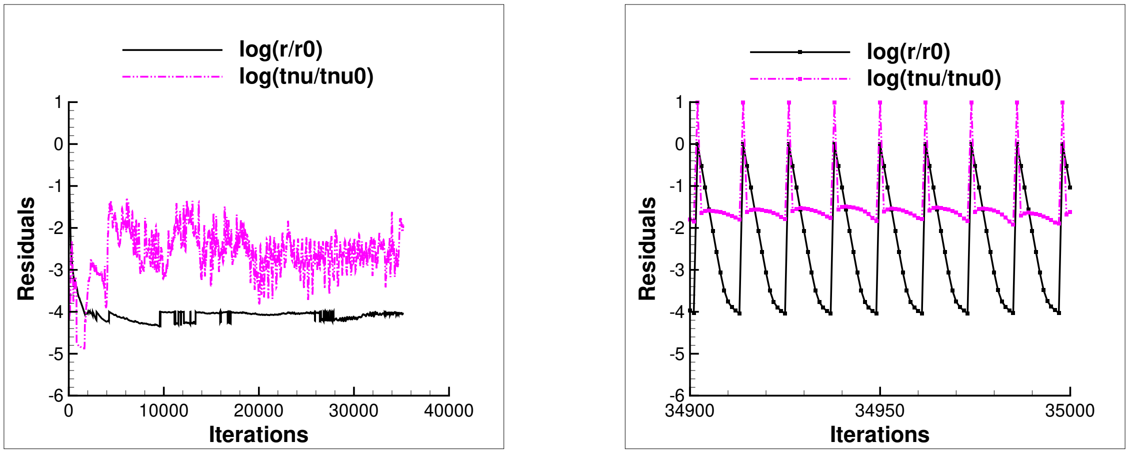

(a) Residuals (b) SubIterations Residuals

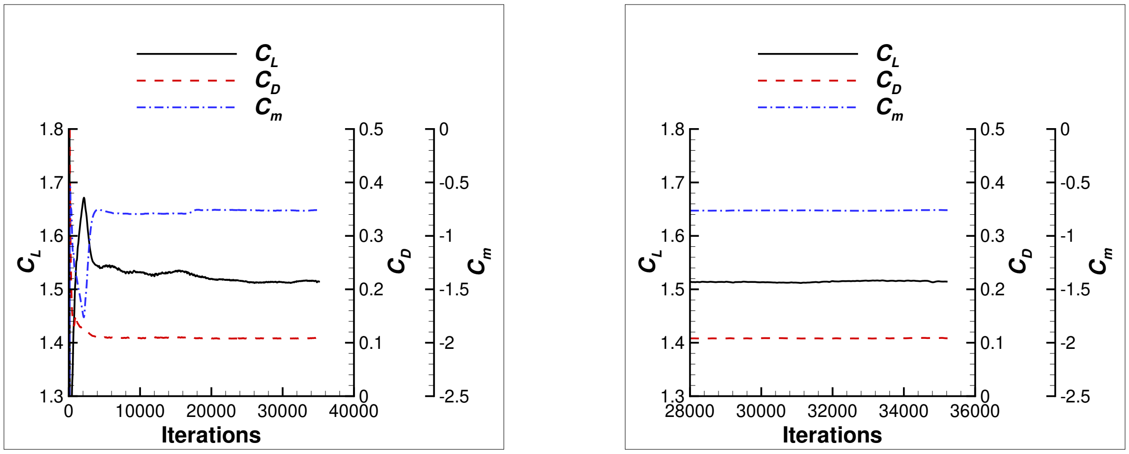

(c) Force and Moment Coefficients (d) Coefficients with a Smaller Iteration Range

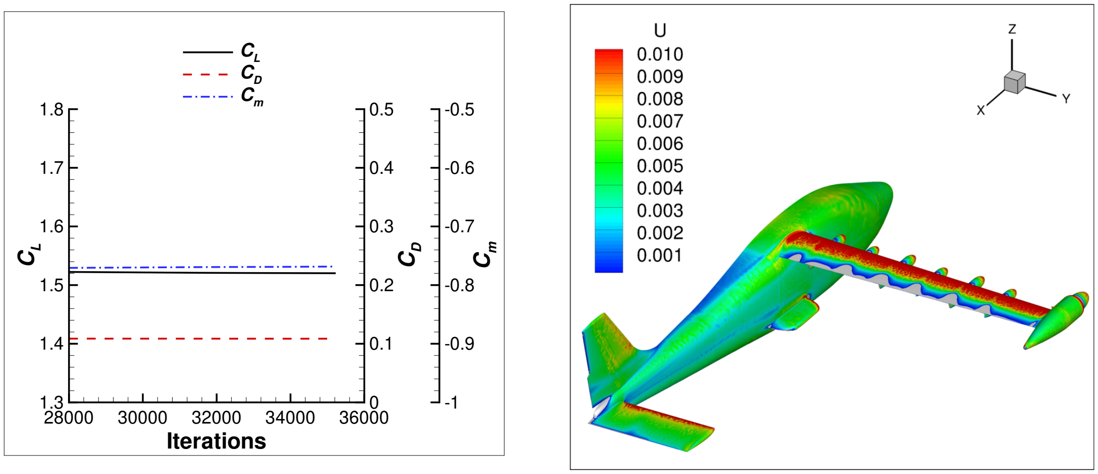

(e) Time-Averaged Coefficients (f) Normalized U Velocity Contours

Figure A172. The Convergence History Data and Normalized U Velocity Contours for the Cruise Configuration at $M = 0.233$ and $\alpha = 8°$, No Cruise Power, and No High-Lift Blowing.

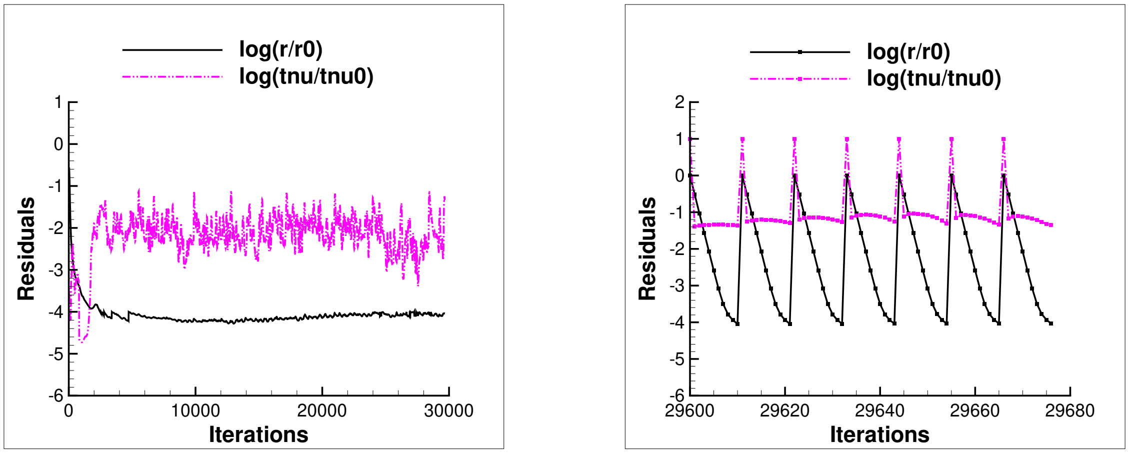

(a) Residuals (b) SubIterations Residuals

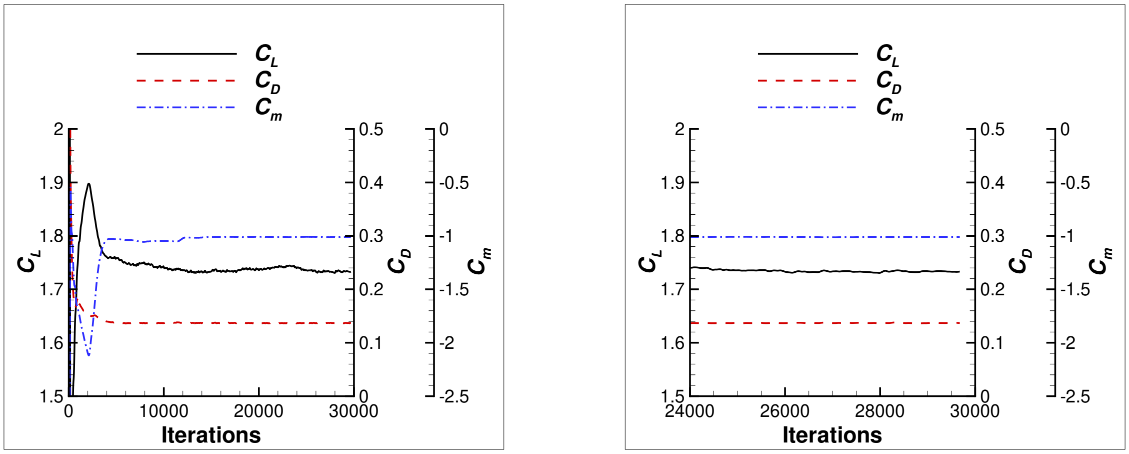

(c) Force and Moment Coefficients (d) Coefficients with a Smaller Iteration Range

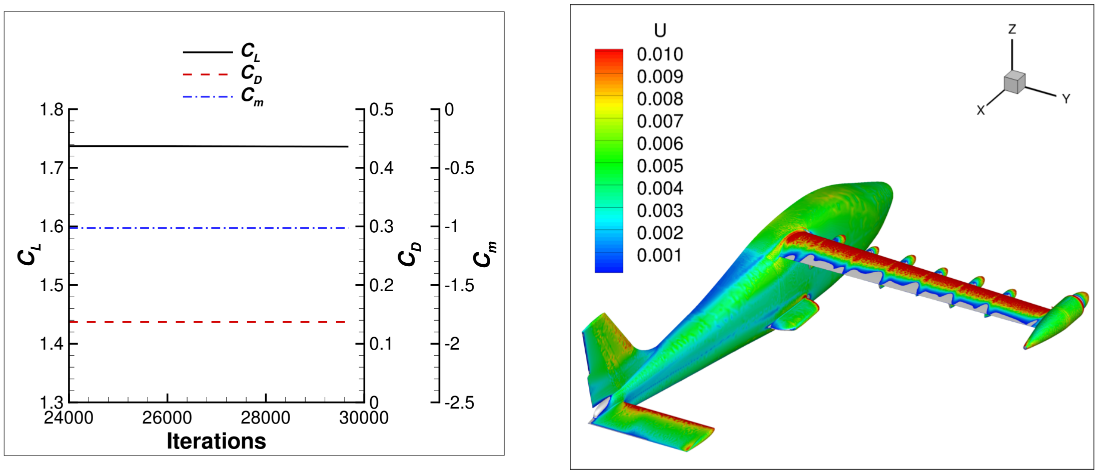

(e) Time-Averaged Coefficients (f) Normalized U Velocity Contours

Figure A173. The Convergence History Data and Normalized U Velocity Contours for the Cruise Configuration at $M = 0.233$ and $\alpha = 10°$, No Cruise Power, and No High-Lift Blowing.

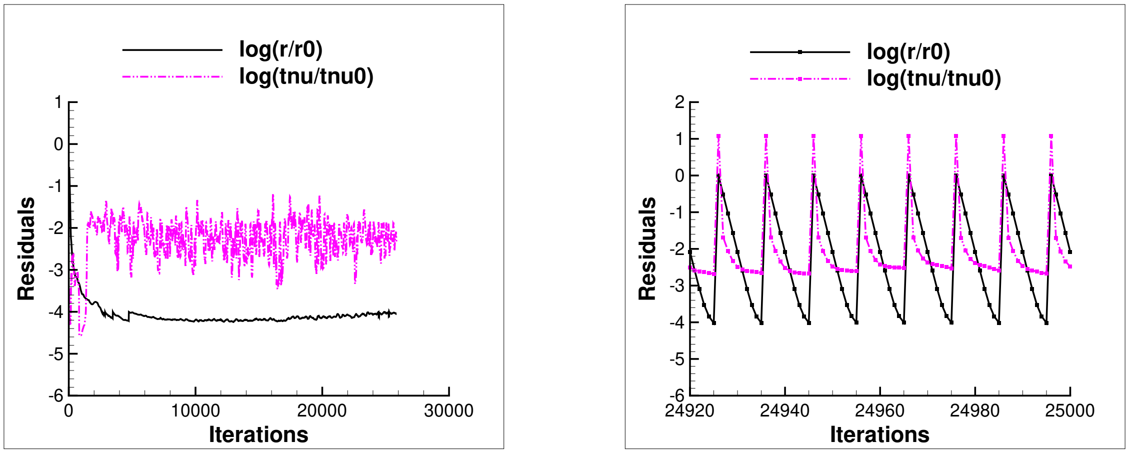

(a) Residuals

(b) SubIterations Residuals

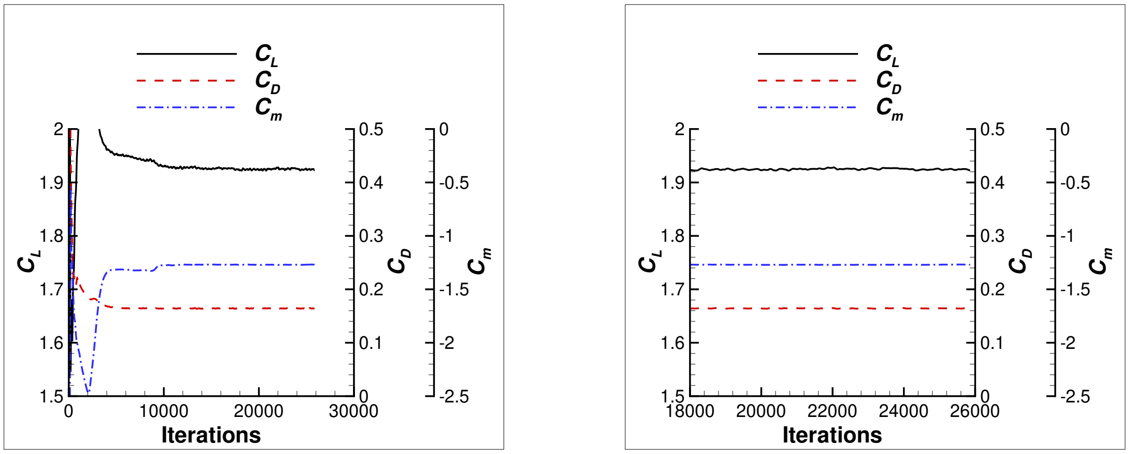

(c) Force and Moment Coefficients

(d) Coefficients with a Smaller Iteration Range

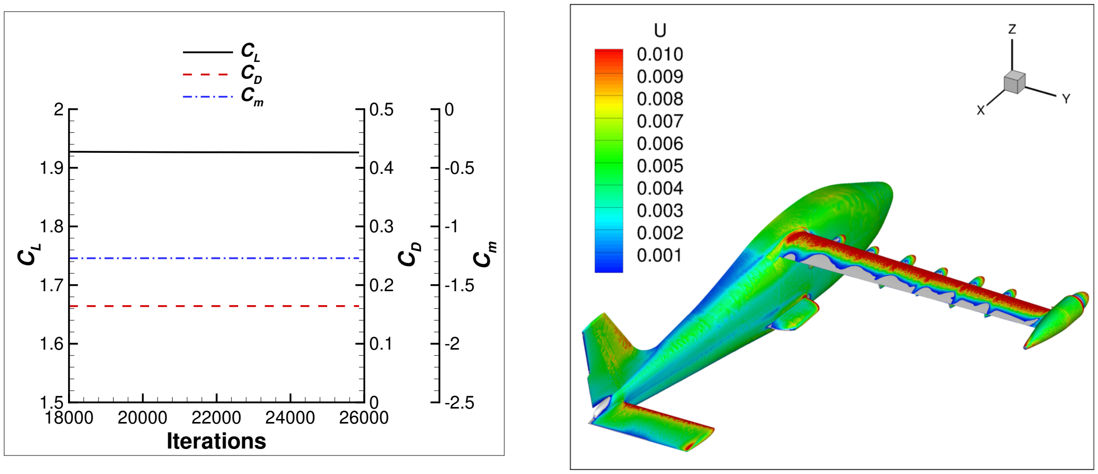

(e) Time-Averaged Coefficients

(f) Normalized U Velocity Contours

Figure A174. The Convergence History Data and Normalized U Velocity Contours for the Cruise Configuration at $M = 0.233$ and $\alpha = 12°$, No Cruise Power, and No High-Lift Blowing.

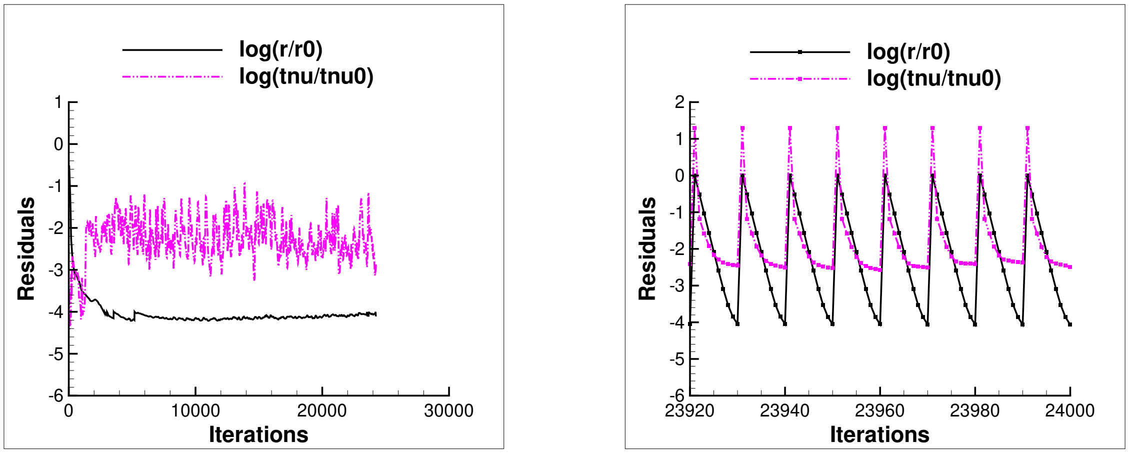

(a) Residuals (b) SubIterations

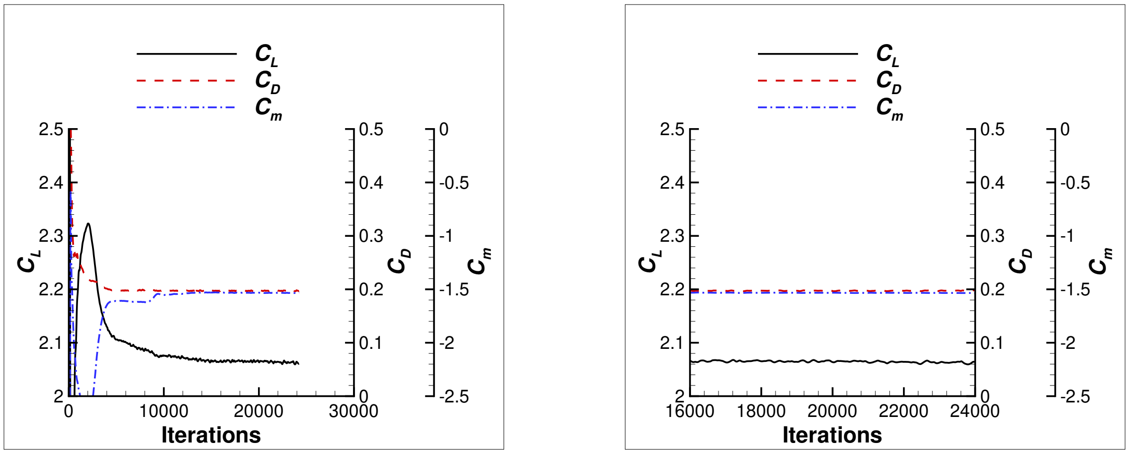

(c) Force and Moment Coefficients (d) Coefficientswith a Smaller Iteration Range

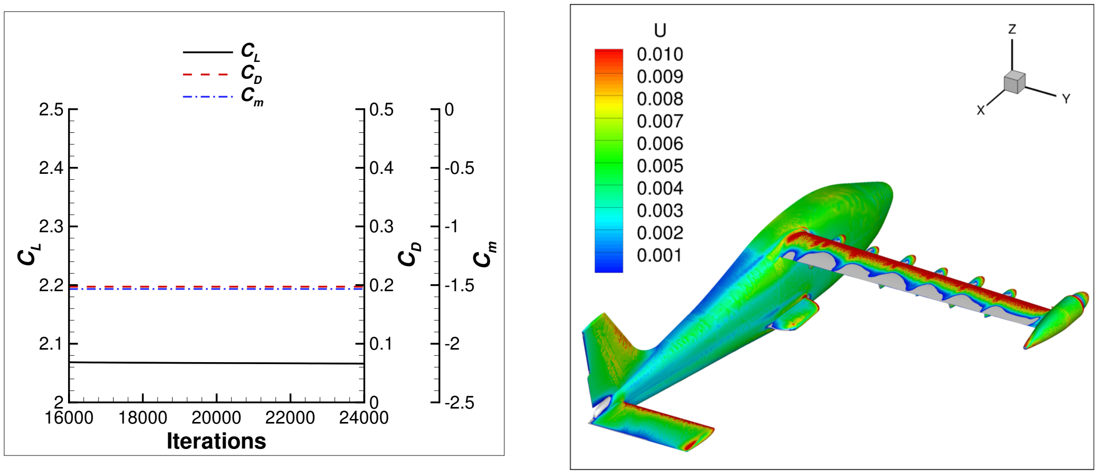

(e) Time-Averaged Coefficients (f) Normalized U Velocity Contours

Figure A175. The Convergence History Data and Normalized U Velocity Contours for the Cruise Configuration at $M = 0.233$ and $\alpha = 14°$, No Cruise Power, and No High-Lift Blowing.

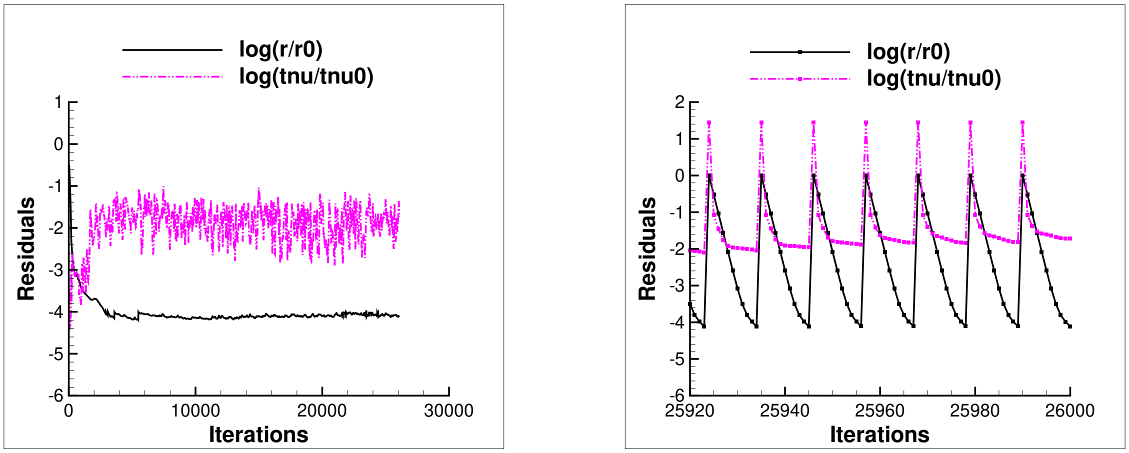

(a) Residuals (b) SubIterations

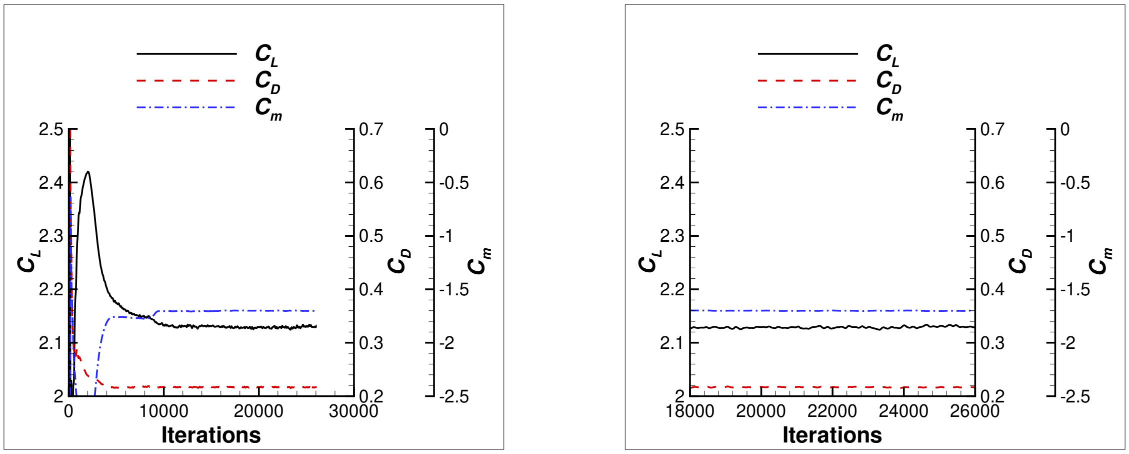

(c) Force and Moment Coefficients (d) Coefficients with a Smaller Iteration Range

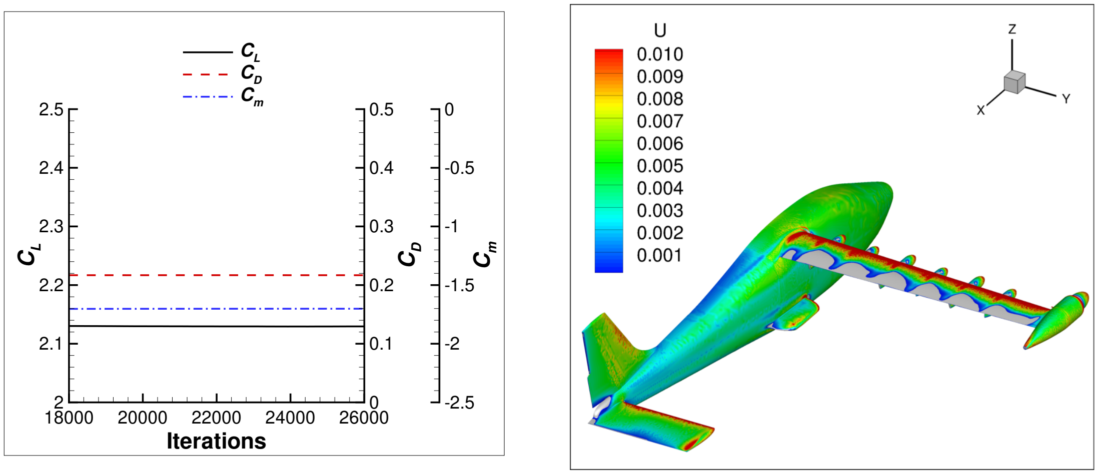

(e) Time-Averaged Coefficients (f) Normalized U Velocity Contours

Figure A176. The Convergence History Data and Normalized U Velocity Contours for the Cruise Configuration at $M = 0.233$ and $\alpha = 15°$, No Cruise Power, and No High-Lift Blowing.

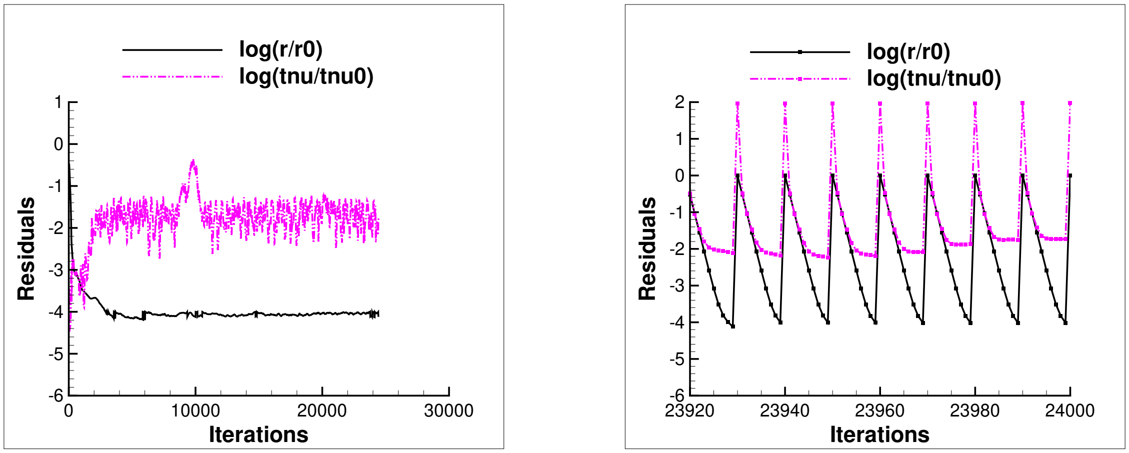

(a) Residuals

(b) SubIterations

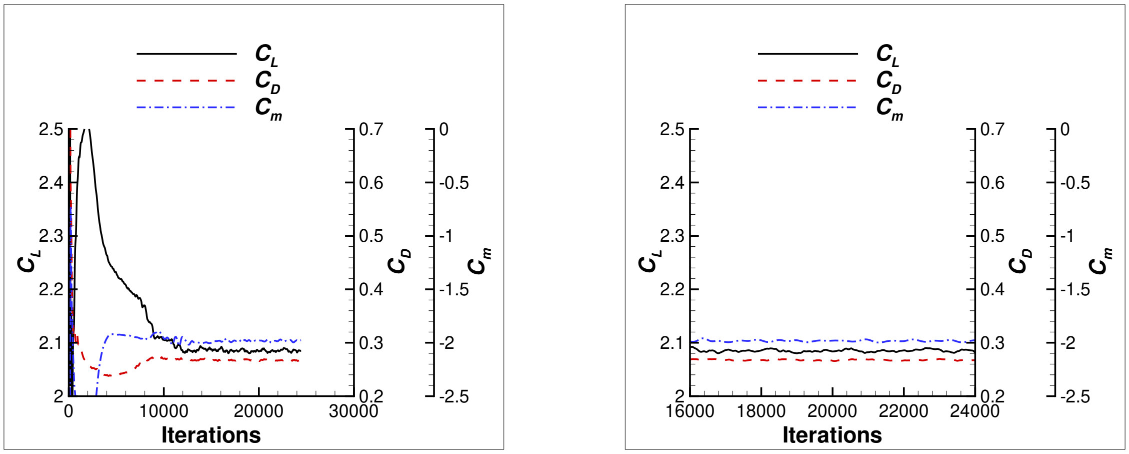

(c) Force and Moment Coefficients

(d) Coefficients with a Smaller Iteration Range

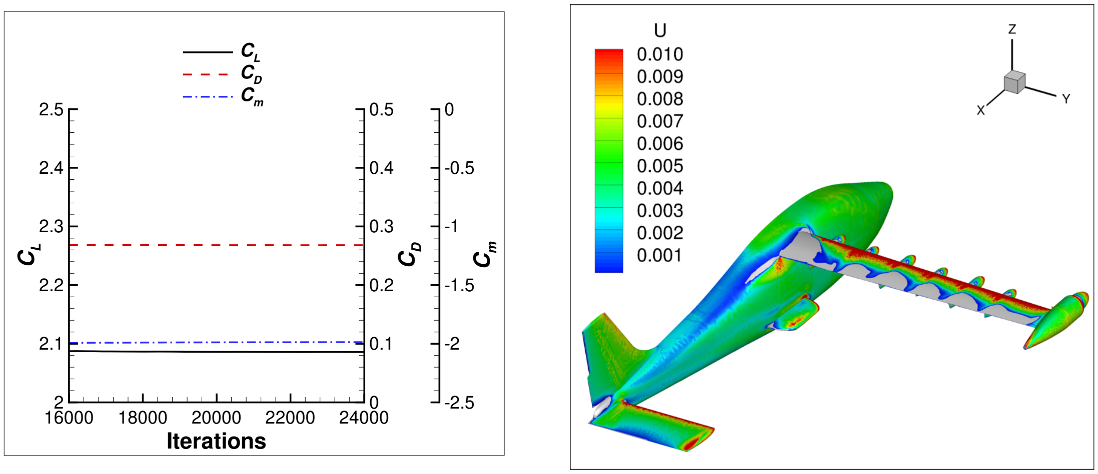

(e) Time-Averaged Coefficients

(f) Normalized U Velocity Contours

Figure A177. The Convergence History Data and Normalized U Velocity Contours for the Cruise Configuration at $M = 0.233$ and $\alpha = 16°$, No Cruise Power, and No High-Lift Blowing.

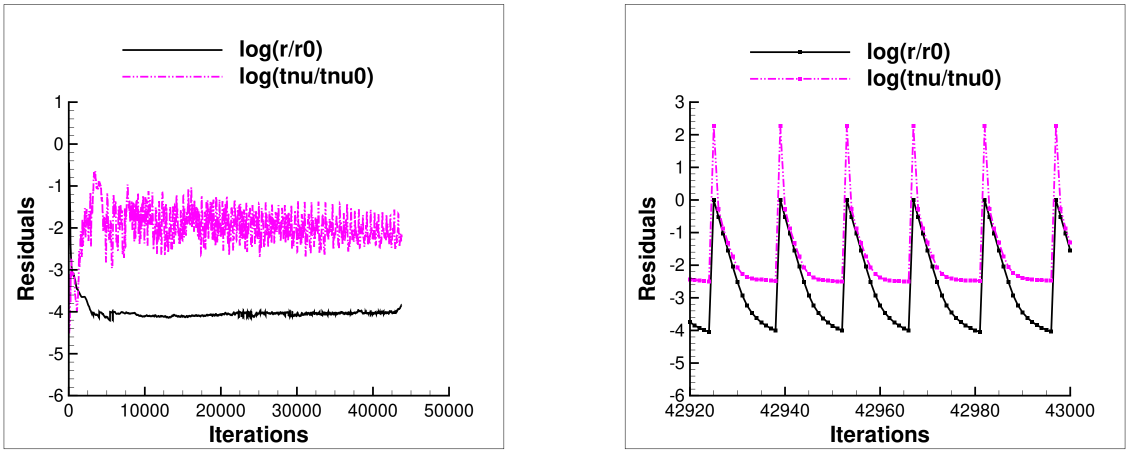

(a) Residuals (b) SubIterations

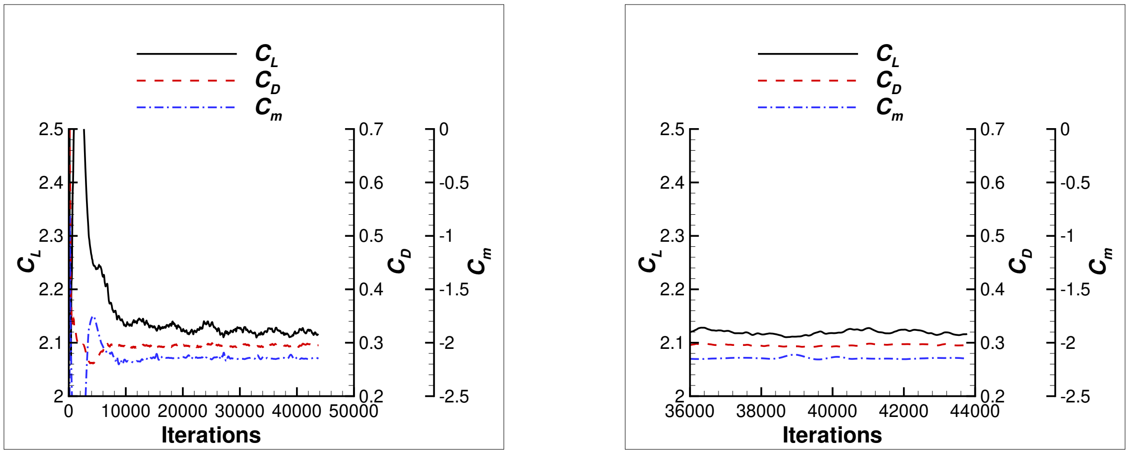

(c) Force and Moment Coefficients (d) Coefficients with a Smaller Iteration Range

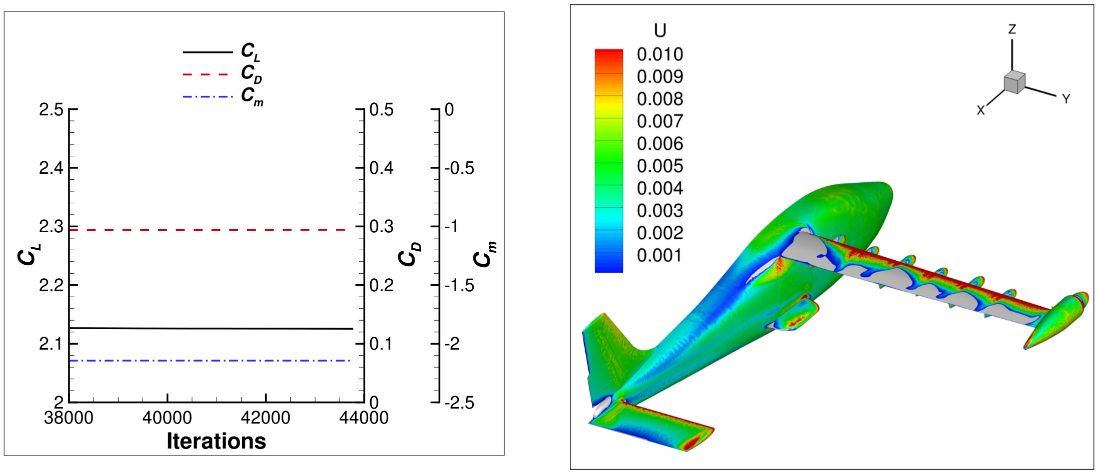

(e) Time-Averaged Coefficients (f) Normalized U Velocity Contours

Figure A178. The Convergence History Data and Normalized U Velocity Contours for the Cruise Configuration at $M = 0.233$ and $\alpha = 17°$, No Cruise Power, and No High-Lift Blowing.

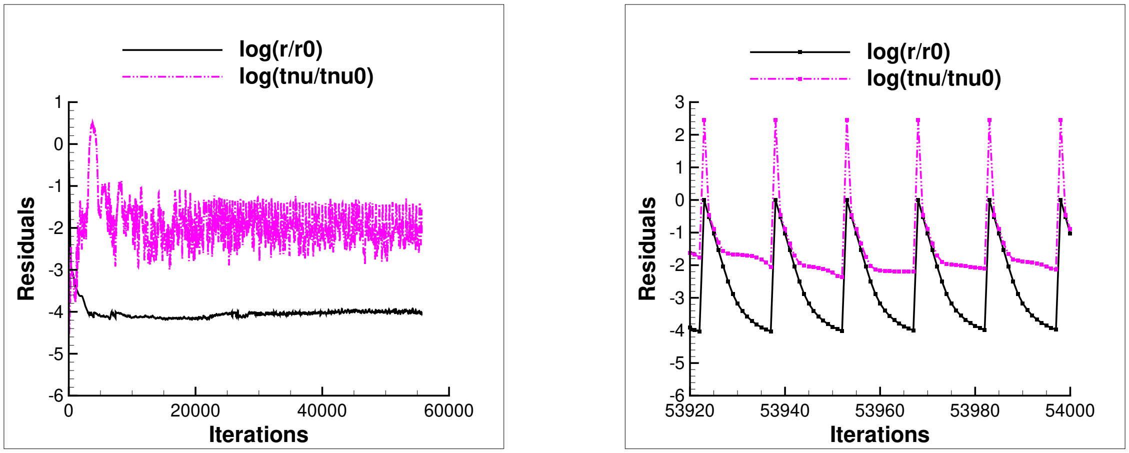

(a) Residuals

(b) SubIterations

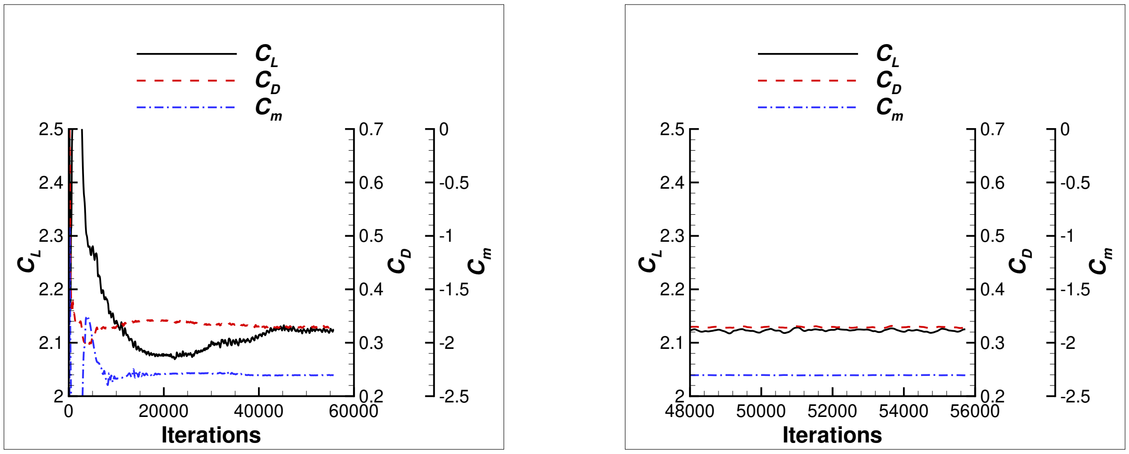

(c) Force and Moment Coefficients

(d) Coefficients with a Smaller Iteration Range

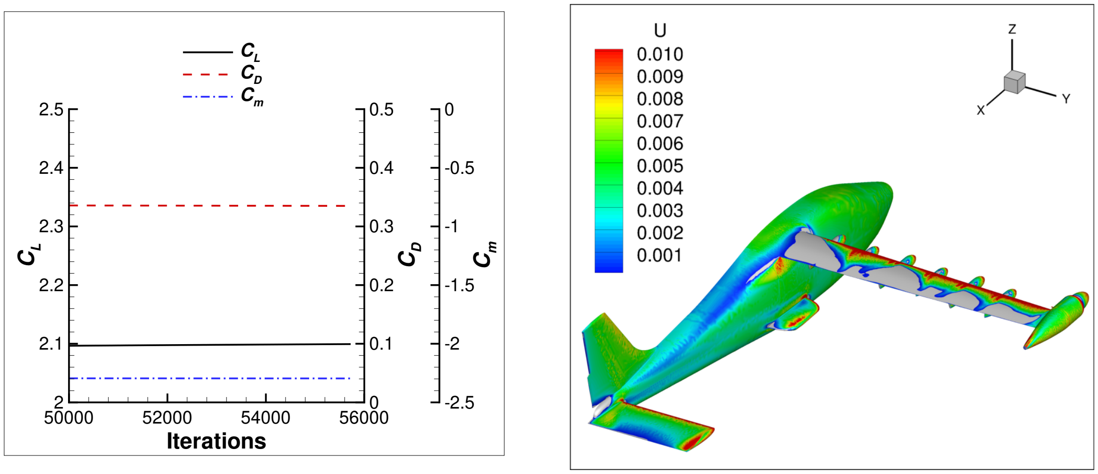

(e) Time-Averaged Coefficients

(f) Normalized U Velocity Contours

Figure A179. The Convergence History Data and Normalized U Velocity Contours for the Cruise Configuration at $M = 0.233$ and $\alpha = 18°$, No Cruise Power, and No High-Lift Blowing.

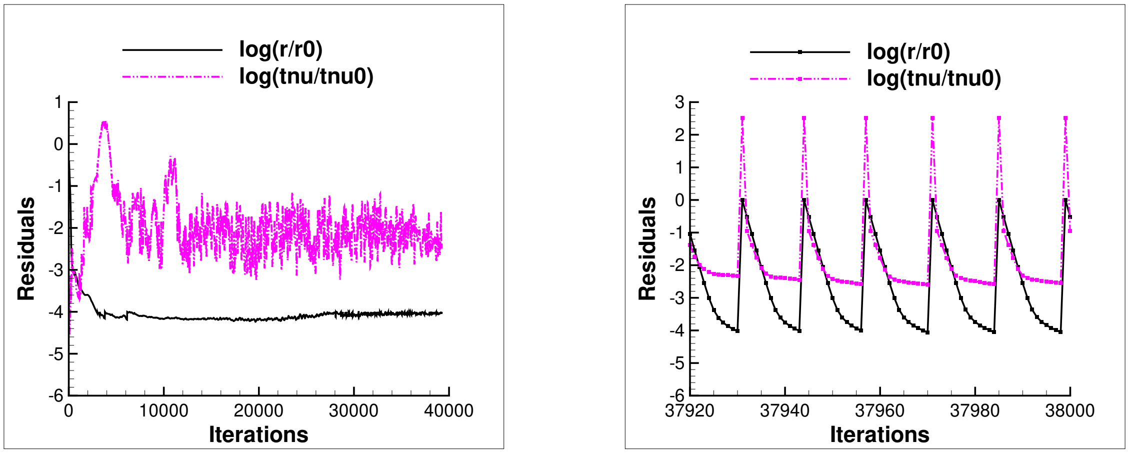

(a) Residuals

(b) SubIterations

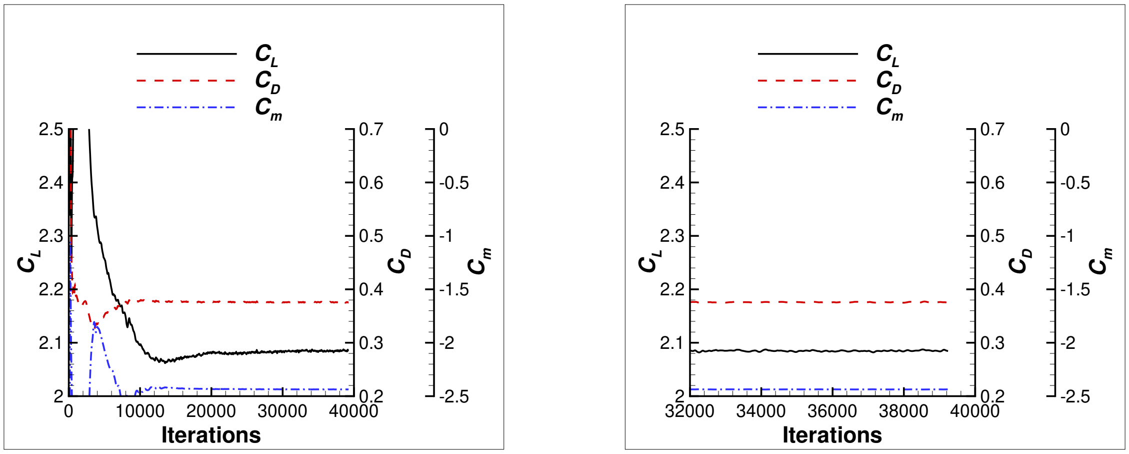

(c) Force and Moment Coefficients

(d) Coefficients with a Smaller Iteration Range

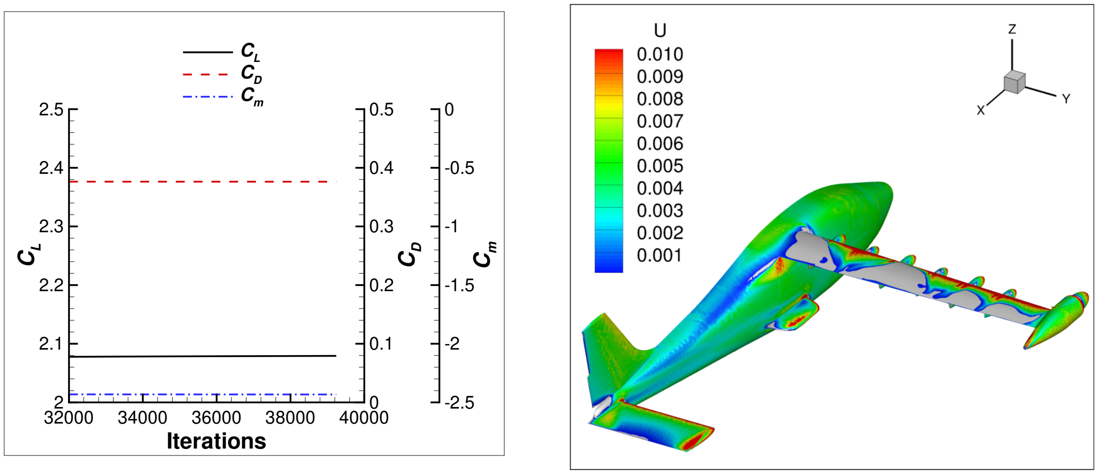

(e) Time-Averaged Coefficients

(f) Normalized U Velocity Contours

Figure A180. The Convergence History Data and Normalized U Velocity Contours for the Cruise Configuration at $M = 0.233$ and $\alpha = 19°$, No Cruise Power, and No High-Lift Blowing.

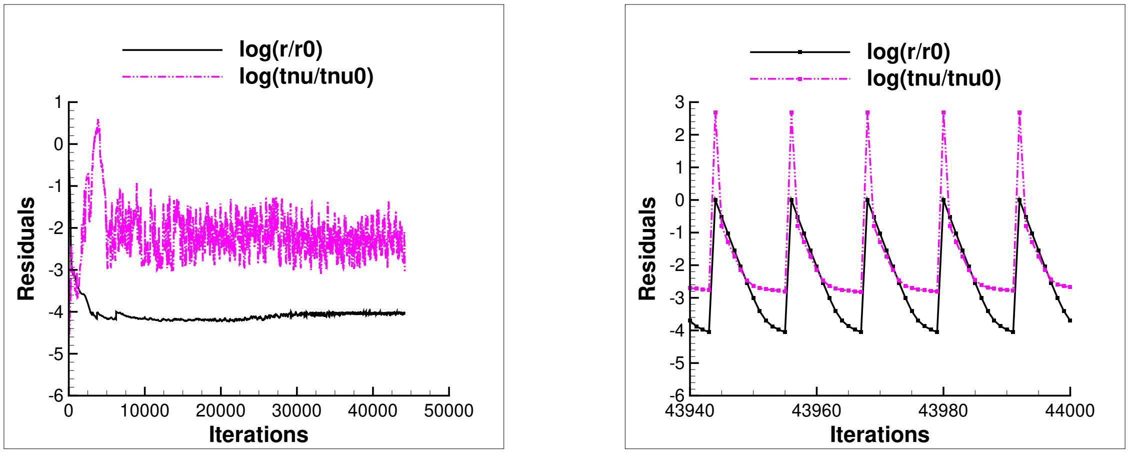

(a) Residuals

(b) SubIterations

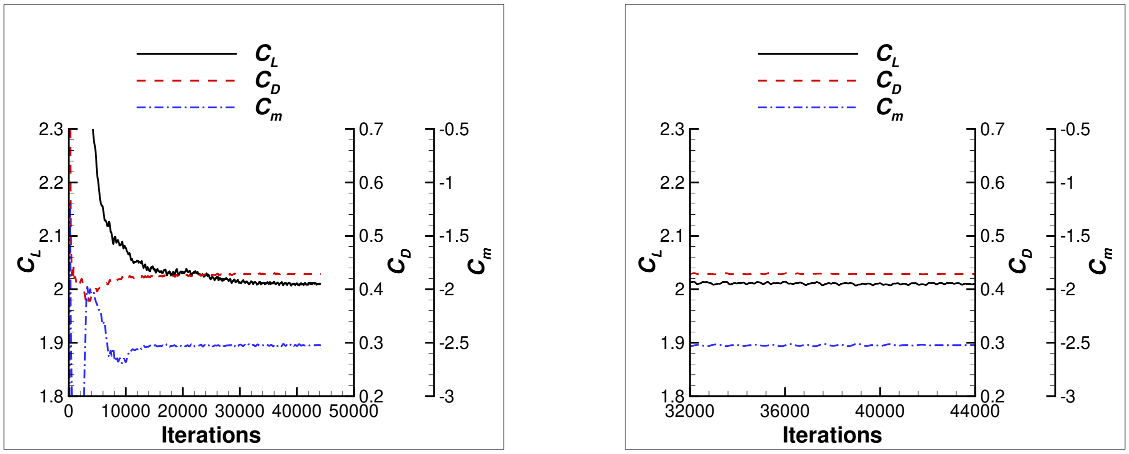

(c) Force and Moment Coefficients

(d) Coefficients with a Smaller Iteration Range

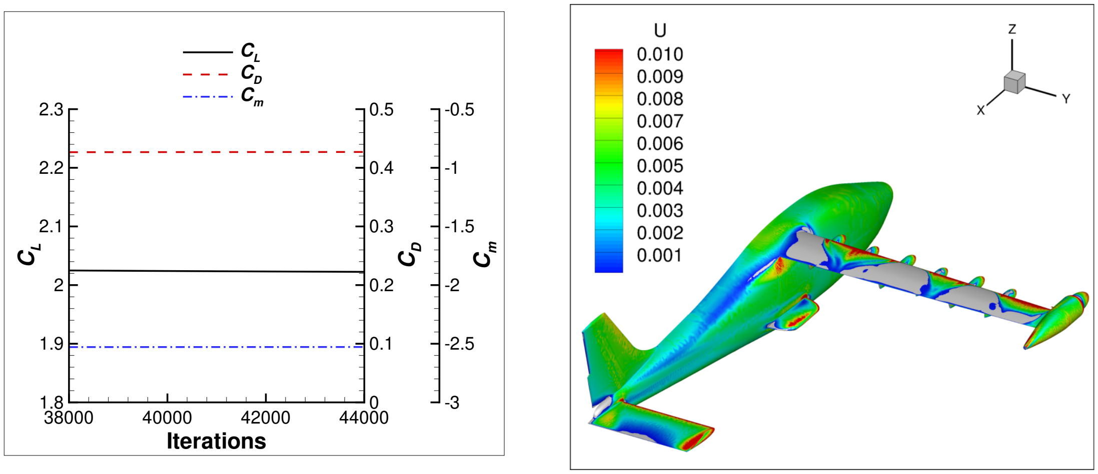

(e) Time-Averaged Coefficients

(f) Normalized U Velocity Contours

Figure A181. The Convergence History Data and Normalized U Velocity Contours for the Cruise Configuration at $M = 0.233$ and $\alpha = 20°$, No Cruise Power, and No High-Lift Blowing.

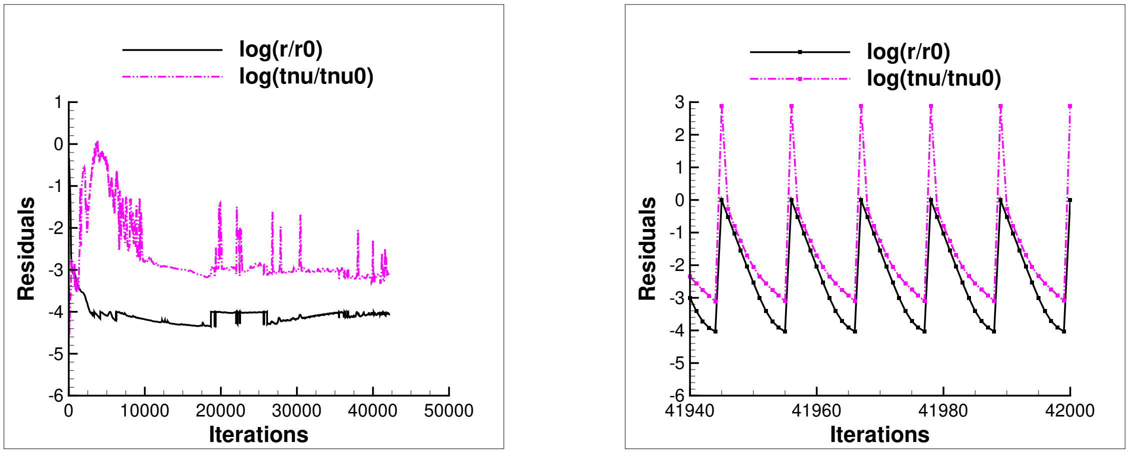

(a) Residuals (b) SubIterations

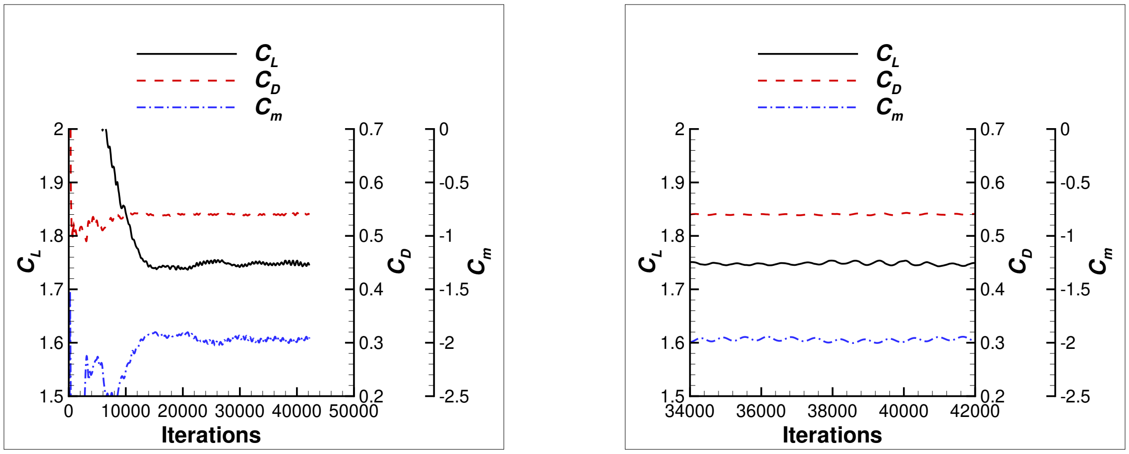

(c) Force and Moment Coefficients (d) Coefficients with a Smaller Iteration Range

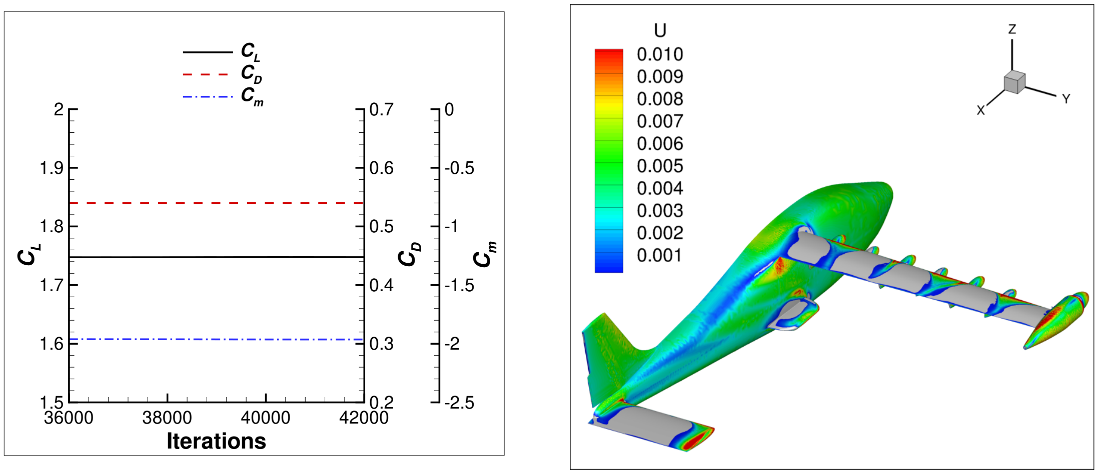

(e) Time-Averaged Coefficients (f) Normalized U Velocity Contours

Figure A182. The Convergence History Data and Normalized U Velocity Contours for the Cruise Configuration at $M = 0.233$ and $\alpha = 22°$, No Cruise Power, and No High-Lift Blowing.

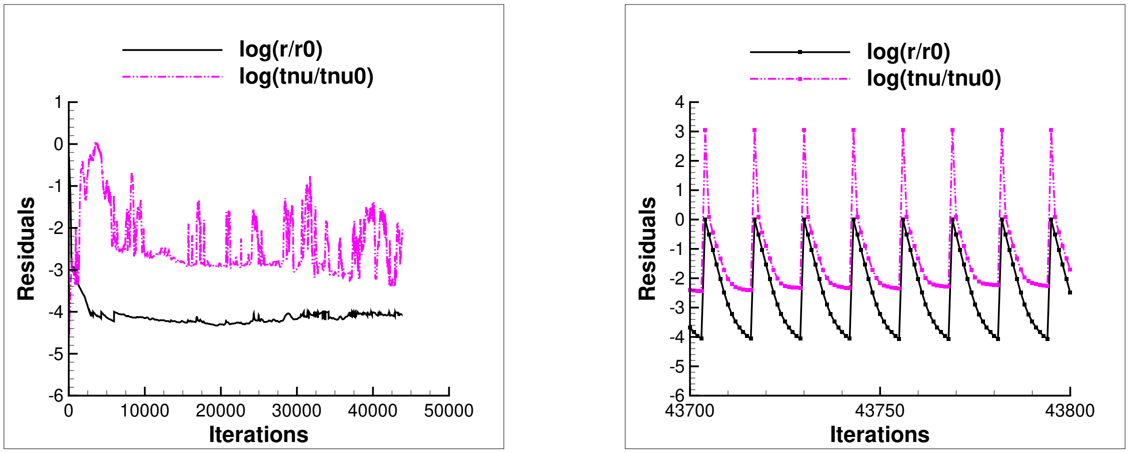

(a) Residuals (b) SubIterations

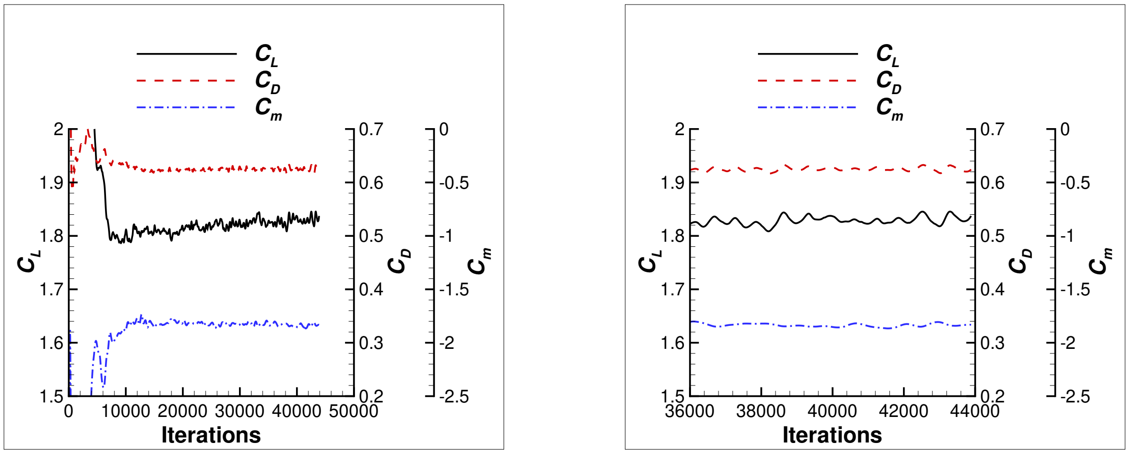

(c) Force and Moment Coefficients (d) Coefficients with a Smaller Iteration Range

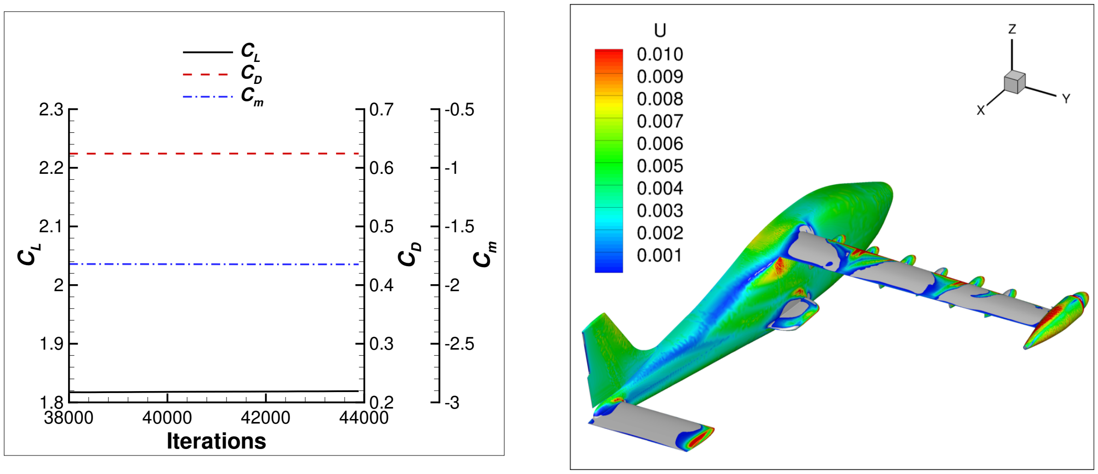

(e) Time-Averaged Coefficients (f) Normalized U Velocity Contours

Figure A183. The Convergence History Data and Normalized U Velocity Contours for the Cruise Configuration at $M = 0.233$ and $\alpha = 24°$, No Cruise Power, and No High-Lift Blowing.

Appendix B

Convergence: Takeoff Configuration with a 10° Flap Deflection

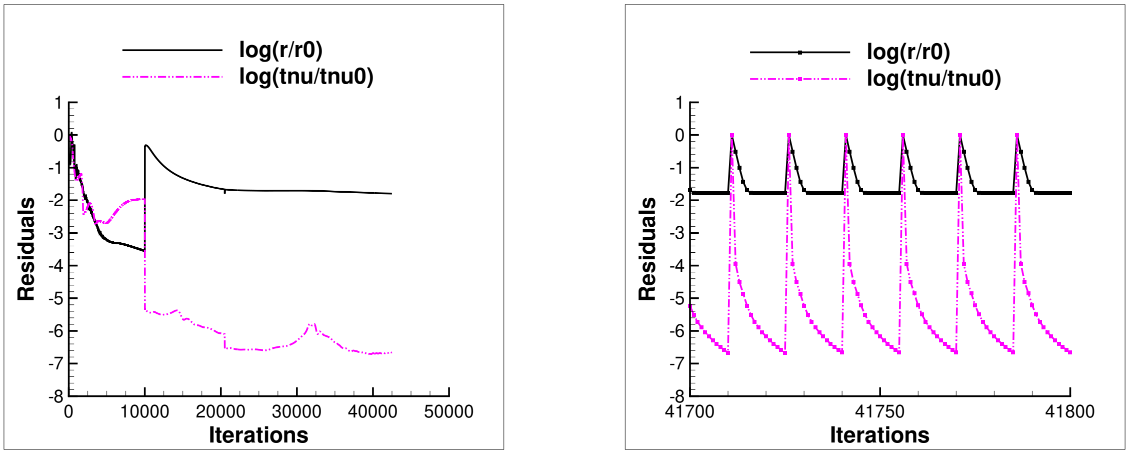

(a) Residuals

(b) SubIterations

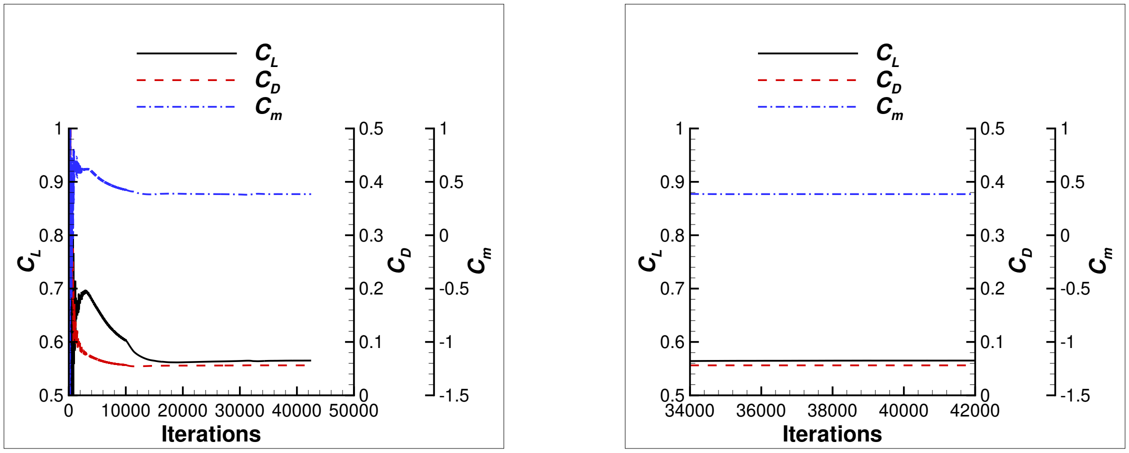

(c) Force and Moment Coefficients

(d) Coefficients with a Smaller Iteration Range

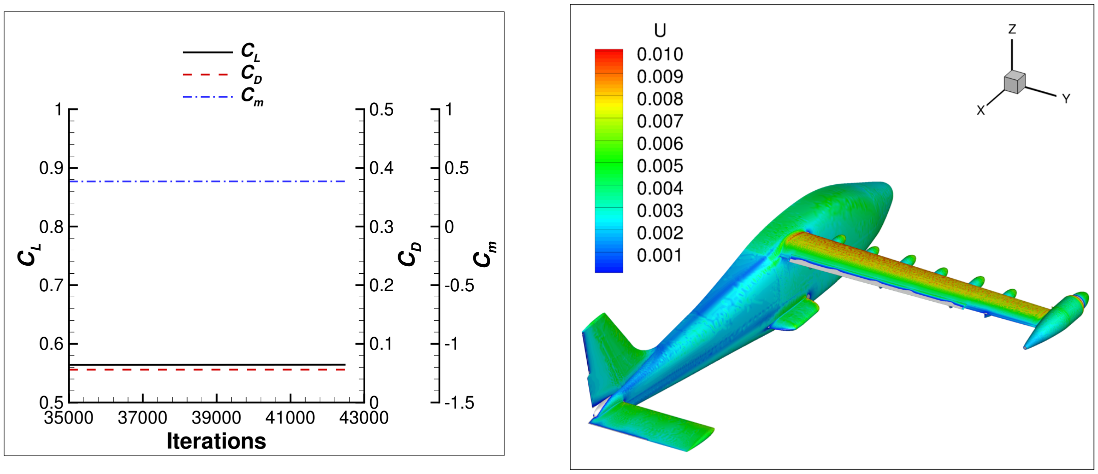

(e) Time-Averaged Coefficients

(f) Normalized U Velocity Contours

Figure B184. Convergence History Data and Normalized U Velocity Contours for the Takeoff Configuration with a 10° Flap Deflection at $M = 0.149$ and $\alpha = -2°$, No Cruise Power, and No High-Lift Blowing.

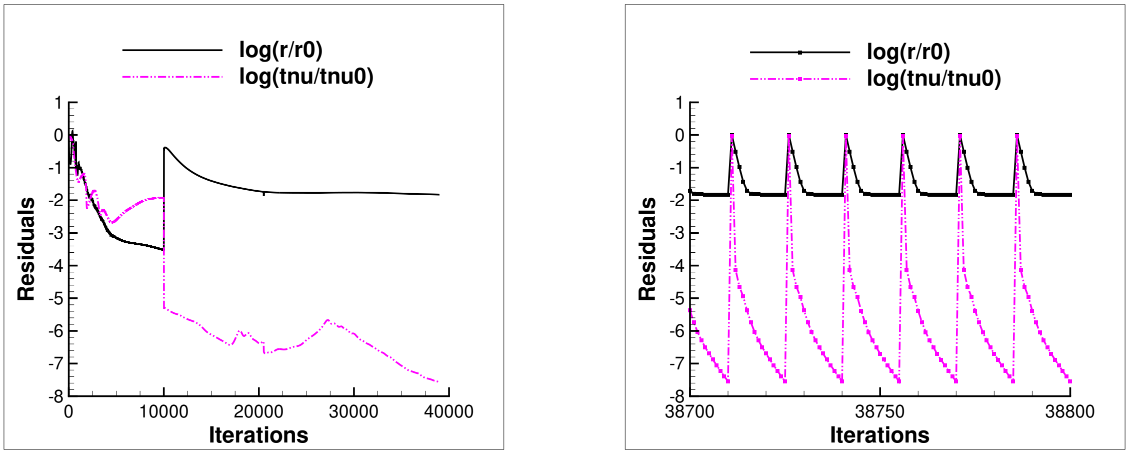

(a) Residuals

(b) SubIterations

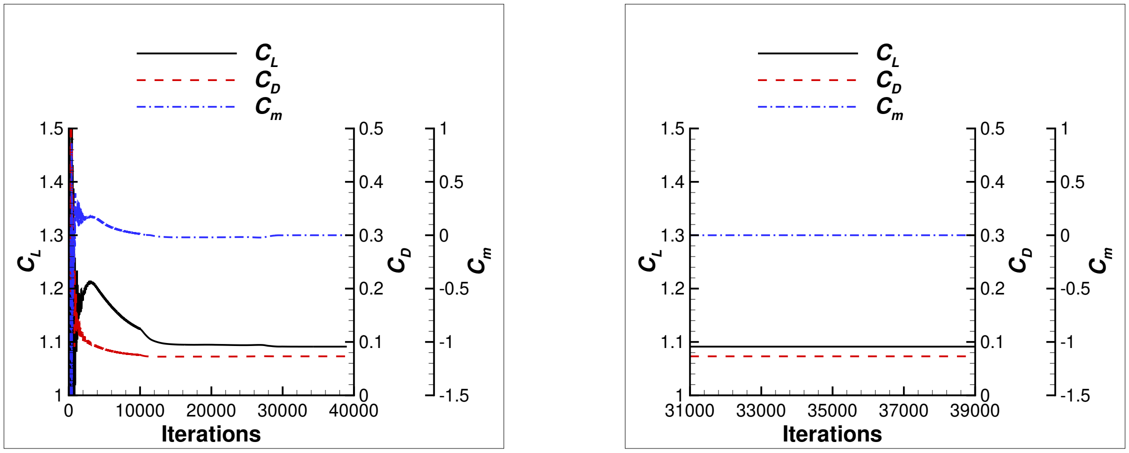

(c) Force and Moment Coefficients

(d) Coefficients with a Smaller Iteration Range

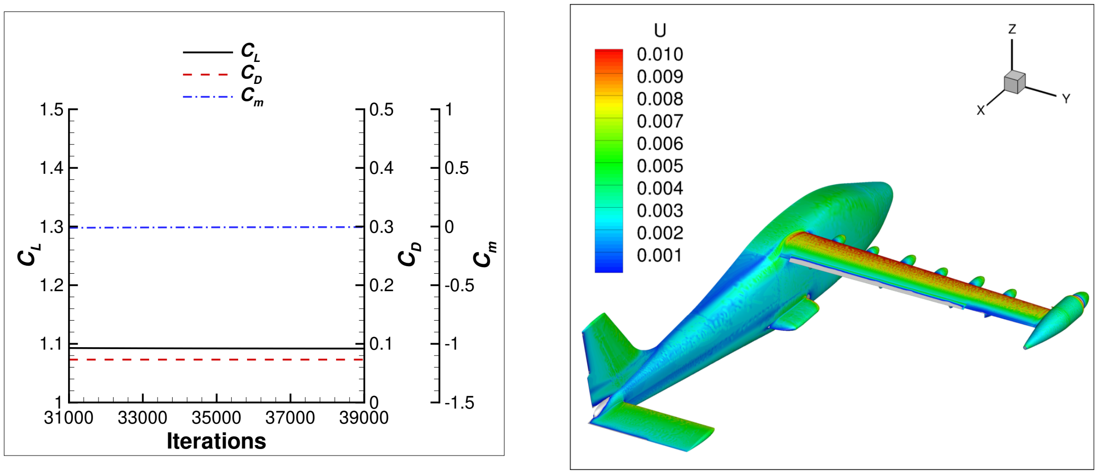

(e) Time-Averaged Coefficients

(f) Normalized U Velocity Contours

Figure B185. Convergence History Data and Normalized U Velocity Contours for the Takeoff Configuration with a 10° Flap Deflection at $M = 0.149$ and $\alpha = 2°$, No Cruise Power, and No High-Lift Blowing.

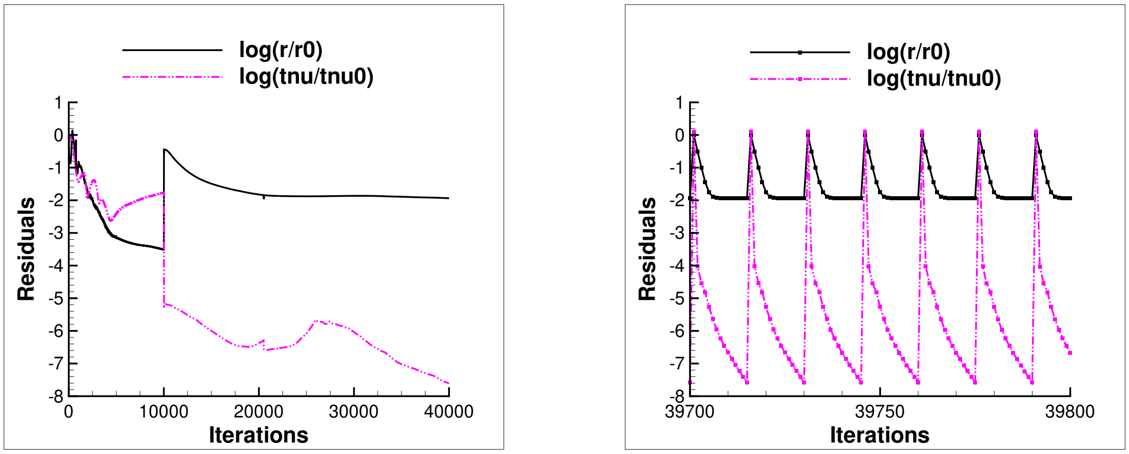

(a) Residuals

(b) SubIterations

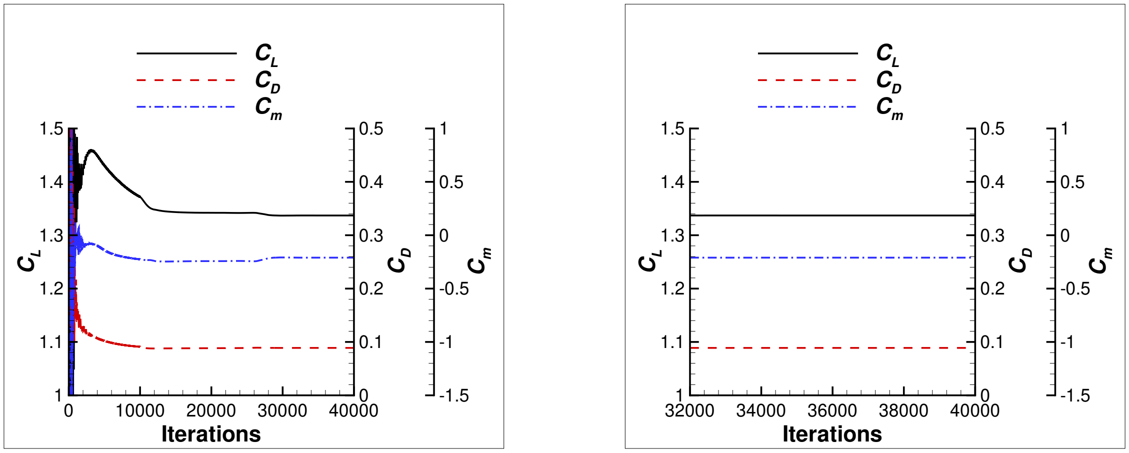

(c) Force and Moment Coefficients

(d) Coefficients with a Smaller Iteration Range

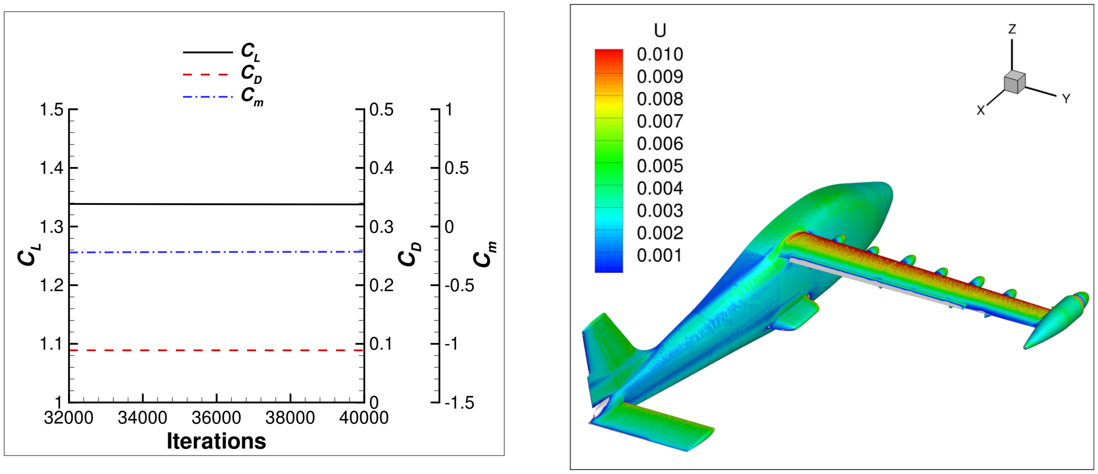

(e) Time-Averaged Coefficients

(f) Normalized U Velocity Contours

Figure B186. Convergence History Data and Normalized U Velocity Contours for the Takeoff Configuration with a 10° Flap Deflection at $M = 0.149$ and $\alpha = 4°$, No Cruise Power, and No High-Lift Blowing.

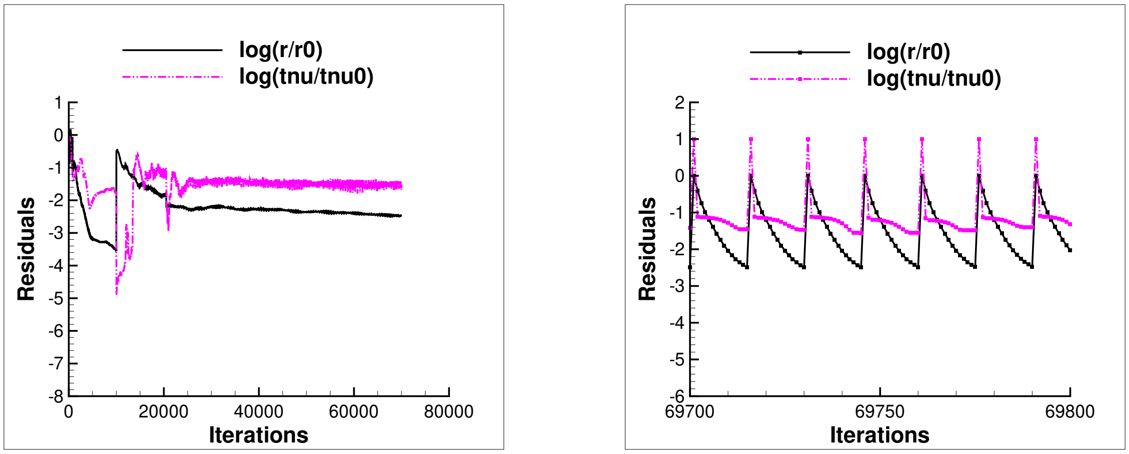

(a) Residuals (b) SubIterations

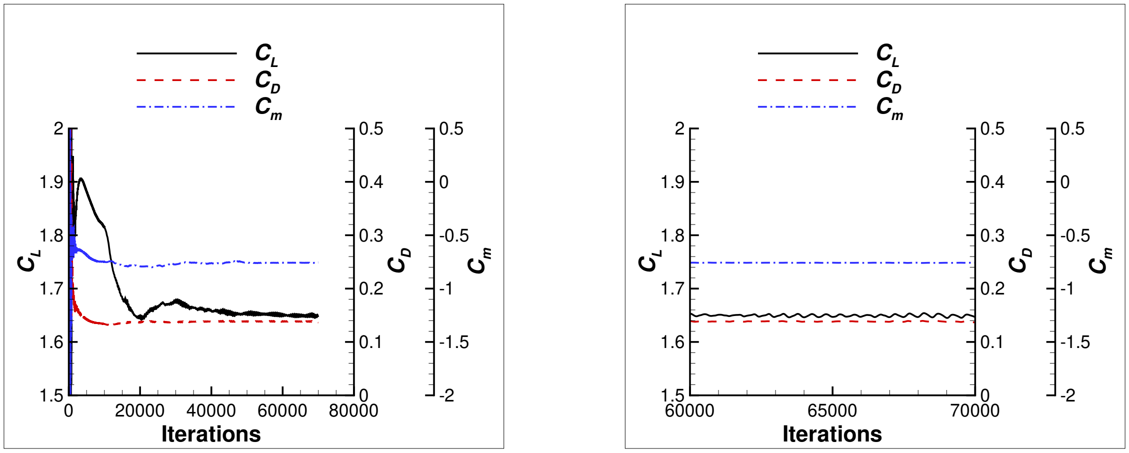

(c) Force and Moment Coefficients (d) Coefficients with a Smaller Iteration Range

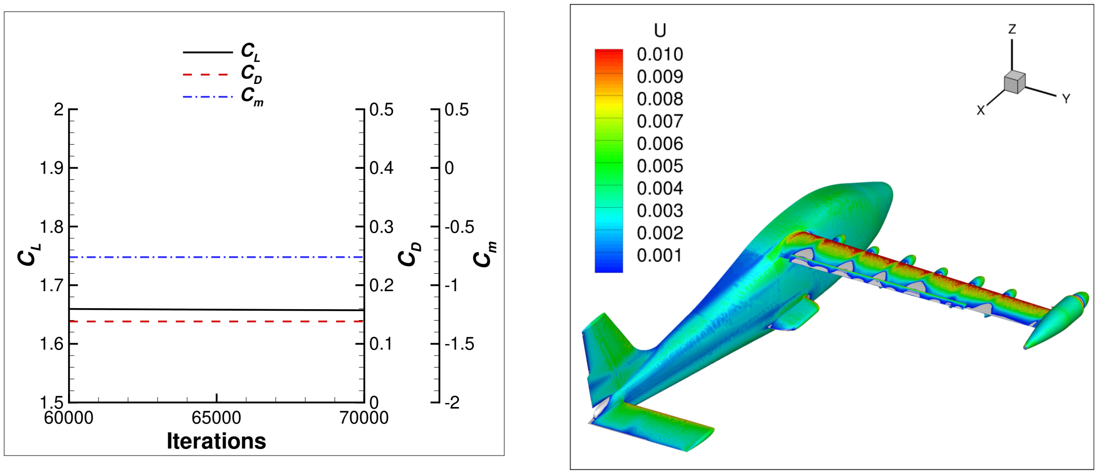

(e) Time-Averaged Coefficients (f) Normalized U Velocity Contours

Figure B187. Convergence History Data and Normalized U Velocity Contours for the Takeoff Configuration with a 10° Flap Deflection at $M = 0.149$ and $\alpha = 8°$, No Cruise Power, and No High-Lift Blowing.

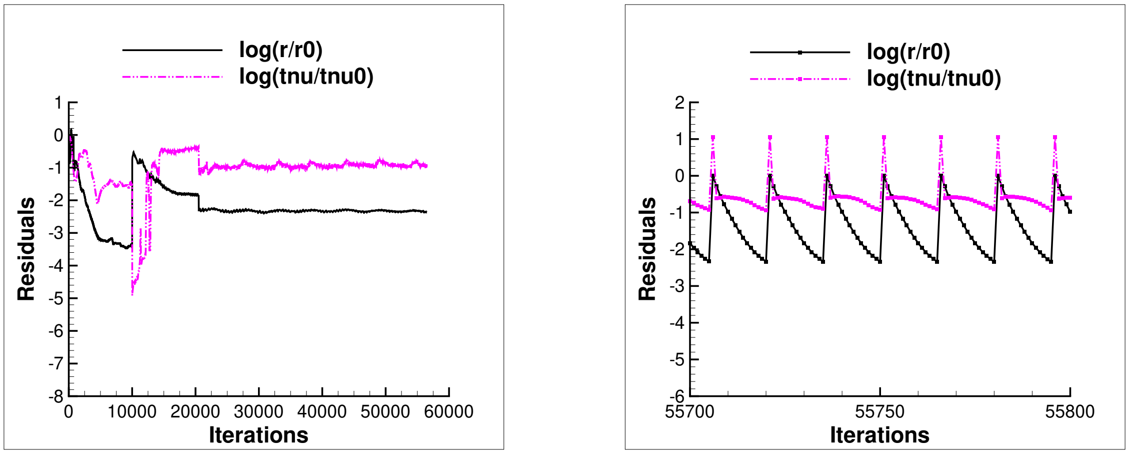

(a) Residuals

(b) SubIterations

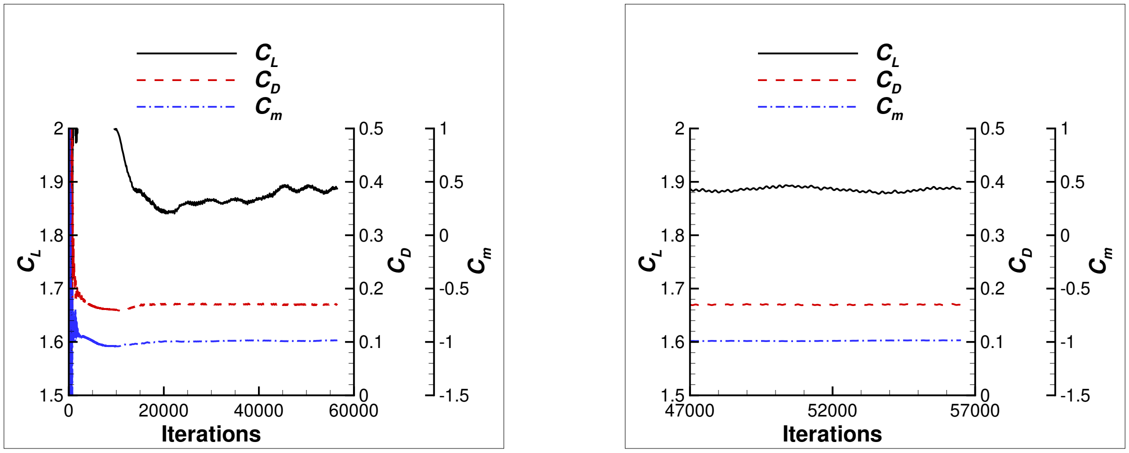

(c) Force and Moment Coefficients

(d) Coefficients with a Smaller Iteration Range

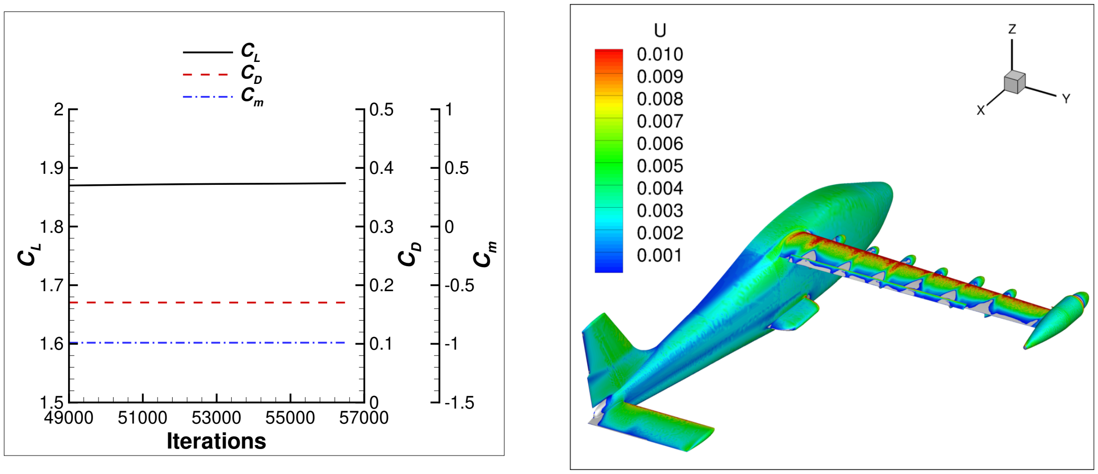

(e) Time-Averaged Coefficients

(f) Normalized U Velocity Contours

Figure B188. Convergence History Data and Normalized U Velocity Contours for the Takeoff Configuration with a 10° Flap Deflection at $M = 0.149$ and $\alpha = 10°$, No Cruise Power, and No High-Lift Blowing.

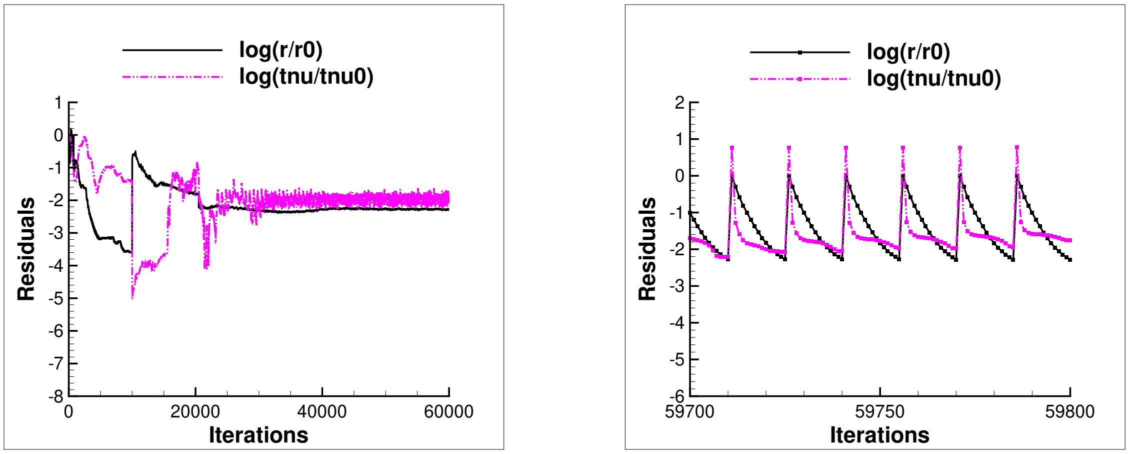

(a) Residuals (b) SubIterations

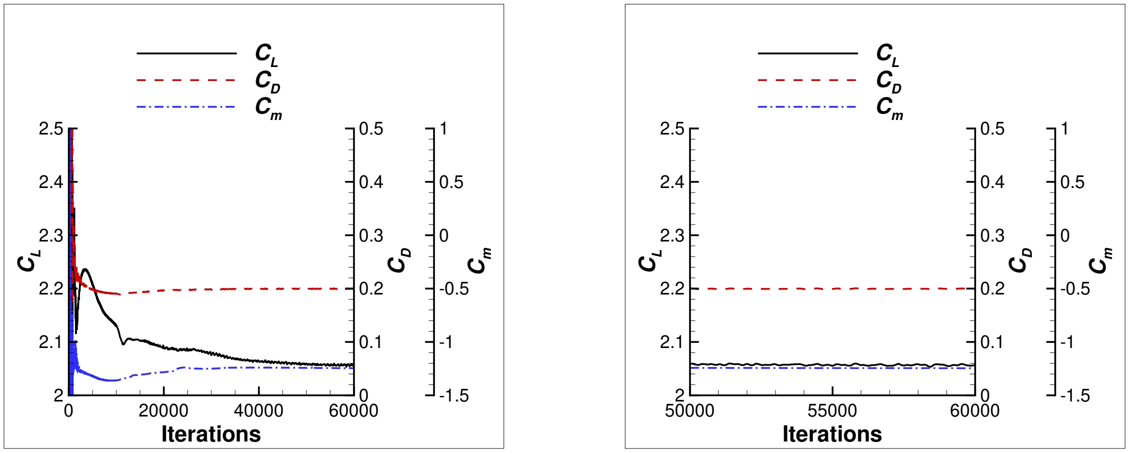

(c) Force and Moment Coefficients (d) Coefficients with a Smaller Iteration Range

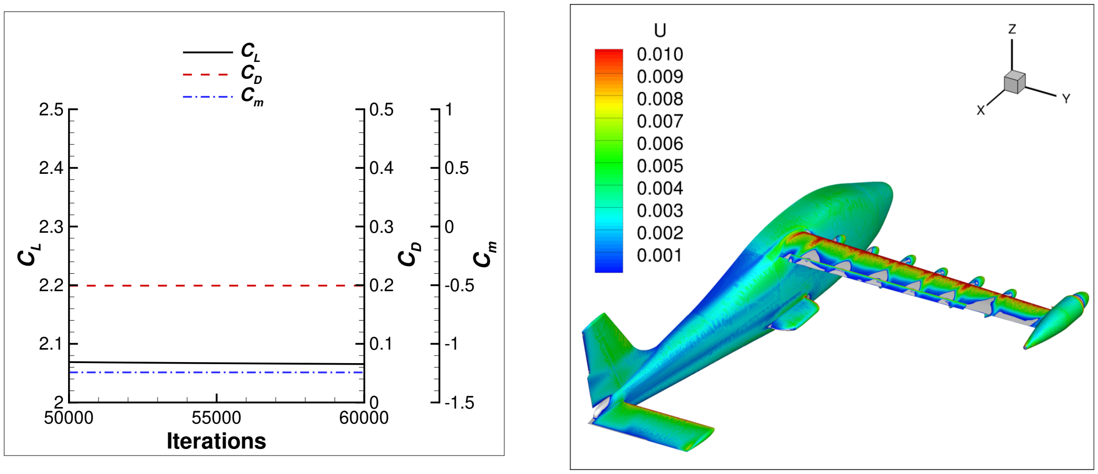

(e) Time-Averaged Coefficients (f) Normalized U Velocity Contours

Figure B189. Convergence History Data and Normalized U Velocity Contours for the Takeoff Configuration with a 10° Flap Deflection at $M = 0.149$ and $\alpha = 12°$, No Cruise Power, and No High-Lift Blowing.

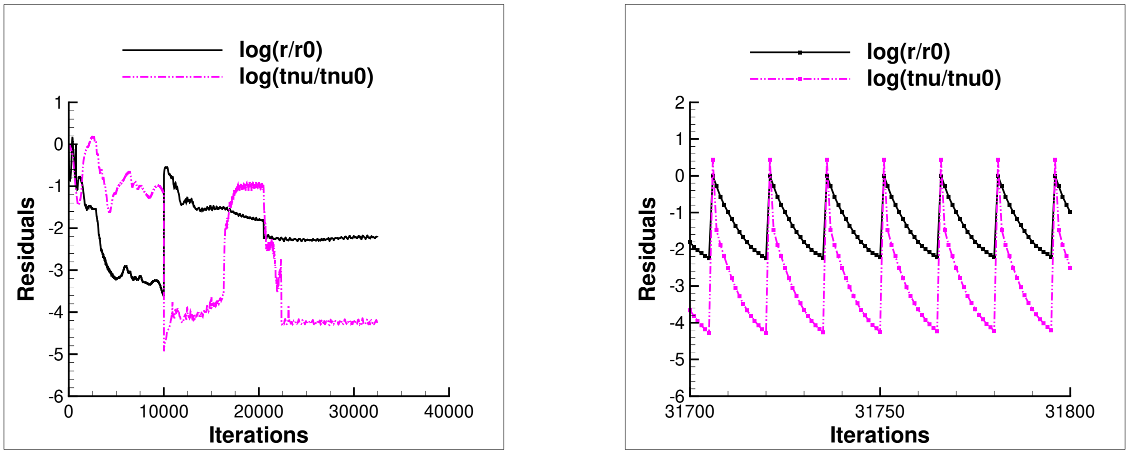

(a) Residuals (b) SubIterations

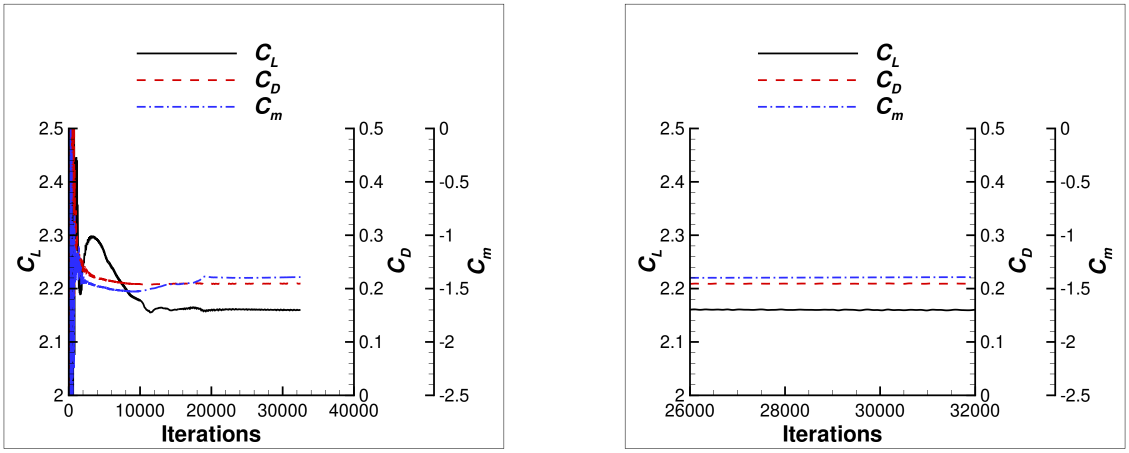

(c) Force and Moment Coefficients (d) Coefficients with a Smaller Iteration Range

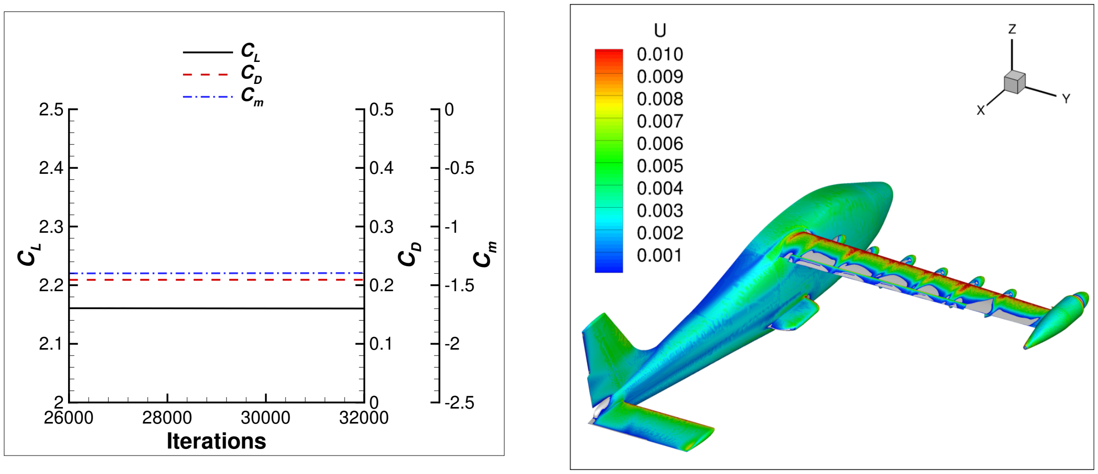

(e) Time-Averaged Coefficients (f) Normalized U Velocity Contours

Figure B190. Convergence History Data and Normalized U Velocity Contours for the Takeoff Configuration with a 10° Flap Deflection at $M = 0.149$ and $\alpha = 13°$, No Cruise Power, and No High-Lift Blowing.

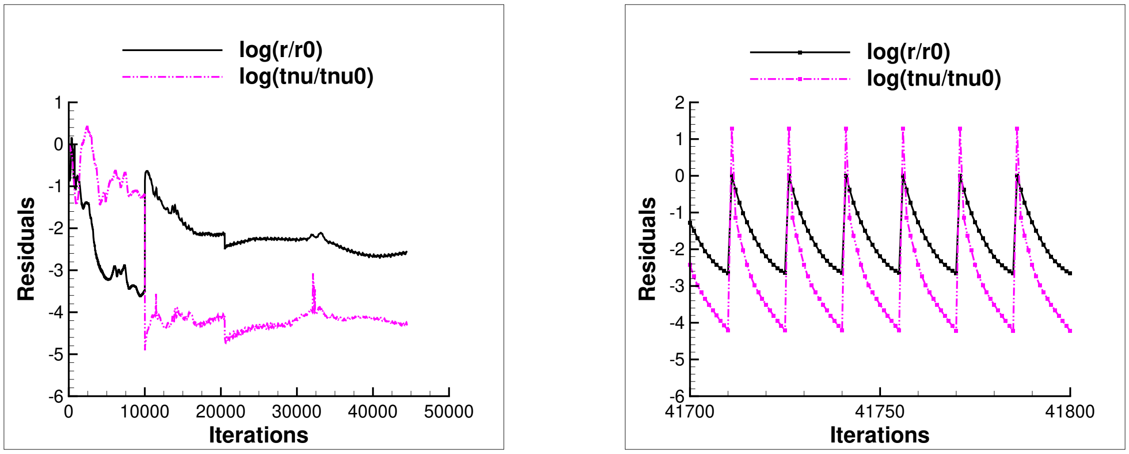

(a) Residuals

(b) SubIterations

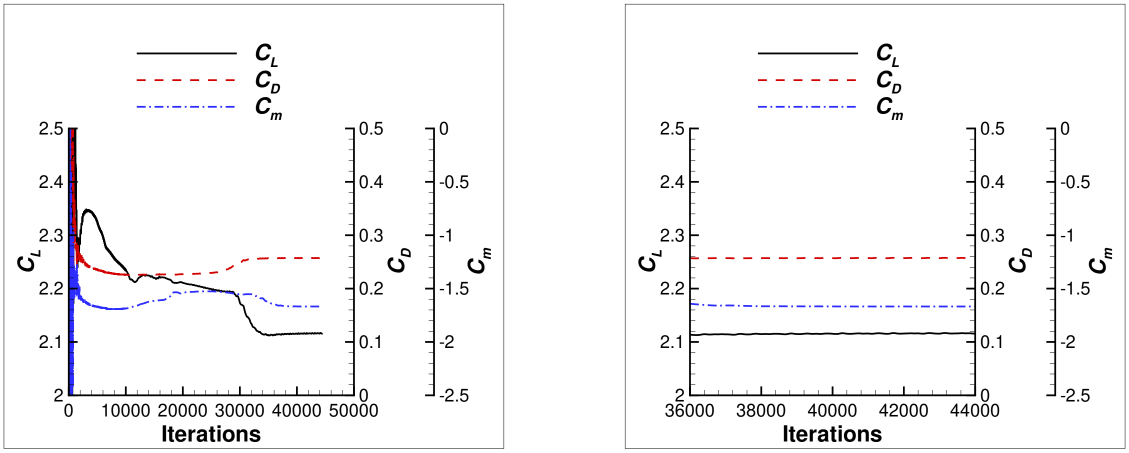

(c) Force and Moment Coefficients

(d) Coefficients with a Smaller Iteration Range

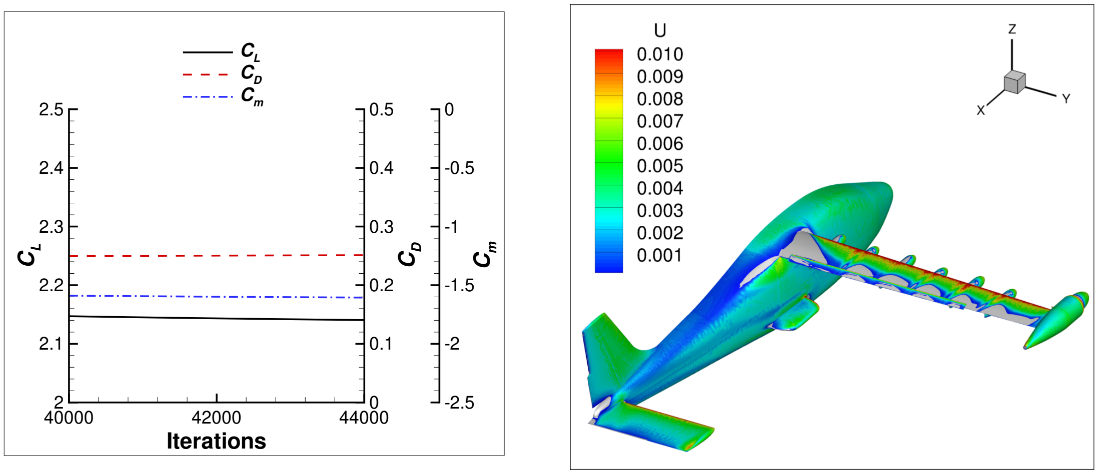

(e) Time-Averaged Coefficients

(f) Normalized U Velocity Contours

Figure B191. Convergence History Data and Normalized U Velocity Contours for the Takeoff Configuration with a 10° Flap Deflection at $M = 0.149$ and $\alpha = 14°$, No Cruise Power, and No High-Lift Blowing.

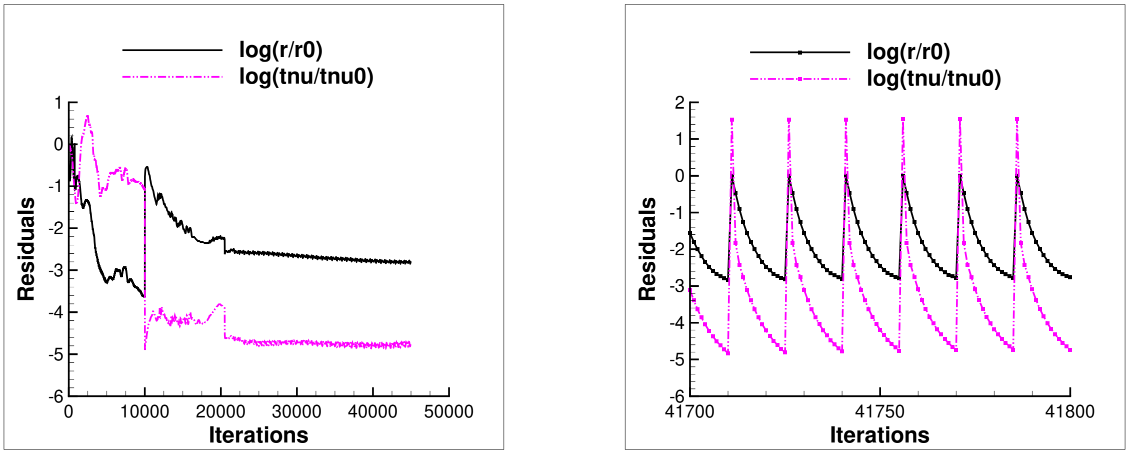

(a) Residuals

(b) SubIterations

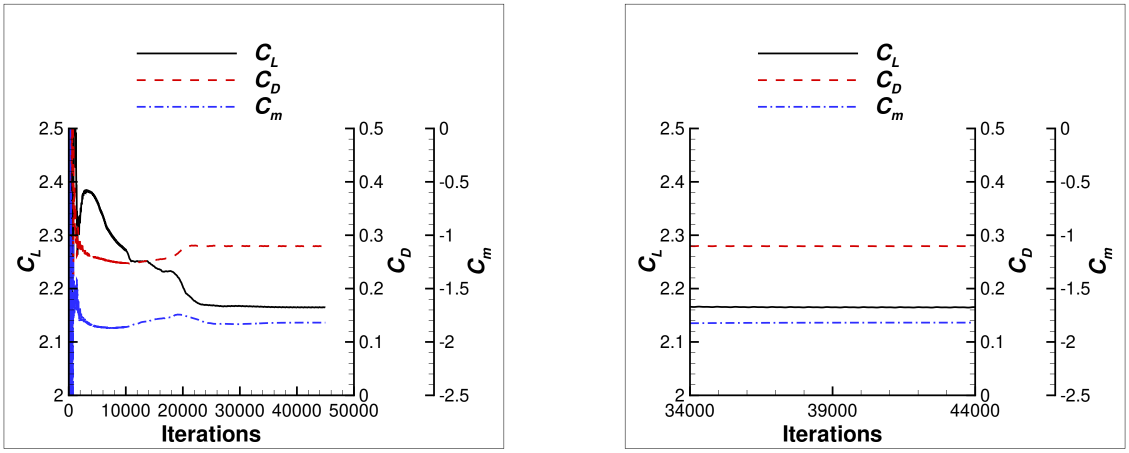

(c) Force and Moment Coefficients

(d) Coefficients with a Smaller Iteration Range

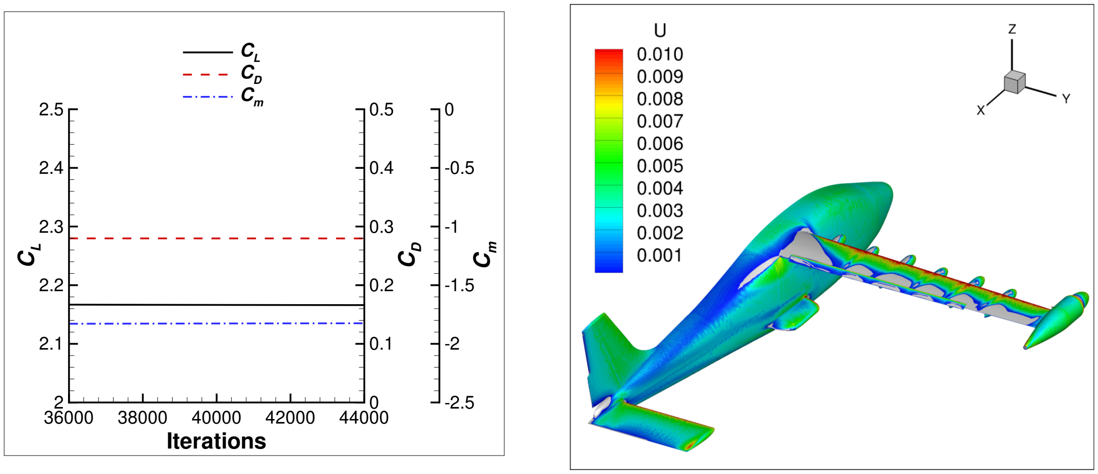

(e) Time-Averaged Coefficients

(f) Normalized U Velocity Contours

Figure B192. Convergence History Data and Normalized U Velocity Contours for the Takeoff Configuration with a 10° Flap Deflection at $M = 0.149$ and $\alpha = 15°$, No Cruise Power, and No High-Lift Blowing.

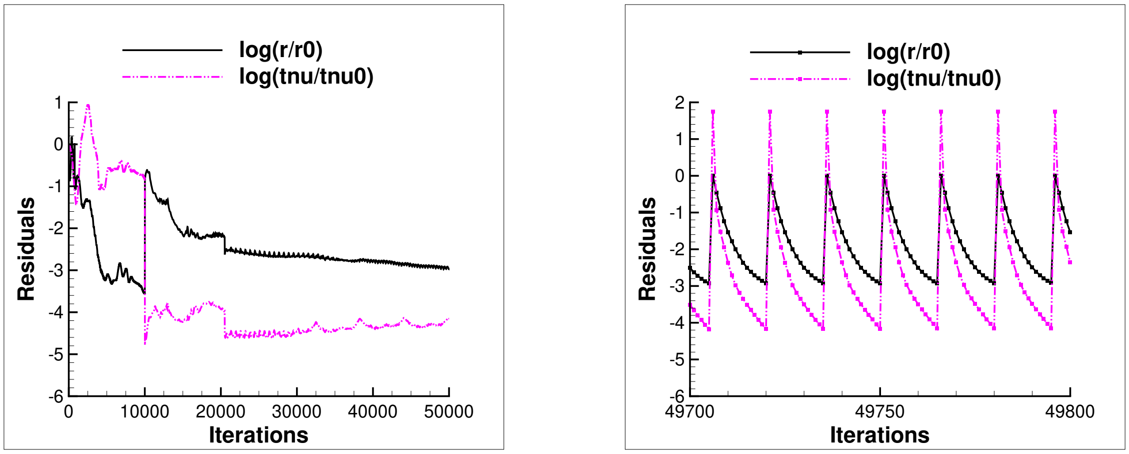

(a) Residuals

(b) SubIterations

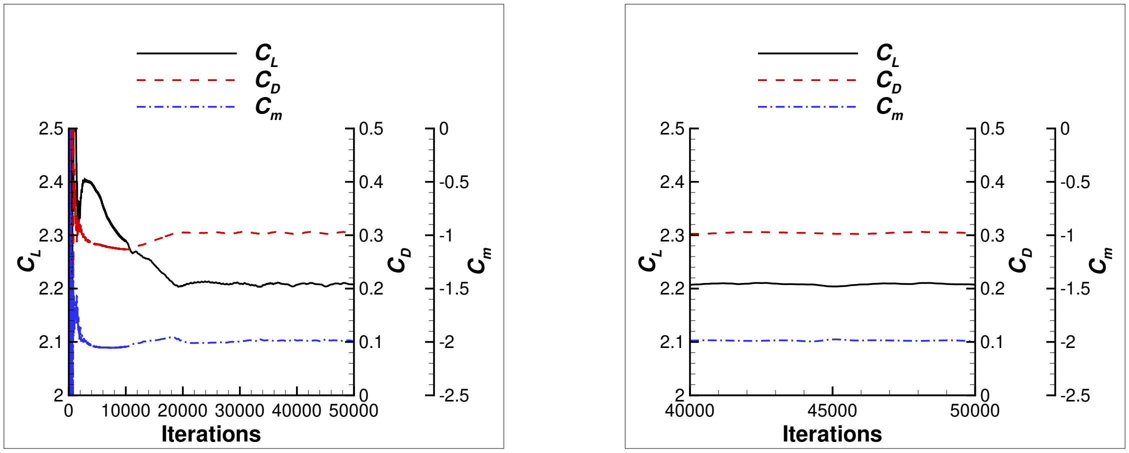

(c) Force and Moment Coefficients

(d) Coefficients with a Smaller Iteration Range

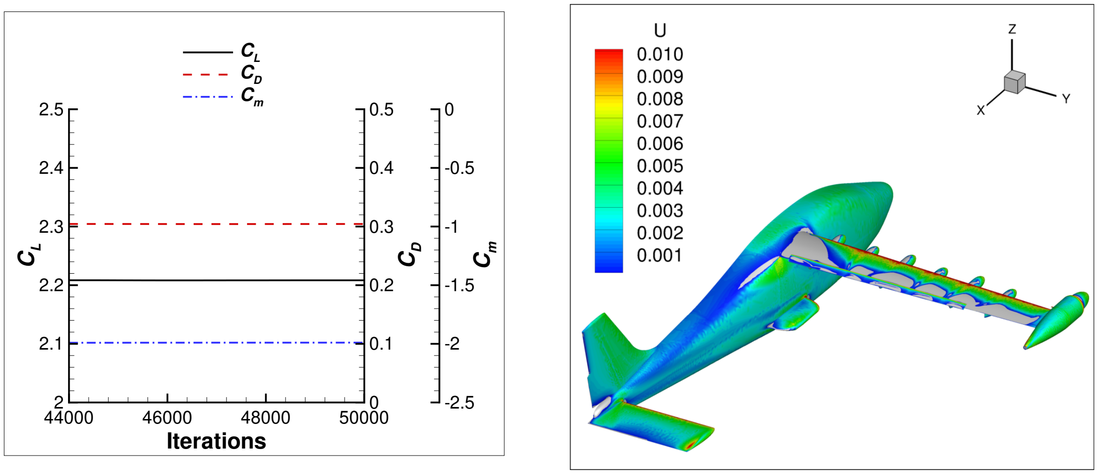

(e) Time-Averaged Coefficients

(f) Normalized U Velocity Contours

Figure B193. Convergence History Data and Normalized U Velocity Contours for the Takeoff Configuration with a 10° Flap Deflection at $M = 0.149$ and $\alpha = 16°$, No Cruise Power, and No High-Lift Blowing.

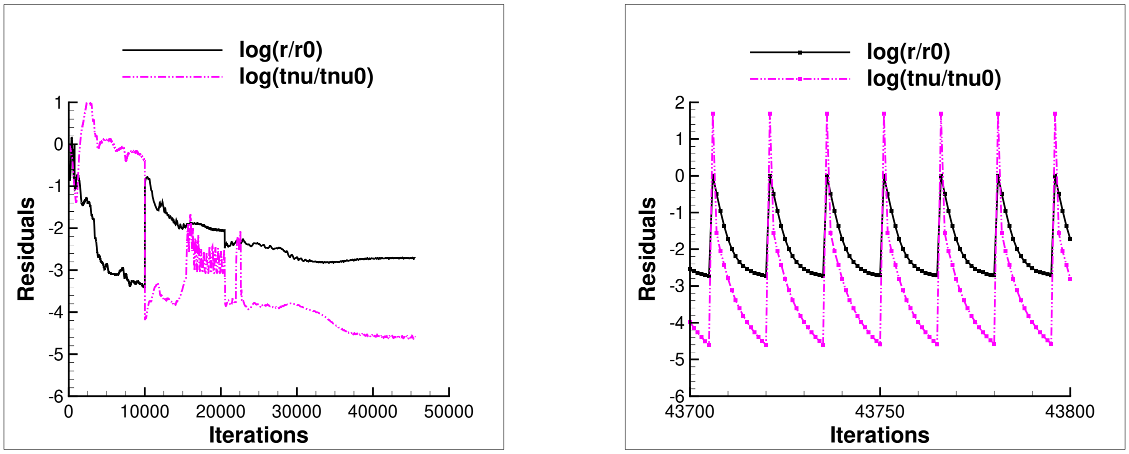

(a) Residuals

(b) SubIterations

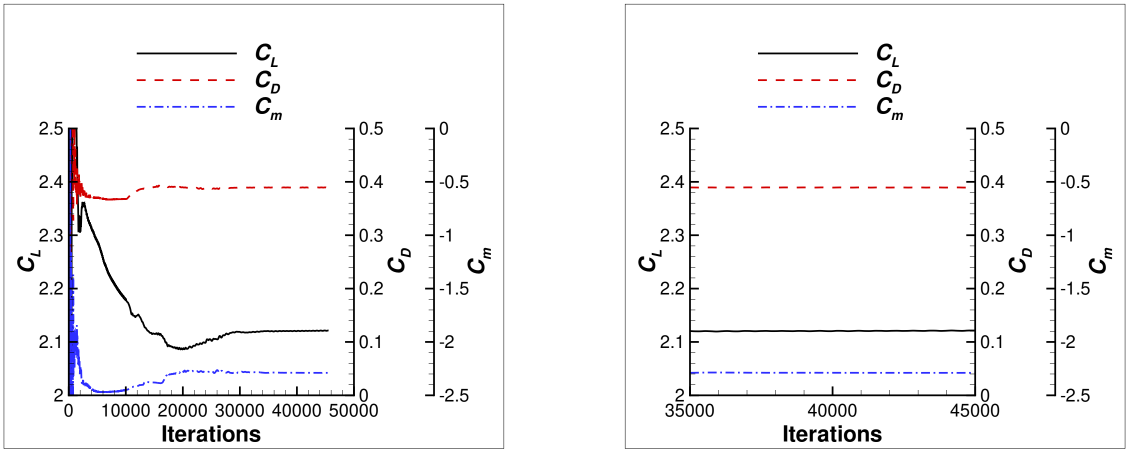

(c) Force and Moment Coefficients

(d) Coefficients with a Smaller Iteration Range

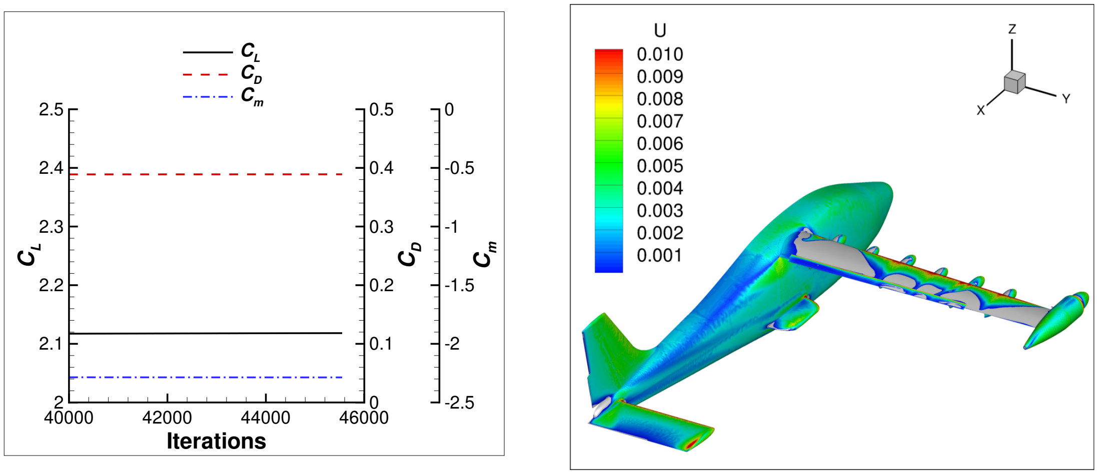

(e) Time-Averaged Coefficients

(f) Normalized U Velocity Contours

Figure B194. Convergence History Data and Normalized U Velocity Contours for the Takeoff Configuration with a 10° Flap Deflection at $M = 0.149$ and $\alpha = 18°$, No Cruise Power, and No High-Lift Blowing.

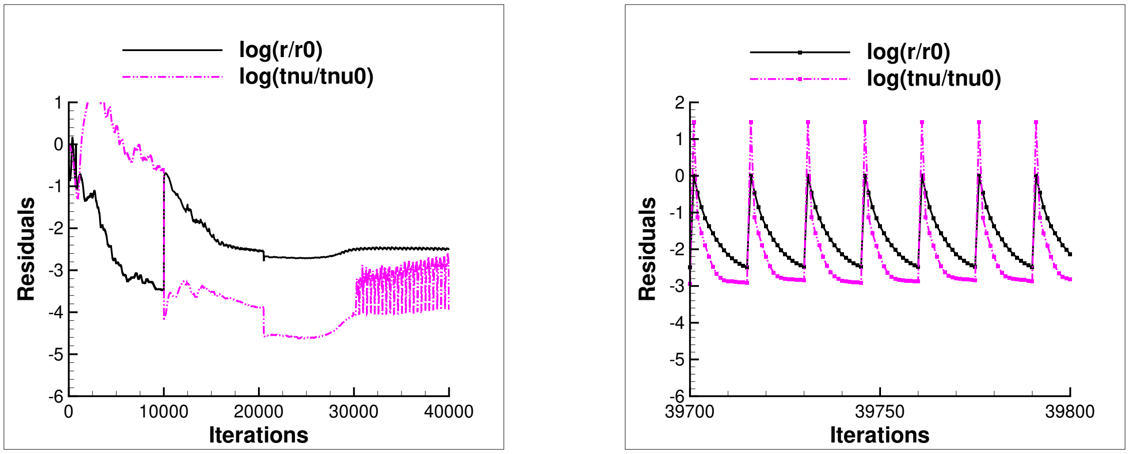

(a) Residuals (b) SubIterations

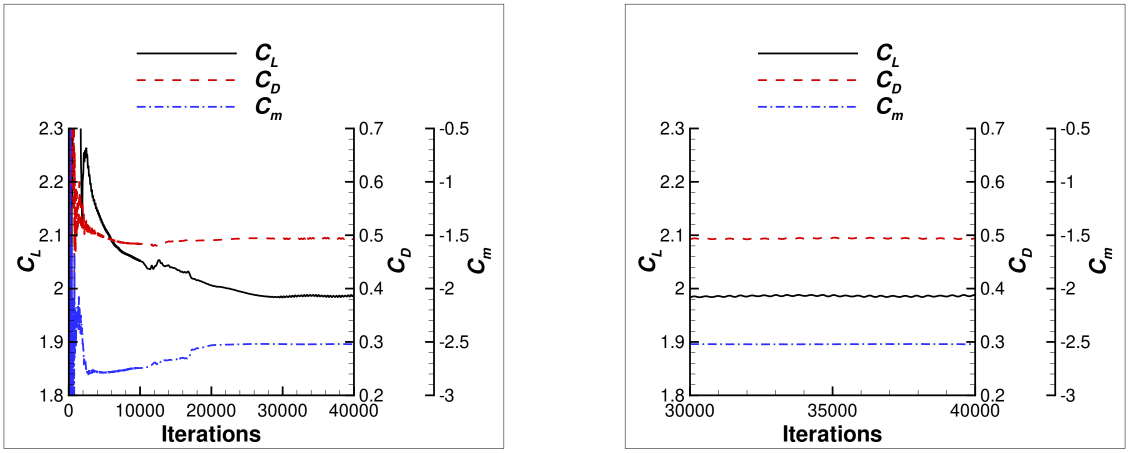

(c) Force and Moment Coefficients (d) Coefficients with a Smaller Iteration Range

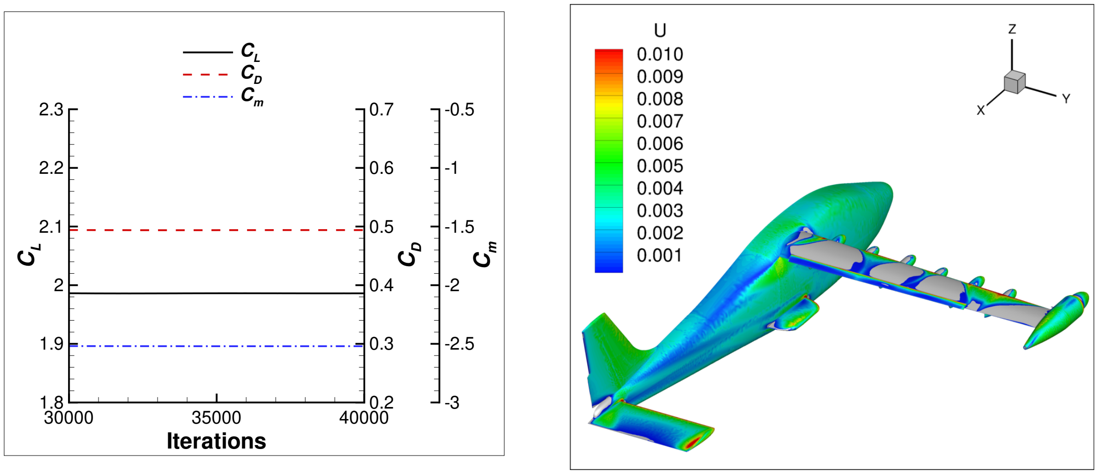

(e) Time-Averaged Coefficients (f) Normalized U Velocity Contours

Figure B195. Convergence History Data and Normalized U Velocity Contours for the Takeoff Configuration with a 10° Flap Deflection at $M = 0.149$ and $\alpha = 20°$, No Cruise Power, and No High-Lift Blowing.

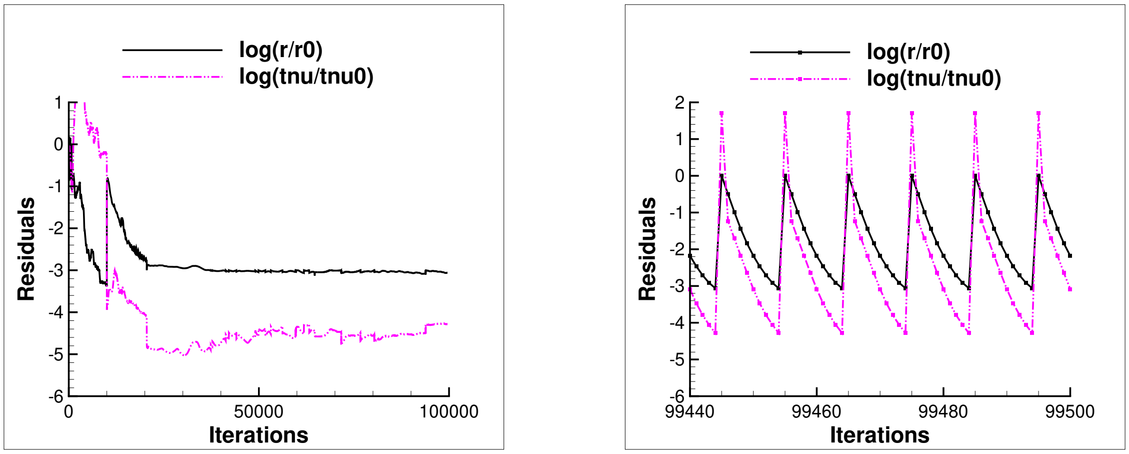

(a) Residuals (b) SubIterations

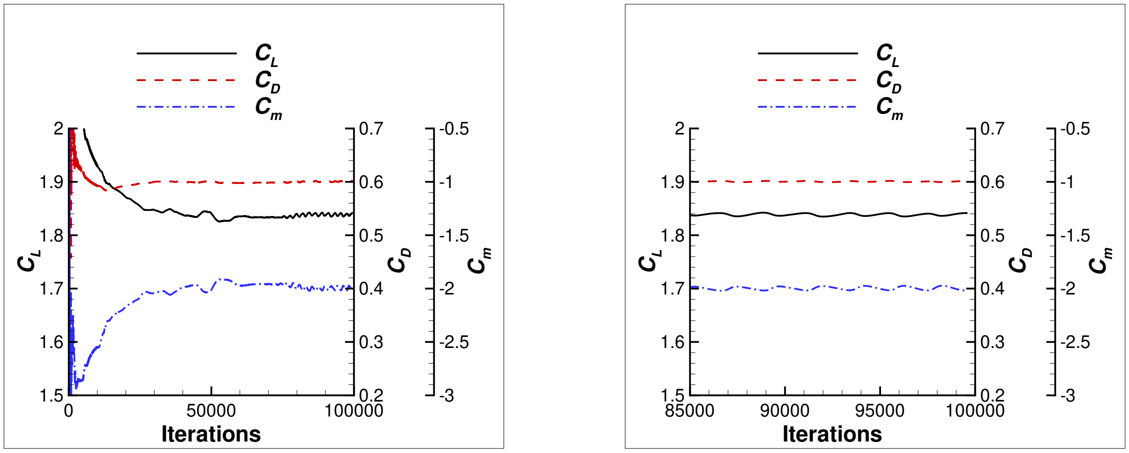

(c) Force and Moment Coefficients (d) Coefficients with a Smaller Iteration Range

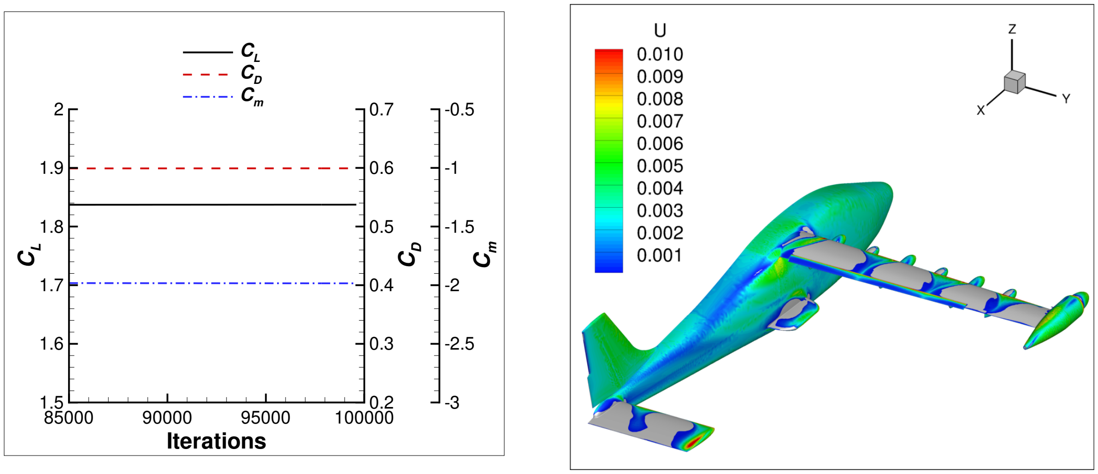

(e) Time-Averaged Coefficients (f) Normalized U Velocity Contours

Figure B196. Convergence History Data and Normalized U Velocity Contours for the Takeoff Configuration with a 10° Flap Deflection at $M = 0.149$ and $\alpha = 22°$, No Cruise Power, and No High-Lift Blowing.

Appendix C

Convergence: Landing Configuration with a 30° Flap Deflection

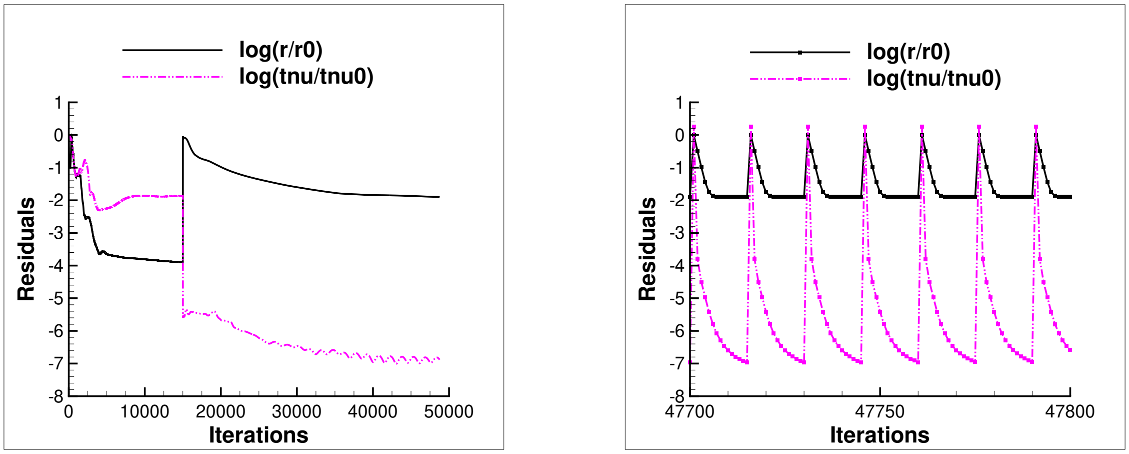

(a) Residuals (b) SubIterations

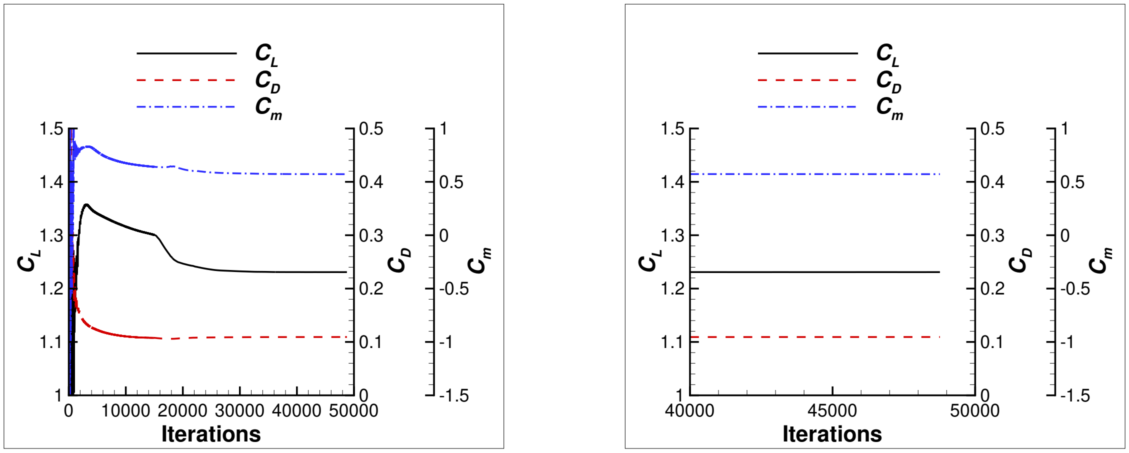

(c) Force and Moment Coefficients (d) Coefficients with a Smaller Iteration Range

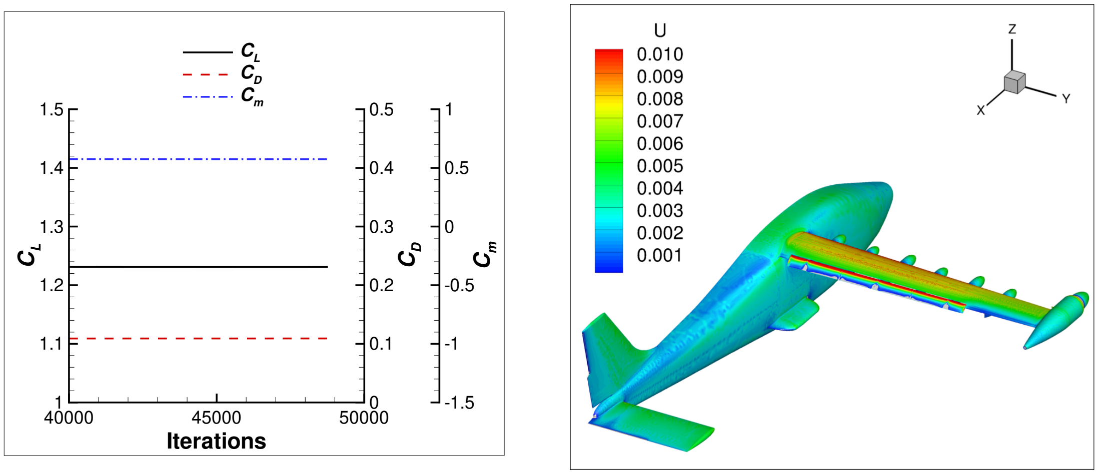

(e) Time-Averaged Coefficients (f) Normalized U Velocity Contours

Figure C197. Convergence History Data and Normalized U Velocity Contours for the Landing Configuration with a 30° Flap Deflection at $M = 0.139$ and $\alpha = -2°$, No Cruise Power, and No High-Lift Blowing.

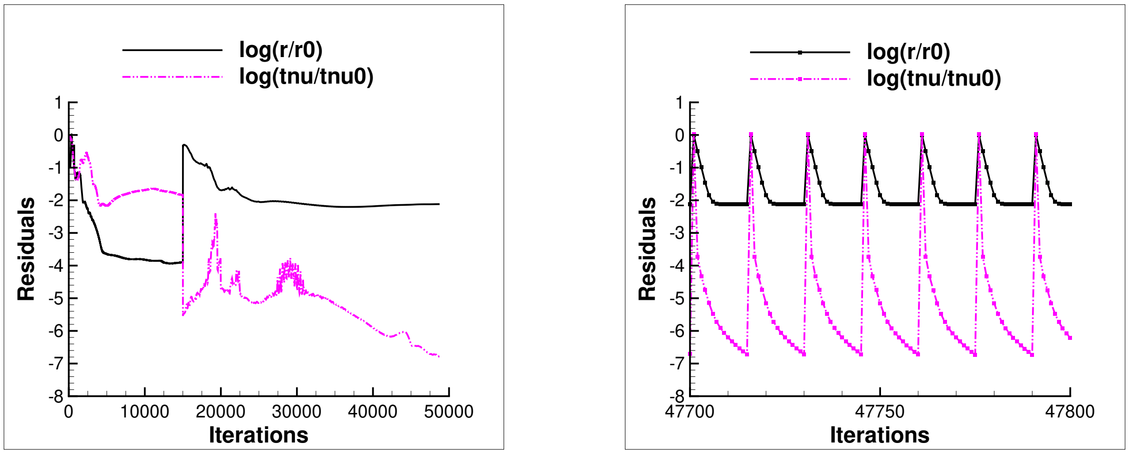

(a) Residuals

(b) SubIterations

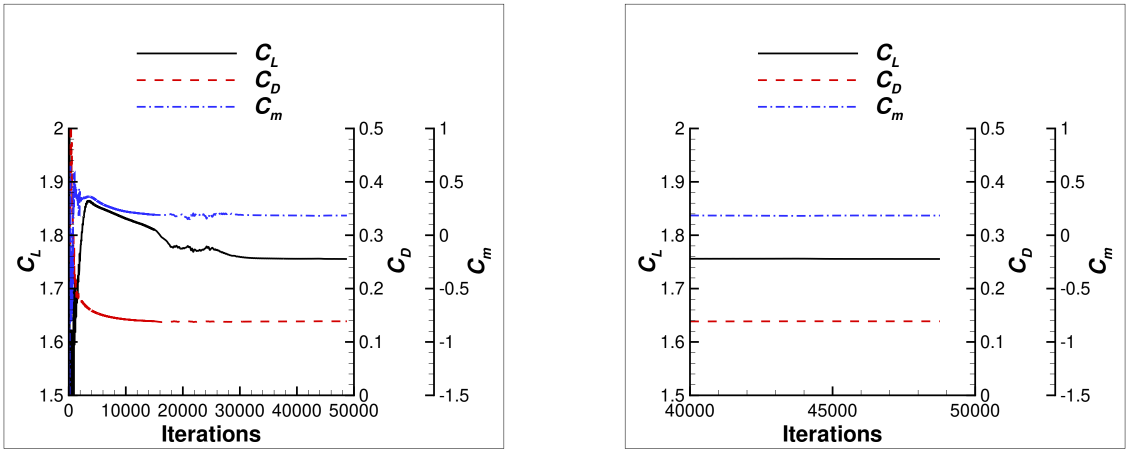

(c) Force and Moment Coefficients

(d) Coefficients with a Smaller Iteration Range

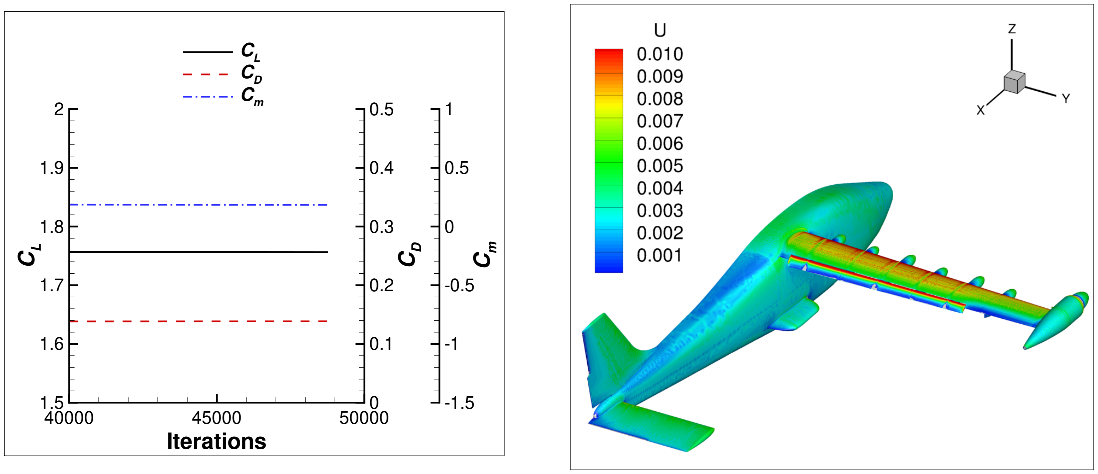

(e) Time-Averaged Coefficients

(f) Normalized U Velocity Contours

Figure C198. Convergence History Data and Normalized U Velocity Contours for the Landing Configuration with a 30° Flap Deflection at $M = 0.139$ and $\alpha = 2°$, No Cruise Power, and No High-Lift Blowing.

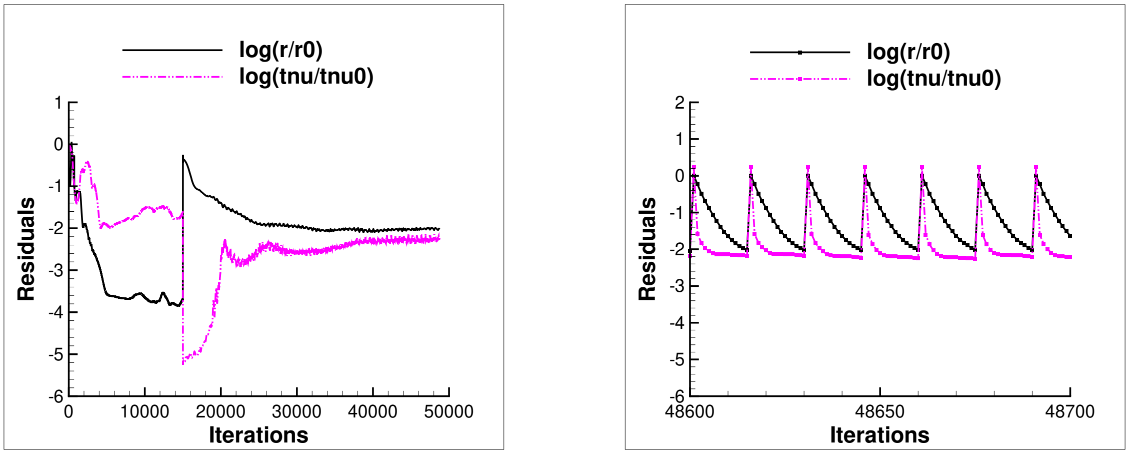

(a) Residuals (b) SubIterations

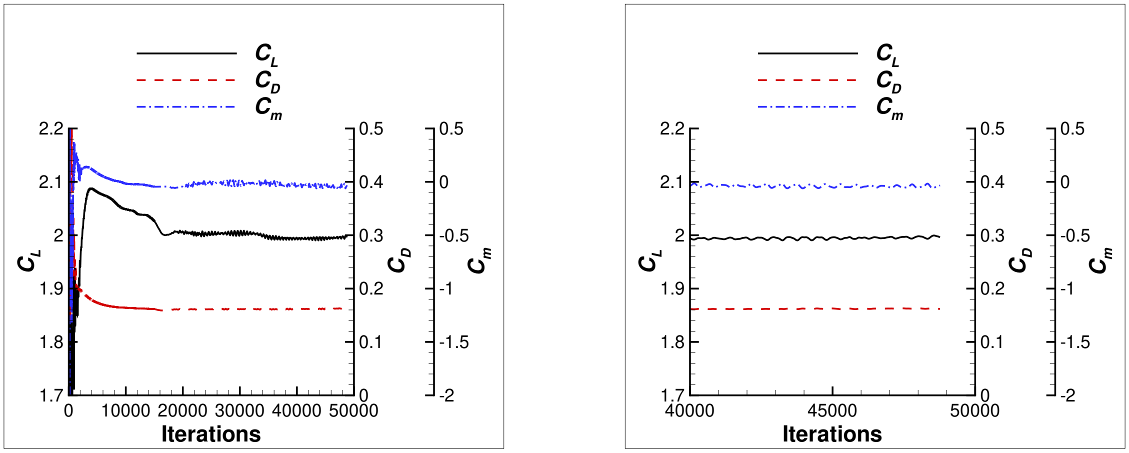

(c) Force and Moment Coefficients (d) Coefficients with a Smaller Iteration Range

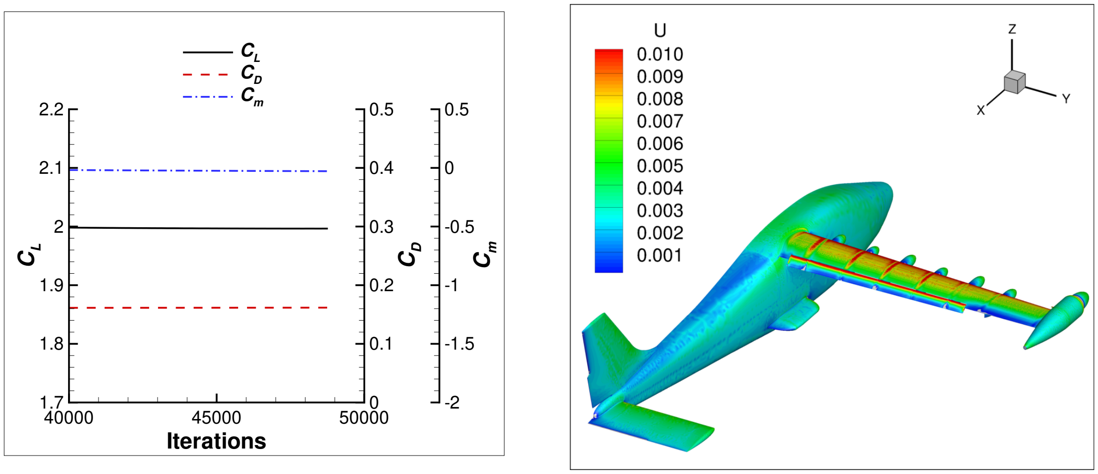

(e) Time-Averaged Coefficients (f) Normalized U Velocity Contours

Figure C199. Convergence History Data and Normalized U Velocity Contours for the Landing Configuration with a 30° Flap Deflection at $M = 0.139$ and $\alpha = 4°$, No Cruise Power, and No High-Lift Blowing.

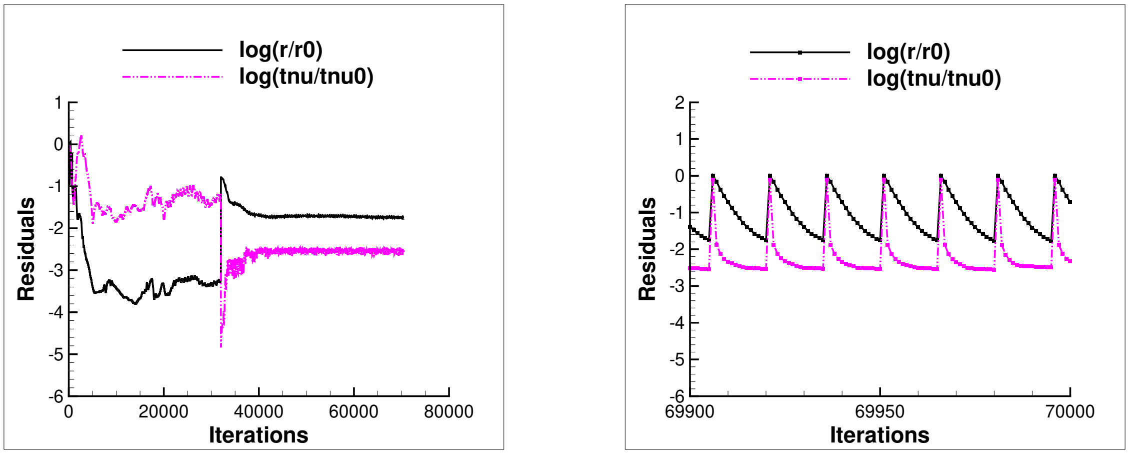

(a) Residuals

(b) SubIterations

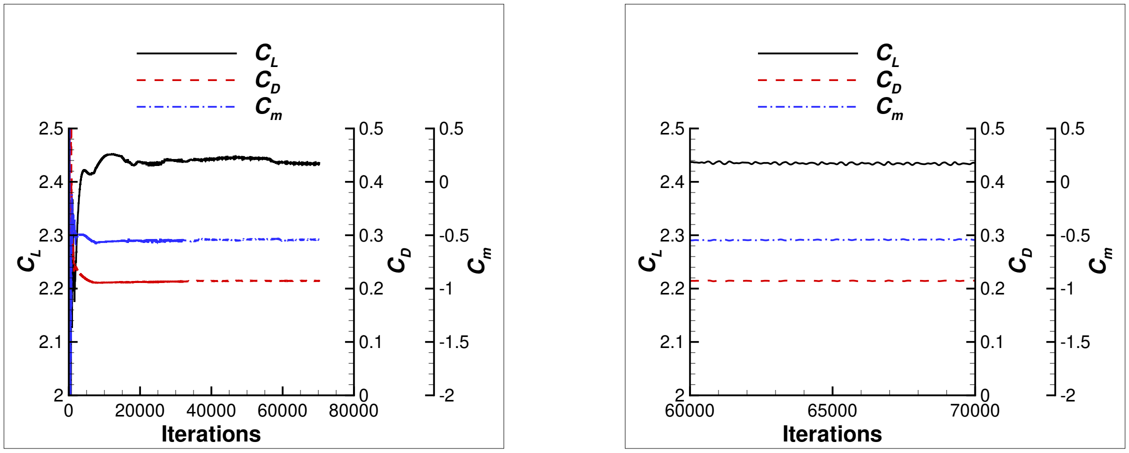

(c) Force and Moment Coefficients

(d) Coefficients with a Smaller Iteration Range

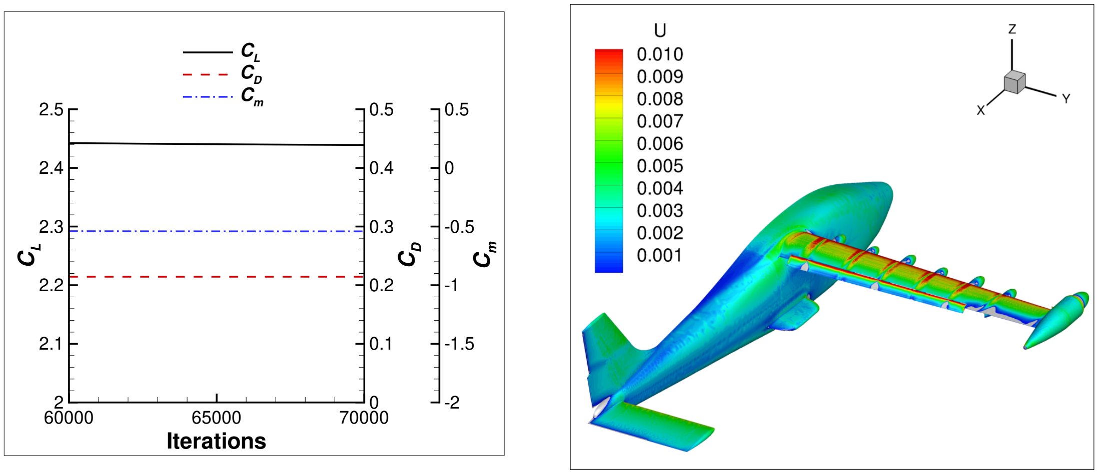

(e) Time-Averaged Coefficients

(f) Normalized U Velocity Contours

Figure C200. Convergence History Data and Normalized U Velocity Contours for the Landing Configuration with a 30° Flap Deflection at $M = 0.139$ and $\alpha = 8°$, No Cruise Power, and No High-Lift Blowing.

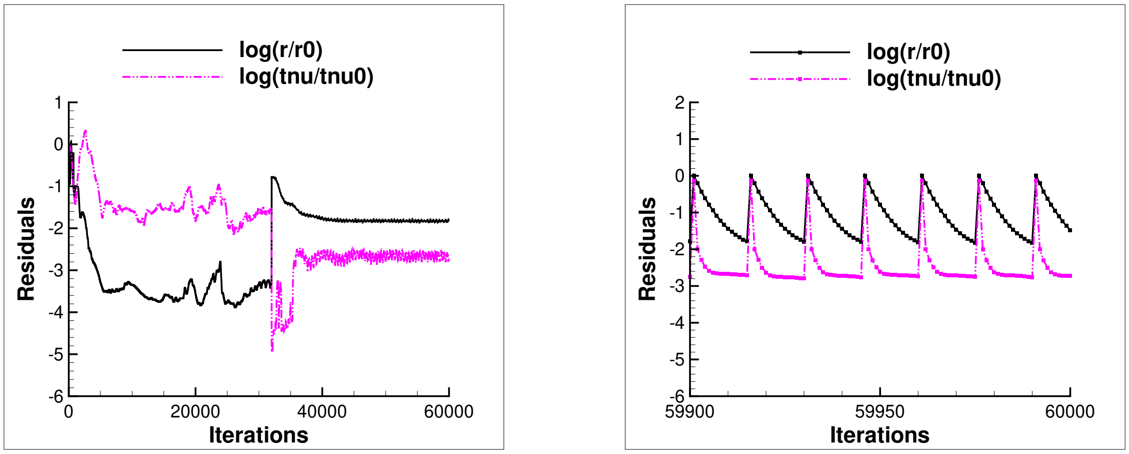

(a) Residuals (b) SubIterations

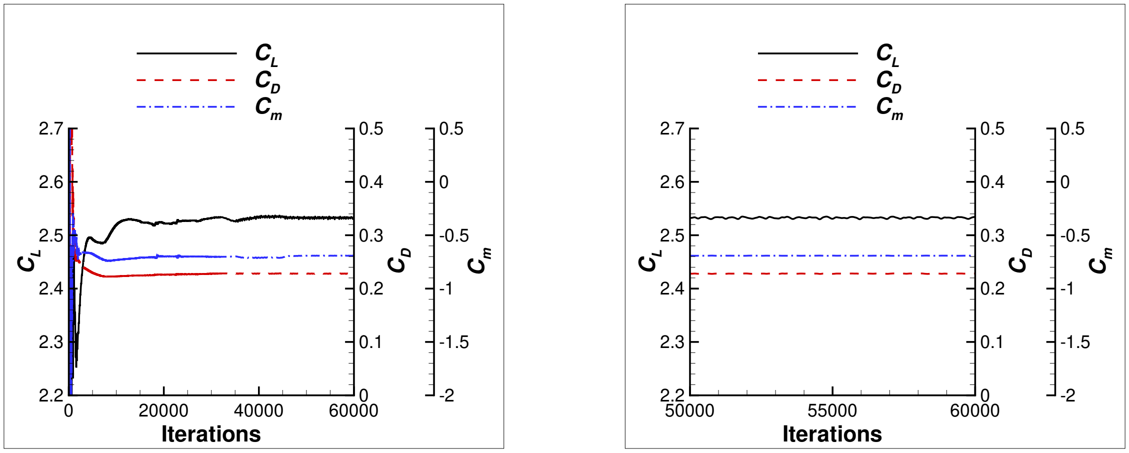

(c) Force and Moment Coefficients (d) Coefficients with a Smaller Iteration Range

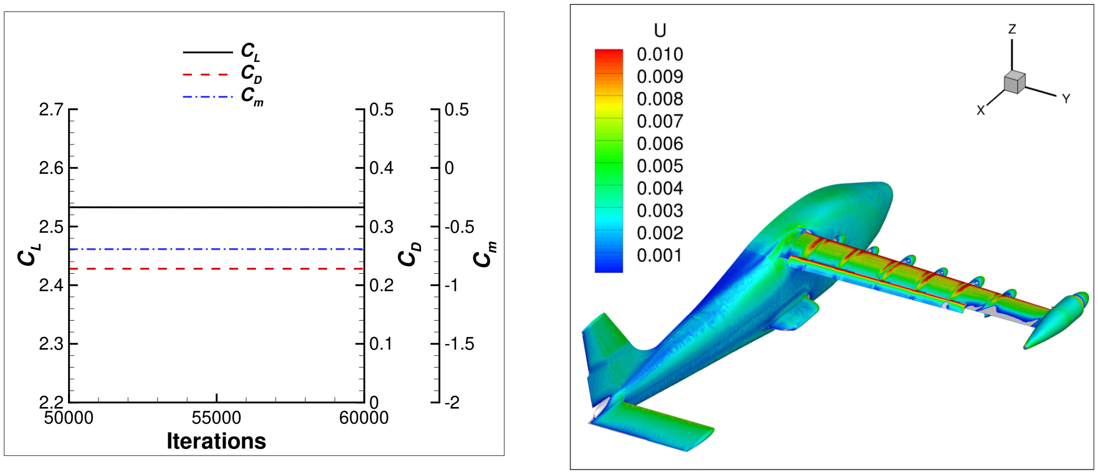

(e) Time-Averaged Coefficients (f) Normalized U Velocity Contours

Figure C201. Convergence History Data and Normalized U Velocity Contours for the Landing Configuration with a 30° Flap Deflection at $M = 0.139$ and $\alpha = 9°$, No Cruise Power, and No High-Lift Blowing.

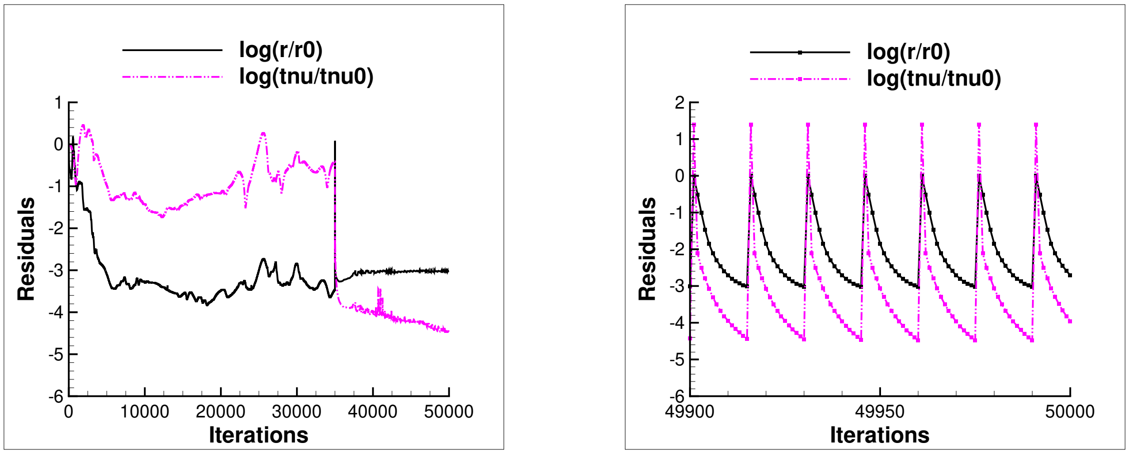

(a) Residuals

(b) SubIterations

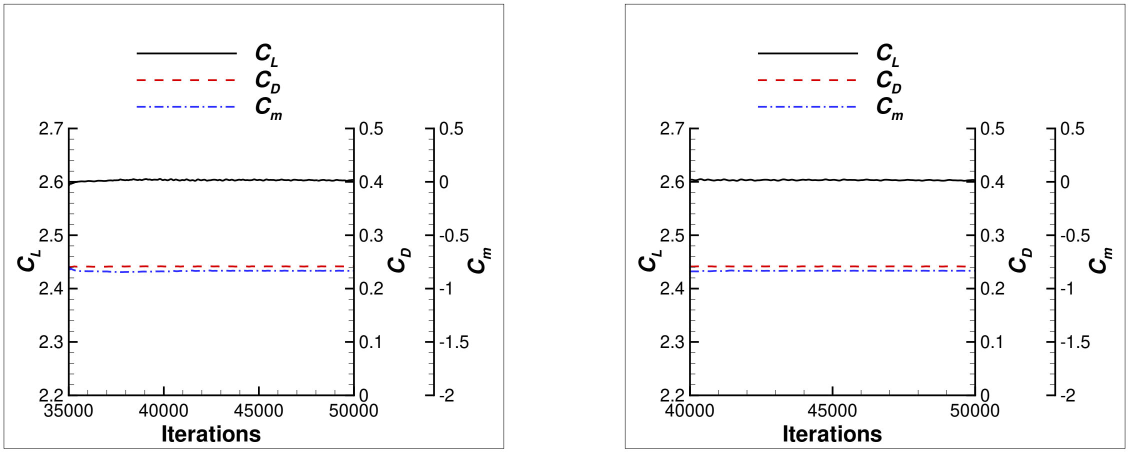

(c) Force and Moment Coefficients

(d) Coefficients with a Smaller Iteration Range

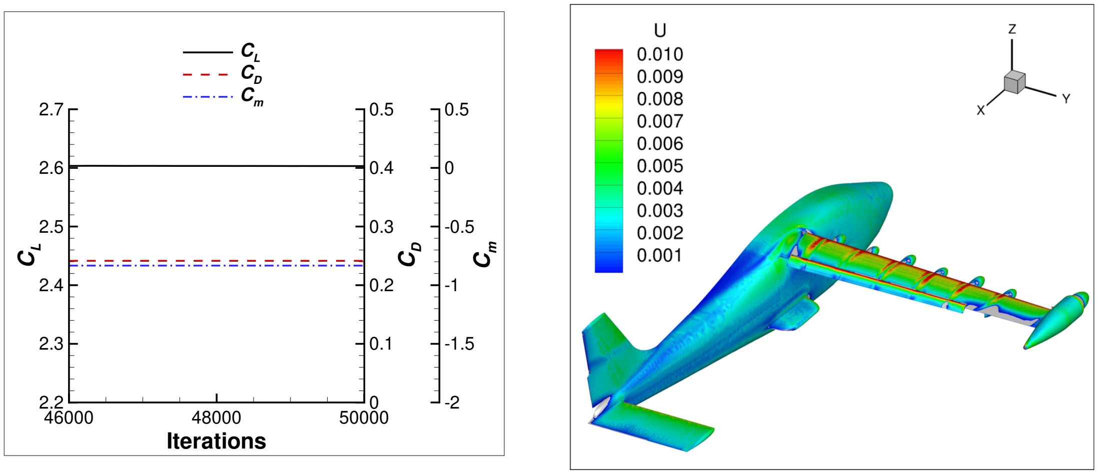

(e) Time-Averaged Coefficients

(f) Normalized U Velocity Contours

Figure C202. Convergence History Data and Normalized U Velocity Contours for the Landing Configuration with a 30° Flap Deflection at $M = 0.139$ and $\alpha = 10°$, No Cruise Power, and No High-Lift Blowing.

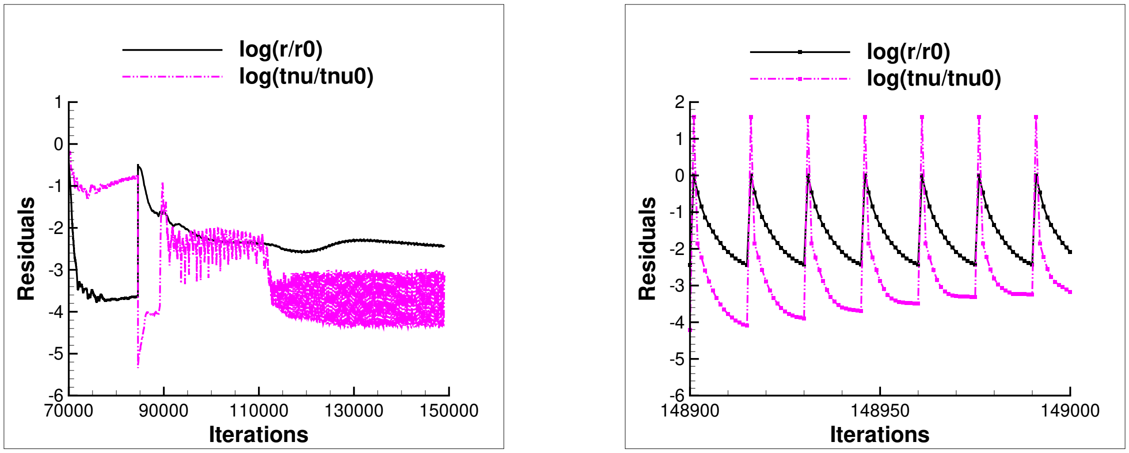

(a) Residuals

(b) SubIterations

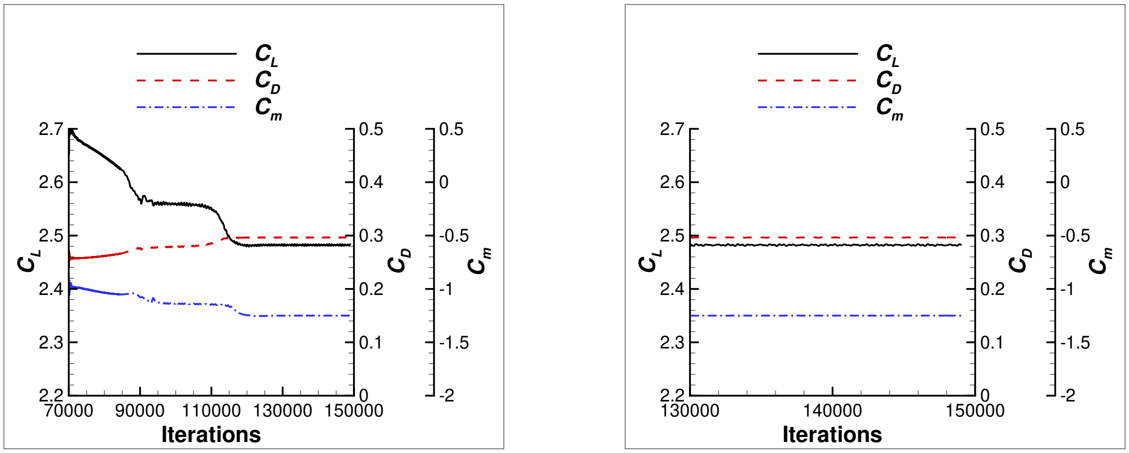

(c) Force and Moment Coefficients

(d) Coefficients with a Smaller Iteration Range

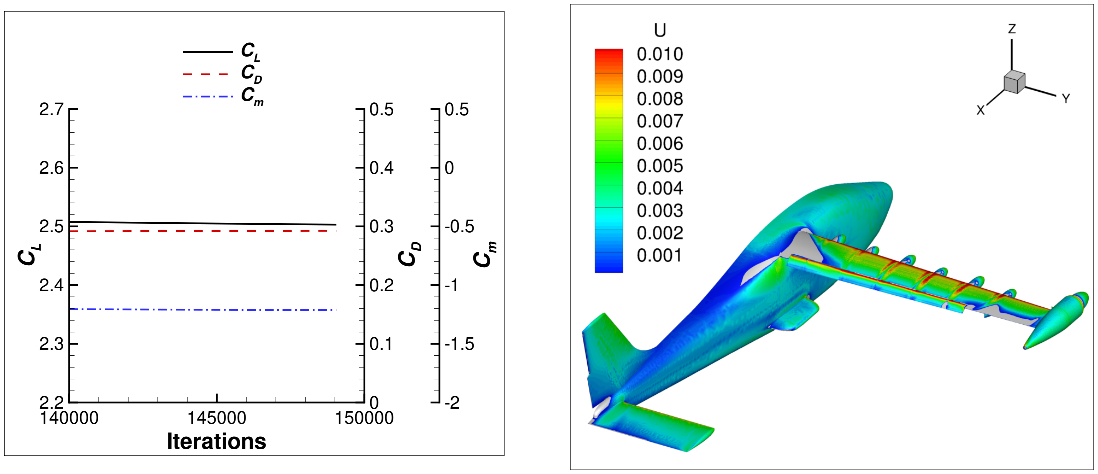

(e) Time-Averaged Coefficients

(f) Normalized U Velocity Contours

Figure C203. Convergence History Data and Normalized U Velocity Contours for the Landing Configuration with a 30° Flap Deflection at $M = 0.139$ and $\alpha = 11°$ (continued from $\alpha = 10°$ solution), No Cruise Power, and No High-Lift Blowing.

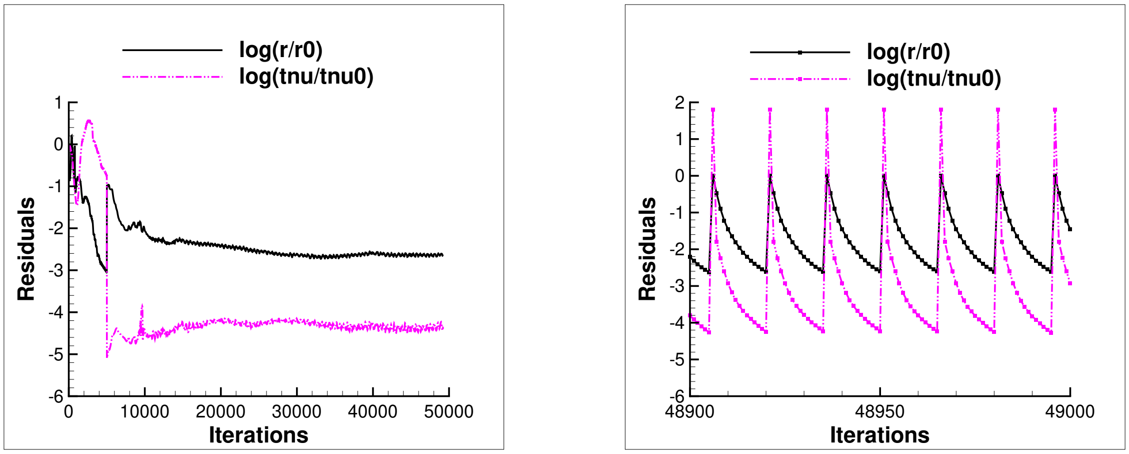

(a) Residuals

(b) SubIterations

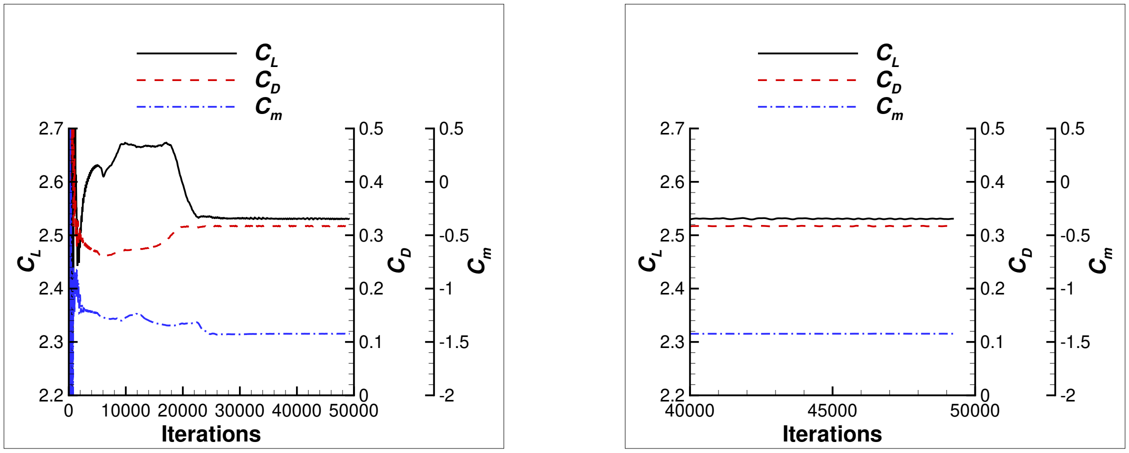

(c) Force and Moment Coefficients

(d) Coefficients with a Smaller Iteration Range

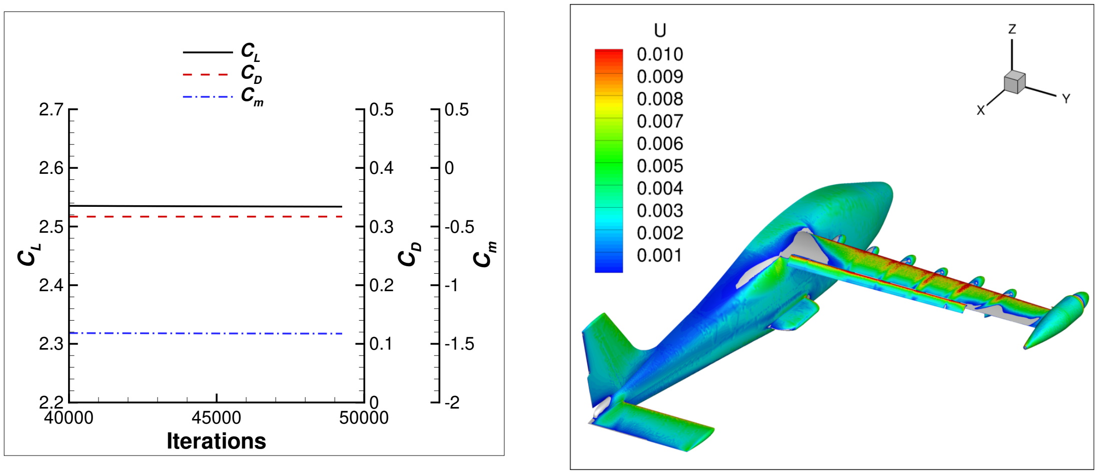

(e) Time-Averaged Coefficients

(f) Normalized U Velocity Contours

Figure C204. Convergence History Data and Normalized U Velocity Contours for the Landing Configuration with a 30° Flap Deflection at $M = 0.139$ and $\alpha = 12°$, No Cruise Power, and No High-Lift Blowing.

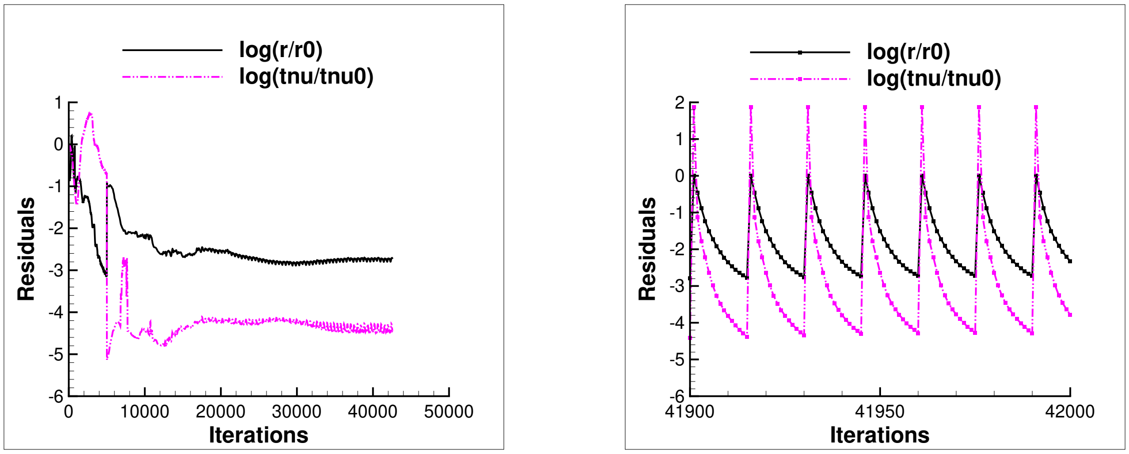

(a) Residuals

(b) SubIterations

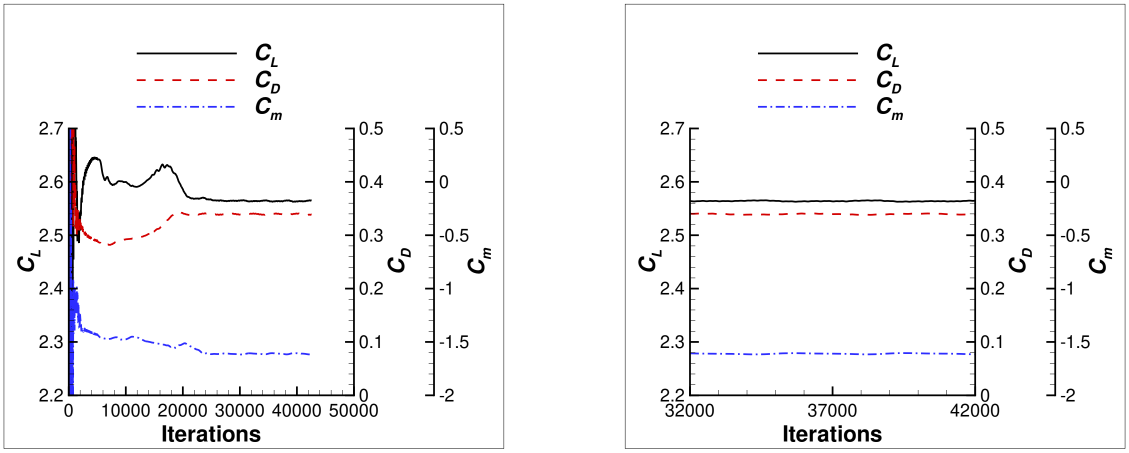

(c) Force and Moment Coefficients

(d) Coefficients with a Smaller Iteration Range

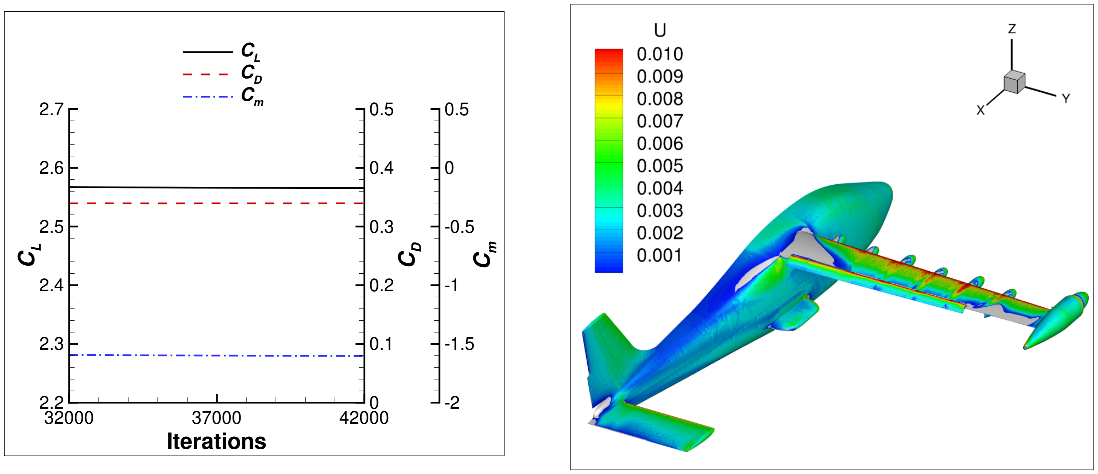

(e) Time-Averaged Coefficients

(f) Normalized U Velocity Contours

Figure C205. Convergence History Data and Normalized U Velocity Contours for the Landing Configuration with a 30° Flap Deflection at $M = 0.139$ and $\alpha = 13°$, No Cruise Power, and No High-Lift Blowing.

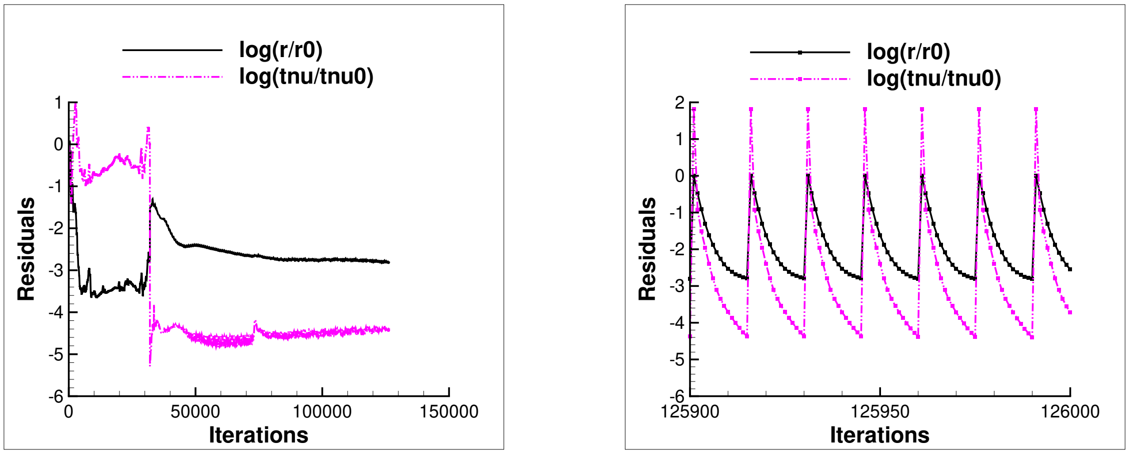

(a) Residuals (b) SubIterations

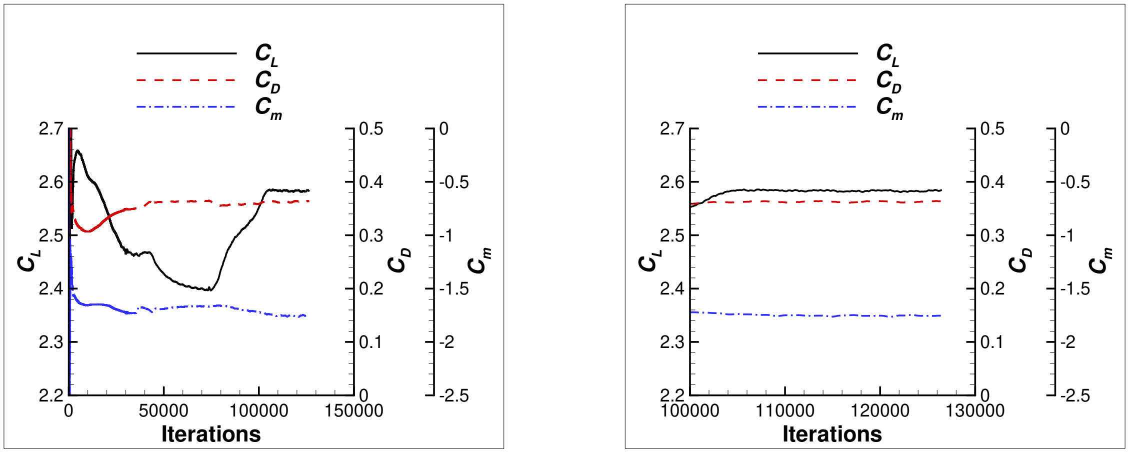

(c) Force and Moment Coefficients (d) Coefficients with a Smaller Iteration Range

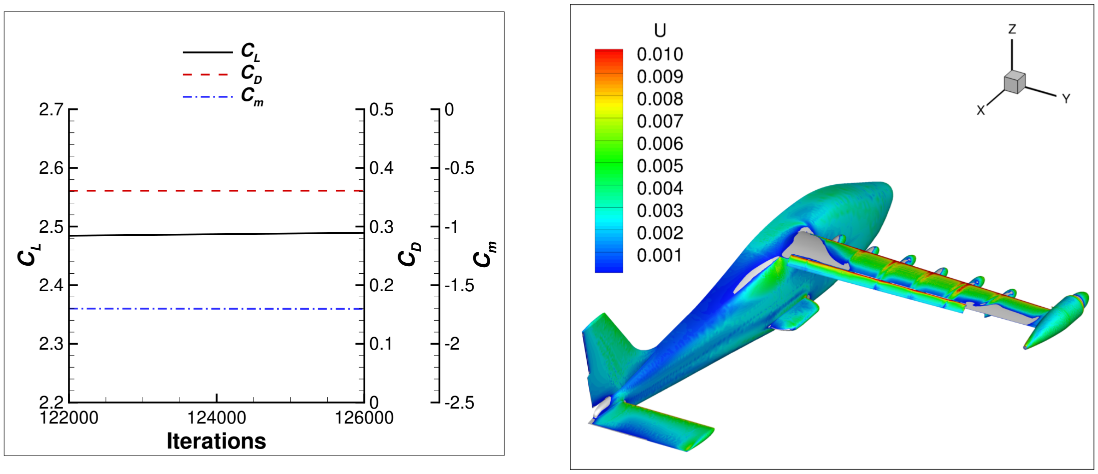

(e) Time-Averaged Coefficients (f) Normalized U Velocity Contours

Figure C206. Convergence History Data and Normalized U Velocity Contours for the Landing Configuration with a 30° Flap Deflection at $M = 0.139$ and $\alpha = 14°$, No Cruise Power, and No High-Lift Blowing.

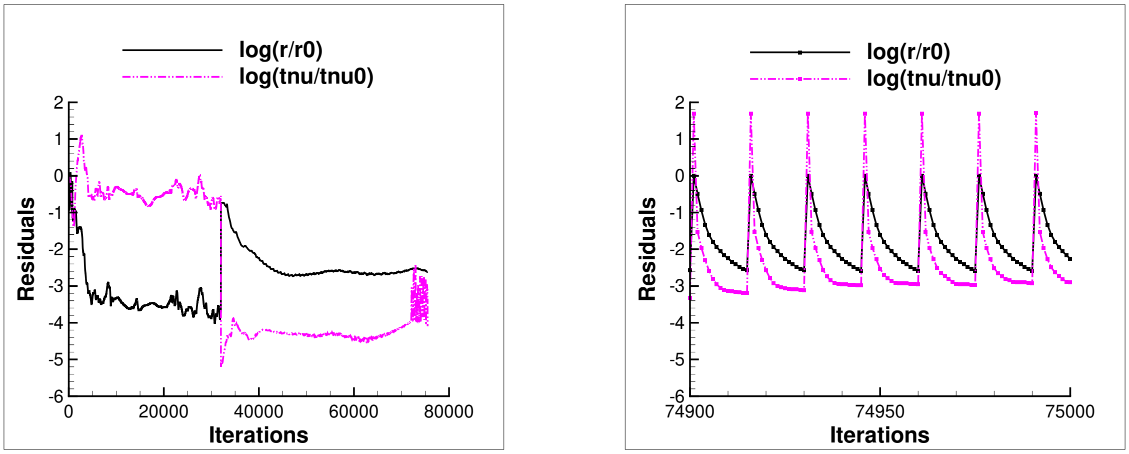

(a) Residuals

(b) SubIterations

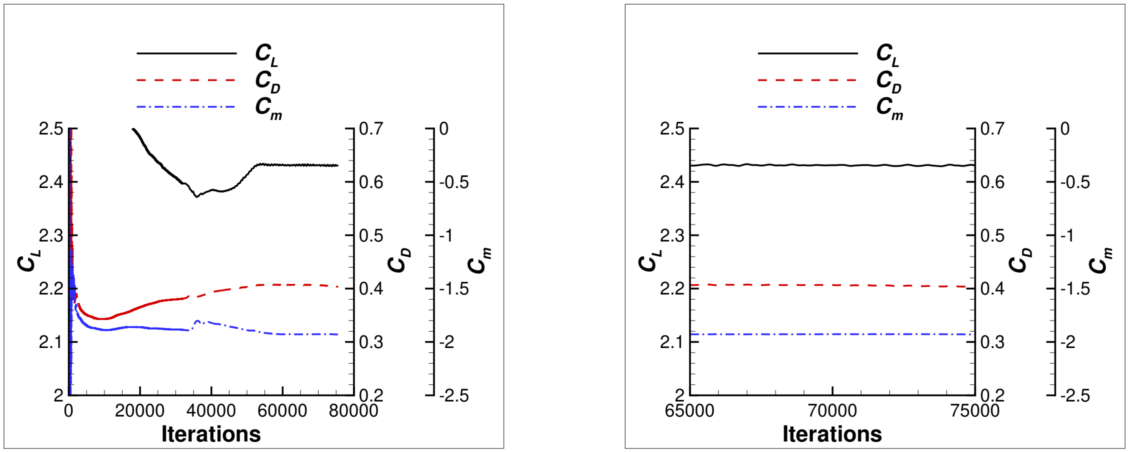

(c) Force and Moment Coefficients

(d) Coefficients with a Smaller Iteration Range

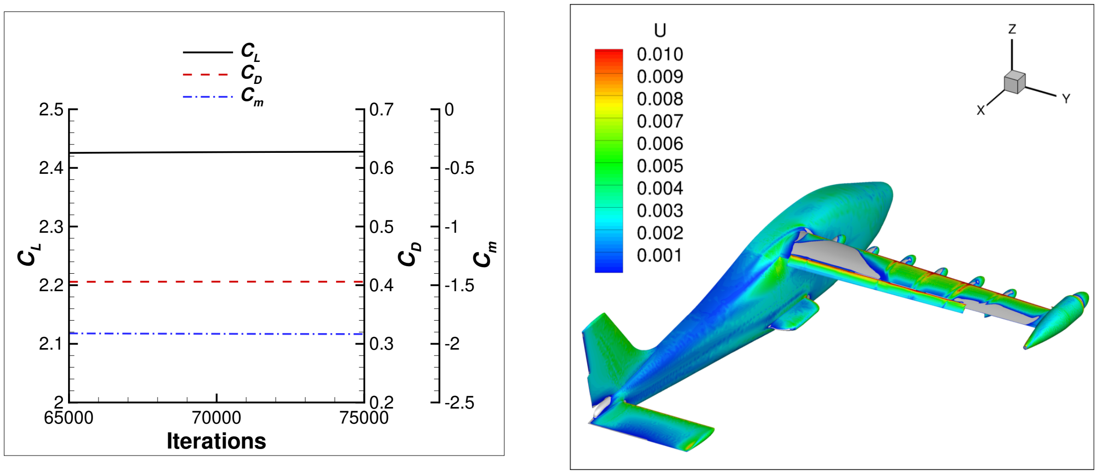

(e) Time-Averaged Coefficients

(f) Normalized U Velocity Contours

Figure C207. Convergence History Data and Normalized U Velocity Contours for the Landing Configuration with a 30° Flap Deflection at $M = 0.139$ and $\alpha = 15°$, No Cruise Power,and No High-Lift Blowing.

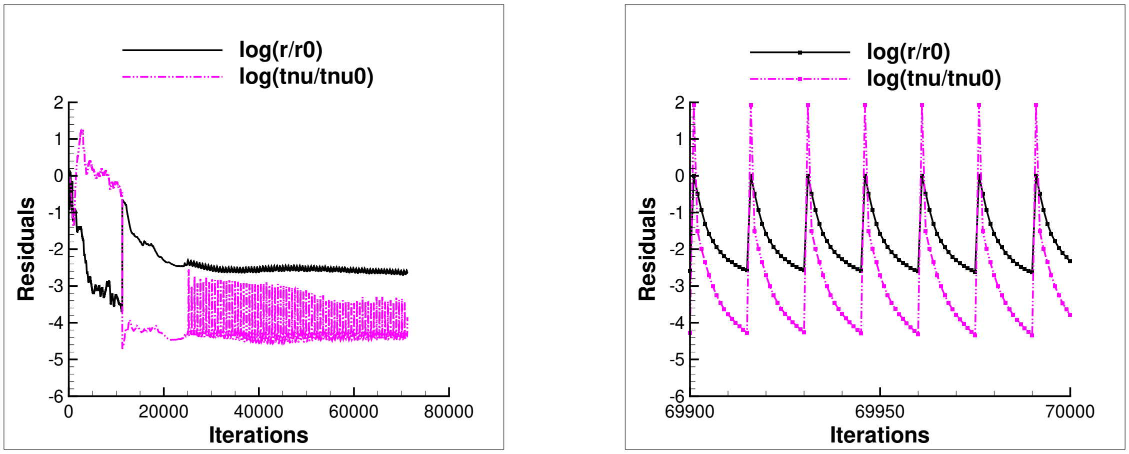

(a) Residuals

(b) SubIterations

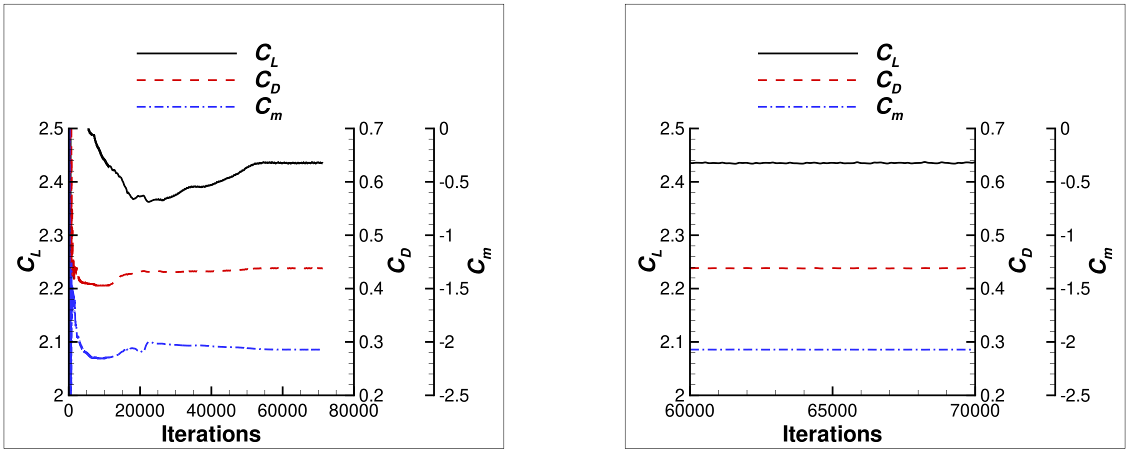

(c) Force and Moment Coefficients

(d) Coefficients with a Smaller Iteration Range

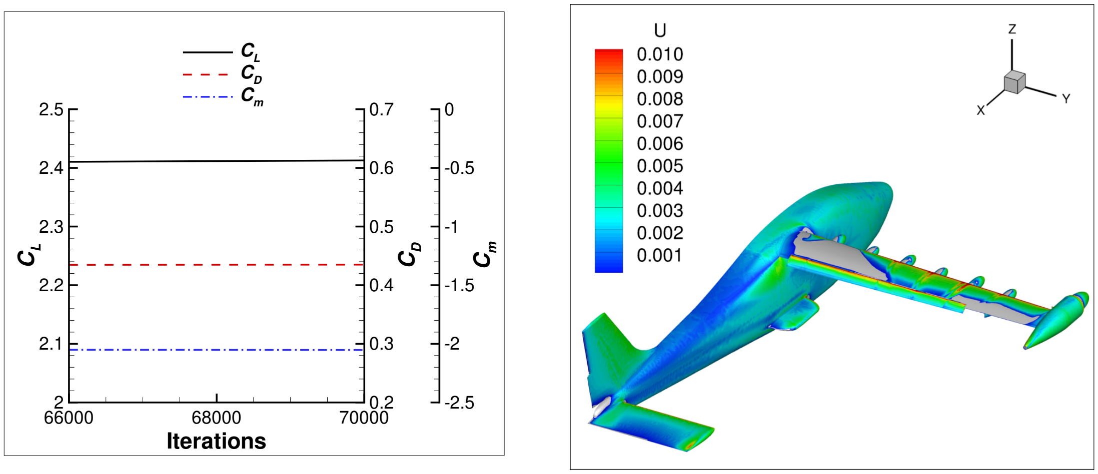

(e) Time-Averaged Coefficients

(f) Normalized U Velocity Contours

Figure C208. Convergence History Data and Normalized U Velocity Contours for the Landing Configuration with a 30° Flap Deflection at $M = 0.139$ and $\alpha = 16°$, No Cruise Power, and No High-Lift Blowing.

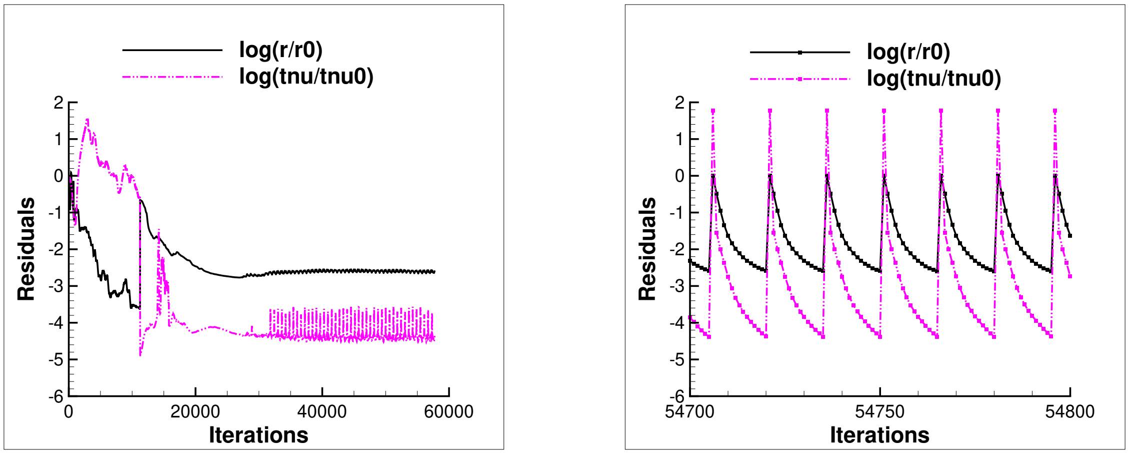

(a) Residuals

(b) SubIterations

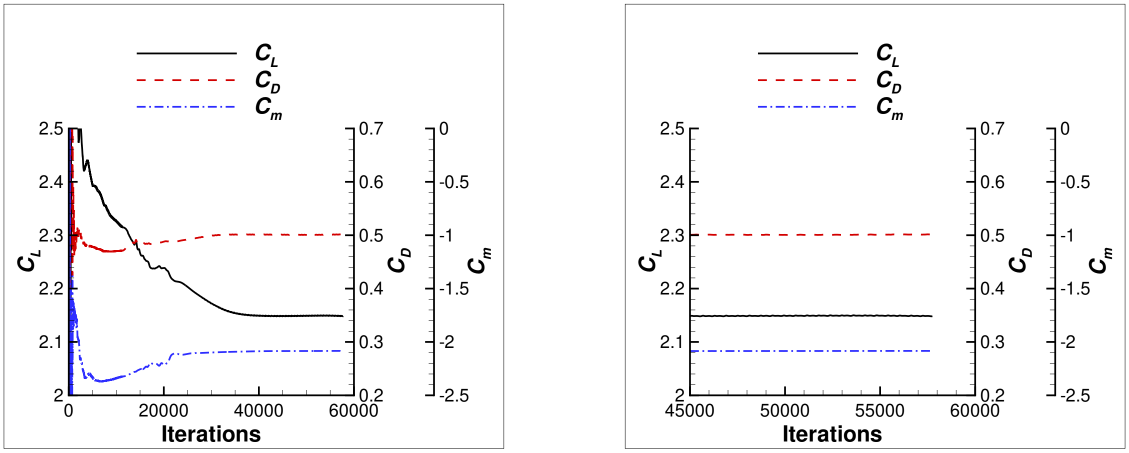

(c) Force and Moment Coefficients

(d) Coefficients with a Smaller Iteration Range

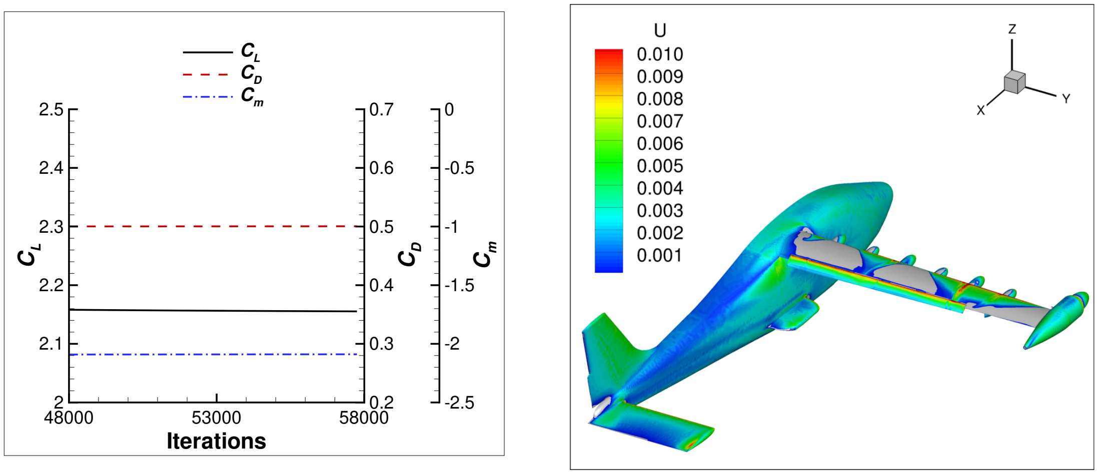

(e) Time-Averaged Coefficients

(f) Normalized U Velocity Contours

Figure C209. Convergence History Data and Normalized U Velocity Contours for the Landing Configuration with a 30° Flap Deflection at $M = 0.139$ and $\alpha = 17°$, No Cruise Power, and No High-Lift Blowing.

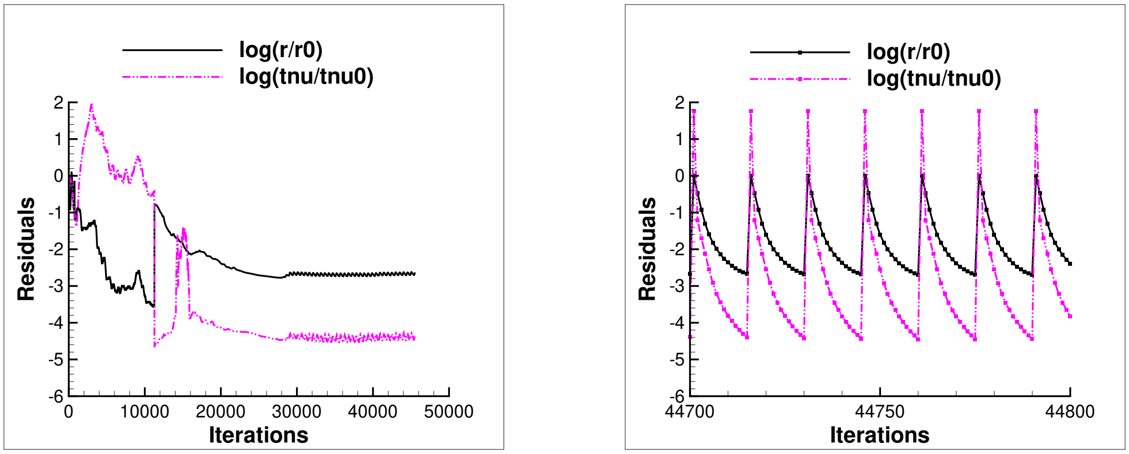

(a) Residuals

(b) SubIterations

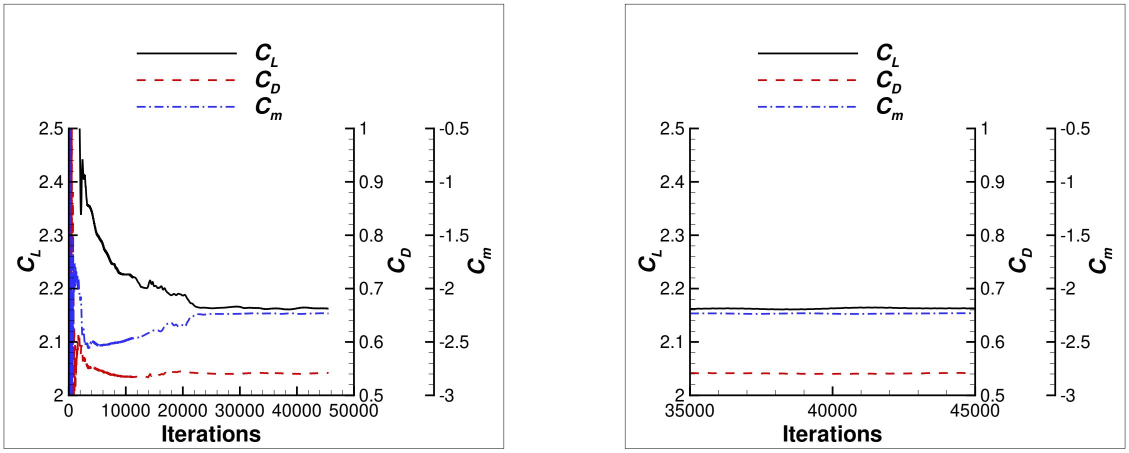

(c) Force and Moment Coefficients

(d) Coefficients with a Smaller Iteration Range

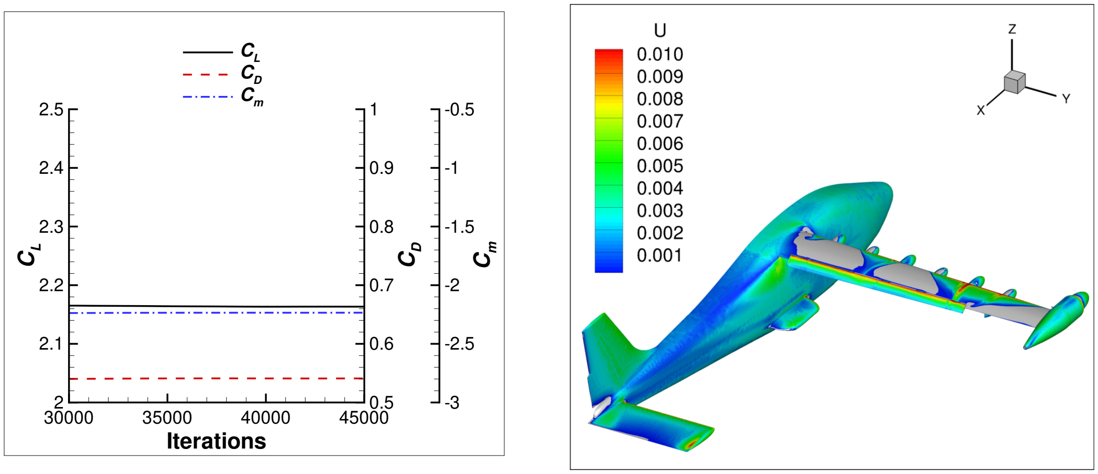

(e) Time-Averaged Coefficients

(f) Normalized U Velocity Contours

Figure C210. Convergence History Data and Normalized U Velocity Contours for the Landing Configuration with a 30° Flap Deflection at $M = 0.139$ and $\alpha = 18°$, No Cruise Power, and No High-Lift Blowing.

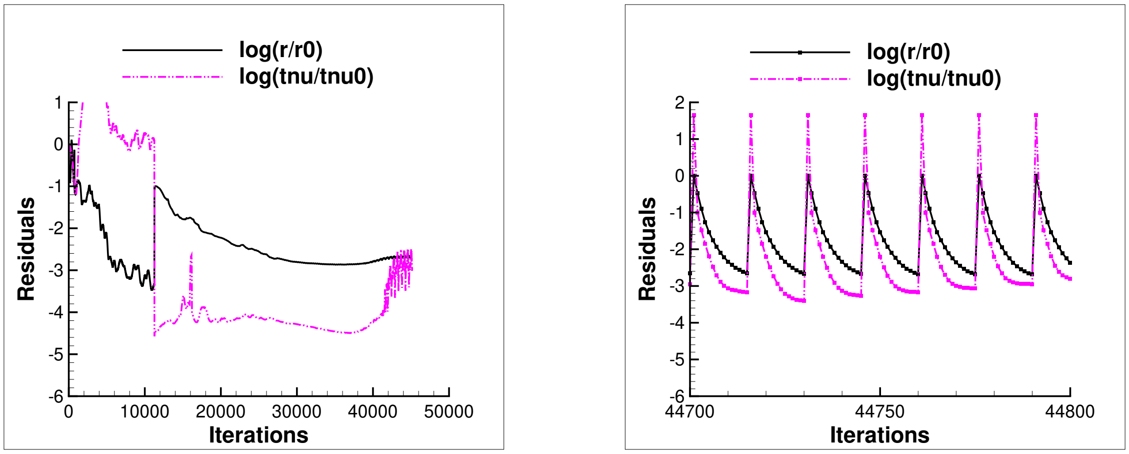

(a) Residuals

(b) SubIterations

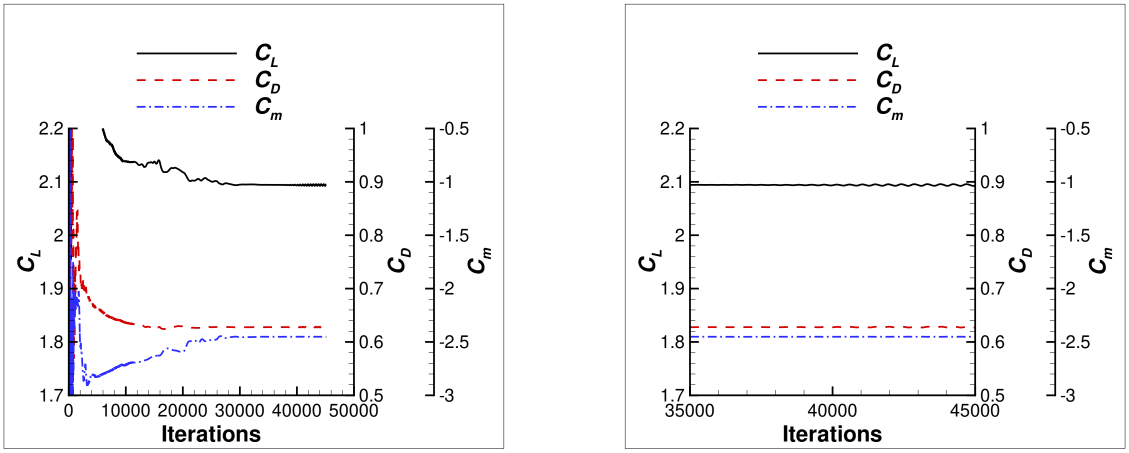

(c) Force and Moment Coefficients

(d) Coefficients with a Smaller Iteration Range

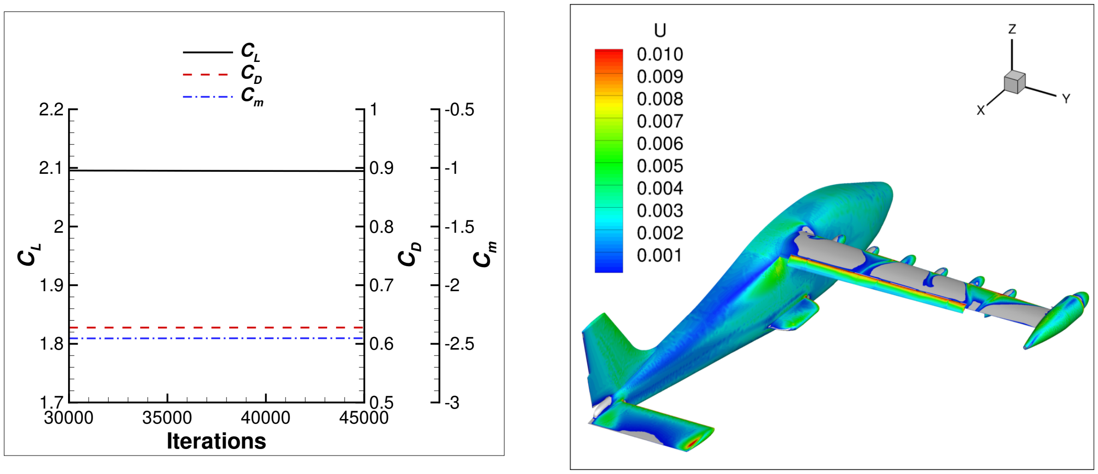

(e) Time-Averaged Coefficients

(f) Normalized U Velocity Contours

Figure C211. Convergence History Data and Normalized U Velocity Contours for the Landing Configuration with a 30° Flap Deflection at $M = 0.139$ and $\alpha = 20°$, No Cruise Power, and No High-Lift Blowing.

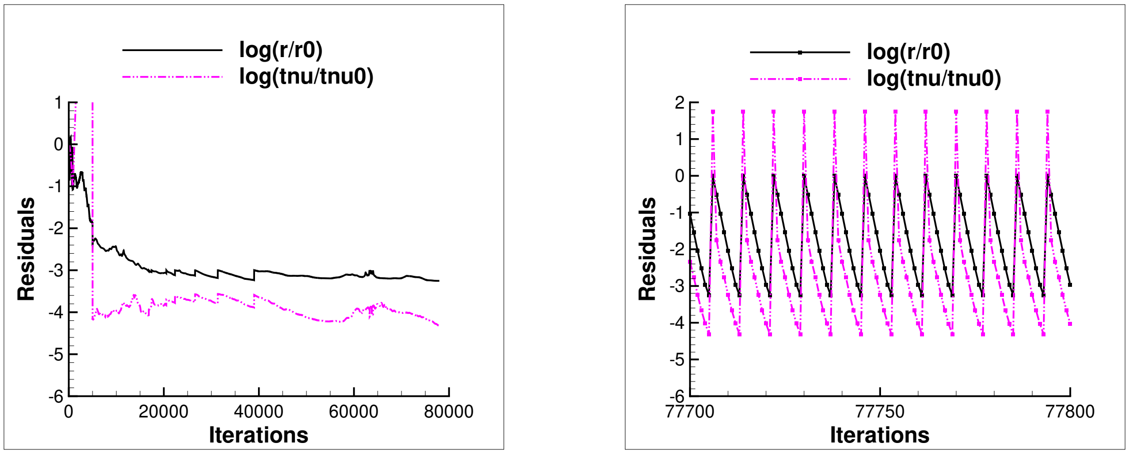

(a) Residuals (b) SubIterations

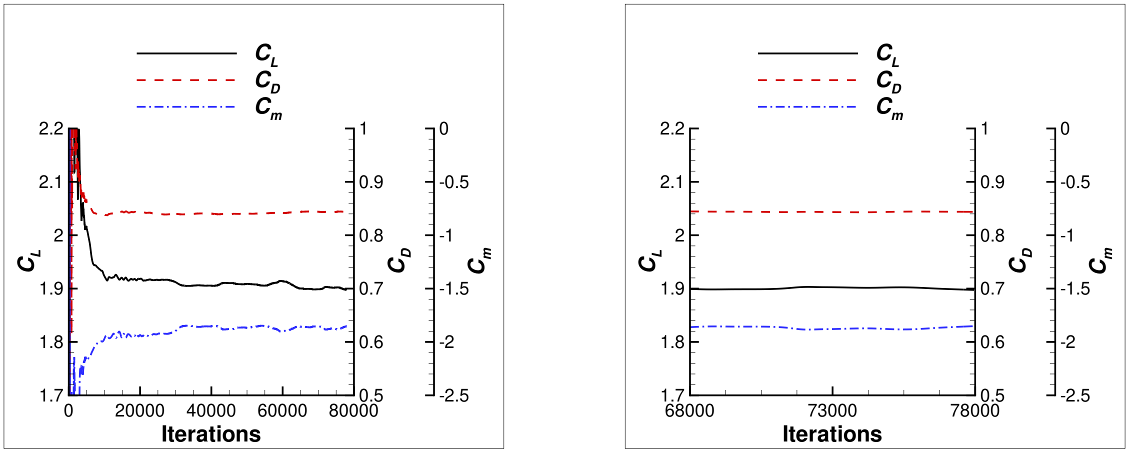

(c) Force and Moment Coefficients (d) Coefficients with a Smaller Iteration Range

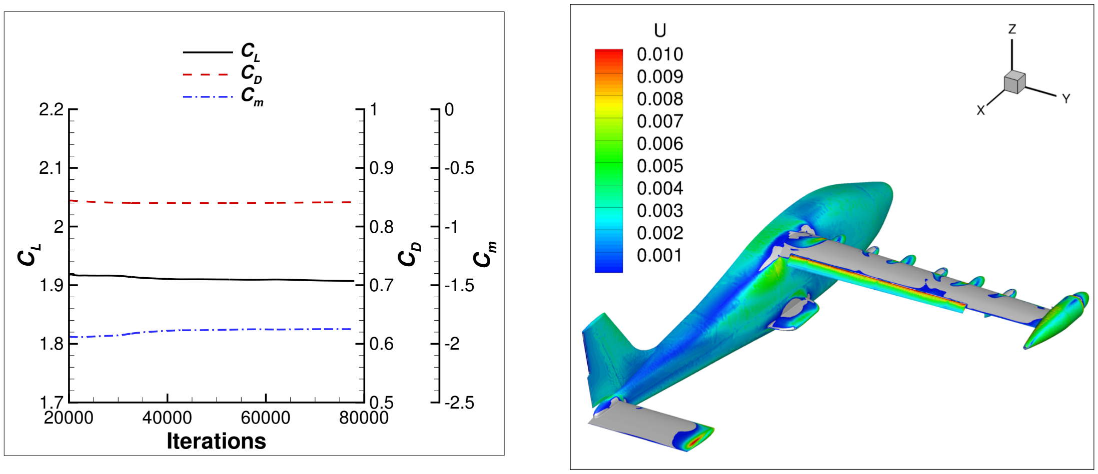

(e) Time-Averaged Coefficients (f) Normalized U Velocity Contours

Figure C212. Convergence History Data and Normalized U Velocity Contours for the Landing Configuration with a 30° Flap Deflection at $M = 0.139$ and $\alpha = 24°$, No Cruise Power, and No High-Lift Blowing.

REPORT DOCUMENTATION PAGE	Form Approved OMB No. 0704–0188

1. REPORT DATE (DD-MM-YYYY) 01-04-2022	2. REPORT TYPE Technical Memorandum	3. DATES COVERED (From - To) 2017-2020

4. TITLE AND SUBTITLE

Computational Analysis of the X-57 Maxwell Airplane at Unpowered Conditions (Preliminary Fuselage)

5a. CONTRACT NUMBER

5b. GRANT NUMBER

5c. PROGRAM ELEMENT NUMBER

6. AUTHOR(S)

Karen A. Deere, Jeffrey K. Viken, Sally A. Viken, Melissa B. Carter, Michael R. Wiese, Norma L. Farr

5d. PROJECT NUMBER

5e. TASK NUMBER

5f. WORK UNIT NUMBER

7. PERFORMING ORGANIZATION NAME(S) AND ADDRESS(ES)

NASA Langley Research Center
Hampton, Virginia 23681-2199

8. PERFORMING ORGANIZATION REPORT NUMBER

9. SPONSORING/MONITORING AGENCY NAME(S) AND ADDRESS(ES)

National Aeronautics and Space Administration
Washington, DC 20546-0001

10. SPONSOR/MONITOR'S ACRONYM(S)

NASA

11. SPONSOR/MONITOR'S REPORT NUMBER(S)

NASA/TM–20210011034

12. DISTRIBUTION/AVAILABILITY STATEMENT

Unclassified-Unlimited
Subject Category 64
Availability: NASA STI Program (757) 864-9658

13. SUPPLEMENTARY NOTES

An electronic version can be found at http://ntrs.nasa.gov.

14. ABSTRACT

The X-57 Maxwell is an all-electric airplane that implements a distributed electric propulsion system to demonstrate that high-efficiency electric propulsion can be integrated with aerodynamics to increase the performance of an airplane. To this end, distributed electric fans were installed on the wing to provide increased flow over the wing at the low takeoff and landing speeds of the X-57. The low-speed lift augmentation allows for a reduction in wing area for cruise optimization. The X-57 wing area was reduced to 42 percent of the wing area of the baseline aircraft, a Tecnam P2006T. With this reduced wing area and the electric propulsion system, it is estimated that the X-57 will cruise on less than one-third the total energy compared to the baseline aircraft. To meet the cruise performance goal at a Mach number of 0.233 at an altitude of 8000 feet, the X-57 has a cruise lift coefficient of 0.7516 and needs to have a cruise drag coefficient of 0.05423 or less. The USM3D computational solver was used to investigate the X-57 performance, without the distributed electric propulsion high-lift system operating. The unpowered X-57 performance is of interest to quantify if the X-57 can meet the cruise drag performance goal, and to document the lift performance of the very small wing at takeoff and landing conditions. The primary configurations investigated in this paper include the cruise configuration with no flap deflection, a takeoff configuration with a 10° flap deflection, and a landing configuration with a 30° flap deflection. The conditions for the cruise configuration were a flight unit Reynolds number of 1.32E+06 per foot, an altitude of 8000 feet, a Mach number of 0.233, and angles of attack from $-2°$ to 24°. At the cruise lift coefficient of 0.7516, the computed drag coefficient is 0.05275. This computed drag is less than the drag coefficient of 0.05423 that is required to meet the X-57 airplane performance goal. However, the computational airplane is a completely smooth geometry and does not account for protuberance drag, nor the drag from steps and gaps in the actual X-57 airplane. Therefore, based upon the CFD drag calculation there is a 10-percent margin to account for some of the differences between the as-built metal fuselage and empennage construction, and the smooth computational geometry. The computed cruise drag also does not account for an induced drag reduction due to the wing-tip propellers and a drag reduction due to laminar flow achieved on the wing. The computed lift to drag ratio is 14.14 at the cruise lift coefficient of 0.7516, and the maximum computed lift to drag ratio is 15.8. The maximum lift coefficient for the cruise configuration was 2.13 at an angle of attack of 15°. The conditions for the takeoff configuration with a 10° flap deflection were a flight unit Reynolds number of 0.986E+06 per foot, an altitude of 2500 feet, a Mach number of 0.149, and angles of attack from $-2°$ to 22°. The maximum lift coefficient for the takeoff configuration was 2.21 at an angle of attack of 16°. The conditions for the landing configuration with a 30° flap deflection were a flight unit Reynolds number of 0.922E+06 per foot, an altitude of 2500 feet, a Mach number of 0.139, and angles of attack from $-2°$ to 24°. The maximum lift coefficient for the landing configuration was 2.58 and occurred at two angles of attack, 10° and 14°. Based on the unpowered maximum lift coefficient of 2.58 for the 30° flap deflection, along with computations of the distributed electric propulsion lift augmentation (not shown in this paper), the X-57 Maxwell is estimated to meet its powered landing goal of a maximum lift coefficient of 4.0.

15. SUBJECT TERMS

X-57 Maxwell Airplane, Distributed Electric Propulsion, CFD, USM3D

16. SECURITY CLASSIFICATION OF:			17. LIMITATION OF ABSTRACT	18. NUMBER OF PAGES	19a. NAME OF RESPONSIBLE PERSON
a. REPORT	b. ABSTRACT	c. THIS PAGE			STI Information Desk (`help@sti.nasa.gov`)
					19b. TELEPHONE NUMBER (Include area code)
U	U	U	UU	198	(757) 864-9658